

5th National Conference on
Technologically Important Crystalline and
Amorphous Solids (TIGAS-2019)

5th & 6th April 2019

Department of Physics & International Research Centre (IRC)



PROCEEDINGS

SPONSORED BY CSIR



KALASALINGAM
Academy of Research and Education
DEEMED TO BE UNIVERSITY

(Under Section 3 of UGC Act 1956)
(Accredited by NAAC with A Grade)

Anand Nagar, Krishnankoil - 626 126,
Srivilliputtur (Via), Virudhunagar (Dt), Tamil Nadu, India



5th National Conference on

**Technologically Important Crystalline and Amorphous Solids
(TICAS-2019)**

5th & 6th April 2019



Sponsored by CSIR

DEPARTMENT OF PHYSICS
School of Advanced Science
Kalasalingam Academy of Research and Education
(Deemed to be University)
(Under Sec. 3 of UGC Act 1956)
(Accredited by NAAC with A Grade)
Anand Nagar, Krishnankoil – 626 126
Srivilliputtur (via), Virudhunagar (Dt.), Tamil Nadu
Ph: 04563-289042, Fax: 04563-289322, www.kalasalingam.ac.in

National Advisory Committee

Dr. S. Athimoolam, Head/ Physics, Anna University, Nagercoil
Dr. D. Basak, Professor, IACS, Kolkata
Dr. J.S. Bhat, professor, Karnatak University, Karnataka
Dr. K. Byrappa, Vice-Chancellor, Mangalore University, Karnataka
Dr. A. Chndrabose, Professor, NIT-Trichy, Tamil Nadu
Dr. K. Chinnakali, Professor, Anna University Chennai
Dr. P.K. Das, Professor, IISC, Bangaluru
Dr. Dipten Bhattacharya, Sr. Principal Scientist, CGCRI, Kolkata
Dr. V. Ganesan, Centre Director, UGC-DAE CSR, Indore, Madhya Pradesh
Dr. L. John Berchmans, Principal Scientist, CECRI, Karaikudi, Tamil Nadu
Dr. A.R. Kulkarni, Professor, IIT Bombay, Mumbai
Dr. Madangopal Krishnan, Scientist, BARC, Mumbai
Dr. Rajnikant, Professor, Jammu University, Jammu & Kashmir
Dr. V. Ramakrishnan, Director, IISER, Thiruvananthapuram, Kerala
Dr. K. Ravi Kumar, Associate Director, AcSIR, Uttar Pradesh
Dr. N. Satyanarayana, Professor, Pondicherry University, Puducherry
Dr. B. Sridhar, Principal Scientist, ICT, Hyderabad, Telangana
Dr. N. Vijayan, Sr. Scientist, NPL, New Delhi

Organizers

Chief Patron

Dr. K. Sridharan, Chancellor
Dr. S. Shasi Anand, Vice President
Mr. S. Arjun Kalasalingam, Vice President

Patrons

Dr. R. Nagaraj, Vice-Chancellor
Dr. V. Vasudevan, Registrar

Conveners

Dr. S. Asath Bahadur, Senior Professor, Department of Physics
Dr. S. Saravanakumar, Assistant Professor, Department of Physics

Organizing Committee Members (Department of Physics)

Dr. M. Muthuvinayagam	Dr. R. Chokkalingam
Dr. N. Nallamuthu	Dr. A. Arivarasan
Dr. D. Vanitha	Dr. M. S. Revathy
Dr. S. Thangarasu	Dr. K.S. Venkatesh
Dr. T. Theivashanthi	Dr. P. Devendran
Dr. S. Jeyavijayan	Dr. N Dhanpal Jeyaram
Dr. M. Krishnakumar	Dr. V. Siva
Dr. V. Sivakumar	Dr. A. Raja
Dr. K. Gurusankar	Dr. S. Sasikumar

Advisors

Dr. P. Selvarengan, Head, Dept. of Physics
Dr. S. R. Srikumar, Professor, Dept. of Physics
Dr. K. Viswanathan, Professor, Dept. of Physics
Dr. E. R. Nagarajan, Head, Dept. of Chemistry

Dr. K. Balamurali, Director - R&D
Dr. K. Sundar, Director,-IRC
Dr. C. Ramalingan, Dean-SAS

April 2019

ISBN 978-81-909237-4-3

Copyright : Department of Physics and Contributors

Published by

Department of Physics, School of Advanced Sciences,
Kalasalingam Academy of Research and Education, Krishnankoil – 626 126, Tamilnadu

Disclaimer

This proceedings consist of papers presented in TICAS-2019 and published in the same version as submitted by the contributors. Any issue of plagiarism / copyright violation will be the sole responsibility of the contributors and not of the Department of Physics, Kalasalingam Academy of Research and Education.



KALASALINGAM
Academy of Research and Education
(DEEMED TO BE UNIVERSITY)
Estd.U/S 3 of UGC Act 1956. Accredited by NAAC with "A" Grade
www.kalasalingam.ac.in | 1800 425 7884

Anand Nagar, Krishnankoil - 626 126
Srivilliputtur (via), Virudhunagar (Dt.)
Tamil Nadu, INDIA.
Ph : 04563 289012 / 42 / 52
e-mail : info@kalasalingam.ac.in
web : www.kalasalingam.ac.in

"Kalvivalal"
Thiru. T. Kalasalingam
Founder Chairman

"Ilayavallal"
Dr. K. Sridharan
Chancellor

Dr. R. Nagaraj
Vice-Chancellor

03.04. 2019

Chancellor's Message



On this new endeavour TICAS-2019, I extend to all my felicitations and welcome with deep appreciation to all the delegates nationwide. I am sure this initiative will give everyone an opportunity to our new ideas on the topics to be discussed. I must congratulate at the kick-off of this conference the organizers for the choosing the right topic for discussion. I am greatly euphoric to learn that the Department of Physics together with the International Research Centre have come together in organizing a National conference on Crystalline and amorphous solids. I have heard about its importance and the importance given to research on this subject. Both types of materials due to its characteristics have found wide range of applications in field of engineering. I am sure towards the end of this seminar all the participants will be enriched with new ideas to carry on their study and research on this topic. I welcome every one of you to the Kalasalingam Academy of Research and Education.

The success of engineering can be attributed to the branch of material science. Materials must be fit enough to endure the stress and strain occurring during its operations. Hence study on inner molecular structure is essential for the manufacture of new materials. In the field of material science, this topic finds importance since the study begins from its molecular structure. Both crystalline and amorphous solids differ in their molecular arrangement thus have drawn attentions of Scientists in development of new materials for varied applications. On the other hand a material that can be easily soluble and can be easily assimilated by human body is used by pharmaceutical researchers. It's my desire that all delegates of this conference by contribute to their best and soak up maximum information for their future perusal. At this moment I must commend the initiatives taken by the Department of Physics together with the International Research Centre in organizing this event and explore the vacuum that is to be filled in the area of crystalline and amorphous solids. Let me assure our continued encouragement to your efforts, till you achieve your objectives.

As I now close my message here I wish to remind you all a famous statement made by Sir. Winston Churchill "in this world of stiff competition the fittest survive", I wish that every one of you become the fittest around.

Dr. K. Sridharan
Chancellor



KALASALINGAM
Academy of Research and Education
(DEEMED TO BE UNIVERSITY)
Estd.U/S 3 of UGC Act 1956. Accredited by NAAC with "A" Grade
www.kalasalingam.ac.in | 1800 425 7884

Anand Nagar, Krishnankoil - 626 126
Srivilliputtur (via), Virudhunagar (Dt.)
Tamil Nadu, INDIA.
Ph : 04563 289012 / 42 / 52
e-mail : info@kalasalingam.ac.in
web : www.kalasalingam.ac.in

"Kalvavallal"
Thiru. T. Kalasalingam
Founder Chairman

"Ilavavallal"
Dr. K. Sridharan
Chancellor

Dr. R. Nagaraj
Vice-Chancellor

03.04. 2019

Vice President's Message



I am contended to know that the Department of Physics, KARE is continuing its efforts in promotion and expansion of knowledge in Physics. The word Physics was first coined by the famous Greek Physicist Tales who thought that all materials are made up of one element water called Physis in ancient Greek. Physics is the fulcrum between all branches of science and inputs theory necessary for further research in every field. The study of matter its physical and chemical properties are the fundamentals for any scientific research. Many Physicists like Archimedes, Anaxagoras, Maria Spiropulu, Sir C. V. Raman and many others dedicated their lifetime towards research in Physics and their findings have become the platform for many researches in modern times. I am confident that the initiative taken by the Department of Physics, KARE will further enhance the research programs in Physics.

Lot of research is being carried out in world today on Crystalline and amorphous solids knowing its applications and advantages in various fields. Their physical and chemical properties draw the attention of scientists and technocrats for their usage in all fields. The word crystal is derived from the Greek word *krustallos*. Development of crystals has found wide applications in development of Lithium batteries that are rechargeable. Such batteries are used in day to day life in mobile batteries. I would like to recollect the Boeing company one of In solid state electronics the crystals are used as source of energy production. And in the study of biology knowledge of crystals are used in the exploration of proteins that is the fundamental constituent of every living organism. The amorphous solids do not have a regular shape in their molecular arrangement and thus called as amorphous solids. They are too widely used in all engineering applications. In the field of electronics these materials are widely used as insulators in the manufacture of MOSFETS and other electronic devices. I must commend the initiatives taken by the Department of Physics together with the International Research Centre in organizing this event and explore the vacuum that is to be filled in the area of crystalline and amorphous solids. Let me assure our continued encouragement to your efforts, till you achieve your objective.

And before I sign off from here my hearty *mazal tovto* all the organizers of TICAS-2019 and wish this event a fruitful outcome. As I welcome all the delegates for the TICAS-2019 I urge all of them to make the best use of this conference and develop their knowledge as a famous goes, "for genius is 99% perspiration and 1% inspiration.

Dr. S. Shasi Anand
Vice President



KALASALINGAM
Academy of Research and Education
(DEEMED TO BE UNIVERSITY)
Estd.U/S 3 of UGC Act 1956. Accredited by NAAC with "A" Grade
www.kalasalingam.ac.in | 1800 425 7884

Anand Nagar, Krishnankoil - 626 126
Srivilliputtur (via), Virudhunagar (Dt.)
Tamil Nadu, INDIA.
Ph : 04563 289012 / 42 / 52
e-mail : info@kalasalingam.ac.in
web : www.kalasalingam.ac.in

"Kalvavallal"
Thiru. T. Kalasalingam
Founder Chairman

"Ilavavallal"
Dr. K. Sridharan
Chancellor

Dr. R. Nagaraj
Vice-Chancellor

Date: 30.03.2019

VICE CHANCELLOR'S MESSAGE

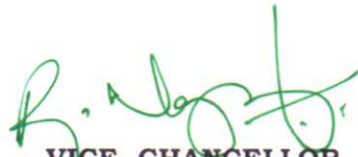


It is my great pleasure to welcome you all to the 5th National conference on Technologically Important Crystalline and Amorphous Solids (TICAS-2019) which takes place in the beautiful premises of Kalasalingam Academy of Research and Education, Krishnankoil on April 5th & 6th, 2019.

The facets of Science, Technology and Engineering are changing very fast. Engineering and Technology is becoming inter and multi-disciplinary, and calls for multi-institutional participation. Major experimental facilities, even in several areas of basic research, require very large material, human and intellectual resources. Science and Technology have become so closely intertwined, and so reinforced each other that, to be effective, any policy needs, to view them together. The continuing revolutions in the field of Advanced Nano and Biomaterials, Spectroscopy and Polymers have had profound impact on the manner and speed with which scientific information becomes available, and scientific interactions take place.

TICAS-2019 provides a forum for the dissemination of original research results, new ideas, research and development, practical experiments, which concentrate on both theory and practices of crystalline and amorphous materials. Academicians, scientists, faculty members, research scholars and students across the India will be participating in this conference.

I wish all the delegates to have a pleasant stay at Kalasalingam Academy of Research and Education. I am certain that this conference will be a nurturing environment for all the participants. I congratulate the Department of Physics for their effort to conduct the conference with the theme technologically important materials which is the need of the day for our Nation.


VICE- CHANCELLOR



KALASALINGAM
Academy of Research and Education
(DEEMED TO BE UNIVERSITY)
Estd.U/S 3 of UGC Act 1956. Accredited by NAAC with "A" Grade
www.kalasalingam.ac.in | 1800 425 7884

Anand Nagar, Krishnankoil - 626 126
Srivilliputtur (via), Virudhunagar (Dt.)
Tamil Nadu, INDIA.
Ph : 04563 289012 / 42 / 52
e-mail : info@kalasalingam.ac.in
web : www.kalasalingam.ac.in

"Kalivallal"
Thiru. T. Kalasalingam
Founder Chairman

"Ilayavallal"
Dr. K. Sridharan
Chancellor

Dr. R. Nagaraj
Vice-Chancellor

Date: 28.03.2019

MESSAGE



With tremendous amount of happiness and satisfaction, I write this foreword to the proceeding of "5th National Conference on Technologically Important crystalline and Amorphous Solid (TICAS-2019)" to be held in our premises between 5th & 6th April 2019.

I have a great pleasure through a varied reading of the abstracts along with the long list of invited speakers that there are more than 100 participants from various institutions across the country in such a way that TICAS-2019 continues to flourish and amplify the tradition of converging all at one place comprising of scientists, researchers, academicians and professionals from all over the Nation. The Conference particularly encourages the interaction of research scholars and budding scientists with the more established scientific community in such a way that it would be a golden opportunity to present and to discuss the systematic investigations of structural, morphological and optical properties of crystals which would enable the progressive path to the state of the art work. I believe that these experts would enlighten the participants to understand and interpret the application oriented details of their research materials in a meaningful way and to open the flood gates of possible emerging areas in the advanced areas of technologically versatile fields.

I congratulate the Department of Physics for organizing this prestigious national event on materials science and related applications. My special thanks are due to the Convenor of the Conference and organizers for their efforts to make this seminar as a grand success.

REGISTRAR

Preface

We are happy to present the proceedings of the 5th National Conference on Technologically Important Crystalline and Amorphous Solids (TICAS-2019) organized by the Department of Physics, School of Advanced Sciences, Kalasalingam Academy of Research and Education, Krishnankoil during 5th & 6th April, 2019. This conference represents the gathering of Materials Science group with 45 research papers presented in this conference and a total of about 150 participants from different states of India. There are 5 invited lectures, 12 oral contributed papers and 33 poster contributed papers are presented in this conference.

The deliberations of the conference cover a wide range of topics of current interest in Materials Science which includes complex solids, energy storage materials, ionic & amorphous solids, optical & optoelectronic materials, magnetic materials, semi-conducting materials, small & macro molecules, smart & nanomaterials and thin films, Theoretical studies on crystalline and amorphous solids, Biomaterials and biosensors and Materials for Environmental and Healthcare. Many contributed papers demonstrate the fundamental inherent strength and application of various materials in crystalline and amorphous nature.

We would like to take this opportunity to thank our Chancellor, Vice President, Vice-Chancellor, Registrar and Advisory committee members who have given constant encouragement and support to organize this conference.

It is a great pleasure to place on record our thanks to the CSIR, New Delhi for the financial support. The members of the local advisory committee and all our colleagues in the Department of Physics, fellow colleagues in other departments, Post Doctoral Fellows and Research Scholars of Physics department who have been a constant source of support in organizing and making this conference a great success, are gratefully acknowledged. The financial support provided by Management, PTA and Alumni association of Kalasalingam Academy of Research and Education is acknowledged gratefully. Finally thanks for all the contributed authors who have given their research papers in time to bring this proceedings successfully.

Dr. S. ASATH BAHADUR
Dr. S. SARAVANAKUMAR
CONVENERS (TICAS-2019)

Content

Sl. No.	Title of the Paper	Page No
INVITED LECTURES		
1	TECHNOLOGICALLY IMPORTANT NANO STRUCTURED MATERIALS FOR INDUSTRIAL APPLICATIONS <i>L. John Berchmans</i>	IL-1
2	STRUCTURAL, SPECTROSCOPIC AND INTERMOLECULAR INTERACTION STUDIES ON A BRONCHODILATOR DRUG <i>S. Athimoolam</i>	IL-2
3	STRUCTURAL AND MAGNETIC PROPERTIES OF Fe-Ga LARGE MAGNETOSTRICTION MATERIALS <i>ManickamMahendran and Vijaynarayanan</i>	IL-3
4	ORGANIC DYES IN DYE SENSITIZED SOLAR CELLS (DSSCS) <i>ChennanRamalingan</i>	IL-4
5	POLYMORPHISM AND X-RAY CRYSTALLOGRAPHY <i>B.Sridhar</i>	IL-5
CONTRIBUTED PAPERS		
1	CYCLIC VOLTAMMETRIC STUDIES OF VANADYL PORPHYRIN <i>A.Murugan, MithunChakrabarty and V. Thandiayyakone</i>	1
2	ELECTRICAL AND DIELECTRIC STUDIES OF L-PHENYLALANINE ADDED Na⁺ ION CONDUCTING POLYMER BLEND ELECTROLYTES <i>S. Shenbagavalli, V. Srividhya Devi, K. Sundaramahalingam, N. Nallamuthu, S. Jayanthi</i>	5
3	SPECTROSCOPIC INVESTIGATION USING DENSITY FUNCTIONAL THEORY CALCULATIONS ON 5-CHLORO-2-HYDROXY ACETOPHENONE <i>V. Lavanya, A. Muthukumar, M. Muthumeenal, R. Muneeswaran, S. Jeyavijayan</i>	10
4	MOLECULAR STRUCTURE AND HYDROGEN BONDING INTERACTIONS OF 7,8-DIHYDRO-3-METHYL-1-PHENYL-1H-PYRAZOLO[3,4-B]QUINOLIN-5(H)-ONE (PYRZ) <i>Arockia Jeya Yasmi Prabha E, Athimoolam S</i>	15
5	APPROACH TO SYNTHESIS, HYDROGEN BONDING ANALYSIS BY HIRSHFELD SURFACE AND MULLIKEN POPULATION ANALYSIS OF PHARMACEUTICAL COCRYSTALS OF THEOPHYLLINE (A BRONCHODILATOR DRUG) <i>L. Mary Novena, S. Suresh Kumar and S. Athimoolam</i>	18
6	STRUCTURAL, SPECTRAL AND ANTICANCER STUDIES ON 5-FLUOROURACIL HYDROQUINONE <i>S. Suresh Kumar and S. Athimoolam</i>	23
7	INVESTIGATION STUDY ON STRUCTURAL AND SPECTROSCOPIC FEATURES OF IMPROVED BIO-ACTIVITY OF NITRATE SALT OF VITAMIN B3 (NICOTINIC ACID) <i>M. Mary Latha, L. MaryNovena, S. Athimoolamand B. Sridhar</i>	26
8	CO-PRECIPIATED NANOSTRUCTURED ZINC SULPHIDE FOR PV TECHNOLOGY <i>S.Rahulgorky, T.Santhosh, R.Chokkalingam, M.S.Revathy</i>	30

Sl. No.	Title of the Paper	Page No
9	STRUCTURAL PHASE TRANSITION ANALYSIS OF LEAD FREE BARIUM TITANATE MODIFIED SODIUM POTASSIUM NIOBATE SOLID SOLUTIONS <i>S. Sasikumar, S. Saravanakumar, S. AsathBahadur, D. Sivaganesh</i>	33
10	EFFECT OF NEODYMIUM DOPING IN BaTiO₃ ON STRUCTURAL PROPERTIES <i>S. Sasikumar, S. Saravanakumar, S. AsathBahadur, D. Sivaganesh</i>	36
11	REVIEW OF DISCRIMINATION OF NORMAL TISSUES FROM CANCER TISSUES BY FLUORESCENCE SPECTROSCOPY <i>M.S.Revathy, K. Viswanathan, Ni Nyoman Tri Puspaningsih, S. Jeyavijayan, K.Rajeswari, K.Gurusankar</i>	39
12	EFFECT OF METAL OXIDE FILLERS ON THE ELECTRICAL AND ELECTROCHEMICAL PROPERTIES OF PVP:NANO₃ SOLID POLYMER ELECTROLYTES <i>M.Vahini, M. Muthuvinayagam</i>	46
13	SYNTHESIS, LATTICE ENERGY CALCULATION AND DOCKING STUDIES ON CINNAMOYLPROLINE <i>M. Venkateshan and J. Suresh</i>	50
14	STRUCTURE AND CHARGE DENSITY ANALYSIS OF (1-x)SrTiO₃-x(Na_{0.5}Bi_{0.5})TiO₃ LEAD FREE CERAMICS <i>O.V. Saravanan, R. Saravanan, S. Sonai, T. Jayapandi, S. Meenadevi, S. Manimegalai</i>	54
15	SYNTHESIS, STRUCTURAL INVESTIGATION AND CHARGE DENSITY ANALYSIS OF (1-x)Na_{0.5}K_{0.5}NbO₃-xSrTiO₃ LEAD FREE PIEZOELECTRIC CERAMICS <i>S. Sonai, O.V. Saravanan, S. Sasikumar, R. Saravanan</i>	57
16	STUDIES ON NIOBIUM DOPED HYDROXYAPATITE NANOCRYSTALS SYNTHESIZED BY SOL GEL METHOD <i>V.Kavitha, S.Saranya, M.Prema Rani</i>	60
17	A THEORETICAL STUDY OF ELECTRONIC AND REACTIVITY PROPERTIES OF ANTI-HYPERSENSITIVE DRUG HYDROCHLOROTHIAZIDE <i>R. Niranjana Devi</i>	64
18	PREPARATION AND CHARACTERIZATION OF PRISTINE BISMUTH MOLYBDATE BY FACILE SINGLE POT MICROWAVE-COMBUSTION METHOD <i>A. Shameem, P.Devendran, V. Siva, A.Murugan, Shamima Hussain, S.A.Bahadur</i>	67
19	PREPARATION AND CHARACTERIZATION OF AMINO ACID ADDED Na⁺ ION CONDUCTING POLYMER BLEND ELECTROLYTE <i>V. Srividhya Devi, S. Shenbagavalli, K. Sundaramahalingam, N. Nallamuthu, S. Jayanthi</i>	71
20	FUNCTIONAL AND AC IMPEDANCE ANALYSIS OF AMMONIUM THIOCYANATE DOPED PEO/PVP POLYMER BLENDS <i>K. Sundaramahalingam, M. Muthuvinaygam, N. Nallamuthu, D. Vanitha</i>	75
21	ELECTRICAL IMPEDANCE STUDIES OF PVA-PVP-Na₂SO₄ POLYMER ELECTROLYTES FOR SOLID STATE BATTERY APPLICATION <i>B. J. Gogoi, K. Sundaramahalingam, N. Nallamuthu, A. Murugan</i>	79

Sl. No.	Title of the Paper	Page No
22	SYNTHESIS OF SURFACE MODIFIED TiO₂ NANO CRYSTALLITES WITH Ag NANOPARTICLE <i>S.Babu, Rajajeyaganthan Ramanathan</i>	82
23	INVESTIGATION OF Mn₃O₄ NANOPARTICLES DECORATED ON CARBON SPHERES BY HYDROTHERMAL METHOD <i>V. Selvabarathi, S. Saraswathi, M. Sindukavi, S. Ezhilarasi, R. Ranjithkumar, C. Sambathkumar, A. Arivarasan, N. Nallamuthu, S. AsathBahadur, P. Devendran</i>	84
24	STRUCTURAL AND IMPEDANCE STUDIES ON POLYVINYL ALCOHOL AND CORNSTARCH BLEND POLYMER ELECTROLYTES <i>M. AnandhaJothi, D. Vanitha, S. AsathBahadur</i>	87
25	STRUCTURAL AND OPTICAL STUDIES ON A NEW THIRD ORDER NONLINEAR OPTICAL CRYSTAL: β - ALANINIUM p - TOLUENESULFONATE <i>M. Suresh, S. AsathBahadur and S. Athimoolam</i>	91
26	SENSITIVITY ENHANCEMENT OF SURFACE PLASMON RESONANCE SENSOR WITH 2D MATERIAL COVERED NOBLE AND MAGNETIC MATERIAL (NI) <i>A. Nisha, P. Maheswari, P. M. Anbarasan, K. B. Rajesh, Z. Jaroszewicz</i>	94
27	QUANTUM CHEMICAL INVESTIGATION ON STRUCTURAL, MOLECULAR ORBITAL AND POPULATION ANALYSIS OF GUANIDINIUM P- TOLUENESULFONATE: A NONLINEAR OPTICAL MATERIAL <i>V. Siva, S. AsathBahadur, A. Shameem, A. Murugan, S. Athimoolam</i>	98
28	INVESTIGATION ON CRYSTAL GROWTH AND SOLID STATE PROPERTIES OF NONLINEAR OPTICAL SINGLE CRYSTAL: 2-AMINOPYRIDINIUM PHTHALATE <i>M. Ajay, A. Ajaykumar, M. Ajitha, V. Siva, S. AsathBahadur</i>	102
29	EFFECT OF EUROPIUM CONCENTRATIONS ON LUMINESCENCE PROPERTIES OF Dy³⁺ DOPED BORATE GLASSES FOR WHITE LEDS <i>M.Vijayakumar, S.K. Tiwary, K.Marimuthu</i>	106
30	STRUCTURAL, MORPHOLOGICAL AND OPTICAL ANALYSIS OF PVP ASSISTED HEMATITE NANOPARTICLES BY CHEMICAL SYNTHESIS METHOD <i>P. Pandiselvi, K. Pavithra, S. Ezhilarasi, S. Arunpandiyam, R. Ranjithkumar, P. Devendran, A. Arivarasan</i>	109
31	STRUCTURAL, MORPHOLOGICAL AND OPTICAL PROPERTIES OF Cu₂CdS₃ THIN FILMS FOR SOLAR CELL APPLICATION <i>S. Abirami, M. Gayathri, S. AsathBahadur</i>	112
32	INVESTIGATION OF NANOCRYSTALLINE Cu₂ZnSnS₄ THIN FILM ABSORBER LAYER FOR PHOTOVOLTAIC APPLICATION <i>A. Murugan, V. Siva, A. Shameem, S. AsathBahadur</i>	115
33	STRUCTURAL CHARACTERIZATION STUDIES OF ZnO/NiO NANOCOMPOSITE, SYNTHESISED BY GEL COMBUSTION METHOD <i>M.Raveena, R. Packiaraj, N. Nallamuthu, K.S.Venkatesh</i>	118
34	SYNTHESIS AND CHARACTERIZATION OF A NON-LINEAR OPTICAL CRYSTAL 2-AMINOPYRIDINIUM TRICHLOROACETATE <i>R. Arunkumar, S. Kamala Sri, S. Sruthi, M. Venkateshan and R. Vishnu Priya</i>	121

Sl. No.	Title of the Paper	Page No
35	PREPARATION AND CHARACTERIZATION OF RUBIDIUM DOPED NiO THIN FILMS <i>S. Sebastian, I. Kulandaisamy, S.Valanarasu, S. Saravanakumar, P.Diana</i>	124
36	GREEN SYNTHESIS OF SILVER SOL USING PHYLLANTHUS RETICULATUS* <i>M.S.Revathy, Gnanalakshmi S, Gunavathi D, Archana R, K.Viswanathan</i>	127
37	ELECTROCHEMICAL ANALYSIS OF CUO NPS FOR SUPERCAPACITOR APPLICATION <i>R. Packiaraj, P.Devendran, K .S.Venkatesh, S. AsathBahadur, N. Nallamuthu</i>	129
38	IMPROVED SUPERCAPACITOR PERFORMANCE OF MnO₂ NANORODS BY REDOX-ACTIVE ELECTROLYTE <i>C. Selvameenakshi, S. Arunpandiyam, S. EzhilArasi, A. Arivarasan</i>	133
39	CHARGE TRANSFER CONTRIBUTIONS NON-LINEAR OPTICAL PROPERTY OF 2-AMINOPYRIDINIUM DIHYDROGEN PHOSPATE BASED ON <i>AB-INITIO</i> HF AND DFT CALCULATIONS <i>G. Sivaraj, N. Jayamani, V. Siva</i>	138
40	COPPER VESSEL EFFICIENCY AGAINST DIFFERENT DRINKING WATERS <i>A. Vinothkumar, S. Mugeshkumar, V. Vanitha, Naidu DhanpalJayram</i>	143
41	PREPARATION AND CHARACTERIZATION OF Zn DOPED TiO₂ NANOPARTICLES FOR PHOTO CATALYTIC ACTIVITY <i>N. Nithya, P. Maheswari, G. Bhoopathi, G. Magesh</i>	146
42	STRUCTURAL AND BONDING BEHAVIOR OF TiO₂ IN RUTILE PHASE <i>D. Sivaganesh, S. Saravanakumar, V. Sivakumar, K.S. Syed Ali, T. K. Thirumalaisamy, P. Meenakshi, S. Meera, S. Monisha</i>	149
43	STRUCTURAL ANALYSIS AND BONDING BEHAVIOR OF BaZrO₃ <i>D. Sivaganesh, T. C. Shamli, S. Saravanakumar, V. Sivakumar, S. Sasikumar, K.S. Syed Ali, T. K. Thirumalaisamy</i>	152
44	X-RAY CHARACTERIZATION OF Ge AND Ge_{0.95}Mn_{0.05} <i>K.S. Syed Ali, Citlalli Alaniz, Emily Covarrubias, R.A.J.R. Sheeba, S. Israel, S. Saravanakumar</i>	155
45	DESIGN OF A MULTI-COMPONENT SYSTEM INVOLVING NUCLEOBASE-GALLIC ACID STABILISED BY TETRAMERIC AND PENTAMERIC WATER CLUSTER <i>Sundaramoorthy Gomathi and Packianathan Thomas Muthiah</i>	160

INVITED LECTURES

TECHNOLOGICALLY IMPORTANT NANO STRUCTURED MATERIALS FOR INDUSTRIAL APPLICATIONS

L. John Berchmans

Senior Principal Scientist & Head,
Electro pyrometallurgy&Electroplating Division,
CSIR - Central Electrochemical Research Institute (CSIR - CECRI),
Karaikudi – 600 003, Tamil Nadu.
E mail: ljberchmansns@gmail.com

Abstract

This lecture deals with the importance of Advanced Nanomaterials specifically for societal applications which relates to energy production, purification of water, nano-electronics and intelligence coating technologies.

India's population around 130 crores is growing at an annual rate of 1.58%. Fossil fuel energy becomes scarcer. India will face energy shortages due to increase in oil prices and energy insecurity within next few decades. The India's economy shows that the GDP growth rate of 7.5% which makes it the second fastest emerging economy.

Energy is the foundation stone for modern life and priority in eradicating the poverty across the globe. The World Energy status and its importance has predicted that fossil based oil, coal and gas reserves will be exhausted in another ten decades. It is most urgent to identify alternate energy sources and its storage in an efficient manner. Such technologies can reduce carbon emissions, clean air and put our civilization on a more sustainable footing.

The energy storage through rechargeable batteries are the potential sources for energy saving and utilization. These batteries are used in Portable consumer electronic devices, automotive and aircraft systems, UPS and hybrid electric vehicle. Rechargeable batteries namely Pb-PbO₂ (2V), Ni-Fe, Ni-Cd, Ag-Zn (1.35V), Li-ion and polymer (4V) are mostly used for energy storage. Nano materials for the fabrication of cathodes namely LiMn₂O₄, LiCoO₂, LiNiO₂, LiFePO₄ are the potential areas for innovation.

The long-term development of the global water situation is closely connected to the growth of the world population and global climate change. Hence, the demand for fresh water is growing dramatically and the food production must also be doubled. About 70% of the world's freshwater is being consumed for agricultural and irrigation processes. Hence, the need for saving the water resources and also utilization of the water and waste water are to be processed.

A variety of methodologies, technologies and innovative nano materials are applied for the purification and regeneration of water from different sources. Conventional decontamination processes such as chlorination and ozone treatment consume a large quantity of chemical agents and can produce toxic byproducts. Hence, improved technologies and materials are to be innovated to reduce the toxicity of the contaminated water. Carbon, Metal-based, Polymeric nano adsorbents and Zeolites are mostly used for the purification of water. Nanocomposite membranes comprising of mixed matrix and surface-functionalized membranes are used as filtration media. Metal oxide nanoparticles (Al₂O₃, TiO₂) can help to increase the mechanical and thermal stability of polymeric membranes. Photocatalysis is an advanced oxidation process which can be employed in the field of water and wastewater treatment, in particular for oxidative elimination of micropollutants and microbial pathogens. TiO₂, WO₃ and complex oxides are used for the purification and photo oxidation of industrial effluents particularly dye stuffs.

Research in magnetism are related to recent advances in nanosciences and nanotechnologies. Nanocrystalline ferromagnetic materials offer a new possibilities for a variety of phenomena including soft, hard and super paramagnetic behaviour. For example, the introduction of relatively soft magnetic steels as magnetic cores in transformers around one hundred years ago enabled the more efficient distribution of electrical energy from its source to factories, public spaces and private homes.

Applications range for instance, from the large variety of hard magnets widely employed in everyday life, to sophisticated magnetic sensors controlling artificial satellites and the mapping of tiny magnetic fields in the human brain.

Piezoelectric and electrostrictive ceramics, fiber optic sensor materials in nano size are to be explored for electrical and electronics for miniaturizing the devices.

In the area of materials protection and to reduce the corrosion, nanostructured materials are to be investigated for the protection corrosion of different materials. Polymer nanocomposite coatings combine with organic polymers and advanced inorganic materials can reduce the materials loss against corrosion.

A variety of methods such as Mechanical alloying, ball milling, Combustion Synthesis, Sol–gel technique, Molten salt synthesis etc. have been developed for the preparation of nano materials. This lecture gives an overview on the Nano structured materials processing and their applications in industries.

STRUCTURAL, SPECTROSCOPIC AND INTERMOLECULAR INTERACTION STUDIES ON A BRONCHODILATOR DRUG

S. Athimoolam

Department of Physics, University College of Engineering, Nagercoil, Anna University, Nagercoil – 629 004

Email: athi81s@yahoo.co.in

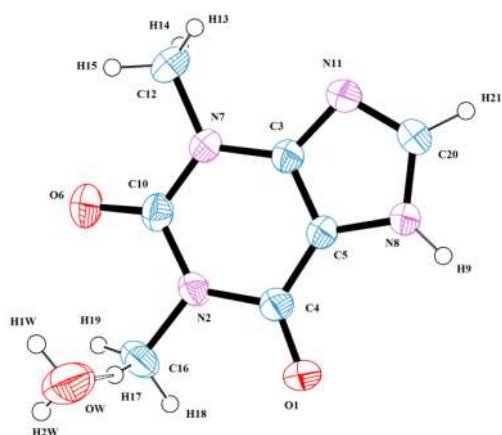
Abstract

Throughout the world of research, development of new drugs and drug-delivery systems are increasing in a rapid manner. To meet the demand of the rapid drug-delivery system, the pharmaceutical industry has to improve the physico-chemical properties of active pharmaceutical ingredient (API) available in market. APIs exist in different solid crystal form such as polymorphs, solvates, hydrates, salts and cocrystals. As the drug substances are unavoidable materials in current societal scenario, more attention has now being paid on discovery of drug. The growing incident of poor solubility and stability of the drug development is a notable factor which lowers the bioavailability of those drugs that are administered by oral route. Even though there are many tactics to enhance the bioavailability of the drug, it depends only on the physical and chemical nature of the fundamental molecules. Solubility is an essential parameter to influence the bioavailability of the drug to reach the site of action. For increasing the solubility and dissolution of the drug, salt formation whereas recently co-crystals have attracted the attention of the researchers. It is possible to alter the acidic and basic nature of the drug which is of poorly soluble in water. Forming salts with inorganic acids and cocrystals with co-formers may increase the solubility and therapeutic effectiveness of the drug. Crystal engineering provides route for this. In order to do the task, a detailed knowledge about crystallization process is crucial. Crystallization is a tool to understand the drug molecules, its structure and inter- or intra- molecular forces involved in the molecules. With the use of X-ray radiation technique the crystal structure is determined which also gives information on the geometry of the molecule and intermolecular interactions. Hydrogen bonds, which plays an important role in crystal engineering controls the crystallization, packing and morphology of the crystal structure. The quantum chemical calculations are performed using Gaussian 09 software package. The experimentally observed vibrational spectra are compared with the data obtained by quantum chemical method.

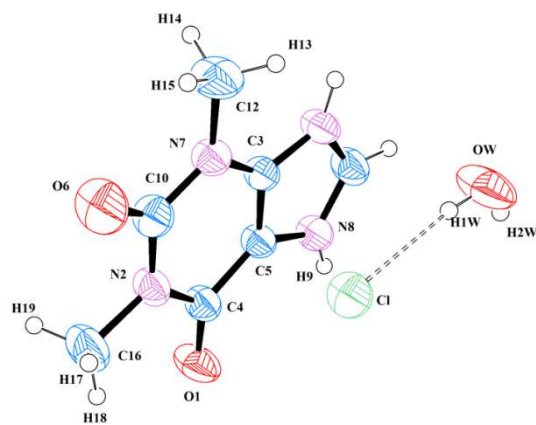
Theophylline and its pharmaceutical application

Xanthines are compounds obtained from plants and it is included in daily life products such as coffee, energetic drinks, tea and chocolate. Methylated xanthines known to be methylxanthines which includes Theophylline, Caffeine and Theobromine. Both Theophylline and Caffeine have pharmacologic mechanism of action. Caffeine plays its role in central nervous stimulant while theophylline in airway borne diseases. Theophylline, most commonly used methylxanthine was first extracted from tea leaves and it has been pharmaceutical use since 1902. Initially, it is used as diuretic and the bronchodilator property was identified later. It becomes the most widely prescribed drugs used as bronchodilator. It is used to treat bronchial asthma and chronic obstructive pulmonary disease (COPD). Recent studies show that theophylline possesses anti-inflammatory effect in asthma and COPD at lower concentration. The solid state properties of theophylline are in the attention of pharmaceutical research. Also, theophylline possesses a pyridine and an imidazole ring structure which is a five-membered nitrogen containing heterocyclic structure.

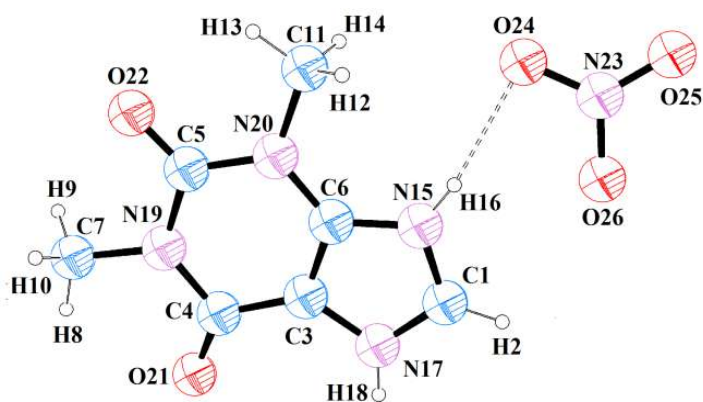
Five crystals of theophylline were grown, namely, Theophylline monohydrate (TH), Theophyllinium chloride monohydrate (THC), Theophyllinium nitrate (THN), Theophylline resorcinol monohydrate (THR) and Theophylline pyrogallol monohydrate (THPY). The Single crystal XRD studies help to identify the structure of the molecule and the interactions involved between the molecules in crystalline assembly. Also, vibrational analysis was done to characterize the spectroscopic features. It is always interesting to correlate the structure activity relation of such type of pharmaceutically important chemical species. The results are really meaningful for the further improvement of the drug for societal applications.



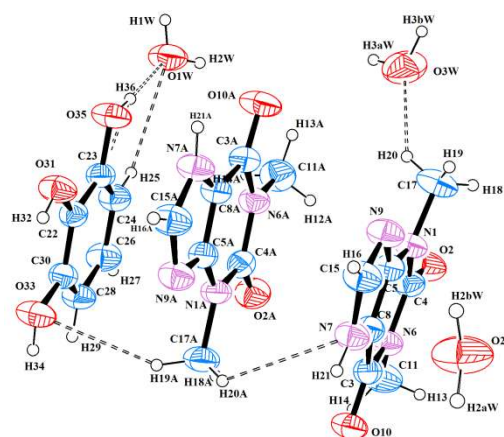
ORTEP diagram of TH - a bronchodilator



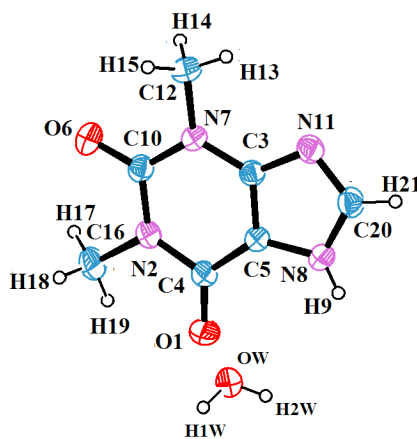
ORTEP diagram of THC - drug salt



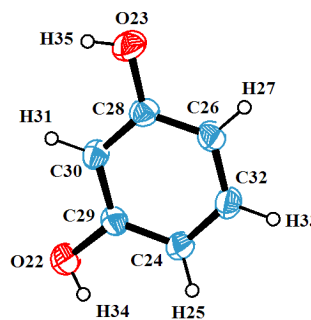
ORTEP diagram of THN - drug salt



ORTEP diagram of THPY - cocrystal



ORTEP diagram of THR - cocrystal



Keywords: Bronchodilator, Theophylline, Crystal Structure, Hydrogen bonding, Spectroscopy

STRUCTURAL AND MAGNETIC PROPERTIES OF Fe-Ga LARGE MAGNETOSTRICTION MATERIALS

ManickamMahendran* and Vijaynarayanan

Smart Materials Lab, Department of Physics

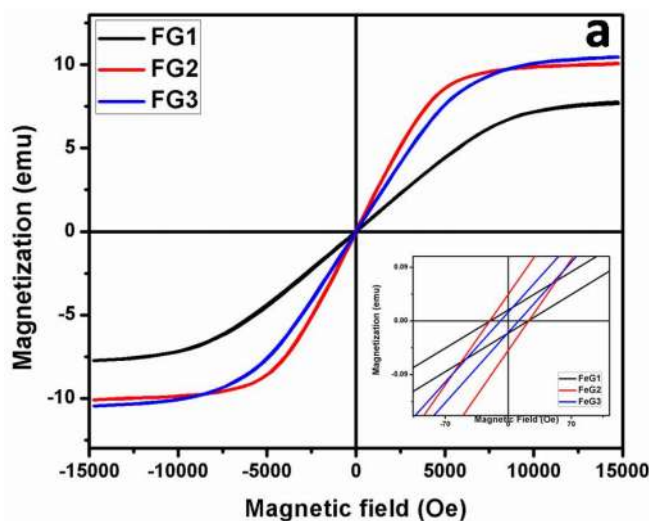
Thiagarajar College of Engineering,

Madurai-625015

*Email: manickam-mahendran@tce.edu

Abstract

Active Magnetic Smart Materials are broadly classified into Ferromagnetic Shape Memory Alloys (FSMAs) and Magnetostrictive (MS) Materials. One of the active FSMAs are Ni-Mn-Ga alloys and the popularly known MS materials are Galfenol (Fe-Ga) and Terfenol-D (Tb-Dy-Fe). Both these materials play a vital role in modern day actuators and sensors. The rare earth based Giant Terfenol-D magnetostrictive material possesses high magneto-mechanical coupling energy to fabricate an actuator. However it has a complex structure and it involves a laborious process to prepare the test sample. On the other hand, a newly developed Fe-Ga alloy can be used as a better actuator than its counterpart Terfenol-D. Fe-Ga possesses stable and remarkable mechanical properties suitable for being used as an effective candidate material for making actuators. MS material is one of the multifunctional materials widely used in actuator applications. Fe-Ga single crystal alloy was crushed into powder form and annealed under various temperatures, to study the magneto-structural-mechanical and thermal property. SEM micrographs exhibited the homogenous rough facets, with the increase of annealing temperature the Ga content gradually diffused inside the sample. The occurrence of exothermic peak in DSC is mainly attributed to the formation of $D0_3$ phase. The elemental mapping of Fe K signal and Ga K signal indicated no gradient in Ga content and the Ga is evenly distributed within the alloy, the selected rectangular area of SEM clearly depict the co-existence of Fe and Ga elements in the alloy. When the magnetic field is increased the magnetization increased linearly until the saturation magnetization is reached, the material changed from disordered A_2 phase into BCC $D0_3$ phase and then back to the disordered A_2 phase this confirms the optimized Fe-Ga samples can be used in sensor and actuator applications.



Keywords: Smart Materials, Ferromagnetic Materials, Magnetostriction Materials, Actuators, Saturation Magnetization

ORGANIC DYES IN DYE SENSITIZED SOLAR CELLS (DSSCS)

ChennanRamalingan

Department of Chemistry, School of Advanced Sciences, Kalasalingam Academy of Research and Education (Deemed to be University), Anandnagar, Krishnankoil – 626 126, India
e-Mail: ramalinganc@gmail.com; c.ramalingan@klu.ac.in

Abstract

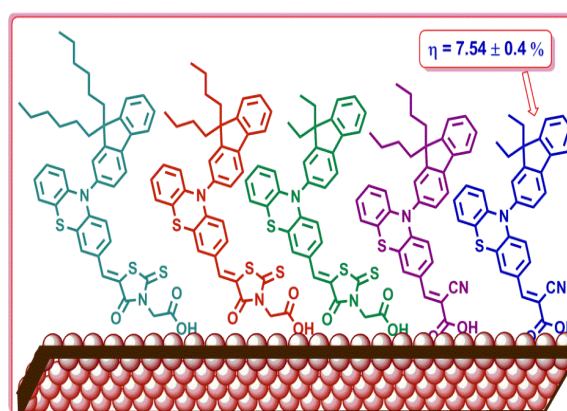
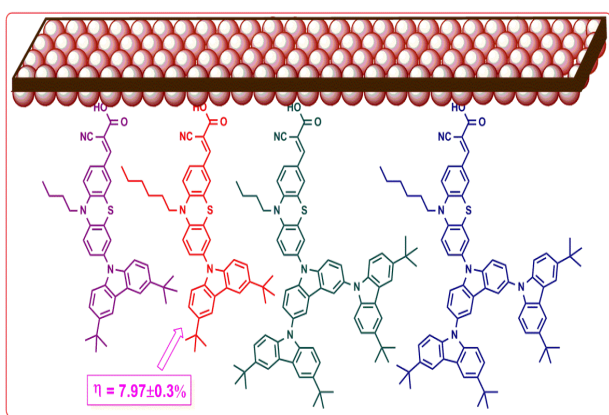
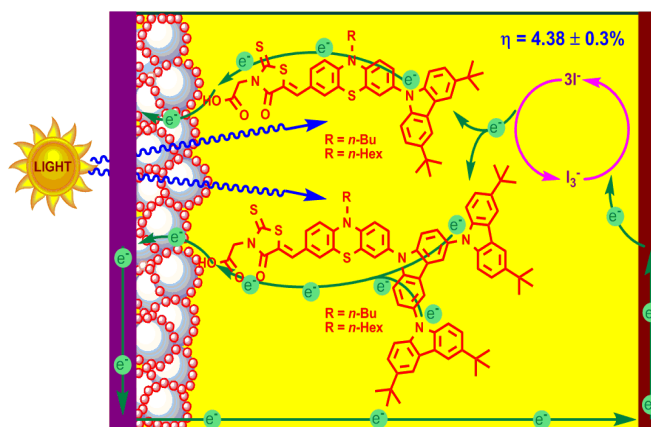
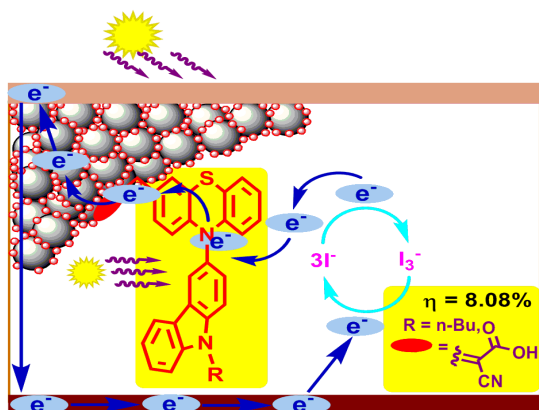
Economically beneficial systems for the exploitation of renewable energy have never been more urgently required: there is a growing consensus that burning fossil fuels is leading to dangerous accumulation of carbon-di-oxide in the environment, and fossil fuel resources are in long term decline. Solar energy, particularly, is the only source with the proven capacity to meet the increasing energy needs of the globe. *Solar Cells*, also called photovoltaics, are devices based on solar technology which convert sunlight directly into electricity under the photovoltaic effect. Although silicon based solar cells conquered the commercial market, their expensive investment made the researchers to develop a new technology, called Dye-Sensitized Solar Cells. The first dye which has been used for DSSC is Ruthenium poly pyridine based one, a noble metal carrying dye.

Organic dyes in dye-sensitized solar cells:

Organic dyes as an alternative to the noble ruthenium based sensitizers exhibit many advantages:

- Can be conveniently designed and synthesized.
- Superior to Ru based dyes in terms of cost and environment issues.
- The molar extinction coefficients of organic dyes are usually higher than those of ruthenium complexes, making them attractive for thin film and solid-state DSSCs.

Recently, we have been involved in design and synthesis of novel metal free organic dyes possessing various homo/heterocyclic structural motifs for efficient dye-sensitized solar cells. A few of our recent findings include design and synthesis of a diverse range of carbazole / multicarbazole / phenothiazine / fluorene possessing dyes as efficient sensitizers for dye-sensitized solar cells. Representative examples of general structure of the dyes which have been developed in our laboratory are furnished below.



The lecture would cover the history, importance, principle, development, and our recent findings related to dye sensitized solar cells.

REFERENCES

1. Grätzel, M. *et al.*, *Nature*, **1991**, 353, 737.
2. Grätzel, M. *et al.*, *Chem. Rev.*, **1995**, 95, 49.
3. Oreskes, N. *Science*, **2004**, 306, 1686.
4. Ramalingan, C. *et al.*, *Phys. Chem. Chem. Phys.*, **2016**, 18, 30105.
5. Ramalingan, C. *et al.*, *Electrochim. Acta.*, **2017**, 246, 1052.
6. Ramalingan, C. *et al.*, *Tetrahedron*, **2017**, 73, 278.
7. Ramalingan, C. *et al.*, *Electrochim. Acta.*, **2018**, 268, 347.

POLYMORPHISM AND X-RAY CRYSTALLOGRAPHY

B.Sridhar

Principle Scientist,
Center for X-ray Crystallography,
CSIR-Indian Institute of Chemical Technology,
Hyderabad – 500 007, India.

Abstract

Polymorphism has important consequences in the development of drugs. Polymorphism is the ability of the same drug molecule to crystallize more than one different crystal structure and that can have profound effect on physical, chemical and pharmaceutical properties of the drug. The variation in properties of a drug substance can lead to differences in dissolution rate, oral absorption, bioavailability, and toxicology. Also, energy differences between forms are relatively small; form inter-conversion is common and can occur during routine manufacturing operations, in drug product formulation, storage and use. Appearance of a new solid form in final drug product can result in product withdrawal.

X-ray diffractometry is a generally applied method in the pharmaceutical industry to investigate the polymorphism of drug substances, as well as to monitor the occasional changes of the modification during different steps of the formulation procedure. X-ray powder diffraction is the best first pass method, to not only discriminate solid-forms but also provide critical data for property determination and structural exploration. The presentation covers the application of X-ray crystallography techniques in drug polymorphism, with specific examples to recent advances.

CONTRIBUTED PAPERS

CYCLIC VOLTAMMETRIC STUDIES OF VANADYL PORPHYRIN

A. Murugan¹, Mithun Chakrabarty² and V. Thandiayyakone³

¹Department of Chemistry, North Eastern Regional Institute of Science and Technology, Nirjuli-791109, Arunachal Pradesh

²Department of Chemistry, St. Anthony's College, Shillong-793001, Meghalaya

³Science and Humanities, P.A.C. Ramasamy Raja Polytechnic College, Rajapalayam, Tamil Nadu

Email: amu@nerist.ac.in

Abstract

The ligand meso-5,10,15,20-Tetrakis(*o*-nitrophenyl)porphyrin, [T(*o*-NO₂)PP] and its vanadyl metal complex [VO(T(*o*-NO₂)PP)] were synthesized and Vanadyl meso-5,10,15,20-Tetrakis(pyridyl)porphyrin VO[TpyP] was prepared from meso-5,10,15,20-Tetrakis(pyridyl)porphyrin [TpyP]. Formation of the vanadyl porphyrin complexes was confirmed by UV-visible spectrophotometer. Oxidation potential of the metalloporphyrins were recorded by cyclic voltammetry (CV). The present studies of [VO(T(*o*-NO₂)PP)] and VO[TpyP] reveals that they undergoes two successive oxidation processes.

Keywords: Vanadyl porphyrin cyclic voltammetry

1. Introduction

Proteins and enzymes are formed from metal complexes of porphyrins and related compounds. They are found to work as redox and rearrangement catalysts¹. The involvement of metalloporphyrins in electron transport in biological systems has made the study of electrochemical properties of particular interest. Both the central metal atoms and the porphyrin ring are electroactive center. The function of the metal present in the chlorophyll is found to change the properties of porphyrin ring reactions through electron transfer. But in the case of cytochromes metal atom is not involved in electron transfer process². Cyclic voltammetric studies have shown some considerable change in the oxidation potentials. Electrophilic substitutions in the *exo*-positions of the pyrrole ring shift the oxidation potentials to higher side. Substitution in the phenyl ring with electron withdrawing substituents is found to shift the oxidation potentials to higher side, while substitution with electron donating group in the phenyl ring lowers the oxidation potentials.

Oxidation of Ni(T(*p*-X)PP) where X = -CH₃, -COOCH₃, -NO₂ in dichloromethane are reported in the literature³. Ni(T(*p*-CH₃)PP) was found to exhibit a single oxidation at 1.00V and 1.20V while Ni(T(*p*-COOCH₃)PP) exhibit only a single oxidation at 1.17V. The peak current of the later indicated two electron transfer processes. For Ni(T(*p*-NO₂)PP) all peaks were found to be shifted anodically. The shift in the first oxidation was found to be more than for the second oxidation. Ni(T(*p*-X)PP), X = electron donating or weak electron- withdrawing group

exhibited two separate oxidations, while for compounds containing X = strong electro withdrawing group exhibited only a single oxidation. The first oxidation of Ni(T(*p*-CH₃)PP) in dichloromethane yielded a brown colour solution which corresponds to [Ni(II)TPP]⁺. Removal of the second electron yielded a green coloured solution. Electrochemical oxidation of MnTPPCL, Mn[T(*p*-OCH₃)PP] and Mn(OEP)Cl have been reported⁴⁻⁶. The one electron oxidation product for each of the system [-1.1 V Vs SCE] have been reported.

Normally, metal d_{xy}/d_{x²-y²}-porphyrin (a_{1u})/(a_{2u}) interaction do not occur in planar porphyrin complexes. This is because the metal d-orbitals are orthogonal to porphyrin ligand a_{1u}/a_{2u} HOMOS. Walker and Co-workers⁷⁻⁹ have reported that d orbitals of the metal and a_{1u}/a_{2u} orbitals of porphyrin ligand can have interactions in ruffle and saddle distortions. Similar view is reported by Ghosh et al¹⁰⁻¹¹, existence of such interactions is reported by Harada et al¹² in vanadyl complexes of octaphenyl porphyrin (VO(OPP)) and vanadyl dodecaphenyl porphyrin (VO(DPP)). They observed that the porphyrin with saddle distortion undergoes disproportionation on oxidation and is attributed to destabilization of a_{1u} orbital leading to accidental degeneracy with a_{2u} orbital. Thus, a_{1u} type cation radical is unstable and disproportionate to dication and neutral species. Thus, HOMO-LUMO gap narrowing down is observed in the voltammogram. They further pointed out that in vanadyl porphyrins (VO(DPP)) (vanadyl dodecaphenyl porphyrin) due to ligand distortion, a_{1u} orbital is elevated leading to the narrowing of HOMO-LUMO gap. This narrowing results in lowering

of the oxidation potentials in the voltammogram. The present work was carried out because of very limited availability of cyclic voltammetric studies on vanadyl porphyrins.

2. Synthesis of Porphyrins

2.1. meso-5,10,15,20-Tetrakis(o-nitrophenyl) porphyrin

meso-5,10,15,20-Tetrakis(o-nitrophenyl) porphyrin was prepared by a literature method¹³. In a 500 mL round bottom flask fitted with nitrogen bubbler *o*-nitro benzaldehyde (0.4952g, 2.98 mmol) and pyrrole (210 μ l, 2.98 mmol) were dissolved in 300 mL of dichloromethane. After purging nitrogen for 10 min, the condensation of *o*-nitro benzaldehyde and pyrrole was initiated by adding catalytic amount of $\text{BF}_3 \cdot \text{OEt}_2$ (120 μ l, of 2.5M stock solution). The reaction mixture was stirred at room temperature for 1hour. The progress of the reaction was monitored by taking aliquots of the reaction mixture at regular intervals and oxidizing with p-chloranil and recording the absorption spectra which clearly confirmed the formation of porphyrin. After 1 hour p-chloranil (0.7327g, 2.98 mmol) was added and the reaction mixture was stirred in air for additional 1 hour. The solvent was removed under reduced pressure and the crude compound was purified by silica gel column chromatography using dichloromethane.

λ_{max} : 421 nm(S), 516nm, 551nm, 593nm, 649nm

2.2. meso-5,10,15,20-Tetrakis(pyridyl) porphyrin [VO[T(o-NO₂)PP]

meso-5,10,15,20-Tetrakis(pyridyl)porphyrin was purchased from Sigma-Aldrich chemical and was used directly.

2.3. Synthesis of metalloporphyrins

The reaction was carried out with a mixture of 13.5 mL of glacial acetic acid, 6.5 mL of pyridine, 297 mg (1.37mmol) of vanadyl sulphate and 358.21 mg (0.42mmol) meso-5,10,15,20-Tetrakis (o-nitrophenyl) porphyrin VO[T(o-NO₂)PP] were taken in a 100 mL round bottom flask and was refluxed until the reaction was essentially complete (usually 4 to 5 hour). The crude product was cooled and washed with water thrice and the crude compound was purified by running through a silica gel column using dichloromethane.

Vanadyl meso-5,10,15,20-Tetrakis(pyridyl) porphyrin VO[TPyP] was prepared by a literature method¹⁴.

VO[T(o-NO₂)PP] : λ_{max} in dichloromethane: 426 nm, 551 nm

VO[TPyP] : λ_{max} in dichloromethane: 420 nm, 545 nm.

2.4. Cyclic voltammetric measurements

Redox potentials were determined using CHI 620B Electrochemical Analyzer, at NEHU, Shillong, Meghalaya, India. The electrolytic cell comprised of the following. A CHI(102) platinum electrode was used as a working electrode. An Ag/AgCl electrode was employed as a reference electrode. A platinum wire was used as an auxiliary electrode. Dry dichloromethane was used as the solvent. The amount of 0.1M of tetra-n-butylammonium perchlorate (TBAP) was used as the supporting electrolyte. The solvent in the electrolyte cell was deaerated with oxygen free dry nitrogen gas before any measurement had been done and nitrogen blanket above the solution has been maintained. Calibration of $E_{1/2}$ values and diffusion current were made by using a known concentration of pure ZnTPP in dichloromethane/TBAP (0.1M) medium.

3. RESULTS

VO[T(o-NO₂)PP], The voltammogram exhibits some additional peaks (fig.1) along with the regular redox couples which are expected. The first oxidation occurs at 0.730V with its corresponding reduction at 0.553V. The $\Delta E = 0.177\text{V}$, $E_{1/2} = 0.6415\text{V}$ and its $I_a/I_c \approx 1$. The second oxidation occurs at 1.2271V with its corresponding reduction peak at 1.055V. Its $\Delta E = 0.1721\text{V}$, $E_{1/2} = 1.1411\text{V}$ and $I_a/I_c \approx 1$.

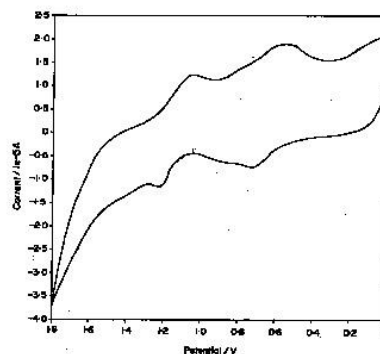


Fig.1.Cyclic voltammetric diagram for VO[T(o-NO₂)PP] **VO[TPyP]** : The voltammogram comprises of two redox couples. The first oxidation occurs at 0.6896V with its corresponding reduction at 0.5185V. The second oxida-

tion peak occurs at 1.0484V with its corresponding reduction peak at 0.8976V (fig.2)

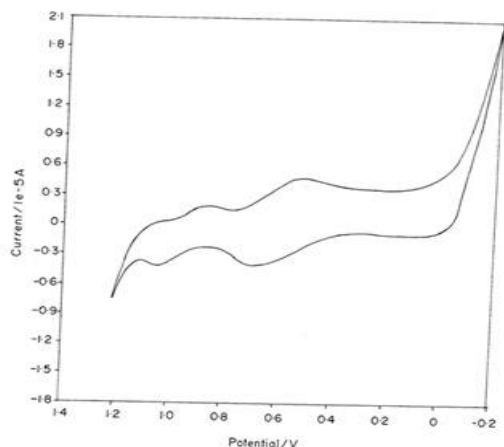
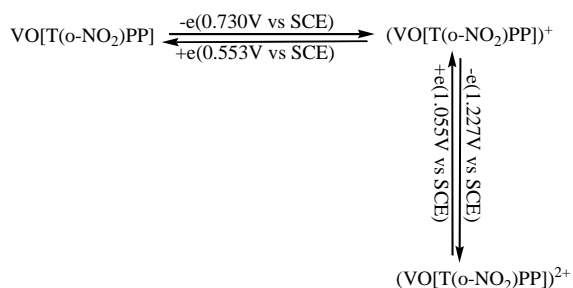


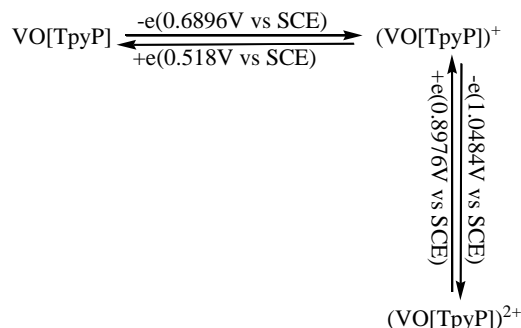
Fig.2.Cyclic voltammetric diagram for VO[TPyP]

4. DISCUSSION

The redox process of VO[T(*o*-NO₂)PP] is in line with the redox process of the VO[T(2,5-(OCH₃)₂)PP]. The first oxidation occurred at a lower potential than that of the VOTPP. This is quite surprising because we expected it to occur at a higher potential. The electron withdrawing -NO₂ group should lower the ring π -electron density thereby making oxidation more difficult. This is what we observed in our earlier work¹⁵⁻¹⁶ with VO[T(*m*-NO₂)PP]. One possible reason could be the presence of -NO₂ at meta position which is in more sterically hindered position making it more strained to take part in the porphyrin ring resonance. Thereby, no effective electron withdrawal from the ring takes place. However, the system undergoes two successive oxidation processes involving one electron transfer in each step which is represented as follows:



VO[TPyP] undergoes oxidation in steps similar to that of the VOTPP oxidation. The oxidation potentials are lower than that of the VOTPP. The substituents enrich the π -electron density making oxidation more easier. The oxidation process is represented as



5. CONCLUSION

From the results of the cyclic voltammetric investigation of VO[T(*o*-NO₂)PP] and VO[TPyP] we put forward the following observations:

When the metal center is non-electro-active such as vanadyl the redox process takes place in the porphyrin ligand system. When substitutions in the phenyl ring of the porphyrin ligand are symmetrical with electron donating group, the oxidation potentials are further lowered. The reverse is also true. It seems the substitution in the ortho-position of the phenyl ring of the porphyrin ligand is more sterically hindered and strained so that the substituents do not contribute much to the resonance. Thus, the oxidation potentials of VO[T(*o*-NO₂)PP] is slightly less than VOTPP (may be due to more puckered structure). In general it appears that substitution on the phenyl ring causes distortions which affect the redox potentials. It is most likely that the lowering in oxidation potentials could be due to metal d_{xy} porphyrin orbital (a_{2u}) in ruffle distortion and metal dx^2-y^2 porphyrin orbital (a_{2u}) in saddle distortion.

REFERENCES

1. R. A. Pasternack, A. Ghetto, P. Pagano, E.J. Gibbs, *J. Am. Chem. Soc.* 113,7799 (1991).
2. George S. Wilson and Bruce P. Neri, *Cyclic voltammetry of porphyrins and Metalloporphyrins*, *Annals of the New Yorks Academy of Sciences*, Vol. 206, (1973), 206:568-578.
3. K .M. Kadish and M. M. Morrison., *Inorg.Chem.*, **15**, 981 (1976).
4. Aaa D.l Heim, K. Seufert, W. Auw rter, C. Aurisicchio, C. Fabbro, D. Bonifazi and J. V. Barth, *Nano Lett.*, **10** (1), pp 122–128 (2010).
5. K. B Rjesson, J. Wiberg, A. H. El-Sagheer, T. Ljungdahl, J. Mårtensson, T. Brown, B. Nord and B. Albinsson, *ACS Nano*, **4** (9), pp 5037–5046 (2010).

6. A. Gold, W. Ivey and M. Bowen., *Chem. Commun.*, 293 (1981).
7. G. Simonneaux, V. Schunemann, C. Morice, L. Carel, L. Toupet, H. Winker, A. X. Trautwein, and F. A. Walker, *J. Am. Chem. Soc.*, **122**, 43666 (2000).
8. K. Safo, M. J. N. Nasset, F. A. Walker, P. G. Debrunner, and W. R. Scheidt, *J. Am. Chem. Soc.*, **119**, 9438 (1997).
9. F. A. Walker, H. Nasri, I. Turowski, K. Mohanrao, C. T. Watson, N. V. Shokhirew, P. G. Debrunner and W. R. Scheidt, *J. Am. Chem. Soc.* **118**, 12109 (1996).
10. A. Ghosh, I. Halvorsen, H. J. Nilsen, E. Steene, T. Wondimagegin, R. Lie, E. Vancaemelbacke, N. Guo, Z. Ou, and M. K. Kadish., *J. Phys. Chem. B.*, **105**, 8120 (2001).
11. A. Ghosh, E. Gonzalez, and T. Vangberg., *J. Phys. Chem. B.*, **103**, 1363 (1999).
12. R. Harada, H. Okawa and T. Kojima., *Inorg. Chim. Acta.*, **358**, 489 (2005).
13. I. Gupta, and M. Ravikanth., *Tetrahedron*, **59**, 6131 (2003),
14. A. D. Alder, F. R. Longo, F. Kampas, and J. Kim., *J. Inorg. Nucl. Chem.*, **32**, 2443 (1970).
15. A. Tomba Singh and A. Lemtur., *Spect. Chim. Acta., Part A.*, **59**, 1549 (2003).
16. A. Murugan, thesis submitted entitled 'Studies on paramagnetic and redox properties of some metalloporphyrins' in NEHU, Shilling, 2008.

ELECTRICAL AND DIELECTRIC STUDIES OF L-PHENYLALANINE ADDED Na⁺ ION CONDUCTING POLYMER BLEND ELECTROLYTES

S. Shenbagavalli¹, V. Srividhya Devi¹, K. Sundaramahalingam²,
N. Nallamuthu^{2*}, S. Jayanthi^{1*}

¹Department of Physics, The Standard Fireworks Rajaratnam College for Women, Sivakasi – 626 123, Tamil Nadu, India.

²Department of Physics, Kalasalingam Academy of Research and Education, Krishnankoil – 626 126, Tamil Nadu, India.

*E-mail id's: nnallamuthu@gmail.com, jayanthi-phy@sfrcollege.edu.in

Abstract

Polymer blend electrolytes comprising of poly (vinyl alcohol) (PVA), poly (N-vinyl pyrrolidone) (PVP) as polymer hosts, sodium nitrate (NaNO₃) as a salt and L-phenylalanine as an amino acid were prepared using solution casting technique. Double distilled water was used as a solvent. The amino acid, L-phenylalanine was varied from 0.5 wt% to 2.5 wt% in steps of 0.5 wt%. The prepared samples were subjected to AC impedance spectroscopy. AC impedance measurements were carried out in the frequency range of 42 Hz to 1 MHz using silver electrodes. The same measurement was also carried out at different temperatures for all the prepared samples. Ionic conductivity reached a maximum value of $1.8686 \times 10^{-5} \text{ Scm}^{-1}$ for 2.5wt.% of L-phenylalanine system at room temperature. Low activation energy of 0.246 eV was observed for the maximum ionic conducting sample. The maxima of tan delta peaks were found to shifted towards the higher frequency side for different temperatures, suggested the increase in amorphicity of the system.

Keywords: Solution casting technique, AC impedance spectroscopy, Activation energy, polymer blend electrolytes, Conductivity.

1. Introduction

Sodium ion conducting solid polymer electrolytes receives a great deal of attention as it acts an excellent substitute for lithium salts. For the present investigation, we have prepared polymer blend electrolytes consisting of poly (vinyl alcohol) (PVA), poly (vinyl pyrrolidone) (PVP) as polymer hosts, sodium nitrate (NaNO₃) as salt and an amino acid L-phenyl alanine as dopant.

2. Experimental

2.1. Materials and Methods

Poly (vinyl alcohol) (PVA) with molecular weight of ~1,25,000 g and poly (vinyl pyrrolidone) (PVP) with molecular weight of ~90,000 g, were purchased from S. D. Fine 5 Chemicals Ltd., and both the polymers were used without further purification. The L-phenylalanine salt (Merck) and sodium Nitrate (NaNO₃) (Merck) are used as raw materials to synthesis the blend polymer electrolyte.

2.2. Preparation of polymer electrolyte

The polymer electrolyte based on the composition of PVA/PVP/L-phenylalanine and NaNO₃ were blended by solution casting technique using double-distilled water (D.D water) as solvent. Stoichiometric quantities of precursor materials, 50wt%PVA/50wt%PVP and 2wt% NaNO₃ dissolved in D.D water separately and the above all solutions are continuously stirred for 1 h at 40 °C to make the transparent solutions. The above PVP/PVA/NaNO₃ transparent solutions are mixed together with stirring until forming homogeneous blend solution. Then the amino acid, L-phenylalanine with various concentrations from 0.5 wt% to 2.5 wt% (in steps of 0.5 wt%) was added to the above solution and stirred well at room temperature. The obtained homogeneous solution, PVA/PVP/L-Phenylalanine/NaNO₃ was then poured into polypropylene dishes and slowly dried at room temperature for 4 days. The obtained blend polymer film is peeled off from dishes and kept inside a desiccator for further characterizations.

3. Results and Discussion

3.1. AC Impedance Spectroscopy

AC impedance plots of the system PVA/PVP/NaNO₃/L-phenylalanine is given in Figure 1. This Figure possesses a depressed semi-circular arc in the high frequency region and an incline spike in the low frequency region. The depressed semi-circle reveals the non-Debye nature of the sample due to the potential well for each site, through which the ion takes place. The presence of an inclined spike at low frequency region at an angle less than 90° is due to the roughness of the electrode-electrolyte interface [1].

Ionic conductivity of the prepared samples can be calculated by using the following relation,

$$\sigma = l/AR_B \quad \dots (1)$$

where, l is the thickness of the sample, A is the area of the electrode used (Silver electrode) and R_B is the bulk resistance. Intercept of the low frequency spike at the real axis of the complex impedance plot gives the value of R_B .

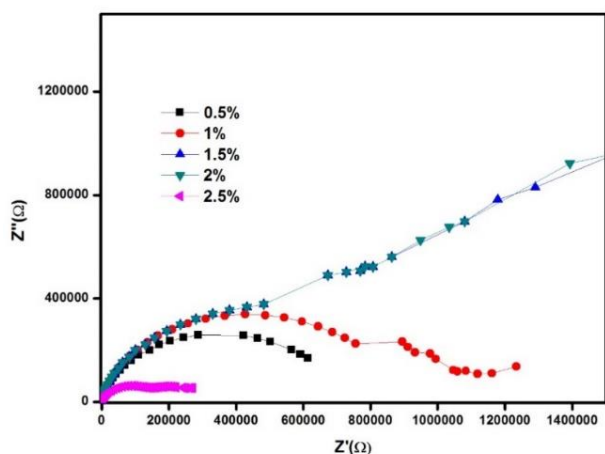


Figure 1 AC impedance plot of PVA/PVP/NaNO₃/L-phenylalanine system

The calculated values of ionic conductivity of the polymer blend electrolyte PVA/PVP/NaNO₃ is varying against the concentration of L-phenylalanine and the variation is shown in the Figure 2.

It is observed from the Figure 2, that the value of ionic conductivity decreases for the addition of 0.5 and 1 wt.% of L-phenylalanine systems. This may

be due to the inadequacy of L-phenylalanine concentrations. When the concentration of L-phenylalanine increased from 1 wt.% to 1.5 wt.%, the value of ionic conductivity seems to increase by an order of magnitude. Further increase in the concentration of L-phenylalanine from 1.5wt.% to 2.5wt.%, an appreciable increase in ionic conductivity was observed and reaches a maximum value of $1.8686 \times 10^{-5} \text{ Scm}^{-1}$.

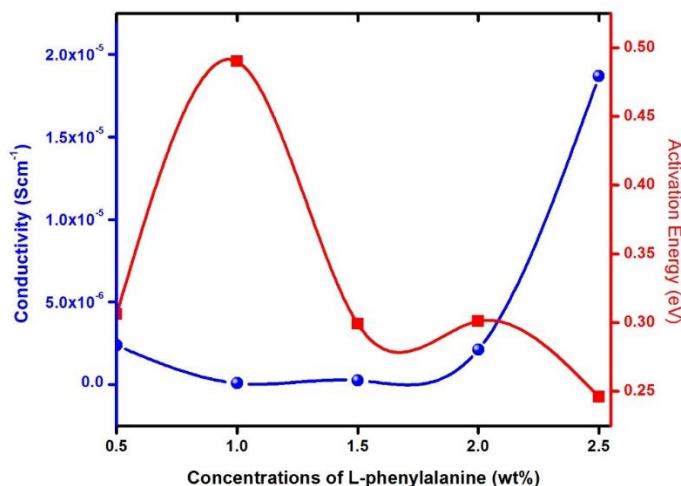


Figure 2 Conductivity Vs Activation energy of L-phenylalanine system.

When the concentrations of L-phenylalanine increased beyond 2.5 wt.%, the film was found to be fragile in nature and hence it was difficult for handling. Hence the concentration of L-phenylalanine is varied up to 2.5wt.% and the same was found to be an optimum concentration based on ionic conductivity results. The obtained ionic conductivity value is comparable to that of PVA/PVP/L-Asparagine/NH₄Br system reported by Parameswaran et al. [2].

The increase in ionic conductivity is due to the increase in the number of mobile charge carrier and also the nature of the polymer blend electrolyte which reduces the energy carrier, there by facilitating the ion transport. [3]

3.2. Temperature dependence of ionic conductivity

The temperature dependence of ionic conductivity for all the prepared system over the temperature 303 K to 363 K is shown in the Figure 3.

Ionic conductivity increases with increase in the temperature for all the samples which implies that it obeys Arrhenius relation given below,

$$\sigma(t) = \sigma_o \exp[-E_a/KT] \dots (2)$$

where, σ_o is the pre-exponential factor, E_a is the activation energy for conduction, and K is the Boltzmann constant. Arrhenius law states that the moment of the charge carrier from one site to its adjacent site without having acquired much energy.

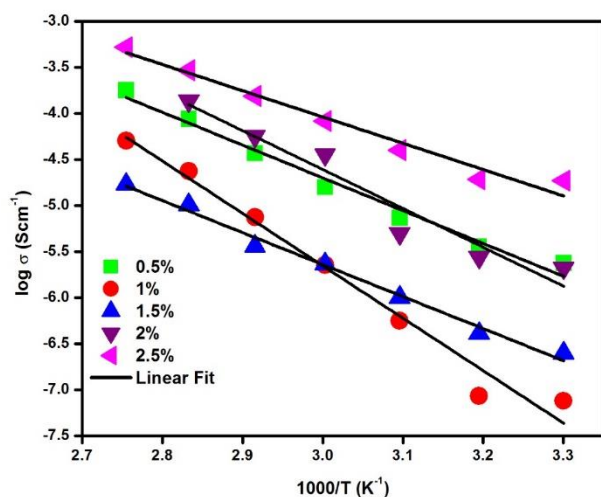


Figure 3 Variation of $\log \sigma$ with increase absolute temperature for PVA/PVP/NaNO₃/L-phenylalanine system.

The increase in ionic conductivity against the increase of temperature in solid polymer electrolyte enhance the segmental (i.e. polymer chain) motion, which resulting in an increase in the free volume of the system. Thus, the segmental motion either permits the ion to hop from one site to another or provides a pathway for ions to move. In other words, the segmental movement of the polymer facilitates, the translation ionic motion. From this, it is clear that the ionic motion is due to translation motion/hopping facilitated by the dynamics segmental motion of the polymer. As the amorphous region increase, the polymer chain acquires faster internal modes in which the bond rotations produced segmental motion to favor inter and intra chain ion

hopping, and thus the value of ionic conductivity becomes high. [4]

The activation energy (combination of energy for defect formation and the energy for migration of ion) is calculated for all the samples and is given in Table 1.

Table 1 The value of activation energy for L-phenylalanine added PVA/PVP/NaNO₃ system.

Concentrations of L-phenylalanine	E_a (eV)
0.5wt. %	0.306
1wt.%	0.490
1.5wt.%	0.299
2wt.%	0.301
2.5wt.%	0.246

It can be seen from the table that the value of E_a of the system is found to decrease from 0.306eV to 0.246eV for the addition of 2.5wt% of the L-phenylalanine system. As a temperature increase, it causes the expansion of polymer blend matrix and thus weakness the interaction within the polymer blend matrix. This initiates the decoupling of Na⁺ ions from the polymer blend matrix. Besides, as the temperature is increased, the polymeric chain acquires faster internal modes and thus promotes the bond rotation, resulting in faster segmental mobility. Consequently, the intrachain and interchain and interchain ion hopping mechanisms are favorable which in turn result in higher ionic conductivity [5].

3.3. Conductance spectra analysis

Conductance spectra for PVA/PVP/NaNO₃/2.5wt%L-phenylalanine system (maximum ionic conducting sample) at various temperatures is shown in the Figure 4. This spectrum possessed three regions. The low frequency dispersion region is due to the overcrowding of ion between the electrode and electrolyte. A mid frequency plateau region is due to the bulk conductivity and the region three is the high frequency dispersion region.

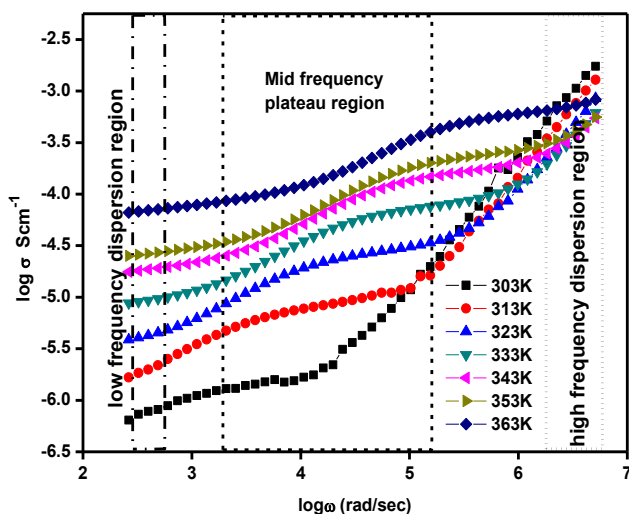


Figure 4 $\log \omega$ Vs $\log \sigma$ for PVA/PVP/NaNO₃/ 2.5wt% L-phenylalanine system at various temperatures.

3.4. Loss Tangent Analysis

The frequency dependence of loss tangent indicates the dissipation of energy in dielectrics. It is used to analyze the electrical properties of polymer. The loss tangent can be expressed as

$$\tan \delta = \varepsilon'' / \varepsilon' = M'' / M' \dots (3)$$

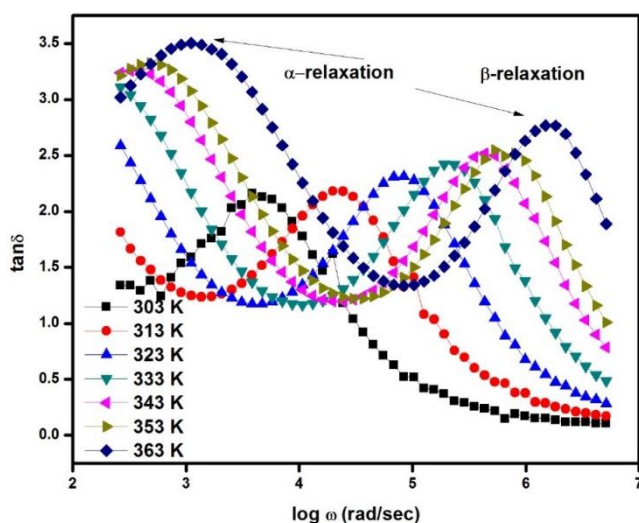


Figure 5 Loss tangent spectra of PVA/PVP/NaNO₃/2.5wt% of L-phenylalanine system at various temperatures

Figure 5 shows that loss tangent spectra of PVA/PVP/NaNO₃/2.5wt% L-phenylalanine system at various temperatures. It shows two humps, which represents the formation of two relaxation time in non-Debye behavior. The low frequency humps are known as α relaxation peaks and it is due to the dynamic dipole rotation, whereas the humps in the higher frequency region are known as β relaxation peaks and it is due to the dipole orientation and static region. β relaxation peak is related to the amorphous phase, whereas α relaxation peak is related to the crystalline. The peak maxima of $\tan \delta$ shift towards the higher frequency range with the increase of temperature. Further, the height of $\tan \delta$ peak due to β relaxation is increased with the increase of temperature. These findings suggested that the amorphous nature of the polymer blend electrolyte system increase with the temperature. [6]

Conclusion

Sodium ion conducting polymer blend electrolytes with different concentrations of L-phenylalanine have been prepared by using solvent casting technique. Maximum ionic conductivity has been found to be $1.8686 \times 10^{-5} \text{ Scm}^{-1}$ for 2.5wt% of L-phenylalanine added system at room temperature. The temperature-dependent ionic conductivity of polymer blend electrolytes obeyed the Arrhenius behaviour. Activation energy of the maximum ionic conducting sample has the low value of 0.246 eV. From loss tangent spectra, it has identified that low frequency α relaxation peaks are due to the dynamic dipole rotation and the high frequency β relaxation peaks are due to dipole orientation in static region. The high frequency peak related to amorphous phase is increased for higher-conductivity polymer electrolyte.

REFERENCES

- [1] S. Jayanthi, K. Kulasekarapandian, A. Arulsankar, K. Sankaranarayanan, B. Sundaresan, *Journal of Composite Materials*, 49 (2015) 1035-1045
- [2] V. Parameswaran, N. Nallamuthu, P. Devendran, E.R. Nagarajan, A. Manikandan, *Physica B*, 515 (2017) 89-98.
- [3] D. Vanitha, S. Asath Bahadur, N. Nallamuthu, S. Athimoolam, *Ionics*, doi: 10.1007/s11581-017-2169-8.
- [4] K. Kiran Kumar, M. Ravi, Y. Pavani, S. Bhavani, A.K. Sharma, V.V.R. Narasimha Rao, *Journal of Non-Crystalline Solids*, 358 (2012) 3205-3211.
- [5] D. Vanitha, Sultan Asath Bahadur, N. Nallaperuma Nallamuthu1, Athimoolam Shunmuganarayanan, A. Manikandan, *Journal of Nanoscience and Nanotechnology*, 18 (2018) 1723–1729.
- [6] K. Sundaramahalingam, M. Muthuvinayagam, N. Nallamuthu, D. Vanitha, M. Vahini, *Polymer Bulletin*, DOI:10.1007/s00289-018-02670-2.

SPECTROSCOPIC INVESTIGATION USING DENSITY FUNCTIONAL THEORY CALCULATIONS ON 5-CHLORO-2-HYDROXY ACETOPHENONE

V. Lavanya¹, A. Muthukumar¹, M. Muthumeenal¹, R. Muneeswaran¹, S. Jeyavijayan^{1,*}

¹Department of Physics, Kalasalingam Academy of Research and Education, Krishnankoil, India

*Email: sjeyavijayan@gmail.com

Abstract

In this study, detailed vibrational spectra of 5-chloro-2-hydroxyacetophenone (CHAP) have been studied by FTIR and FT-Raman spectra in the regions 4000-400 cm⁻¹ and 3500-50 cm⁻¹, respectively. The optimum geometrical parameters, frequencies, infrared intensities and Raman activities were calculated by density functional theory (DFT/B3LYP) method with 6-31+G(d,p) and 6-311++G(d,p) basis sets. The HOMO-LUMO energy gap has been computed which confirms the charge transfer of the molecular system. Mulliken's atomic charges associated with each atom and thermodynamic parameters have also been reported with the same level of DFT.

Keywords: 5-chloro-2-hydroxy acetophenone; FTIR; FT-Raman; DFT

1. Introduction

Acetophenones are compounds that exhibit interesting physicochemical and biological properties. They are found in nature [1] and they can also be obtained by means of diverse synthesis procedures [2]. A recent study has linked the antibacterial activity of 20 acetophenones with their structural characteristics by using electronic and topological indices [3]. Particularly, hydroxy acetophenone is used as building block for the synthesis of rubbers, plastics, pharmaceuticals, agrochemicals and flavour and fragrances (odour, sweet, heavy floral). Because of these versatile behaviors of acetophenone, Seth *et al.* investigated the spectroscopic and X-ray structure of ortho-hydroxy acetophenones [4]. Anbarasu *et al.*, have extensively studied the scaled quantum study and vibrational spectra of 5-fluoro-2-hydroxyacetophenone [5]. Recently, the crystallographic, spectroscopic and DFT studies of 5-methyl-2-hydroxy-acetophenone-thiosemicarbazone and its nickel(II) complex has been studied by Cıkla *et al.* [6]. Consideration of these factors leads to study the detailed spectral investigation of 5-chloro-2-hydroxyacetophenone (CHAP).

2. Experimental

The fine polycrystalline sample of CHAP was purchased from commercial sources with a stated purity of 99% and they were used as such without further purification. The Fourier transform infrared spectra was recorded in the region 4000-400 cm⁻¹, using Perkin Elmer FTIR spectrometer equipped with an MCT detector, a KBr beam splitter and globar source. The FT-Raman spectrum of CHAP was recorded on a computer interfaced BRUKER RFS-66V model interferometer in the Stokes region 4000-50 cm⁻¹ using Nd: YAG laser operating at 200 mW power continuously with 1064nm excitation.

3. Computational Details

In the quantum chemical calculations, DFT has proved to be very useful in treating electronic structure of molecules. The DFT calculations were carried out for CHAP with GAUSSIAN 09W program package [7] using the Becke's three parameter hybrids functional combined with the Lee-Yang-Parr correlation (B3LYP) functional [8,9] with standard 6-31+G(d,p) and 6-311++G(d,p) basis sets. The total energy distribution (TED) associated with each vibration is calculated by the MOLVIB program (version V7.0-G77) written by Sundius [10]. The HOMO-LUMO and Mulliken charge analyses have been computed with same level of calculations to elucidate information regarding charge transfer within the molecule.

4. Result and Discussion

4.1. Molecular geometry

The optimized molecular structure of CHAP having C₁ symmetry is shown in Fig. 1. The global minimum energy obtained by DFT structure optimization with standard 6-31+G(d,p) and 6-311++G(d,p) basis sets is calculated as -919.577287 and -919.709992 Hartrees, respectively. The optimized geometrical parameters of CHAP calculated by using the above methods in comparison with the experimental data [11] are presented in the Table 1. The thermodynamic properties like heat capacity, entropy, dipole moment and zero point vibrational energy (ZPVE) have also been computed at same level of calculations for CHAP and they are presented in Table 2. In this study, the dipole moment molecule of CHAP is found to be 3.8702 and 3.8537 Debye, for lower and higher basis sets, respectively. All the thermodynamic data provide helpful information for the further study on the CHAP.

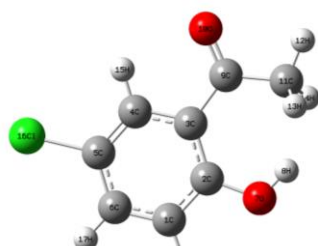


Figure 1. Molecular Structure of 5-chloro-2-hydroxyacetophenone

4.2. Vibrational spectral analysis

The molecule under investigation contains 18 atoms and hence it has 48 modes ($3N-6$) of vibrations. The geometry of the molecule CHAP is considered to possess C_1 point group symmetry. All the vibrations are active in both IR and Raman spectra. The observed FTIR and FT-Raman spectra of CHAP are presented in Fig. 2. The detailed vibrational assignment of fundamental modes of CHAP along with the calculated IR, Raman intensities, and normal mode descriptions (characterised by TED) are reported in Table 3.

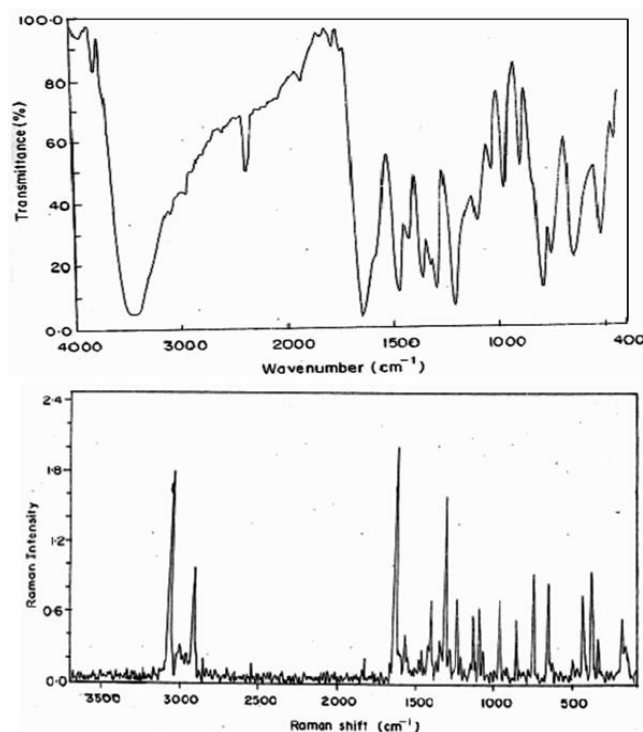


Figure 2. FTIR and FT-Raman spectra of 5-chloro-2-hydroxyacetophenone

The calculated wavenumbers are usually higher than the corresponding experimental quantities because of the anharmonicity and the general tendency of the quantum mechanical methods to overestimate the force constants at the equilibrium geometry. Therefore, in order to

improve the calculated values in agreement with the experimental ones, it is necessary to scale down the calculated harmonic frequencies. A better agreement between the computed and experimental frequencies can be obtained by using scale factor [12] of 0.96 for B3LYP method. The resultant scaled frequencies are also listed in Table 3.

Table 1. Experimental (XRD) and optimized geometrical parameters of 5-chloro-2-hydroxyacetophenone obtained by B3LYP method using 6-31+G(d,p) and 6-311++G(d,p) basis sets.

Bond length (Å)	B3LYP/6-31+G(d,p)	B3LYP/6-311++G(d,p)	Experimental ¹¹
C1-C2	1.405	1.402	1.390
C1-C6	1.391	1.387	1.377
C2-C3	1.417	1.414	1.419
C2-O7	1.391	1.391	1.352
C3-C4	1.418	1.416	1.405
C3-C9	1.495	1.494	1.477
C4-C5	1.381	1.377	1.376
C5-C6	1.400	1.397	1.392
C5-C116	1.825	1.827	1.750
C9-O10	1.250	1.247	1.237
C9-C11	1.518	1.516	1.500
Bond angle (°)			
C2-C1-C6	120.84	120.86	120.6
C1-C2-C3	120.60	120.57	120.0
C1-C2-O7	113.24	113.31	117.9
C3-C2-O7	126.16	126.12	122.1
C2-C3-C4	117.56	117.58	118.7
C2-C3-C9	126.92	126.87	119.8
C4-C3-C9	115.52	115.55	121.5
C3-C4-C5	120.88	120.79	119.8
C4-C5-C6	121.42	121.53	121.5
C4-C5-C116	119.64	119.58	118.9
C6-C5-C116	118.95	118.89	119.6
C1-C6-C5	118.71	118.67	119.4
C3-C9-O10	119.84	119.71	120.3
C3-C9-C11	122.18	122.20	120.0
O10-C9-C11	117.98	118.08	119.7

Table 2. Theoretically computed thermodynamic parameters of 5-chloro-2-hydroxyacetophenone.

Parameter	B3LYP/6-31+G(d,p)	B3LYP/6-311++G(d,p)
Zeropoint vibrational energy(kcal mol ⁻¹)	89.4635	82.5431
Thermal energy (kcal mol ⁻¹)	89.805	88.544
Heat capacity, C _v (calmol ⁻¹ K ⁻¹)	37.579	36.121
Entropy (cal mol ⁻¹ K ⁻¹)		
<i>Total</i>	102.153	97.020
<i>Translational</i>	41.300	41.300
<i>Rotational</i>	30.957	30.949
<i>Vibrational</i>	29.896	24.771
Dipole moment (Debye)		
μ_x	-2.6790	-2.6826
μ_y	2.7931	2.7667
μ_z	0.0014	0.0011
μ_{total}	3.8702	3.8537

Table 3. Experimental and calculated (unscaled and scaled) vibrational frequencies (cm^{-1}) by B3LYP method with 6-31+G(d,p) and 6-311++G(d,p) levels, IR intensity (km mol^{-1}), Raman activity ($\text{\AA}^4 \text{amu}^{-1}$) and probable assignments of 5-chloro-2-hydroxy acetophenone.

Sl. No	Experimental frequencies (cm^{-1})		Calculated frequencies (cm^{-1})								Assignment with TED (%)
			B3LYP/6-31+G(d,p)				B3LYP/6-311++G(d,p)				
	FTIR	FT-Raman	Un Scaled	Scaled	IR intensity	Raman intensity	Un Scaled	Scaled	IR intensity	Raman intensity	
1	3544(s)	-	3731	3582	142.15	60.08	3748	3598	171.85	99.39	v OH (98)
2	3080(vw)	-	3248	3118	4.28	39.48	3218	3089	8.33	46.74	v CH (96)
3	-	3075(vs)	3246	3117	2.48	140.22	3216	3088	1.13	161.55	v CH (97)
4	-	3011(w)	3231	3102	1.47	52.92	3200	3072	1.19	64.13	v CH (95)
5	2927(w)	2927(vw)	3160	3034	8.95	79.90	3133	3008	5.00	110.34	CH ₃ ips (92)
6	-	2862(s)	3090	2966	10.09	54.61	3064	2941	5.14	40.00	CH ₃ ss (94)
7	2913(s)	-	3021	2900	9.89	125.91	2997	2877	5.85	151.00	CH ₃ ops (90)
8	-	1831(vs)	1665	1599	301.27	40.34	1651	1585	212.01	63.50	CH ₃ ipr (89)
9	1762(w)	-	1633	1568	53.07	47.06	1619	1554	54.98	60.09	v CC (88)
10	1642(vs)	-	1608	1544	33.53	10.51	1594	1530	22.89	15.20	v CC (89)
11	-	1577(ms)	1540	1478	219.91	2.37	1535	1474	189.76	4.83	v CC (85)
12	1470(s)	-	1522	1461	10.98	8.29	1517	1456	12.55	9.11	v CC (86)
13	-	1468(ms)	1512	1451	7.47	5.48	1503	1443	34.12	4.13	v CC (85)
14	1418(ms)	-	1447	1389	81.58	0.42	1436	1379	72.96	0.35	v CC (87)
15	-	1410(s)	1427	1370	27.96	1.76	1424	1367	51.77	1.74	v CC (84)
16	1356(ms)	-	1379	1324	13.56	1.26	1356	1301	3.96	13.26	v CC (82)
17	-	1349(s)	1334	1281	76.70	33.93	1327	1274	10.09	13.15	v CO (80)
18	1318(s)	-	1284	1233	267.53	14.58	1277	1225	254.65	5.89	v CO (81)
19	-	1317(ms)	1252	1202	18.93	1.56	1242	1193	83.82	28.07	b OH (78)
20	1289(ms)	-	1180	1133	33.07	6.14	1170	1123	131.90	7.81	CH ₃ ipb (79)
21	-	1286(s)	1140	1094	66.95	3.42	1133	1088	2.64	7.97	CH ₃ sb (76)
22	-	1239(ms)	1115	1071	22.04	9.05	1105	1061	8.28	21.14	b CH (75)
23	-	1213(s)	1097	1053	13.22	4.74	1091	1047	2.55	4.25	b CH (74)
24	1208(s)	-	1081	1037	7.33	1.22	1074	1031	0.82	0.20	b CH (72)
25	-	1140(s)	1015	974	1.73	0.33	1003	963	2.08	0.07	CH ₃ opb (68)
26	-	1097(ms)	993	953	10.93	10.90	987	948	18.19	15.86	CH ₃ opr (67)
27	-	1070(s)	982	943	12.65	0.12	958	919	11.75	0.13	R asymd (70)
28	1024(w)	-	870	835	40.06	0.56	867	832	5.14	11.87	R asymd (71)
29	-	966(w)	870	835	7.41	13.56	866	831	29.39	0.25	ω CC (65)
30	963(w)	-	751	721	4.62	1.48	733	703	22.37	13.22	ω CC (64)
31	938(s)	-	734	705	17.86	10.56	730	701	0.03	0.33	R trigd (69)
32	881(s)	-	662	636	50.12	4.17	659	633	34.00	4.15	ω OH (63)
33	-	859(w)	644	618	7.59	1.21	628	603	0.06	0.69	b CC (70)
34	791(s)	-	598	574	35.21	3.19	596	572	38.34	2.48	b CC (68)
35	-	748(s)	562	539	24.60	0.89	559	537	9.72	2.53	v CCl (69)
36	746(w)	-	548	526	14.82	1.28	542	521	13.16	0.17	b CO (70)
37	-	654(w)	443	425	0.14	0.19	439	421	0.29	0.03	b CO (67)
38	-	650(w)	390	375	2.95	8.85	389	373	2.40	7.83	t R symd (63)
39	-	648(vw)	378	363	1.72	2.34	376	361	0.74	3.95	t R trigd (60)
40	644(ms)	-	357	343	0.95	2.94	346	332	3.21	4.38	t R symd (62)
41	640(ms)	-	340	326	1.85	1.68	337	324	5.13	0.43	ω CH (61)
42	512(w)	-	325	312	17.95	0.77	294	282	25.43	0.53	ω CH (60)
43	-	498(ms)	297	285	18.81	0.68	281	270	2.66	0.82	ω CH (58)
44	436(vw)	436(s)	248	238	68.30	0.70	172	165	48.08	0.83	b CCl (65)
45	-	378(w)	172	165	8.36	1.37	167	161	0.80	2.08	ω CO (56)
46	-	337(vw)	148	142	10.95	0.83	126	121	5.74	0.35	ω CO (55)
47	-	185(w)	102	97	8.79	1.42	54	52	6.49	1.53	ω CC (54)l
48	-	170(ms)	11	10	3.92	0.33	11	11	1.17	0.17	t CH ₃ (51)

Abbreviations used : v-stretching; ss – symmetric stretching; ips – in-plane stretching; sb – symmetric bending; ipr – in-plane rocking; opr – out-of-plane rocking; ops – out-of-plane stretching; b-bending; ω -out-of-plane bending; R-ring; trigd-

trigonal deformation; symd-symmetric deformation; asymd-antisymmetric deformation; t-torsion; s-strong; vs-very strong; ms-medium strong; w-weak; vw-very weak.

O-H Vibrations

The precise positions of O–H band are dependent on the strength of hydrogen bond. The O–H stretching appears at 3500–3600 cm^{-1} in the intermolecular hydrogen bonded systems [13]. The observed peaks in this region are strong. The title compound in this study showed a strong absorption peak at 3544 cm^{-1} in FTIR, which are due to the O–H stretching vibration. This is further supported by the TED contribution of almost 100%. The in-plane and out-of-plane bending vibrations of the hydroxyl groups are identified and they are listed in the Table 3.

C-H Vibrations

Aromatic structure shows the presence of C–H stretching vibration in the region 3100–3000 cm^{-1} . This is the characteristic region for the ready identification of C–H stretching vibration. In this region, the bands are not affected appreciably by the nature of the substituents. In the present investigation, the C–H stretching bands observed at 3080 cm^{-1} in IR, at 3075 and 3011 cm^{-1} in the FT–Raman spectrum. The in-plane and out-of-plane bending vibrations of C–H group were found well within the characteristic region [14] and are depicted in the Table 3.

CH₃ Vibrations

For the assignments of CH₃ group frequencies, nine fundamental vibrations can be associated to each CH₃ group. Three stretching, three bending, two rocking modes and single torsional mode describe the motion of the methyl group. In this study, the CH₃ symmetric stretch frequency is established at 2862 cm^{-1} in Raman and CH₃ in-plane stretch frequencies are assigned at 2927 cm^{-1} in both IR and Raman spectra for the title compound. These assignments are also supported by the literature [15] in addition to TED output. The two in-plane methyl hydrogen deformation modes are also well established. We have observed the symmetrical methyl deformation mode at 1286 cm^{-1} in the Raman spectrum. The band at 2913 cm^{-1} in infrared and 1140 cm^{-1} in Raman is attributed to CH₃ out-of-plane stretching and out-of-plane bending modes, respectively. The methyl deformation modes mainly coupled with in-plane bending vibrations. The FT-Raman bands obtained at 1831 and 1097 cm^{-1} are assigned to CH₃ in-plane and out-of-plane rocking modes, respectively. The assignment of the band at 170 cm^{-1} in Raman is attributed to methyl twisting mode.

C=O Vibrations

The carbonyl bonds are the most characteristic bands of infrared spectrum. Both the carbon and oxygen atoms of the carbonyl group move during vibration and they have nearly equal amplitudes. Normally carbonyl group vibrations [16] occur in the region 1800–1700 cm^{-1} . Accordingly, the band appeared at 1318 and 1349 cm^{-1} in the FTIR and FT-Raman spectra, respectively, are assigned as C=O stretching vibrations of CHAP.

C-Cl Vibrations

The vibrations belonging to the bond between the ring and the halogen atoms are worth to discuss here, since

mixing of vibrations are possible due to the lowering of the molecular symmetry and the presence of heavy atoms on the periphery of molecule [17]. The FT–Raman band at 748 cm^{-1} has been assigned to C–Cl stretching mode. The C–Cl in-plane bending and out-of-plane bending vibrations are also summarized in the Table 3.

C-C Vibrations

The bands between 1400–1650 cm^{-1} in the aromatic and hetero aromatic compounds are assigned to C–C stretching vibrations [18]. The benzene ring modes predominantly involve C–C bonds. The vibrational frequencies at 1762, 1642, 1470, 1418, 1356 cm^{-1} in IR and 1577, 1468, 1410 cm^{-1} in Raman are associated with C–C stretching modes of carbon skeleton. The ring out-of-plane and in-plane bending modes have also been summarized in the Table 3.

4.3. Mulliken charges analysis

The calculation of atomic charges describes a significant task in the application of quantum mechanical calculations to molecular systems [19]. Mulliken population analysis has been carried out for the comparison of different choice of the basis sets to describe the electron distribution in CHAP. The Mulliken charges calculated at different basis set calculations are listed in Table 4. The carbon atom C2 has the high negative charge, atoms C3 and C5 have positive charges since they are attached with OH, CO-CH₃ and Cl groups, respectively, which leads to redistribution of electron density. All the hydrogen atoms have a net positive charge because they are electron acceptors.

Table 4. Mulliken charges analysis for 5-chloro-2-hydroxy acetophenone

Atoms	Atomic charges (Mulliken)	
	B3LYP/6-31+G(d,p)	B3LYP/6-311++G(d,p)
C1	-0.3403	-0.5451
C2	-1.1625	-1.4285
C3	1.4382	1.3485
C4	-1.5897	-1.0586
C5	0.9714	0.9027
C6	-0.6300	-0.3865
O7	-0.6046	-0.4873
H8	0.4427	0.4248
C9	0.4770	0.0506
O10	-0.4178	-0.3351
C11	-0.9938	-1.1044
H12	0.2529	0.3420
H13	0.2209	0.2650
H14	0.2209	0.2649
H15	0.2535	0.3680
C116	0.3640	0.7515
H17	0.2117	0.3039
H18	0.2047	0.3234

4.4. HOMO-LUMO analysis

The frontier molecular orbitals (FMOs) such as highest occupied molecular orbital (HOMO) and lowest unoccupied molecular orbital (LUMO) play an important role in the electric and optical properties, as well as in UV–vis spectra and chemical reactions [20]. The

HOMO-LUMO orbital for CHAP is shown in Fig. 3. In this study, the HOMO is located over ring system, chlorine and hydroxyl atoms and LUMO: of π nature, (i.e. benzene ring) is delocalized over the whole C-C bond; consequently the HOMO→LUMO transition implies an electron density transfer to the C-C bond of the benzene ring and CO-CH₃ group from chlorine atom. Moreover, these orbital significantly overlap in their position for CHAP. The HOMO–LUMO energy gap is found to be 4.501 eV by B3LYP/6-311++G(d,p) method. This explains the ultimate charge transfer interaction within the molecule, which influences the biological activity of the molecule.

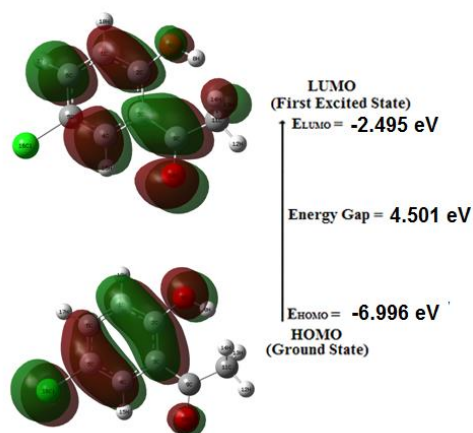


Figure 3. HOMO-LUMO for 5-chloro-2-hydroxy acetophenone

5. Conclusion

The optimized geometries, harmonic vibrational wavenumbers and intensities of vibrational bands of 5-chloro-2-hydroxy acetophenone have been determined using DFT-B3LYP with 6-31+G(d,p) and 6-311++G(d,p) level calculations. The normal modes of CHAP have been studied by FTIR and FT-Raman spectroscopies on the basis of C₁ point group symmetry. The frequency assignment for normal modes is supported by the TED calculation. The lowering of HOMO-LUMO band gap may lead to the understanding of properties and chemical activity of the molecule. Furthermore, the Mulliken's charge and thermodynamic properties of CHAP have been calculated and the results are discussed. These results will be of assistance in the quest of the experimental and theoretical evidence for 5-chloro-2-hydroxy acetophenone in reaction intermediates, pharmaceuticals and agrochemicals industries.

REFERENCES

- [1] X. Zhang, L. Shan, H. Huang, X. Yang, X. Liang, A. Xing, H. Huang, X. Liu, J. Su, W. Zhang, *J. Pharm. Biomed. Anal.* 49 (2009) 715–725.
- [2] Y.R. Prasad, A.S. Rao, R. Rambabu, *Asian J. Chem.* 21 (2009) 907–914.
- [3] P.M. Sivakumar, G. Sheshayan, M. Doble, *Chem. Biol. Drug Des.* 72 (2008) 303–313.
- [4] S.K. Seth, D.K. Hazra, Monika Mukherjee, Tanusree Kar, *J. Mol. Struct.* 936 (2009) 277–282.
- [5] P. Anbarasu, M. Arivazhagan, *Indian. J. Pure and Appl. Phys.* 49 (2011) 227–233.
- [6] I. Cıkkla, ŞükriyeGüveli, M.Yavuz, T. Demirci, BahriÜlküseven, *Polyhedron*,105 (2016) 104–114.
- [7] H.J. Frisch, G.W. Trucks, H.B. Schlegel, et al., Gaussian O.G., Revision A.O2, Gaussian Inc., Wallingford, CT, 2009.
- [8] A. D. Becke, *J. Chem. Phys.* 98 (1992) 5648–5652.
- [9] C. Lee, W. Yang and R.G. Parr, *Phys. Rev.* B37 (1998) 785–789.
- [10] MOLVIB (V.7.0): Calculation of Harmonic Force Fields and Vibrational Modes of Molecules, QCPE Program No. 807 (2002).
- [11] A. Filarowski, A. Koll, A. Kochel, J. Kalenik, P.E. Hansen, *J. Mol. Struct.* 700 (2004) 67–72.
- [12] D.C. Young, *Computational Chemistry: A Pratical Guide for Applying Techniques to Real-World Problems*, John Wiley & Sons, Inc., New York, 2001.
- [13] V. Krishnakmar. R. Mathammal. R. Muthunatesan, *Spectrochim Acta A Mol Biomol Spectrosc.* 70 (2008) 201–209.
- [14] D. Sajan, J. Binoy, I. Hubert Joe, V.S. Jayakumar and J. Zaleski, *J. Raman Spectrosc.* 36 (2005) 221–236.
- [15] N. Y. SugirthaSuni, L. GuruPrasad, R. GanapathiRaman, *Orient. J. Chem.* 34(3) (2018) 1638–1645.
- [16] S. Ievavijayan, *Spectrochim Acta A Mol Biomol Spectrosc.* 136 (2015) 553–566.
- [17] D.M. Chemes, D.J.A. de Armiño, E.H. Cutin, H. Oberhammer and N.L. Robles, *J. Mol. Struct.* 1127 (2017) 191–198.
- [18] T. Gnanasambandan, S. Gunasekaran, S. Seshadri, *J. Mol. Struct.* 1052 (2013) 38–49.
- [19] S. Gunasekaran, S. Kumaresan, R. Arunbalaji, G. Anand, S. Srinivasan, *J. Chem. Sci.* 120 (2008) 315–324.
- [20] I. Fleming, *Frontier Orbitals and Organic Chemical Reactions*, Wiley, London, 1976.

MOLECULAR STRUCTURE AND HYDROGEN BONDING INTERACTIONS OF 7,8-DIHYDRO-3-METHYL-1-PHENYL-1H-PYRAZOLO[3,4-B]QUINOLIN-5(H)-ONE (PYRZ)

Arockia Jeya Yasmi Prabha E, Athimoolam S

Department of Physics, University College of Engineering, Nagercoil, Anna University, Nagercoil – 629 004
Email: athi81s@yahoo.co.in

Abstract

The crystal is crystallized in the centrosymmetric monoclinic $P2_1/n$ space group space group. The crystal and molecular structures of the grown PYRZ compound shows that existence of electron delocalization leads to the variation in bond lengths and bond angles. the dihedral angles between the phenyl rings and the plane of the pyrazole rings range from $8.8 (1)^\circ$ to $32.9 (1)^\circ$.

Keywords: Pyrazole, Crystal Structure, Hydrogen bonding, Bifurcated

1. Introduction

The Pyrazole and its derivatives are the subject of many research studies due to their widespread potential biological activities such as antifungal, antimicrobial and antiviral activities [1-4]. They can also be used as a pesticide and biodegradable agrochemicals. A wide variety of biological effects of pyrazole provoked interest for their crystal and molecular structure study.

2. Experimental

2.1. Preparation

A mixture of 3-aminocrotononitrile (1 mmol), 1-phenylhydrazine (1 mmol) and L-proline (0.4 mmol) was taken in water (10 mL) and heated to reflux. After 1 h of continuous reflux, 2-((dimethylamino)methylene) cyclohexane-1,3-dione (1 mmol) was added and the reflux continued for another 1 h. Upon addition, the mixture turned homogeneous. The completion of the reaction was evident from the formation of a precipitate, which was filtered, washed with water, and dried under vacuum and obtained a pale yellow solid.

2.2. Single crystal XRD studies

The crystallographic calculations of PYRZ2 were done by Bruker AXS KAPPA APEX-2 diffractometer equipped with graphite monochromator. The structure was solved by direct methods and refined by full-matrix least-squares calculations using SHELXL-2014. Relia-

bility index (R-factor) for $F_2 > 2\sigma(F_2)$ was found to be 6.11%, which confirmed the convergence of the reliable structure.

3. Results and Discussion

3.1. Structural Commentary

The crystal PYRZ2 was crystallized in a monoclinic $P2_1/n$ space group (Table 1). The asymmetric part of the crystal PYRZ contains four units of the molecule (Figure 1).

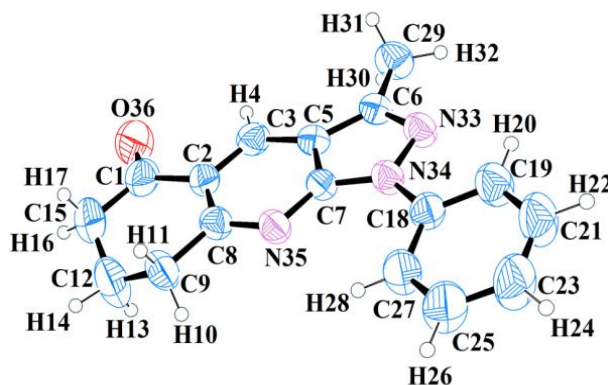


Figure 1. The molecular structure of PYRZ2 with the numbering scheme for the atoms and 50% probability displacement ellipsoids

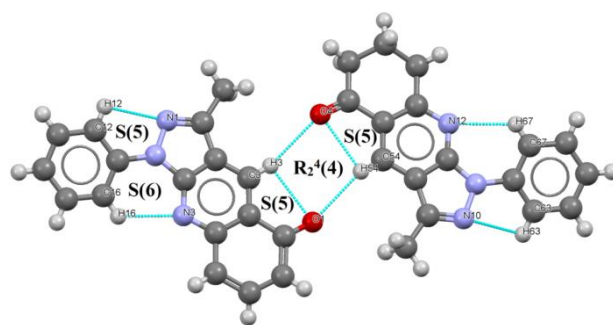
The molecular geometry of one of the four units shows that the dihedral angles between the phenyl rings and the plane of the pyrazole rings ranges from 8.8 (1)° to 32.9 (1)°. The phenyl ring is planar, with r.m.s. deviations ranging from 0.132 to 0.191 Å. All C–N bond lengths varies from 1.308 (2) to 1.370 (3) Å. Also in the cyclohexanone group of the quinoline ring, all the C–C bond distances, ranges from 1.48 to 1.49 Å. The lengthening of the C–C bond is due to electrostatic interactions between the formal positive charges on the carbonatoms.

Table 1 Crystallographic data, intensity data collection and structure refinement parameters for PYRZ

Experimental Details	PYRZ
Empirical formula	C ₁₇ H ₁₅ N ₃ O
Formula weight	276.06
Temperature	293(2) K
Crystal system, space group	Monoclinic, P2 ₁ /n
Unit cell dimensions	a = 13.693 (10) Å, b = 18.400 (1) Å c = 22.782 (2) Å, β = 99.4 (1)°
Volume	5663.2 (7) Å ³
Z, Calculated density	16, 1.295 Mg/m ³
F(000)	2316
Crystal size	0.23 × 0.19 × 0.18 mm ³
Theta range for data collection	1.4 to 25.0°
Limiting indices	-16 ≤ h ≤ 16, -21 ≤ k ≤ 21, -27 ≤ l ≤ 27
Reflections collected / unique	53897 / 9976 [R(int) = 0.0377]
Completeness to theta = 25.2°	97.30%
Final R indices [I > 2σ(I)]	R1 = 0.0667, wR2 = 0.1886
R indices (all data)	R1 = 0.1047, wR2 = 0.2245
Largest diff. peak and hole	0.505 and -0.267 e. Å ⁻³

3.2. Supramolecular features

The crystal structure is also influenced by C–H···O and C–H···N interactions (Table 2). The self-associated graph-set S(5) and S(6) motifs are formed through C–H···N intramolecular interaction. Another self-associated S(5) motif is observed by weak intra molecular interaction. This ring motif is connected to neighbor's unit through C–H···O hydrogen bond making bifurcated ring R₂⁴(4) motifs (Figure 2). These ring motifs form layers like structure along the *b*-axis of the unit cell (Figure 3).



A view of ring motifs connecting the molecules through C–H···N and C–H···O interactions in PYRZ

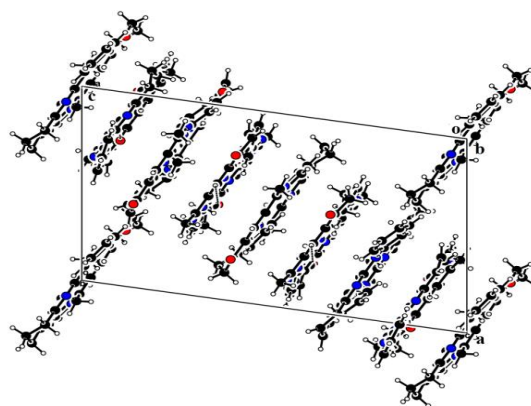


Figure 3. The packing diagram of PYRZ2, viewed along *b*-axis

Table 2 Hydrogen bonds geometry for PYRZ2

D–H...A (Å, °)	d(D–H) Å	d(H...A) Å	d(D...A) Å	(DHA) (°)
C19–H20···N33	0.93	2.432(2)	2.769(4)	101
C27–H28···N35	0.93	2.369(2)	3.004(4)	125
C55–H56···N69	0.93	2.989(3)	3.517(5)	117
C63–H64···N71	0.93	2.434(2)	3.030(4)	121
C3–H4···O72 ^{#1}	0.93	2.594(3)	3.458(4)	154
C39–H40···O36 ^{#2}	0.93	2.536(3)	3.399(4)	154

4. Conclusion

In PYRZ2, the dihedral angles between the phenyl rings and the plane of the pyrazole rings range from 8.8 (1)° to 32.9 (1)° for the four units. This orientation liberty is raised due to the packing specificity of the crystal.

REFERENCES

- [1] S. Mert, R. Kasimogullari, T. Ica, F. Colak, A. Altun and S. Ok, "Synthesis, structure-activity relationships, and in vitro antibacterial and antifungal activity evaluations of novel pyrazole carboxylic and dicarboxylic acid derivatives", *Eur. J. Med. Chem.*, vol. 78, 2014, pp. 86–96.
- [2] S. Velaparthi, M. Brunsteiner, R. Uddin, B. Wan, S.G. Franzblau and P. A. Petukhov, "5- tertbutyl- N- pyrazol- 4- yl- 4,5,6,7 tetrahydrobenzo [d] isoxazole-3-carboxamidederivatives as novel potent inhibitors of Mycobacterium tuberculosis pantothenate synthetase: initiating a quest for new antitubercular drugs", *J. Med. Chem.*, vol. 51, 2008, pp. 1999-2002.
- [3] P. Baraldi, S. Manfredini, R. Romagnoli, L. Stevanato, A.N. Zaid, and R. Manservigi, "Synthesis and Anti-HSV-1 Activity of 6 Substituted Pyrazolo[3,4-d]Pyridazin-7-one Nucleosides", *Nucleosides Nucleotides*, vol. 17, 1998, pp. 2165–2171.
- [4] P.D. Mishra, S. Wahidullah and S.Y. Kamat, "A heteroaromatic acid from marine sponge *Suberites vestigium*", *Indian J. Chem. Sect. B*, vol. 37, 1998, pp. 199–200

APPROACH TO SYNTHESIS, HYDROGEN BONDING ANALYSIS BY HIRSHFELD SURFACE AND MULLIKEN POPULATION ANALYSIS OF PHARMACEUTICAL COCRYSTALS OF THEOPHYLLINE (A BRONCHODILATOR DRUG)

L. Mary Novena, S. Suresh Kumar and S. Athimoolam

Department of Physics, University College Engineering, Nagercoil, Anna University
Nagercoil - 629 004, India.

Correspondence email: cystallographer@rediffmail.com

Abstract

Co-crystals of Theophylline Resorcinol and Pyrogallol have been crystallized and their crystal structure was determined by single crystal X-ray studies. The optimized geometry for both the crystals are employed using HF and DFT calculations with B3LYP method. The hydrogen bonding analysis shows that TR is closely packed than TPY which influence the structure stability. Hirshfeld surface analysis confirms the structure stability of the compound, which shows that there exhibits imbalance in TPY due to the presence of N-H...N interaction, which does not exhibit in TR. The mulliken charge analysis confirms the redistribution of electron density due to the substitution of the cofomers.

Keywords: Hydrogen bond, Hirshfeld, HF, DFT, mulliken.

1. Introduction

Cocrystallization of an active pharmaceutical ingredient (API) with a pharmaceutically acceptable molecule forms an attractive route for the development of pharmaceutical products. Cocrystallization alters the molecular interactions and composition of pharmaceutical materials to optimize drug properties thereby improving bioactivity [1]. Cocrystallization of API with water soluble cofomers has been used in altering the physicochemical properties to overcome the difficulties associated with poor aqueous solubility [2]. Hydrogen bonding plays a vital role in determining the stability of the structure with respect to biological and chemical entities. Theophylline is an API similar to caffeine and theobromine which belongs to xanthine family closely related to plant alkaloids and show many distinct biological and pharmacological activities [3]. Also theophylline, an imidazole molecule is a biologically important one having the capability of forming hydrogen bonding with -NH group act as hydrogen-bond donors and the two carboxyl oxygen atoms act as hydrogen-bond acceptors [4]. The present study is used to attempt cocrystallization of catechin compounds such as resorcinol and pyrogallol with theophylline. Moreover the phenolic -OH group can also be used to cocrystallize with theophylline which may be possible by inclusion of water molecules into the crystalline lattice [5], which plays an important role

in the formation of pharmaceutical cocrystal. Resorcinol and Pyrogallol is a safe cofomer molecule and its derivatives exhibit anticancer activity. Pyrogallol is an active ingredient of *Emblia officinalis* (Amla), which has the potential to develop as nontoxic anti-cancer agent [6]. The present study herein reports the monohydrate structures of Theophylline resorcinol (TR) and Theophylline pyrogallol (TPY), where the former one is the redetermination work [7] and latter one is newly synthesized cocrystal. Density Functional Theory (DFT) has been employed to refine and check their microscopic molecular structure. To the best of our knowledge, no work dealing with computational studies has been reported so far. Also, computational investigations have been made to compare with the experimental methods in computing the molecular structure to analyse the chemical properties of the compounds.

Single-crystal X-ray analysis is the most powerful method for structural characterization of complexes including co-crystals. The aim of present investigation is the synthesis, structural and spectroscopic characterization of theophylline complex with resorcinol and pyrogallol. Further, the venture to understand the nature of intermolecular interactions throughout the structure or around the surface of the molecule Hirshfeld surface analysis is carried out. Also, it helps to reveal about close and weak contacts and also more distant interactions. To identify the delocalization activity of the electron clouds in the optimized

molecular structure were performed using Hartree-Fock method (HF) and Density functional theory (DFT).

2. Experimental

Anhydrous Theophylline and resorcinol were dissolved in distilled water in 1:1 ratio and the resulting solution was stirred for 2 to 3 hrs at room temperature. A small cube-shaped crystal suitable for X-ray diffraction was obtained after four days. Anhydrous Theophylline and pyrogallol were dissolved in distilled water in 1:1 ratio. The resulting solution was stirred for 2 to 3 hrs at room temperature. A light brown coloured solution obtained after filtration was left to evaporate slowly at room temperature. Small brown colour block type single crystals suitable for X-ray diffraction were obtained after two days. The densities of the crystals were measured by sink and swim method (flotation technique). The densities of TR and TPY observed to be 1.52(1) and 1.67(3) Mg.m⁻³, respectively. X-ray intensity data of the grown crystals of TR and TPY were collected at room temperature with MoK_α radiation ($\lambda = 0.71073 \text{ \AA}$) using Bruker AXS KAPPA APEX-2 diffractometer at room temperature. The structure was solved by direct methods and refined by full-matrix least square calculations using SHELXL-2014 software [8]. All the H atoms were positioned geometrically and refined using riding model approximation, with C-H = 0.93–0.96 \AA , N-H = 0.86 \AA and $U_{\text{iso}}(\text{H}) = xU_{\text{eq}}(\text{C}, \text{N})$ where $x = 1.5$ for methyl H and 1.2 for all other H atoms. Infrared spectrum using KBr pellet of the sample was recorded in the region of 4000–400 cm⁻¹ using Perkin Elmer Spectrometer at a resolution of 1 cm⁻¹. The FT-Raman spectrum was recorded in the frequency range of 50–4000 cm⁻¹ using a BRUKER RFS 27 FT-Raman Spectrometer module and the Nd:YAG Laser source was operated at 1064 nm with the resolution of 2 cm⁻¹.

3. Computational details

Theoretical calculations were carried out using Gaussian 09[9] software package. The geometry optimization and vibrational modes calculation of TR and TPY were carried out with both Density Functional Theory (DFT) and Hartree-Fock (HF) method, which gives the structural and spectral characteristics. The starting geometry for both the compound was taken from final X-ray refinement cycle. The geometry of the molecule without considering the water molecule was optimized using DFT employing the Becke-3-Lee-Yang-Parr (B3LYP) and HF methods supplemented with the standard 6-311++G(d,p) basis set. In TPY after several attempts, the theoretical calculation for DFT is done in 6-31++G (d,p) basis set. The molecule was not optimized in 6-311++G (d,p)

basis set. The vibrational frequency calculations were performed based on the minimum energy conformer derived from the gas-phase calculation at the DFT level using Gaussian 09. The electronic properties of the compounds have been computed, which determines the way a molecule interacts with other species [10]. HOMO-LUMO for both TR and TPY were performed theoretically. Both the compounds were compared to analyze the charge interaction and activity of the compound. In the study of chemical kinetics and chemical equilibria, the knowledge of thermodynamic function is of great importance. Hirshfeld surfaces and their corresponding fingerprint plots were calculated and analyzed by reading the CIF file into software CrystalExplorer [11]. The Hirshfeld molecular surfaces of the complexes TR and TPY were generated and finger print plots were plotted using Crystal Explorer 3.1 which accepts the crystal data in CIF format. The bond lengths of hydrogen were automatically modified to typical standard neutron values (C-H=1.083 \AA and N-H=1.009 \AA) [17]. In order to describe the various intermolecular interactions like O \cdots H, C \cdots H, N \cdots H, C \cdots C and other contacts present in the crystal structures, the 2D finger plots were displayed on the graph axes.

4. Result and discussion

4.1 Molecular geometry

The molecular structure of TR and TPY was confirmed by X-ray diffraction studies and optimized through HF and DFT calculations are shown in Fig.1 and 2. TR crystallizes in monoclinic space group Cc. The crystal structure of TPY 2:1 is observed in triclinic space group P1 with an asymmetric unit that contains two theophylline molecules and one pyrogallol molecule. The optimized bond length and bond angles of TR and TPY are computed using HF and DFT methods. The computed values are then compared with the experimental values. The bond lengths of theophylline in both the compounds are similar, which indicate that there is no transfer of proton from cofomers. The optimized and experimental value of C=O bond distance in theophylline agrees well with the actual value (1.2 \AA) indicating the bonds are dominant in their double bond character. In TR, there is a slight difference in bond angle (O10-C3-C8) / (N9-C15-N7) which may be due to oxygen atom of one O-H group of resorcinol reacts with *exo*-carbonyl group and imidazole of theophylline. Also, the bond angles O23-C28-C30 and O23-C28-C26 deviates due to the formation of N-H \cdots O hydrogen bonding network. In TPY, the increase in bond distances (C22-O31 and C30-O33) and bond angles may be due to the formation of N-H \cdots O and O-H \cdots O hydrogen bonding network. The two theophylline molecules are interconnected through N-H \cdots N interaction between the imidazole rings thereby altering the bond angles within the ring. There is a slight variation between the

experimental and computed values. The difference is due to the fact that one isolated molecule is carried out in gas phase in theoretical calculation and many packing molecules are carried out in solid phase in experimental measurement.

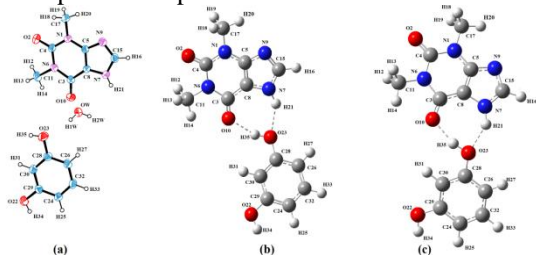


Fig.1 The molecular structure of the TR with the numbering scheme for the atoms and 50% probability displacement ellipsoids (a), optimized molecular geometry and atomic numbering scheme by (b) HF and (c) B3LYP method

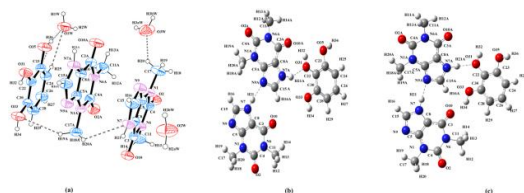


Fig.2 The molecular structure of the TPY with the numbering scheme for the atoms and 50% probability displacement ellipsoids (a), optimized molecular geometry and atomic numbering scheme by (b) HF and (c) B3LYP method.

4.2 Hydrogen bonding

Hydrogen bonds are frequently engaged in co-crystal design due to their characteristics nature. It has been prominent that the H-bonds which are linear and closer to linearity are stronger than bonds that are far from 180° . The crystal structure of both the compounds is stabilized by two classical N-H \cdots O, O-H \cdots O intermolecular hydrogen bonds and non-classical C-H \cdots O, C-H \cdots N intermolecular interactions. The crystal packing of TR is extended by a water linkage forming a 1D tape running along crystallographic *b* axis and they form an infinite one-dimensional chain parallel to (0 0 2) and (0 0 -2) planes making strong intensity peak at X-ray diffraction. The water molecule acts as a bridge for connecting two theophylline and one resorcinol molecule by N-H \cdots O, O-H \cdots O hydrogen bonds in the co crystal Hence, the water molecules act as both H-bond donors to carbonyl group and imidazole ring in theophylline and acceptor to phenolic group of resorcinol. Further one of the OH group in resorcinol is hydrogen bonded to theophylline forming a dimer ring $R_2^2(7)$ motif through N-H \cdots O and C-H \cdots O hydrogen bonding network lies in the hydrophilic region as shown in Fig.3a. Also, a ring $R_2^3(9)$ motif is formed between resorcinol and theophylline through one classical O-H \cdots O hydrogen bonding and two non-classical C-H \cdots O, C-H \cdots N interactions (Fig.4). Both the ring

motifs in TR molecule aggregate as layer and separated by a distance of 13.90Å.

The crystal packing of TPY is extended by three water molecules leads to the formation of an infinite one-dimensional hydrogen-bonded ribbon parallel to (-1 0 -1) and (1 0 1) planes with dimer ring $R_2^2(10)$ and $R_2^2(6)$ motifs utilizing a single C-H \cdots O hydrogen bond and C-H \cdots N interactions. Also, a ring $R_2^2(8)$ motif is formed between two theophylline molecules by C-H \cdots O and N-H \cdots N interactions. The water molecules connect two theophylline and one pyrogallol molecule thus, creating two trimeric ring $R_3^3(11)$, $R_3^3(7)$ motifs (Fig.5). The hydroxyl group in pyrogallol are involved in hydrogen bonding through N-H \cdots O, O-H \cdots O and C-H \cdots O hydrogen bonding network thereby forming ring $R_2^1(5)$, $R_3^3(9)$ motifs which lies in the hydrophilic region as shown in Fig.3b. The packing structure of TPY is aggregated as layer like structure (Fig. 3b) in which the water molecule occurs in $\frac{1}{4}$ of the hydrophilic region and separated by a distance of 11.90Å. A two bifurcated ring $R_2^1(6)$, $R_2^1(5)$ motifs observed in TPY contribute greatly in constructing the structure. It is concluded that all the donors and acceptor atoms of theophylline are utilized in the presence of cofomers. As there is a difference in stoichiometric ratio of both the compounds, hydrogen bond pattern also differs. The oxygen atom in water molecules with O22-OW /O35-O1W distance less than 3Å with a suggestive that the water molecules act as hydrogen donor. Also, the molecules with smaller volume suggest closely packed structure. This shows TR molecule will be closely packed than TPY, which influences the stability of the crystal structure.

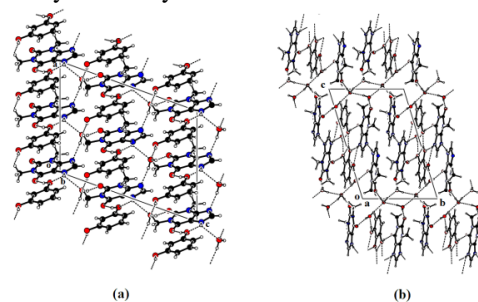


Fig.3 The packing diagram of (a) TR and (b) TPY viewed down *c* axis. Dashed line indicate Hydrogen bond

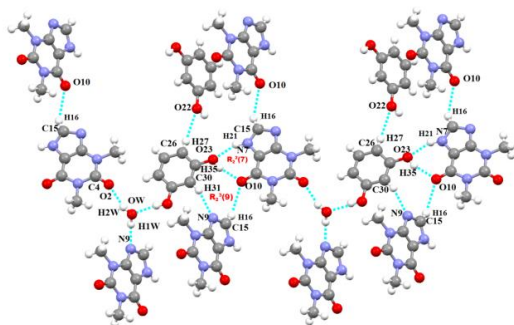


Fig.4 Ring motifs $R_2^2(9)$ and $R_2^2(9)$ diagram for TR

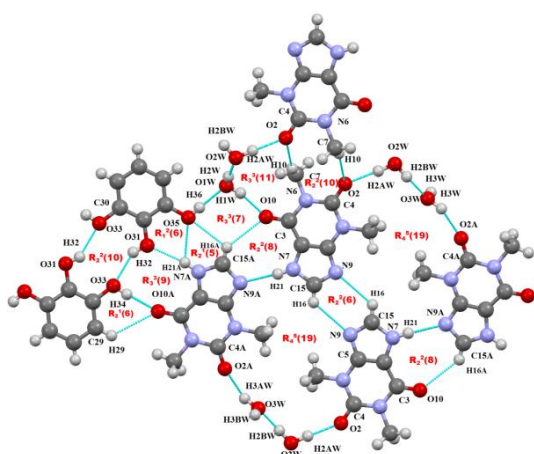


Fig.5 Ring motifs $R_1^2(6)$, $R_2^2(10)$, $R_3^3(9)$, $R_4^5(19)$, and $R_2^2(8)$ diagram for TPY

4.3 Hirshfeld surface analysis

The Hirshfeld surface analysis of two co-crystals of theophylline was generated by Crystal Explorer 3.1. The two dimensional finger plots enumerate the intermolecular interactions involved in packing of crystal. Using Hirshfeld surface diagram, the intermolecular interactions are identified, which are possible for the stability of the crystal structure. The 3D Hirshfeld surfaces and 2D fingerprint maps of the cocrystals are shown in Figure. The distance from the Hirshfeld surface to the nearest atoms outside and inside the surface are characterized by the quantities d_e and d_i , respectively [12]. The d_{norm} mapped by Hirshfeld surface is indicated by red-blue-white colour scheme, where red represents closer contacts and a negative value, blue represents longer contacts and a positive value and white represent distance of contacts exactly corresponding to the VanderWaals separation with a d_{norm} value of zero (Fig. 6 and 7). The $N\cdots H/H\cdots N$ interactions regions are visible in finger plots where one molecule acts as a donor and other one acts as an acceptor. In TR and TPY, the $N\cdots H/H\cdots N$ contact is 6.5 and 8.1% respectively. This imbalance in TPY is due to the presence of N-

$H\cdots N$ interaction, which does not exhibit in TR, showing $C-H\cdots N$ interaction which is reflected in Hirshfeld surfaces as light red spot. Aromatic compounds possessing hetero atoms in the ring show more intensity in $C-C$ contacts between the rings. In TPY/TR, the $\pi-\pi$ stacking occupies with a distance $3.8 \text{ \AA}/3.3 \text{ \AA}$ showing $C-C$ contact is more in TPY than TR. The most interesting feature is that $H\cdots H$ contacts are predominant in the total Hirshfeld surface especially for TPY (48.5%) having huge proportion of hydrogen atoms in the structure. The contribution of $O\cdots H/H\cdots O$ interactions in both the co-crystal shows similar percentage. For TR and TPY, $O-H\cdots O$ hydrogen bonding intermolecular interaction appear as two sharp spikes in the 2D fingerprint map, which influences the total Hirshfeld surfaces comprised of 31.7 and 32.4% respectively. Also the $N-H\cdots O$ hydrogen intermolecular interaction appears as sharp spikes in both the compound comprised of 19.9%. Apart from above interactions, $O-C$ and $O-O$ interactions are also observed.

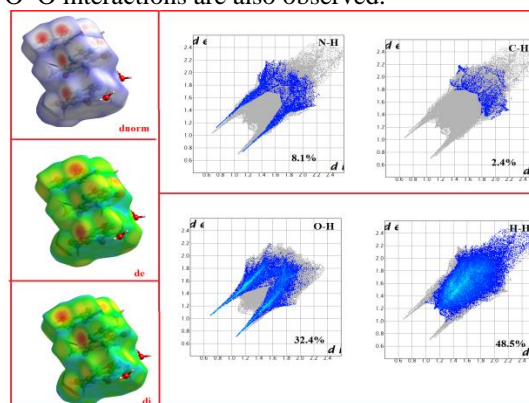


Fig.6 Hirshfeld surfaces and 2D fingerprint plots of TR

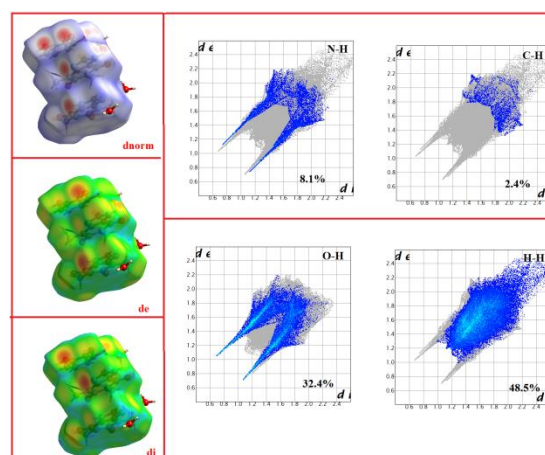


Fig.7 Hirshfeld surfaces and 2D fingerprint plots of TPY

positive charge, in particular, the hydrogen atoms H35 and H54 in TR (Fig.9a) and TPY that have charge of 0.500/0.461 and 0.635/0.649 in HF/DFT methods respectively (Fig.9b). The presence of large amounts of negative charge on oxygen and

net positive charge on hydrogen atoms may suggest the presence of intramolecular hydrogen bonding in the crystalline phase. In both the compounds, the methyl carbons (C11 and C17 atoms) possess negative charge due to electron withdrawing character of nitrogen atom. The carbonyl atom C3

4.4 Conclusion

Recently, for the research of molecular structures, DFT has become an important tool that is widely used. In TR and TPY, the experimental geometry agree well with the theoretical values. The deviation in the bond length and bond angles is confirmed by the hydrogen bonding network in both the compound. The stability of the crystal structure is attributed by Hirshfeld analysis in which TPY possess imbalance in their structure due to the presence of N-H \cdots N interaction.

REFERENCES

1. B.S. Sekhon, "Pharmaceutical cocrystal-a R" *Ars Pharm*, Vol. 50, 2009, pp. 99-117.
2. S. Ranjan, R. Devarapalli, S. Kundu, V.R. Vangala, S. Ghodh, C.M. Reddy, "Three new hydrochlorothiazide cocrystals: Structural analyses and solubility studies" *Journal of molecular Structure* vol/ 1133,2017, 405-410.
3. A.M. Chen, M. E. Ellison, A. Peresykin, R.M. Wenslow, N. Variankaval, C.G. Savarin, T.K. Natishan, D.J. Mathre, P.G. Dormer, D.H. Euler, R.G. Ball, Z. Ye, Y. Wang and Ivan Santos, "Development of a pharmaceutical cocrystal of a monophosphate salt with phosphoric acid," *Chem. Commun*, 2007, pp. 419-421.
4. B. Sarma, B. Saikia, "Hydrogen bond synthon competition in the stabilization of theophylline cocrystals" *CrystEngComm*, vol. 16, No. 22, 2014, pp. 4753-4765.
5. G. B. Mahady, S. L. Pendland, G. Yun, Z. Z. Lu, "Turmeric (*Curcuma longa*) and curcumin inhibit the growth of *Helicobacter pylori*, a group I carcinogen" *Anticancer Res.*, vol. 22, 2002, pp. 4179-81.
6. Y. Sugiyama, S. Kawakishi, T. Osawa, "Involvement of the β -diketone moiety in the antioxidative Mechanism of Tetrahydrocurcumin" *Biochem.Pharmacol.*, vol. 52, 1996, pp. 519.
7. N. Pal, D. Singha, A.D. Jana, "Synthesis, crystal structure, Hirshfeld surface analysis, electronic structure through DFT study and fluorescence properties of a new anthracene based organic tecton" *Journal of Molecular Structure* vol. 1145 2017, pp. 102-111.
8. G.M. Sheldrick, *Acta Cryst. C* 71 (2015), 3-8
9. M.J. Frisch, G.W. Trucks, H.B. Schlegel, G.E. Scuseria, M.A. Robb, J.R. Cheesman, V.G. Zakrzewski, J.A. Montgomery Jr., R.E. Stratmann, J.C. Burant, S. Dapprich, J.M. Millam, A.D. Daniels, K.N. Kudin, M.C. Strain, O. Farkas, J. Tomasi, V. Barone, M. Cossi, R. Cammi, B. Mennucci, C. Pomelli, C. Adamo, S. Clifford, J. Ochterski, G.A. Petersson, P.Y. Ayala, Q. Cui, K. Morokuma, N. Rega, P. Salvador, J.J. Dannenberg, D.K. Malich, A.D. Rabuck, K. Raghavachari, J.B. Foresman, J. Cioslowski, J.V. Ortiz, A.G. Baboul, B.B. Stetanov, G. Liu, A. Liashenko, P. Piskorz, I. Komaromi, R. Gomperts, R.L. Martin, D.J. Fox, T. Keith, M.A. Al-Laham, C.Y. Peng, A. Nanayakkara, M. Challacombe, P.M.W. Gill, B. Johnson, W. Chen, M.W. Wong, J.L. Andres, C. Gonzalez, M. Head-Gordon, E.S. Replogle, J.A. Pople, GAUSSIAN 09, Revision A 11.4, Gaussian Inc., Pittsburgh, PA, 2009.
10. P. Venkatesan, S. Thamothran, A. Ilangovan, H. Liang, T. Sundius, "Crystal structure, Hirshfeld surfaces and DFT computation of NLO active (2E)-2-(ethoxycarbonyl)-3-[(1-methoxy-1-oxo-3-phenylpropan-2-yl)amino] prop-2-enoic acid" *Spectrochimica Acta Part A: Molecular and Biomolecular Spectroscopy* vol. 153, 201, pp. 625-636.
11. K. Wolff, D.J. Grimwood, J.J. McKinnon, M.J. Turner, D. Jayatilaka, M.A. Spackman, *Crystal Explorer (Version 3.1)*, University of Western Australia, 2012.
12. F.L., Hirshfeld, *Theor. Chim. Acta.* 44 1977, 129-133

STRUCTURAL, SPECTRAL AND ANTICANCER STUDIES ON 5-FLUOROURACIL HYDROQUINONE

S. Suresh Kumar and S. Athimoolam

Department of Physics, University College Engineering, Nagercoil, Anna University
Nagercoil - 629 004, India.

Correspondence email: crystallographer@rediffmail.com

Abstract

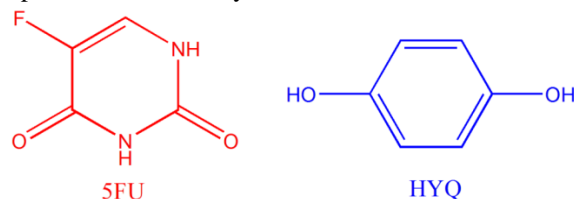
New co-crystal containing 5-Fluorouracil (an anticancer drug) as an active pharmaceutical ingredient (API) was prepared by the liquid-assisted grinding method. The prepared co-crystal namely, 5-fluorouracil hydroquinone (5FUHYQ) was studied through single X-ray diffraction. It reveals that the crystal packing is supported by N–H···O and O–H···O classical hydrogen bonds forming a sheet-like molecular architecture. The drug molecules are connected themselves through three N–H···O intermolecular hydrogen bonds leading to two dimeric ring R22(8) motifs. These two ring motifs are placed adjacently forming two chain C21(6) motifs which are running along the a-axis of the unit cell, oppositely. The drug molecules are sandwiched at $y = 1/2$ and the cofomers are placed at $y = 0$ and 1 making the supramolecular assembly. These ring and chain motifs to form a hydrogen-bonded sheeted. The 5FUHYQ has lower calculated density than the parent drug which favour the improved membrane permeability of the drug. The anticancer activity of the parent drug is retained against human cervical cancer cell line (HeLa) in this new co-crystalline form.

Keywords: XRD, Anticancer activity, FT-IR, FT-Raman, DFT and FMO

1. Introduction

5-Fluorouracil (5FU) is one of the fluorine-based derivatives and a well-known anticancer drug. It was first prepared in 1957 [6] and used in the treatment of solid tumors, such as colorectal, breast, gastrointestinal and ovarian cancers [7-9]. Also, it is used as an ointment, particularly in skin cancer [10-13]. It is one of the antimetabolite drugs and also the pyrimidine analogue [14]. From the crystal engineering perspective, the 5FU has hydrogen bonding donors (two N–H) and hydrogen bonding acceptors (two C=O) in the molecular structure [15]. It act as strong hydrogen bonding synthon with neighbouring molecules in crystalline assembly. In this point of view, number of co-crystals were attempted with 5FU, with the cofomers of cytosine [16], 1-methylcytosine [17], theophylline [18], urea, thiourea, 2,2' -bipyridine & 4,4' -bipyridine [19], acridine, phenazine & 4,4-bispyridylethene [20], adipic, succinic, terephthalic, benzoic & malic acid [21], 4-hydroxybenzoic acids [22] and 3-hydroxybenzoic acid, 4-aminobenzoic acid & cinnamic acid [23] etc. The present work was initiated with the series of hydroxyl aromatic compounds like catechol, resorcinol and

hydroquinone as acoformers. In which, the co-crystal of hydroquinone was successfully crystallized with the 5FU using the liquid-assisted grinding method and reported here as a first time in literature (scheme 1). Further, the several characterizations, such as vibrational and cytotoxicity studies were also done to describe the properties of new co-crystal.



Scheme 1 Structures of 5-Fluorouracil (5FU) and Hydroquinone (HYQ)

2. Experimental

2.1. Preparation

The co-crystal of 5-fluorouracil hydroquinone (5FUHYQ) was synthesized by the liquid-assisted grinding method. The experiment was performed by adding an equimolar of 5FU (0.130 g) and the hydroquinone (0.110 g) with few drops of distilled water to make the paste using mortar pestle. Finally, this paste

was dissolved in the methanolic solution to allow the slow evaporation at room temperature. After two week period, the needle-shaped crystal was harvested.

2.2. Single Crystal XRD studies

The necessary crystallographic calculations, i.e., the unit cell parameters of 5FUHYQ and full data collections were done from single-crystal X-ray diffraction studies by Bruker SMART APEX CCD area detector diffractometer (graphite- monochromated, MoK α = 0.71073 Å) [24]. Crystallographic data, details of the data collection and refinement statistics are given in Table 1. The structure was solved by direct methods using SHELXL 2014 [25]. All the H atoms were positioned geometrically and refined using riding model approximation, with C–H = 0.86-0.93 Å and Uiso(H) = 1.2 Ueq (parent atom). The R-factor (0.035 %) of the compound confirms the convergence of the crystal structure.

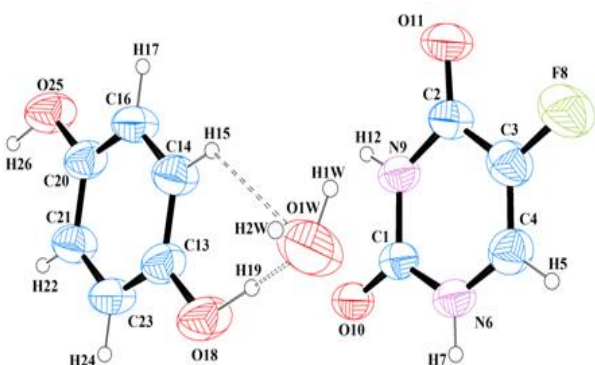


Figure 1. ORTEP diagram of title compound

2.3. FT-IR studies

The FTIR spectroscopy studies were used to analyze the presence of functional groups in synthesized compound. The FTIR spectra of title compound were recorded using Jasco spectrometer FTIR, model 410 under a resolution of 4 cm⁻¹ and with a scanning speed of 2 mm/sec was used for IR spectral measurements. The samples were prepared using pellet technique and the spectra were recorded over the range 4000–400 cm⁻¹, shown in the figure 2.

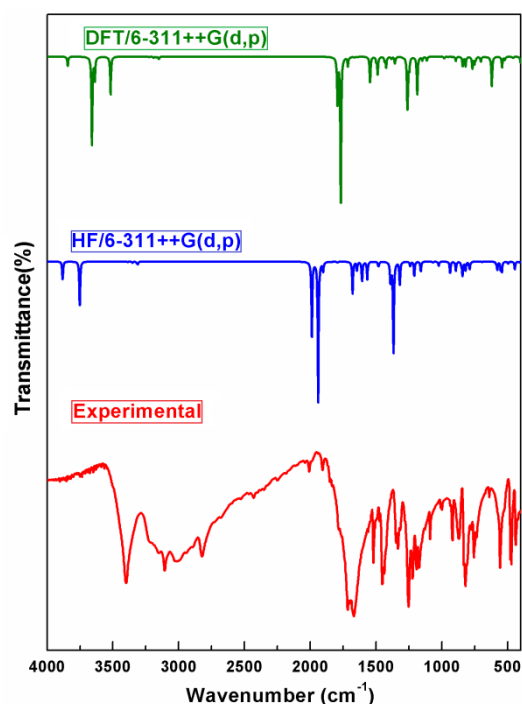


Figure 2. FT-IR spectrum of title compound

2.4. Anticancer activity Studies

The cytotoxicity of the grown crystal (5FUHYQ) was investigated against human cervical cancer cell line (HeLa) and compared with the parent drug 5FU. The above cell line was acquired from the National Centre for Cell Science (NCCS), Pune. It was grown in Eagles Minimum Essential Medium, which is containing 10% Fetal Bovine Serum (FBS). These cells were sustained at 37 °C, 5% CO₂, 95% air and 100% relative humidity (Figure 3).

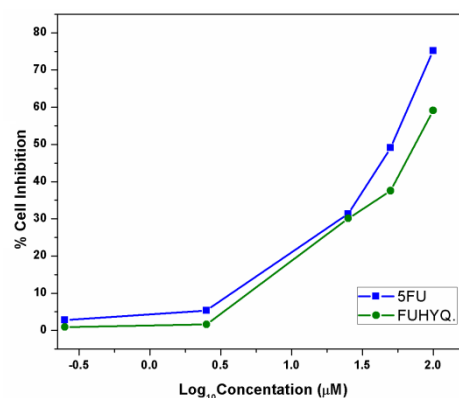


Figure 3. Cytotoxic activity of 5FUHYQ and 5FU

3. Results and Discussion

New co-crystal of 5-fluorouracil hydroquinone (5FUHYQ) was prepared by the liquid-assisted grinding method. The molecular structure of the present compound is confirmed by single crystal X-ray diffraction technique. The crystal packing is stabilized through the three-dimensional network of intricate N–H···O and O–H···O classical hydrogen bonds forming sheet-like architecture. This sheets are parallel to the (0 4 $\bar{2}$) and (0 $\bar{4}$ 2) planes of the unit cell. The drug molecules are situated midpoint of the sheet and the cofomers are placed at $y = 0$ and 1. The present compound has lower calculated density than the parent drug which favour the improved membrane permeability of the drug. The anticancer activity of the present compound was analyzed against the human cervical cancer cell line (HeLa). This study reveals that 5FUHYQ retains its activity against human cervical cancer cell line (HeLa) with possible improved physiochemical and pharmacokinetic properties.

REFERENCES

- [1] I. T. Fuchikami, I. Ojima, J. Am. Chem. Soc. 104 (1982) 3527
- [2] V.A. Soloshonok, T. Hayashi, Tetrahedron Lett. 35 (1994) 2713
- [3] I. Ojima, K. Kato, K. Nakahashi, T. Fuchikami, M. Fujita, J. Organomet. Chem. 54(1989) 4511.
- [4] R. Mohamed Asath, R. Premkumar, T. Mathavan, A. Milton Franklin Benial, SpectrochimicaActa Part A: Molecular and Biomolecular Spectroscopy 175 (2017) 51–60.
- [5] J. Wang, M. Sanchez-Rosello, J.L. Acena, Carlos del Pozo, Alexander E.Sorochinsky, Santos Fustero, Vadim A. Soloshonok, and Hong Liu, Chem. Rev., DOI:10.1021/cr4002879.
- [6] C. Heidelberger, N.K. Chaudhuri, P. Danneberg, D. Mooren, L. Griesback, Nature 179 (1957) 663–666.
- [7] P. T. A. Galek, E. Pidcock, P. A. Wood, I. J. Bruno and C. R. Groom, CrystEngComm, 14 (2012) 2391–2403.
- [8] P. G. Johnston, H.-J. Lenz, C. G. Leichman, K.D. Danenberg, C. J. Allegra, P. V. Danenberg and L. Leichman, Cancer Res., 55 (1995) 1407–1412
- [9] E. Raymond, C. Buquet-Fagot, S. Djelloul, J. Mester, E. Cvitkovic, P. Allain, C. Louvet and C. Gespach, Anti-Cancer Drugs, 8 (1997) 876–885.
- [10] A.D. Vivier, Clinical and Experimental Dermatology 7 (1982) 89-92.
- [11] S. P. Delaney, E. M. Witko, T. M. Smith and T. M. Korter, J. Phys. Chem. A, 116 (2012) 8051–8057. Suter, P. M. (2004). SchweizRundsch. Med. Prax. 93, 857–863.
- [12] Krampitz, L. O. (1969). Annu. Rev. Biochem. 38, 213–240
- [13] Breslow, R. (1958). J. Am. Chem. Soc. 80, 3719–3726
- [14] Kraut, J. & Reed, H. J. (1962). Acta Cryst. 15, 747–757.
- [15] Pletcher, J. & Sax, M. (1972). J. Am. Chem. Soc. 94, 3998–4005.
- [16] Shiro, M., Nakai, H. & Makino, I. (1978). Acta Cryst. B34, 3424–3426.
- [17] MacLaurin, C. L. & Richardson, M. F. (1983). Acta Cryst. C39, 854–856.
- [18] Ishida, T., Tanaka, A. & Inoue, M. (1984). Acta Cryst. C40, 437–439.
- [19] Shin, W. & Chun, K. S. (1987). Acta Cryst. C43, 2123–2125.
- [20] Koziół, A. E., Palenik, R. C. & Palenik, G. J. (1987). Acta Cryst. C43, 1555-1557.
- [21] Kim, M. J., Suh, I. H., Aoki, K. & Yamazaki, H. (1988). Acta Cryst. C44, 725–727.
- [22] Casas, J. S., Castin~eiras, A., Couce, M. D., Sordo, J. & Varela, J. M. (1994). Acta Cryst. C50, 1265–1267.
- [23] Hu, N. H., Kiyota, Y. & Aoki, K. (2000). Acta Cryst. C56, 1284–1286.
- [24] Bruker (2000). SHELXTL/PC. Version 6.10. Bruker AXS Inc., Madison Wisconsin, USA.

INVESTIGATION STUDY ON STRUCTURAL AND SPECTROSCOPIC FEATURES OF IMPROVED BIO-ACTIVITY OF NITRATE SALT OF VITAMIN B3 (NICOTINIC ACID)

M. Mary Latha^a, L. MaryNovena^a, S. Athimoolam^{a*} and B. Sridhar^b

^aDepartment of Physics, University College of Engineering Nagercoil, Anna University, Nagercoil 629004

^bLaboratory of X-ray Crystallography, Indian Institute of Chemical Technology, 500 007, Hyderabad, India

*e-mail: athi81s@yahoo.co.in

Abstract

Nitrate salt of nicotinic acid is grown by slow solvent evaporation technique and subjected to single crystal XRD. The arrangement of molecules and hydrogen bonding were analyzed using single crystal XRD. The optimized structure and vibrational analysis are calculated by DFT method using 6-311++G (d,p) basis set. The N-H...O and O-H...O hydrogen bond forms predominant interactions whereas H...O interactions range from to 2.7 to 3.1 Å. The oxygen atom in the water molecule acts as a donor to form two ring R₂¹ (4) and R₃² (6) motifs. The compound is subjected to vibrational analysis (FT-IR and FT-Raman) to identify the functional groups present in the compound and the assignments are made using gaussview software by DFT method using 6-311++G(d,p).

Keywords: XRD, DFT, FT-IR, FT-Raman, basis set.

1. Introduction

In drug development, most of the drugs exist in crystalline solid state because of stability and easy handling. Recently salts of active pharmaceutical ingredients (APIs) are increasingly grabbing the attention of the researchers in order to overcome the problem in solubility. Besides solubility, the physical and chemical stability of the drug must be characterized mainly in order to improve the pharmaceutical activity of API. Nicotinic acid (NIC) known to be a 3-pyridine carboxylic acid, used to treat hypercholesterolemia [1]. Nicotinic acid derivatives show better activity against leukemia and it is widely used in many applications due to their biological activity. Nicotinic acid produces itching of skin, facial flushing and sensation of feeling hot, diarrhea and hyperglycerin [2]. This adverse reaction hampered the use of nicotinic acid in many patients.. Nitrate salts are grown in order to improve the physicochemical properties of the drug by acting as an effective cofomer. In the present work quantum chemical calculations has been carried out using Density functional theory (DFT). DFT is the prominent tool for studying the molecular structure, spectroscopic and electronic properties. Theoretical studies gives solution to the problems confronted in the experimental and computational techniques.

In the present work a dual approach comprising of theoretical and experimental methodologies are carried out. The structural characteristic feature of the compound is carried out using single crystal XRD. The optimized geometry, vibrational wavenumbers, electronic properties have been calculated using B3LYP/6-311++G (d,p) level of theory. The FT-IR and FT-Raman spectra are analyzed using vibrational spectroscopy with the calculated values which helps to identify the shifting of wave numbers due to the intermolecular interactions that takes place within the molecule.

2. Experimental

Nicotinic acid was dissolved in 10 ml of water with few drops of Nitric acid. The solution is stirred well until a clear solution is obtained. By slow evaporation technique, the solution is slowly evaporated and hence good quality crystals were obtained within one 3 week. By Flotation technique (Sink and swim method), the density of the grown crystals were measured, The X-ray intensity data was collected at room temperature for the grown crystal with moka radiation ($\lambda=0.71073\text{\AA}$) using Bruker AXS KAPPA APEX--2 diffractometer at room temperature. By direct methods the structure is solved and refined by full matrix least - squares calculation using SHELX - 2014. A Jasco Spectrometer FT-IR model410 under

a resolution of 4cm^{-1} with the searing speed of $2\text{mm}/\text{Sec}$ was used for infrared measurement. The observed spectrum was recorded over a range of $40\text{-}400\text{cm}^{-1}$. FT-Raman measurements were made with FRA106 Raman Module. Nd:YAG Laser operated at 1064nm with a power output of 20mw is used as a source.

3. Computational details

The theoretical calculation for NICN was carried out by Density Functional Theory using Gaussian09w [3]. They provide information regarding optimized molecular structure, vibrational frequencies using 6-31++G (d,p) basis set employing the Becke-3-lee-yang-parr (B3LYP) method. The positive values of all wavenumbers confirm the optimized geometry of the molecule. Finally the theoretically calculated frequencies are compared with experimentally measured frequencies.

4. Result and discussion

4.1 Molecular geometry

The molecular structure of the title compound (NICN) with atom numbering is shown in fig (1). The compound crystallizes in monoclinic system with $P2_1/n$ space group. The geometrical parameters (Table.2) such as bond length and bond angle are theoretically calculated by DFT method using 6-311++G (d,p) basis set. The parameters of NICN are compared with pure nicotinic acid previously reported. The protonation of the cation is confirmed by the C-N bond distance and widening of C-N-C bond angle which is deviated by 4.8° from parent compound. The C-N bond distance is observed to be 1.33 and 1.329 \AA whereas the computed value is 1.336 \AA respectively.

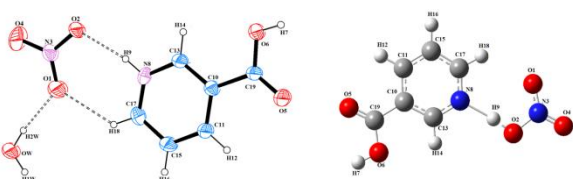


Fig. 1 (a) ORTEP view of NICN and (b) Optimized structure with DFT-6-311++G(d,p)

4.2 Hydrogen bonding

The properties of the materials are not only determined by the molecular structure but also the way with which it interacts with the ions [4]. Therefore strength and nature of the intermolecular interactions forms the fundamental in crystal

engineering and supramolecular chemistry. The crystal packing of NICN is stabilized through an extensive classical and non-classical hydrogen bonding interaction. The nitrate anion plays a significant role by forming hydrogen bonds with the cations. The crystal packing viewed in the present crystal structure shows C-H \cdots O dimer which is not observed in previous reported compound. Further the cations and anions are interconnected through O-H \cdots O hydrogen interactions and are almost linear ($175.6(5)^\circ$).

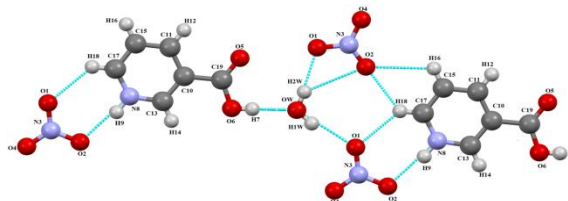


Fig. 2. A view of molecular assembly showing ring motifs formed through classical N-H \cdots O and O-H \cdots O hydrogen bonds (shown as dashed lines)

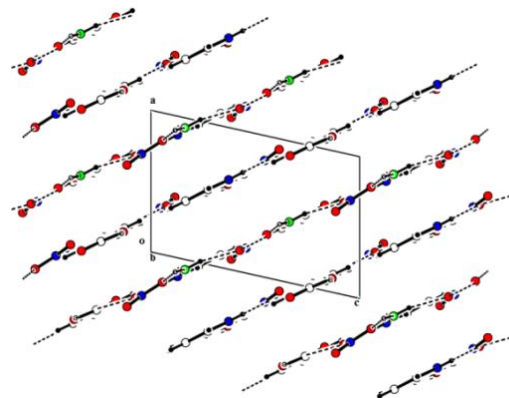


Fig. 3 Packing diagram of the molecules showing alternate hydrophilic and hydrophobic regions at $y = 0,1$ and $y = 1/2$ respectively. H bonds are drawn as dashed lines

4.3 Vibrational analysis

The vibrational spectroscopy plays an important role to find the strength of intermolecular forces. Depending upon their strength (strong/ normal /weak) the hydrogen bonds causes up-shift of deformation mode and down-shift of stretching mode of vibrations [5]. The present compound consists of 19 atoms with 51 normal modes. In the present work, the vibrational analysis is discussed on the basis of vibrations of pyridine ring modes and carboxylic acid group. Theoretical calculations were done for free vacuum whereas experimental values are carried out in solid samples. The calculated wavenumbers are

compared with the experimentally obtained values and the differences in the wavenumbers may be due to the molecular conformation and hydrogen bonding [6].

Vibrations of Pyridine ring

The structure of pyridine ring occurs in many pharmaceutical, natural and commercial products. In pyridine ring the C-H stretching vibration occurs at the region $31500\text{-}3000\text{ cm}^{-1}$. In NICN, the C-H stretching vibration is observed as a medium band FT-IR and a sharp band in FT-Raman. The modes (47-50) are assigned to be C-H stretching vibration. A sharp band observed in the region 1566 cm^{-1} in FT-IR is assigned to be C-H in plane bending. The C-H in plane bending vibrations is coupled with N-H and O-H in plane bending vibration. The experimental values are in good agreement with theoretical data. The N-H stretching vibration in the pyridine ring compound is usually observed in the region $3000\text{-}3500\text{ cm}^{-1}$. In NICN, a strong broad band observed in B3LYP method in the region 2738 cm^{-1} is attributed to N-H \cdots O stretching vibration but it is not observed experimentally.

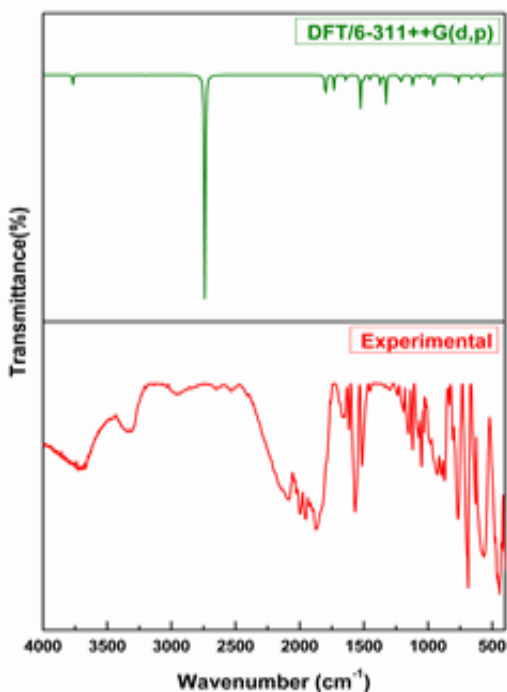


Fig. 6 FT-IR spectrum of NICN

Carboxylic group vibration

The O-H stretching vibrations of carbonyl group are generally observed in the region 3500 cm^{-1} . In NICN, the O-H stretching vibration is not observed experimentally but it is predicted in DFT method. Generally the O-H in-plane bending vibration occurs

in the region $1440\text{-}1395\text{ cm}^{-1}$ and out-of-plane bending vibration occurs between $960\text{ and }875\text{ cm}^{-1}$. In NICN, the O-H in-plane bending vibration occurs as a strong peak in the region 1533 cm^{-1} in FT-IR and 1566 cm^{-1} in Raman.

Vibrations of nitrate anion

In NICN, the nitrate anion exists in planar form. The nitrate anion in the unit cell helps to stabilize the structure of crystal through hydrogen bonding interaction. Nitrate ions are not free as the oxygen atoms form hydrogen bonding with the N atom in the pyridine ring of nicotinic acid. The NO_3 stretching vibrations are normally expected to occur in the region $1049, 830, 1355\text{ and }690\text{ cm}^{-1}$. In NICN, NO_3 stretching vibration is predicted in B3LYP method in the region 1326 cm^{-1} .

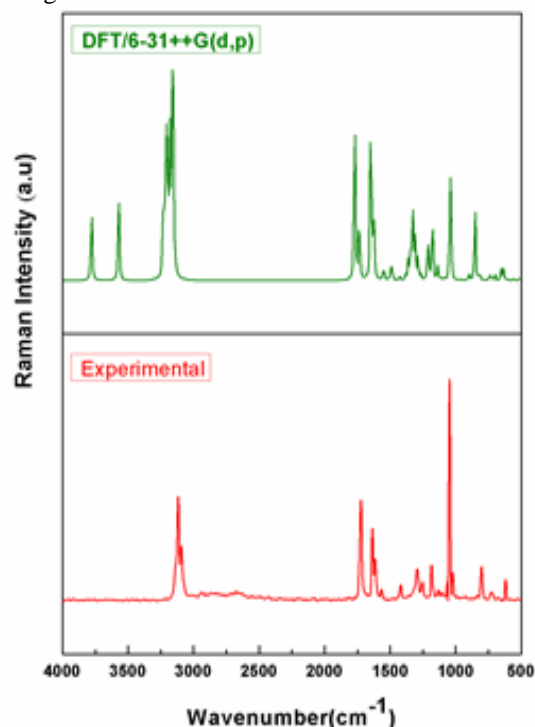


Fig.7 FT-Raman spectrum of NICN

5. Conclusion

NICN crystals were grown by slow solvent evaporation technique and the structure is determined by single crystal XRD studies. Theoretical computations were carried out by B3LYP method using 6-311++G (d,p) basis set. The optimized structure is compared with the geometrical parameters and there is slight deviation from the experimental value. The N-H \cdots O and O-H \cdots O hydrogen bonding dominates the crystal structure.

The FT-IR and FT-Raman bands are assigned using B3LYP method. The vibrational assignments are compared with the experimental values. The upshift

and downshift in the vibrational spectra maybe due to the occurrence of hydrogen bonding network.

REFERENCES

[1]. T.Z. Shah, A.B. Ali, S.A. Jafri and M.H. Qazi Pak, "Effect of Nicotinic Acid on the lipid lowering of diabetic and non-diabetic rats." *J. Med. Sci.* vol. 29, 2013, pp. 1259-1264.

[2]. P.I .Nagy, M.V. Putz, "Int. Quantum-SAR Extension of the Spectral-SAR Algorithm. Application to Polyphenolic Anticancer Bioactivity" *J. Mol. Sci.* vol. 15, 2014, pp. 19562-19633.

[3]. V.S. Kamanna, S.H. Ganji, and M.L. Kashyap. The mechanism and mitigation of niacin-induced flushing" *Int. J. Clin. Pract.* Vol. 63, 2009, pp. 1369-1377.

[4]. N.A. Khalil, E.M. Ahmed, K.O. Mohamed, S.A. Zaitone, "Synthesis and biological evaluation of novel pyrazoline derivatives as anti-inflammatory

and antioxidant agents" *Chem and Phar Bulletin.* Vol. 61, 2013, pp. 933-940.

[5]. V. Judge, B. Narasimhan, M. Ahuja, D. Sriram, "Synthesis, antimycobacterial, antiviral, antimicrobial activities, and QSAR studies of isonicotinic acid-1-(substitutedphenyl)-ethylidene/cycloheptylidene hydrazides 21 (2011) 1-18.

[6].B. Muller, M. Kasper, C. Surber, G. Imanidis, "Europ. Application of Thin-Layer Chromatography and Gas Chromatography–Mass Spectrometry for Evaluation of the Chemical Stability of Hexyl Nicotinate" *J. Phar. Sci.*vol. 20, 2003, pp. 181-195.

CO-PRECIPIATED NANOSTRUCTURED ZINC SULPHIDE FOR PV TECHNOLOGY

S. Rahulgorky¹, T. Santhosh¹, R. Chokkalingam¹, M.S. Revathy*

¹Department of Physics, School of Advanced Sciences, Kalasalingam Academy of Research and Education, Krishnankovil, India,

*Corresponding Author email: revz.vijay@gmail.com

Abstract

Co-precipitated zinc sulphide nanoparticles were synthesized and the as obtained nanoparticle was characterized for structure studies using x-ray diffraction tool and FTIR studies, morphological studies with Scanning electron microscope, and optical studies were carried out using UV-Vis spectrophotometer and Photoluminescence. A noteworthy particle size of about 10 nm from XRD was in good agreement with SEM studies. The obtained optical absorption of 325 nm is blue shifted and 448 nm emission wavelength of PL makes ZnS NPs suitable for PV application.

Keywords — Coprecipitation, FTIR, PL, SEM, XRD, ZnS.

I. INTRODUCTION

The renowned first semiconductor discovered with extraordinary properties is ZnS; owing to its wide band gap (~3.7 eV) belonging to II-VI group with an exciton binding energy of 40 meV [1]. Biomedical technology, bio sensors, optical sensor, solid state solar window layers, photoconductors, catalysts, field emitters, light emitting diodes[2-8] and electroluminescence, [9] are the wide range of applications of ZnS due to its non-toxicity[10] and stability. In recent times, ZnS is been employed as a buffer layer in hetero-junction solar cell like CIGS(Copper Indium Gallium diSelenide) and CZTS(Copper Zinc Tellurium Sulphide). During the past three decades, ZnS has been successfully prepared from conventional synthetic routes such as one pot synthesis, sol gel formation, hydrothermal preparation, solid state reaction as well as coprecipitation. Many researchers have reported and designed ZnS NPs in many characteristic shapes such as spherical, tube, rod like features [11]. The wider bandgap of ZnS facilitate more number of photons to reach the window-absorber interface, thereby enhancing the blue response of the PV(photovoltaic) cells that paves for enhanced cell performance [11].

Recently, efficiency improvisation of solar cells has become more significant with an aim of choosing environmentally friendly materials. In this work, ZnS nanoparticles (NPs) was synthesized cost effectively using coprecipitation route and the synthesized ZnS NPs were investigated from the structure studies using x-ray diffraction tool, morphological studies with Scanning electron microscope, FTIR studies and optical studies via UV-Vis spectrophotometer and Photoluminescence.

II. EXPERIMENTAL WORK

The precursors are zinc acetate ($Zn(CH_3COOH)_2 \cdot 2H_2O$) for Zn source and thiourea ($SC(NH_2)_2$) for S source. 0.1M of Zinc Acetate was prepared in ethanol and 1 M thiourea

solution was taken in a burette. Under controlled addition of thiourea drops to Zinc acetate solution and constant stirring for 12 hours, a white precipitate was obtained. The precipitate was centrifuged and sonicated using ultrasonic cleaner and washed 4 to 5 times with deionized water. The precipitate was dried in muffle furnace at 200°C for 4 hours. Then, the as obtained powder sample was stored for further characterization studies. The procedure was repeated for the concentration of ZnS 1M.

III. CHARACTERIZATION

XRD, FTIR, SEM, UV and PL studies were carried out using PANalytical X'PertPRO X-Ray Diffractometer) with $Cu\alpha$ ($\lambda=1.54060 \text{ \AA}$), SHIMADZU IR-TRACER 100, Zeiss Scanning Electron Microscope, Perkin Elmer Spectrophotometer in the absorption mode at room temperature, Photoluminescence instrument respectively.

IV. RESULTS AND DISCUSSION

A. Structural studies

X-ray diffraction spectrum of ZnS NPs is shown in figure 1. The peak broadening of XRD spectra reveals the confirmation of nanosized Zinc Sulphide[12]. 28.54° , 47.79° and 56.56° are the three major peaks appeared for the (hkl) planes (111), (220) and (311) respectively. The elucidation of cubic Zinc blende structure was well coordinated with JCPDS DATA BASE No. 05-0566. The average particle size was around 5.3898 \AA by Debye- Scherrer formula. Cell volume 156.57 \AA^3 .

Table 1: d-spacing values of ZnS

2θ	(hkl)	d(Obs)	d(calc)
28.54	111	3.12495	3.11178
47.79	220	1.90162	1.90557
56.56	311	1.62580	1.62507

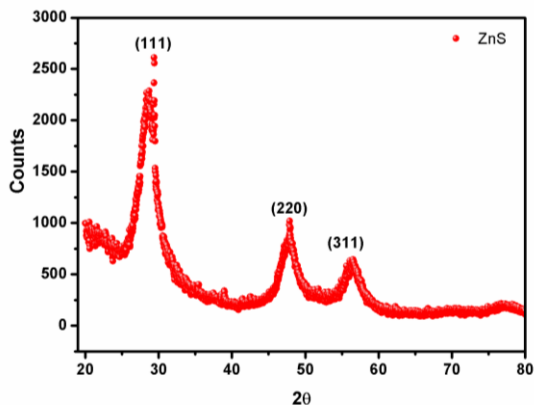


Figure 1. XRD spectrum of ZnS NP

B. FTIR studies

The spectrum in the range 500-4000 cm^{-1} of ZnS 0.1 M and ZnS 1 M concentration shows IR absorption due to the various vibrations involved is shown in Figure 2. The major peaks are at 733 cm^{-1} , 1074 cm^{-1} and 716 cm^{-1} , 1126 cm^{-1} are in good agreement with the reported results in Refs. [13] and [14]. 1412 cm^{-1} and 1403 cm^{-1} are assigned to the C=O stretching modes. 2351 cm^{-1} , 2686 cm^{-1} are the other peaks present along with water peaks of O-H stretching and bending was observed in 3389, 3386 cm^{-1} and 1616 and 1622 cm^{-1} . It was evident from the spectra that as the concentration was increased to 0.1 to 1 M, the transmittance intensity was reduced and absence of some peaks.

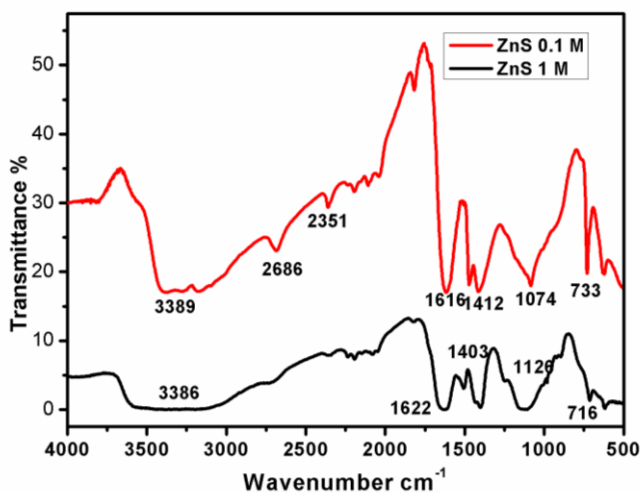
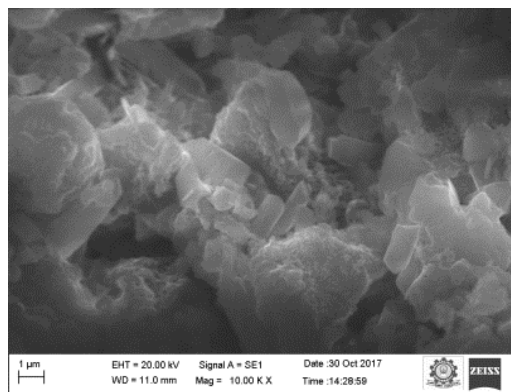


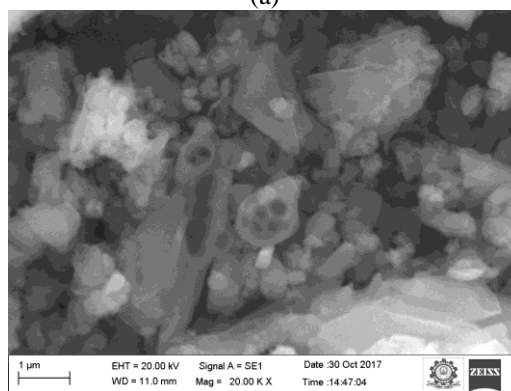
Figure 2. FTIR spectrum of ZnS NP 0.1 M and 1 M.

C. Morphological studies

From the SEM images of ZnS nanostructures it can be seen that ZnS nanoparticle have been synthesized in rock like structure, they are agglomerated and appeared in the form of nanocrystallites [15] and the size was approximately 50 nm.



(a)



(b)

Figure 3. SEM image of ZnS 0.1 M and 1 M

D. Optical studies

i. UV-Visible measurements:

UV-Visible spectra is a best supporting tool to identify and to recognize the optical absorption actions of semiconductor nanoparticles. The optical absorption spectrum of ZnS NPs is shown in figure-4. An absorption peak was observed in 325 nm for as synthesized ZnS nanoparticles and was in good agreement with the reported articles [16,1].

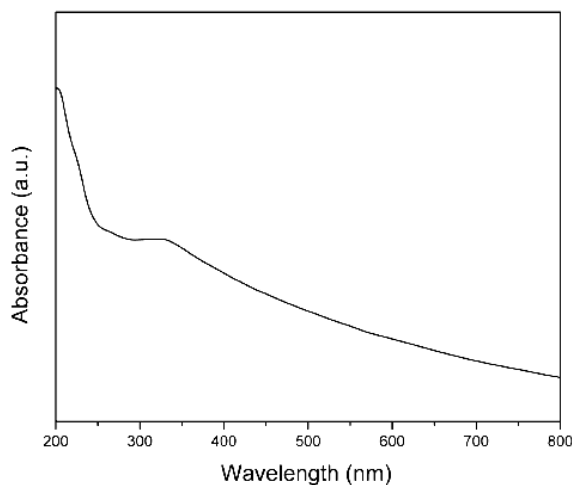


Figure 4. UV absorption spectrum of ZnS NP

ii. Photoluminescence:

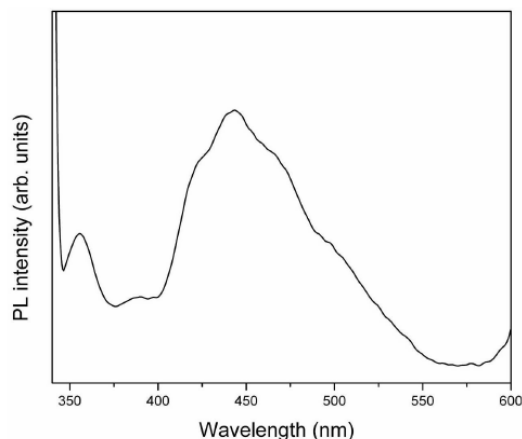


Figure 5. PL emission spectrum of ZnS NP

The PL spectrum of the as-synthesized ZnS NPs is shown in figure.5. From the data it is evident that there is a strong emission band at about 448 nm and this could be due to the emission of blue fluorescence attributed to the recombination that has been taken place between the shallow electron trap states (i.e) S vacancy - the VB(valence band) and CB(conduction band) – Zn vacancy trap, respectively[18].

V. CONCLUSION

ZnS NPs were successfully synthesized by coprecipitation method. The calculated particle size from Debye-Scherrer formula was approximately 10 nm. A morphological study of SEM show rock-like structure and is in good agreement with XRD. The FTIR studies inferred the presence of stretching and bending assignments. The inference from UV absorption of 325 nm clearly indicates the blue shift. The investigation on photoluminescence evidenced 448 nm. These results affirm that the synthesized material can be used in photovoltaic technology especially as a buffer layer in solar cells.

Acknowledgment

The authors are grateful to International Research Centre, Kalasalingam Academy of Research and Education for performing the research and for providing SEM, FTIR, UV facilities.

REFERENCES

- [1] N. Karar, F. Singh, B.R. Mehta, *Journal of Applied Physics*, vol. 95, pp. 48, 2004.
- [2] L.E. Brus, *Accounts of Chemical Research*, vol. 23, 183, 1990.
- [3] B.Y. Geng, L.D. Zhang, G.Z. Wang, T. Xie, Y.G. Zhang, G.W. Meng, *Applied Physics Letters* vol.84, pp. 2157, 2004.
- [4] B. Bhattacharjee, D. Ganguli, K. Iakoubovskii, A. Stesmans, S. Chaudhuri, *Bulletin of Materials Science* vol. 25, pp. 175, 2002.
- [5] A.A. Khosravi, M. Kundu, L. Jatwa, S.K. Deshpande, U.A. Bhagwat, M. Sastry, S.K. Kulkarni, *Applied Physics Letter*, vol. 67, (pp. 2702, 1995
- [6] S. Lee, D. Song, D. Kim, J. Lee, S. Kim, I.Y. Park, Y.D. Choi, *Materials Letters*, vol. 58, pp. 342, 2004.
- [7] W. Chen, J.O. Malm, V. Zwiller, Y. Huang, S. Liu, R. Wallenberg, J.O. Bovin, L. Samuelson, *Physical Review B*, vol. 61, pp.11021, 2000.
- [8] S.J. Xu, S.J. Chua, B. Liu, L.M. Gan, C.H. Chew, G.Q. Xu, *Applied Physics Letters*, vol.73, pp.478, 1998.
- [9] Kaur N, Kaur S, Singh J, Rawat M. A Review on Zinc Sulphide Nanoparticles: From Synthesis, Properties to Applications. *J Bioelectron Nanotechnol*, vol. 1pp.1-5.2016
- [10] T. Kobayashi, T. Nakada, Efficient Cu(In,Ga)Se₂ thin film solar cells with reduced thickness of ZnS(O,OH) Buffer Layer, *Solar Energy Materials and Solar Cells* vol. 117, pp. 526-530, 2013.
- [11] Fang X, et al. ZnS nanostructures: from synthesis to applications. *Prog Mater Sci*, vol. 56, pp.175–287, 2011.
- [12] S.W. Lu, B. Lee, Z.L. Wang, W. Tong, B.K. Wanger, W. Park, J. Christopher, *Journal of Luminescence*, vol. 92, pp. 73, 2001.
- [13] Kuppayee M, Vanathi Nachiyar G K and Ramasamy V *Appl. Surf. Sci*, vol. 257, pp. 6779, 2011.
- [14] Nakamoto K Infrared and Raman Spectra of Inorganic and Coordination Compounds, *John Wiley, New York* vol. 5, 1997
- [15] Sobia Dilpazir, Muhammad Siddiq and Azhar Iqbal, "Synthesis of Zinc Sulphide Nanostructures by Coprecipitation: Effects of Doping on Electro-optical Properties" *Kenkyu Journal of Nanotechnology & Nanoscience*, vol. 1, pp. 34-39, 2015.
- [16] S. Sapra, A. Prakash, A. Ghanrekar, N. Periasamy, D.D. Sharma, *Journal of Physical Chemistry*, vol. 109, pp. 1663, 2005.
- [17] Parvaneh Iranmanesha, Samira Saeedniab, and Mohsen Nourzpoor, "Characterization of ZnS nanoparticles synthesized by co-precipitation method", *Chin. Phys. B*, vol. 24, no. 4, pp. 046104, 2015.
- [18] Q. Liu, M. Goubing, A. Jianping, Chemical bath-deposited ZnS thin films: Preparation and characterization, *Applied Surface Science*, vol. 254, pp. 5711-5714, 2008

STRUCTURAL PHASE TRANSITION ANALYSIS OF LEAD FREE BARIUM TITANATE MODIFIED SODIUM POSTTASIUM NIOBATE SOLID SOLUTIONS

S. Sasikumar, S. Saravanakumar, S. AsathBahadur*, D. Sivaganesh

Department of Physics, International Research Centre, Kalasalingam Academy of Research and Education, Krishnankoil, Viruthunagar, India
Email: s_a_bahadur@yahoo.co.in

Abstract

Lead free NKN-xBT ($x=0.1, 0.2$) ceramics were synthesized by solid state reaction method. The powder X-ray diffraction (PXRD) analysis reveals that the crystal structure of the sintered samples was transformed from tetragonal ($P4mm$) to cubic ($Pm\bar{3}m$). Surface morphology of the NKN-xBT ($x=0.1, 0.2$) ceramics were analyzed by scanning electron microscope. Ferroelectric behavior of the samples was examined by P-E hysteresis loop measurements and maximum polarization decreases with increasing substitution of Ba^{2+} ions.

Keywords: Lead free, ceramics, Rietveld refinement, phase transition, optical properties

1. Introduction

Perovskite $Pb(Ti,Zr)O_3$ and $Pb(Mg_{1/3}Nb_{2/3})O_3$ based piezoelectric and ferroelectric materials have been widely used in transforms, actuators and sensor due to the higher piezoelectric properties near the phase transition. As a lead-free, environmental friendly material, $Na_{0.5}K_{0.5}NbO_3$ based ceramics have been widely used in technological applications as ceramics capacitors, positive temperature coefficient (PTC) thermistors, piezoelectric devices, optoelectronic elements and semiconductors, and so on [1-4]. Pure $Na_{0.5}K_{0.5}NbO_3$ ceramics have low piezoelectric properties. Different dopants like $BaTiO_3$, $Bi(Zn_{0.5}Ti_{0.5})O_3$ modified ceramics shows improved piezoelectric properties ($d_{33}=104pC/N$) fabricated by the hot pressing method [5]. In the present work, Ba^{2+} ions substituted on $Na_{0.5}K_{0.5}NbO_3$ and the structural, optical and morphological properties have been analyzed.

2. Experimental

2.1. Preparation

Polycrystalline NKN-xBT ($x=0.1, 0.2$) ceramics were synthesized by solid state reaction method. Na_2CO_3 , K_2CO_3 , Nb_2O_5 , $BaCO_3$ and TiO_2 were used as precursor materials. The starting materials were mixed according to the molar mass of the desired formula and ball milled for 3 h, then calcined at $1000^\circ C$ for 3 h. The mixture was again ball milled for 3 h, then mixed with poly (vinyl alcohol) and pressed into disk. Finally, the samples were sintered at $1200^\circ C$ for 2h using tubular furnace.

3. Results and Discussion

3.1 Powder X-ray diffraction

The room temperature X-ray diffraction patterns of NKN-xBT, ($x=0.1, 0.2$) ceramics sintered at $1200^\circ C$ are shown in figure 1. The compositions $x=0.1, x=0.2$ indexed for tetragonal phase ($P4mm$) and cubic phase ($Pm\bar{3}m$), respectively. The inset of figure 1 shows the peak splitting for (200) and (002) around $45^\circ-47^\circ$. The (200) and (002) peaks are merged into single (200) peak, which is revealed that the tetragonal phase ($x=0.1$) transformed to cubic phase ($x=0.2$). The inset of figure 1 also represents the shifting of diffraction peaks. The peaks are shifted towards the lower angle side of 2θ due to the higher ionic radii of Ba^{2+} ions substituted in Na^+ and K^+ ions [6].

The structural refinement was done using Rietveld refinement method [7] and JANA2006 software [8]. A good agreement between the observed and calculated patterns was obtained and the profiles are presented in figures 2 (a) and (b). The refined structural parameters are listed in Table 1.

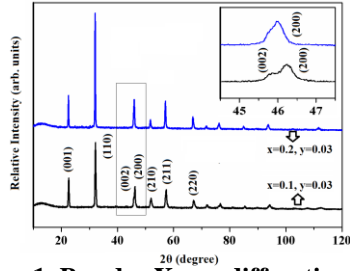


Figure 1. Powder X-ray diffraction patterns of NKN-xBT

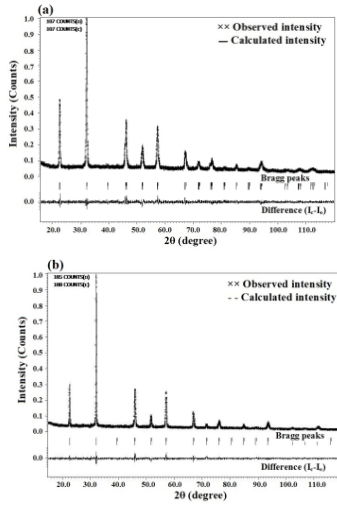


Figure 2. Fitted X-ray profiles for NKN-xBT ceramics (a) $x=0.1$, (b) $x=0.2$

Table 1. Structural parameters of NKN-xBT ceramics.

Parameters	$x = 0.1$; $y = 0.03$	$x = 0.2$; $y = 0.03$
$a = b$ (Å)	3.9507 (8)	3.9607(3)
c (Å)	3.9283 (7)	3.9607(1)
c/a	1.008	1
Space group	$P4mm$	$Pm\bar{3}m$
Volume (Å ³)	61.30(2)	62.13 (1)
Density (gm/cc)	4.45	4.39
R_p (%)	6.30	6.66
R_{obs} (%)	2.13	2.05
GOF	0.21	0.22
$F_{(000)}$	76	76

R_p - Profile reliability factor; R_{obs} - Observed profile reliability factor; GOF- Goodness of fit; $F_{(000)}$ - Number of electrons in the unit cell

3.1. Microstructural properties

The microstructure was investigated using scanning electron microscopy shown in figure 3. The SEM images show particles with agglomeration. The SEM images of the NKN-xBT, ($x=0.1, 0.2$) ceramics with an average grain size of about 350 nm.

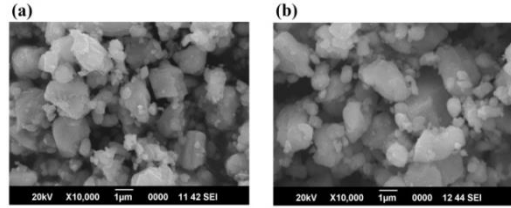


Figure 3. SEM images of NKN-xBT ceramics.

3.2. Optical properties

The optical band gap of NKN-xBT, ($x=0.1, 0.2$) ceramics determined by Tauc's relation. Optical band gap and the absorption coefficient are related by the relation; $\alpha h\nu = A(h\nu - E_g)^n$ [9]. The variation with $(\alpha h\nu)$ the photon energy ($h\nu$) is shown in figure 4. The estimated band gaps for NKN-xBT, ($x=0.1, 0.2$) ceramics is found to be 3.412 and 3.356 respectively. With the increase of the Ba^{2+} dopant content, the band gap of doped sample was decreased, in turn leading to a higher absorption capability.

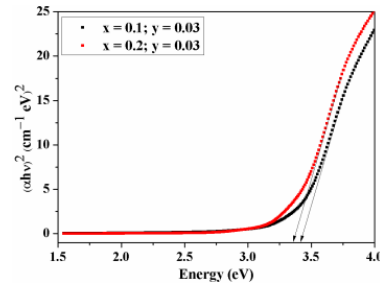


Figure 4. Tauc plot for NKN-xBT ceramics.

3.3 Ferroelectric properties

The ferroelectric properties of NKN-xBT, ($x=0.1$) ceramics are shown in figure 5. The ferroelectric phase for $x=0.1$ compositions shows polarization-electric field (P-E) loop at room temperature. The values of maximum polarization (P_{max}), coercive field for ferroelectric phase at room temperature are $12.25 \mu C/cm^2$ and $6.56 kV/cm$ respectively. However, it is clearly observed that the higher polarization in $x=0.1$ samples, whereas the polarization decreases in $x=0.2$. It is also observed that the remnant polarization (P_r) and ferroelectricity of the samples decrease as the particular concentration of Ba^{2+} ion increases. As polarization decreases, it may be due to the

changes from non-centro-symmetric to centro-symmetric.

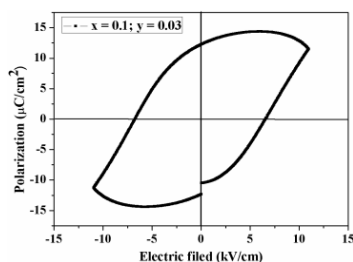


Figure 5. Ferroelectric hysteresis loop for NKN-0.1BT.

4. Conclusion

NKN-xBT ($x=0.1, 0.2$) ceramics synthesized through solid state reaction method. The X-ray diffraction results showed that the formation of pure perovskite phase for the samples. The profile refinement was performed to analyze crystal structure of the samples. Microstructural properties and optical properties of NKN-BT were analyzed by scanning electron microscopy and UV-Visible spectroscopy, respectively. Ferroelectric properties of the samples found to improve for $x=0.1$ composition.

Acknowledgements

The institution of Kalasalingam Academy of Research and Education, Krishnankoil is gratefully acknowledged

for their stable encouragement to the research activities for the authors.

REFERENCES

- [1] G.H. Haertling (1999) *J Am Ceram Soc* 82(4):797.
- [2] Y. Saito, H. Takao, I. Tani, T. Nonoyama, K. Takatori, T. Homma, T. Nagaya, M.Nakamura, *Nature* 432 (2004) pp.84-87.
- [3] B.Q. Ming, J.F. Wang, P. Qi, G.Z. Zang, *J. Appl. Phys.* 101 (2007) pp.054103-054106.
- [4] K. Wang, J.F. Li, *Adv. Funct. Mater.* 20 (2010) pp.1924-1929.
- [5] H. Park, C. Ahn, H. Song, J. Lee, S. Nahma, K. Uchino, H. Lee, H. Lee, *Appl. Phys.Lett.* 89 (2006) pp.062906-062909.
- [6] R.D. Shannon, Revised effective ionic radii and systematic studies of interatomic distances in halides and chalcogenides, *ActaCryst.* A32 (1976) pp.751-767.
- [7] H.M. Rietveld, A profile refinement method for nuclear and magnetic, *J. Appl. Crystallogr.* 2 (1969) pp.65-71.
- [8] V. Petricek, M. Dusek, L. Palatinus, Jana, *The crystallographic computing system* (Institute of Physics), Praha, Czech Republic, 2006.
- [9] D.L. Wood, J. Tauc, *Phys. Rev. B* 5(8), (1972) pp. 3144.

EFFECT OF NEODYMIUM DOPING IN BaTiO₃ ON STRUCTURAL PROPERTIES

S. Sasikumar¹, S. Saravanakumar¹, T.K. Thirumalaichamy², S. Asath Bahadur^{1,*}, D. Sivaganesh¹

¹Department of Physics, International Research Centre, Kalasalingam Academy of Research and Education, Krishnankoil, Viruthunagar, India

²Department of Physics, H.K.R.H College, Uthamapalayam, India
Email: s_a_bahadur@yahoo.co.in

Abstract

Ba_{1-x}Nd_xTiO₃ (x=0.00, 0.02, 0.04, 0.06, 0.08) ceramics were synthesized by solid state reaction method. The structural analysis performed by powder X-ray diffraction and Rietveld refinement method. The ceramic samples crystallized with tetragonal and cubic phases. A phase transition identified from tetragonal (x≥0.04) to cubic (x≤0.06). Microstructural properties of ceramics were analyzed by scanning electron microscopy. Energy band gap values were evaluated by UV-visible spectroscopy.

Keywords: Ceramics, Rietveld refinement, phase transition, optical properties, perovskites

1. Introduction

As a lead-free, environmental-friendly material, BaTiO₃ has been widely used in technological applications such as ceramics capacitors, positive temperature coefficient (PTC) thermistors, piezoelectric devices, optoelectronic elements and semiconductors, and so on [1-4]. In the dielectric field, BaTiO₃ with a high dielectric permittivity is the most important dielectric material [5,6]. Barium titanate is one of the most attractive materials due to multifunctional behavior based on electrical property. The doped barium titanate ceramic materials are mainly used in the application of capacitor, sensors and actuators [7]. Recently, researchers have investigated the doping of rare ions on BaTiO₃ materials to control grain size and to improve dielectric properties for multifunctional applications [8]. In the present work, Nd³⁺ ions substituted on Ba²⁺ at A-site and the structural, optical and morphological properties have been analyzed.

2. Experimental

2.1. Preparation

The polycrystalline Ba_{1-x}Nd_xTiO₃ (x=0.00, 0.02, 0.04, 0.06, 0.08) samples were synthesized by conventional solid state reaction method. Stoichiometric mixture of starting precursors BaCO₃ (purity: 99.9%), TiO₂ (purity: 99.9%) and Nd₂O₃ (purity: 99.99%) powders were ground using agate mortar for 6 h. Then the mixed powder samples were calcined at 1200°C for 5 h. The various compositions were sintered at 1350°C for using tubular furnace for 2 h.

2.2. Powder X-ray diffraction studies

The phase structure was analyzed by powder X-ray diffraction (Burker advance D8 EVO) in the 2θ range from 10-100° with step size of 0.02° using CuKα radiation (λ=1.54056 Å). The Rietveld refinement [9] was done on the XRD pattern by JANA2006 [10] software.

2.3. Morphological and optical studies

The microstructures and elemental present of the samples were examined using scanning electron microscope (Carl Zeiss EVO 18) equipped with energy dispersive spectroscope (EDS) (Carl Zeiss EVO 18). The Ultraviolet-visible (UV-vis) absorption spectra were employed for optical band gap measurements.

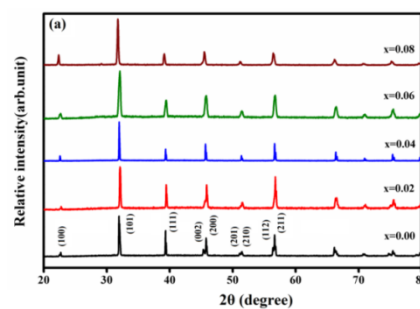


Figure 1. Powder X-ray diffraction patterns of Ba_{1-x}Nd_xTiO₃.

3. Results and Discussion

3.1 Powder X-ray diffraction

Figure 1(a) shows the powder X-ray diffraction patterns for $Ba_{1-x}Nd_xTiO_3$ ($x=0.00, 0.02, 0.04, 0.06, 0.08$) ceramics measured at room temperature. All the experimental diffraction peaks well matched with the JCPDS standard patterns corresponding to the tetragonal and cubic structures (JCPDS No. 05-0626, space group $P4mm$ and JCPDS No. 31-0174, space group $Pm\bar{3}m$). The X-ray diffraction clearly indicates that no other secondary phase could be detected in the samples. XRD patterns clearly indicate crystal structure of pure $BaTiO_3$ at room temperature is tetragonal. With the addition of Nd^{3+} , it reveals that the crystal structure of the samples changes from tetragonal ($x \geq 0.04$) to cubic ($x \leq 0.06$). This is evidenced that the two separate (002) and (200) characteristic peaks at $\sim 46^\circ$ is merged into a single (200) peak from $x \leq 0.06$. As it can be seen from figure 1, the diffraction peaks shift towards lower Bragg angle side of 2θ , which will result in a gradual decrease in the unit cell parameters (Table 1). This is attributed that the ionic radius of Nd^{3+} (1.08 Å) is much smaller than that of Ba^{2+} (1.35 Å) [11]. The structural refinement was done using Rietveld refinement method [9] and JANA2006 software [10]. The refined cell parameter values are given in Table 1.

Table 1. Structural parameters of $Ba_{1-x}Nd_xTiO_3$ ceramics.

Parameters	x = 0.00	x = 0.02	x = 0.04	x = 0.06	x = 0.08
a = b (Å)	4.003	4.002	3.999	4.016	3.999
c (Å)	4.038	4.025	4.002	4.016	3.999
c/a	1.008	1.005	1.0006	1	1
Space group	$P4mm$	$P4mm$	$Pm\bar{3}m$	$P4mm$	$Pm\bar{3}m$
Volume (Å ³)	64.73	64.49	64.02	64.79	63.95
Density (gm/cc)	5.98	6.00	6.05	5.98	6.06
R_p (%)	7.30	10.04	6.63	7.37	7.03
R_{obs} (%)	2.90	5.79	1.36	4.00	1.29
GOF	0.21	0.26	0.20	0.23	0.22
$F_{(000)}$	102	102	102	102	102

R_p - Profile reliability factor; R_{obs} - Observed profile reliability factor; GOF- Goodness of fit; $F_{(000)}$ - Number of electrons in the unit cell

3.1. Microstructural properties

Figures 2 (a)-(e) display the surface morphology images of $Ba_{1-x}Nd_xTiO_3$ ($x=0.00, 0.02, 0.04, 0.06, 0.08$) ceramics prepared by solid state reaction method. The SEM images reveal that particles uniformly arranged with different grain sizes. For $x=0.00$, for the $BaTiO_3$ ceramic,

the grains have an average grain size of about 3.18 μm . After the partial substitution of Nd^{3+} for Ba^{2+} , the grain size of the ceramics gradually becomes increases and the average grain sizes of the ceramics with $x=0.02, 0.04, 0.06$ and 0.08 are about 4.12 $\mu m, 4.88 \mu m, 5.97$ and $6.58 \mu m$, respectively.

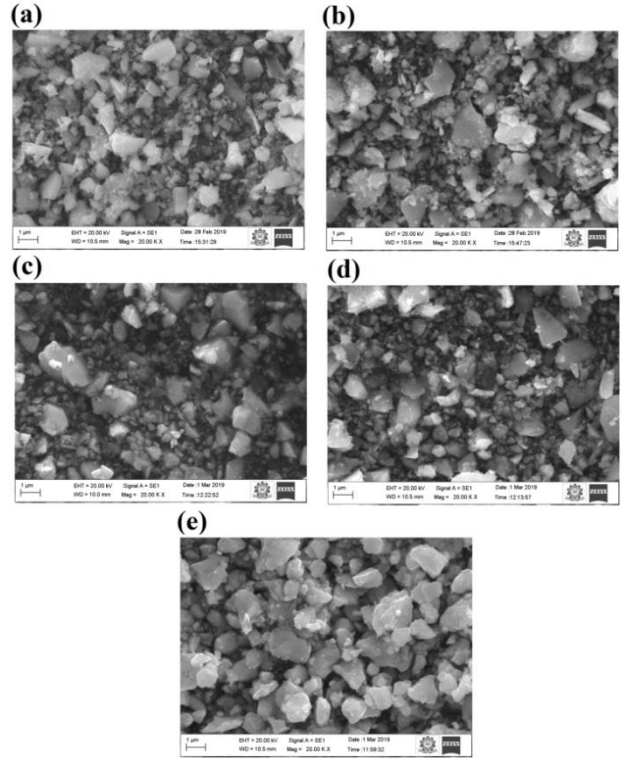


Figure 2. SEM images of $Ba_{1-x}Nd_xTiO_3$ ceramics.

3.2. Optical properties

The absorption edge of $Ba_{1-x}Nd_xTiO_3$ appeared at around 290 nm, which was similar to previously reported work. Compared to pure $BaTiO_3$, the Nd -doped $BaTiO_3$ samples exhibited enhanced absorption capability especially in the visible light region, and the absorption intensity became gradually stronger as increasing the Nd dopant content. Moreover, the band gap could be calculated from the Tauc plot using following equation $\alpha h\nu = A(h\nu - E_g)^{1/2}$ [12]. $((\alpha h\nu)^2$ vs photon energy ($h\nu$)) for the direct band gap semiconductor, as presented in figure 3. The estimated band gaps vary from 3.55-3.41 eV for the $Ba_{1-x}Nd_xTiO_3$ samples. With the increase of the Nd dopant content, the band gap of doped samples was gradually decreased, in turn leading to a higher absorption capability.

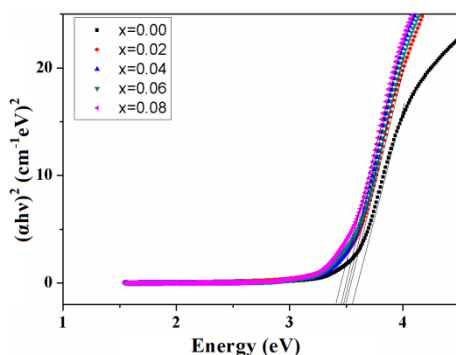


Figure 3. Tauc plot for $\text{Ba}_{1-x}\text{Nd}_x\text{TiO}_3$ ceramics.

4. Conclusion

The polycrystalline $\text{Ba}_{1-x}\text{Nd}_x\text{TiO}_3$ ($x=0.00, 0.02, 0.04, 0.06, 0.08$) samples were successfully prepared by solid state reaction method. Phase transition behavior of the prepared samples was investigated by powder X-ray diffraction data. A tetragonal to cubic phase transitions was indentified. Surface morphological analysis shows the particle size of the prepared samples increased with addition of Ba^{2+} content. Optical band gap values are determined from Tauc plot.

5. Acknowledgements

The institution of Kalasalingam Academy of Research and Education, Krishnankoil is gratefully acknowledged for their stable encouragement to the research activities for the authors.

REFERENCES

- [1] Z.B. Tian, X.H. Wang, L.K. Shu, et al., Preparation of nano BaTiO_3 -based ceramics for multilayer ceramic capacitor application by chemical coating method, *J. Am. Ceram. Soc.* 92 (4) (2009) pp.830-833.
- [2] H.A. Sauer, J.R. Fisher, Processing of positive temperature coefficient thermistors, *J. Am. Ceram. Soc.* 43 (6) (1960) pp.297-301.
- [3] H.J. Sun, S.H. Duan, X.F. Liu, et al., Lead-free $\text{Ba}_{0.98}\text{Ca}_{0.02}\text{Zr}_{0.02}\text{Ti}_{0.98}\text{O}_3$ ceramics with enhanced electrical performance by modifying MnO_2 doping content and sintering temperature, *J. Alloys Compd.* 670 (2016) pp.262-267.
- [4] A.Y. Fasasi, B.D. Ngom, J.B. Kana-Kana, et al., Synthesis and characterization of Gd-doped BaTiO_3 thin films prepared by laser ablation for optoelectronic applications, *J. Phys. Chem. Solids* 70 (10) (2009) pp.1322-1329.
- [5] W.J. Merz, The electric and optical behavior of BaTiO_3 single-domain crystals, *Phys. Rev.* 76 (1949) pp.1221-1226.
- [6] K. Okazaki, *Ceramic Engineering for Dielectrics*, Gakken-Sha Publishing, Tokyo, 1983.
- [7] T. Badapanda, S. Sarangi, B. Behera, P.K. Sahoo, S. Anwar, T.P. Sinha, G.E. Luz Jr., E. Longo, L.S. Cavalcante, *Curr. Appl. Phys.*, 14 [5] (2014) pp.708-715.
- [8] W. Cai, C.L. Fu, Z.B. Lin, X.L. Deng, *Ceram. Int.*, 37 [8] (2011) pp.3643-3650.
- [9] H.M. Rietveld, A profile refinement method for nuclear and magnetic, *J. Appl. Crystallogr.* 2 (1969) pp.65-71.
- [10] V. Petricek, M. Dusek, L. Palatinus, Jana, *The crystallographic computing system* (Institute of Physics), Praha, Czech Republic, 2006.
- [11] R.D. Shannon, Revised effective ionic radii and systematic studies of interatomic distances in halides and chalcogenides, *Acta Cryst.* A32 (1976) pp.751-767.
- [12] D.L. Wood, J. Tauc, *Phys. Rev. B* 5(8), (1972) pp. 3144.

REVIEW OF DISCRIMINATION OF NORMAL TISSUES FROM CANCER TISSUES BY FLUORESCENCE SPECTROSCOPY

M.S. Revathy^a, K. Viswanathan^a, Ni Nyoman Tri Puspaningsih^b, S. Jeyavijayan^a, K. Rajeswari^a, K.Gurusankar^{a*}

^a Department of Physics, Kalasalingam Academy of Research and Education, Krishnankoil, Tamilnadu, India-626126

^b Proteomic Laboratory, Institute of Tropical Disease, University of Airlangga, Kampus C, Mulyorejo, Surabaya, Indonesia.

Corresponding Author Email:kgurumsc@yahoo.com

Abstract

Cancer is a major health problem worldwide and it affects 12 million people each year. Based on a 1% yearly increase, there will be 27 million new cancer cases per year, 17 million cancer deaths each year and 75 million persons alive with cancer within 5 years of diagnosis by 2030. More than 20 million persons around the world live with a diagnosis of cancer and more than half all cancer cases occur in the developing countries. Cancer is responsible for about 20% of all deaths in high income countries and 10% in low- income countries. Despite significant advances in cancer treatment, early detection of oral cancer and its curable precursors remains the best way to ensure patient survival and improved quality of life. In this review an attempt is made to understand the nature of endogenous fluorophores and cellular metabolism that occur in the experimental oral carcinogenesis and to assess their feasibility for antitumor efficacy by using autofluorescence spectroscopy. The results of this study raise the important possibility that fluorescence spectroscopy in conjunction with PC-LDA has tremendous potential to monitor and potentially predict response to therapy.

Keywords: Cancer, Early detection, Fluorescence spectroscopy, PC-LDA

1. Introduction

Oral squamous cell carcinoma (OSCC) is the sixth most common cancer worldwide with increasing incidence and mortality rate (Gillison, 2007). Its early detection is crucial to improve survival and reduce morbidity, disfigurement, loss of function, poor quality of life, duration of treatment and hospital costs (Scott et al., 2008; Rogers et al., 2009). Despite numerous technological advances over the last fifty years, the survival rate linked to OSCC did not undergo a marked improvement and it amounts to approximately 50% at five years (Hayat et al., 2007). Therefore, early detection of oral cancer is very important for improving five year survival. Unfortunately, early diagnosis has a very low rate mainly due to low rates of screening. The gold standard for oral cancer diagnosis remains tissue biopsy with histological assessment, but this technique needs a trained health-care provider, and is considered invasive, painful, expensive and time consuming (Nair et al., 2012). As a consequence, in recent years there has been a growing and persisting demand towards developing new non-invasive, practical diagnostic tools that might facilitate the early detection of oral cancer (Mercadante et al., 2012). Optical spectroscopy methods are fast emerging as potential alternatives for early diagnosis of cancer (Sharwani et al., 2006; Liu, 2011). A number of optical spectroscopic techniques have recently been explored as tools to improve the *in vivo*, real-time detection of pre-cancers and cancers. Based on strong clinical rationale, many researchers have investigated the autofluorescence spectroscopy of tissues in the head and neck region and in various other organs, such as the bronchus, colon, cervix and esophagus for developing non-

invasive screening methodologies for early diagnosis of cancer (Liu et al., 2013). Over the last decade many reports promising for *in vivo* fluorescence spectroscopy can detect high-grade pre-cancer with good accuracy and also in drug monitoring. Autofluorescence of tissues is produced by fluorophores that naturally occur in living cells after excitation with a suitable wavelength (De Veld et al., 2005; Li and Xie, 2005; Zhang et al., 2014). Early pilot studies focused on UV and blue excitation wavelengths. More recently, a study of 146 patients comparing 18 different excitation wavelengths found that three broad ranges of excitations, 330–340 nm (UV), 350–380 nm (UV) and 400–450 nm (blue)-gave the best sensitivity and specificity for detection of high-grade pre-cancer (Chang et al., 2002). Autofluorescence spectroscopy seeks to exploit biochemical information provided by prominent tissue fluorophores such as collagen, NADH, FAD and porphyrin (Sulfikkarali and Krishnakumar, 2013) NADH and FAD are involved in the oxidation of metabolic molecules; therefore, direct monitoring of their fluorescence dynamically can be used to report the metabolic activity of cells and tissues (Rajaram et al., 2010). Metabolic activity of the relative amounts of reduced NADH and FAD and the microenvironment of these metabolic electron carriers can be used to non-invasively monitor changes in metabolism, which is one of the hallmarks of carcinogenesis (Skala et al., 2007). The optical “redox ratio” (fluorescence intensity of FAD divided by that sum of FAD and NADH) is widely used to monitor cellular metabolism in cells, *ex vivo* tissues and *in vivo* tissues in order to diagnose disease, monitor cellular differentiation and characterize other metabolic perturbations (Skala et al., 2007; Ostrander et al., 2010;

Shah et al., 2014). Moreover it is sensitive to early metabolic shifts after cancer treatment and has potential to non-invasively detect treatment response sooner than current methods. Hence, large-scale cell proliferation or tumor growth can be identified by significant changes in NADH and FAD fluorescence (Skala et al., 2007). Animal models are of great importance in attempting to better understand the natural history and molecular biology of carcinogenesis. The hamster cheek pouch carcinogenesis model is a well-known and well-characterized animal model of human oral cancer and squamous cell carcinomas (SCC) (Nagini et al., 2009). Animal models of hamster buccal pouch have become an imperative tool in the development and testing of new anticancer drugs (Krishnakumar et al., 2013). The combination of autofluorescence methods provides a novel integrated environment in which a collection of spectral biomarkers validated on well-defined animal models may provide important clues to tumor biology and response to treatment, with potential applications in human neoplasms. Hence, the present literature survey gives the importance of the fluorescence spectroscopy can provide valuable information regarding the NADH, FAD and cellular metabolism present in the tissues.

2. Fluorescence

The phenomenon, fluorescence of substances, had been observed for hundreds of years and was explained by the British scientist Sir George G. Stokes in 1852 that fluorescence can be induced in certain substances by illuminated with ultraviolet light. He formulated Stokes's law, which states that the wavelength of the fluorescent light is always greater than that of the exciting radiation; therefore fluorescence is the phenomenon in which absorption of light of a given wavelength by a fluorescent molecule is followed by the emission of light at longer wavelengths. Thus, fluorescence is the emission that results from the return to the lower orbital of the paired electron. Such transitions are quantum mechanically allowed and the emissive rates are typically of nearly 10^8 Sec^{-1} . These high emissive rates result in fluorescence lifetimes of nearly 10 nano seconds.

The lifetime is the average period of time when a fluorescence biomolecule, fluorophore remains in the excited state. For atoms excited by a high temperature energy source, this emission is commonly termed as optical emission. For molecules, it is termed fluorescence if the transition occurs between states of the same spin. There are certain factors that control the occurrence of fluorescence. It is seen that whenever the interaction between excited molecules and surrounding is strong, radiation less decay will occur. But if the interaction between them is ineffective at achieving large energy, transfer needs to take it to the lower electronic state. The radiative decay thus dominates and the molecule fluoresces. The various energy levels involved in the absorption and emission of light by a molecule is classically presented by a Jablonski energy diagram, named in honor of the Polish physicist Professor Alexander-Jablonski. A typical Jablonski diagram illustrates the singlet ground ($S(0)$) state, as well as the first ($S(1)$) and second ($S(2)$) excited singlet states as a stack of

horizontal lines as shown in Figure.1. The thicker lines represent electronic energy levels, while the thinner lines denote the various vibrational energy states (rotational energy states are ignored). Transitions between the states are illustrated as straight or wavy arrows, depending upon whether the transition is associated with absorption or emission of a photon (straight arrow) or results from a molecular internal conversion or non-radiative relaxation process (wavy arrows). Vertical upward arrows are utilized to indicate the instantaneous nature of excitation processes, while the wavy arrows are reserved for those events that occur on a much longer timescale.

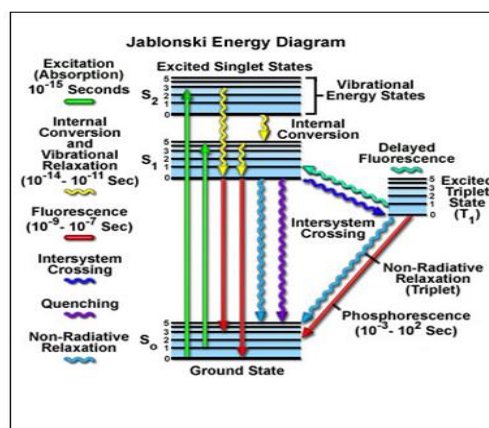


Figure.1. Jablonski diagram

Absorption of light occurs very quickly (approximately a femto second, the time necessary for the photon to travel a single wavelength) in discrete amounts termed quanta and corresponds to excitation of the fluorophore from the ground state to an excited state. Likewise, emission of a photon through fluorescence or phosphorescence is also measured in terms of quanta. The excess vibrational energy is converted into heat, which is absorbed by neighboring solvent molecules upon colliding with the excited state fluorophore. An excited molecule exists in the lowest excited singlet state ($S(1)$) for periods on the order of nanoseconds (the longest time period in the fluorescence process by several orders of magnitude) before finally relaxing to the ground state. If relaxation from this long-lived state is accompanied by emission of a photon, the process is formally known as fluorescence. The closely spaced vibrational energy levels of the ground state, when coupled with normal thermal motion, produce a wide range of photon energies during emission. As a result, fluorescence is normally observed as emission intensity over a band of wavelengths rather than a sharp line.

The diagnostic potential of fluorescence from biological tissues was first described by Stübel in 1911. Stübel investigated the native fluorescence (autofluorescence) of animal tissue under illumination with UV light (Stübel, 1911). In 1924 the French Policard observed the red fluorescence from porphyrins when examining tumor lesions with light from a Wood lamp (Policard, 1924). Indeed, Policard observed the endogenous porphyrins in tumor tissues. Several years later, the Germans Auler and Banzer first described the localisation and fluorescence of exogenously administered porphyrins in malignant tumors. Malignant tumors in the oral cavity and

oropharynx are in many cases visualized by the naked eye, but early recurrent malignancies and precancerous lesions may be difficult to visualize, particularly when they appear in cicatrices (Westbury et al., 1962). In these cases fluorescence diagnostics is valuable. It helps to identify the

real margins of the malignant tumor. This diagnostics of malignant tumors is based on a quite selective accumulation of porphyrins in tumor tissues. In fluorescence spectroscopy of tissue, several fluorophores present in tissue provide important biochemical bases for optical contrasts.

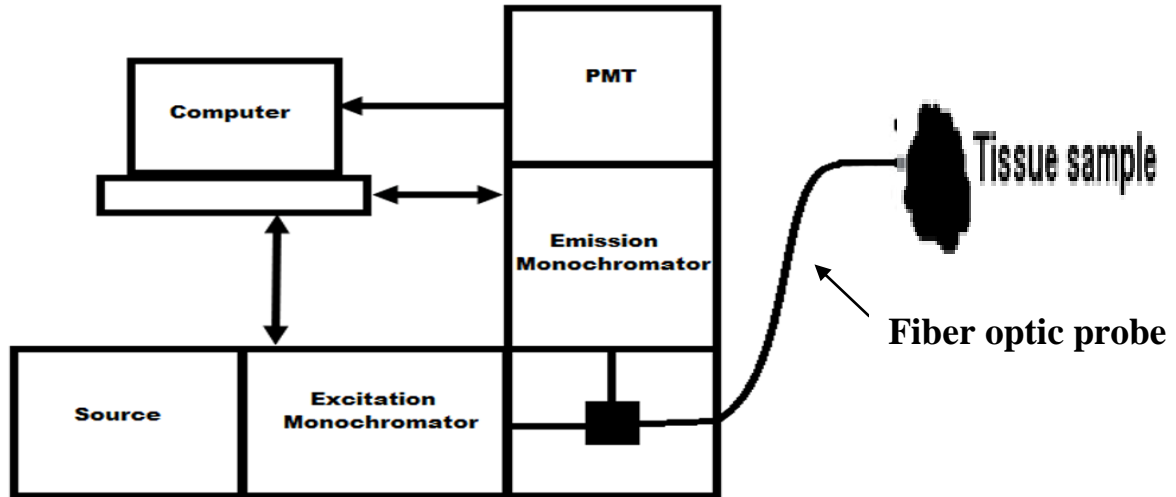


Figure.2. Schematic representation of *in vivo* fluorescence measurement setup

The fluorescent properties of most fluorophores present in tissue are correlated with certain pathological conditions and this allows tissue diagnosis through fluorescence spectroscopy. Some fluorophores that are in tissue include collagen, elastin, flavin adenine dinucleotide (FAD) and reduced nicotinamide adenine dinucleotide (NADH) and porphyrin. The oxidized forms NAD and FAD are electron acceptors in the metabolism of the cell. After accepting an electron the carriers are reduced into the forms NADH and FADH₂, respectively. Later these reduced forms transfer the electrons to oxygen in the mitochondria and they once again become oxidized. It is the reduced form NADH and the oxidized form FAD that are fluorescent in the visible region. Depending on the state of the cell the balance between the concentrations of oxidized and reduced forms will change and lead to differences in the fluorescence spectrum, which therefore can give information about the metabolic function of the cell and tissue. Collagen and elastin are proteins that are found in supportive tissue and are important fluorophores in the extracellular matrix (Monici, 2005). Porphyrin is a component of heme derived from intermediate porphyrinogens in the biosynthesis pathway to proto-heme and it occurs naturally in small amounts in all living cells. Under normal conditions, the synthesis of protoporphyrin is under feedback control; that is, cells produce it at a rate just sufficient to match their heme levels, but with excessive cellular proliferation the feedback mechanism loses control and the excess porphyrin thus produced appears in the tissues and blood. Therefore, the relatively narrow porphyrin fluorescence peaks from Pp-IX could be informative about the condition of the mucosa under investigation. Carcinogenic processes produce

alterations not only at the cellular level but also in the structural tissue composition and this gets reflected in autofluorescence spectral shape and intensity. Usually, alterations in the concentration of these fluorophores take place prior to major structural tissue changes and this makes autofluorescence spectroscopy very sensitive to early tissue transformation.

Fluorescence spectroscopy has gained increasing importance in recent years, especially in molecular and cellular biology and in many associated areas of biochemical analysis, because it offers many advantages such as extreme sensitivity, a high degree of selectivity, gives a wide spectrum of information in very short time and exceptional flexibility in measuring a range of solid and liquid sample formats.

Light-induced fluorescence spectroscopy of biological tissues is based on the physical phenomenon that when with a light beam in appropriate spectral region one irradiates some biological sample it could re-emit the light with a spectrum, related to its biochemical content. These molecules, which are in the tissue and re-emit the light, are called fluorophores and the process itself is called fluorescence. Light sources that can be used include incoherent light sources such as Xe or Hg lamps, light-emitting diodes or monochromatic laser light. When light penetrate into the tissue, it could cause reflection from the tissue layers and non-homogeneities in the tissue; could cause absorption, as well as fluorescence (Figure. 2). When fluorescence is observed *in situ* the resultant spectrum is superposition of several overlapping contributions of various fluorophores, concentrations and special distribution vary depend on the stage of tissue pathology. It is typical to

observe changes in intensity, or appearance/disappearance of fluorescent maxima with progression towards neoplasia. These spectral changes could indicate tissue pathological condition and stage of the lesion growth. The principle of autofluorescence spectroscopy is based on the fact that different diseased tissues contain different morphohistological characteristics and intrinsic fluorophores that give rise to different fluorescence emission spectra when the tissues are excited at a suitable wavelength (Richards-Kortum et al., 1996). If only endogenous fluorophores, naturally existing in the sample, are used to obtain fluorescent signal from the tissue one could observe autofluorescence. Several endogenous fluorophores are often involved in the transformations that occur in the neoplastic process and are therefore interesting for quantitative research. These include: tryptophan, tyrosine, collagen, elastin, NADH, FAD and porphyrin.

When the light emitted by a sample is measured and the excitation light is at a constant wavelength, an emission spectrum is collected. Excitation of the tissue autofluorescence may be done with the excitation light delivery fibre or fibre bundle is placed in direct contact with the tissue.

Differences in tissue components and structure modify the fluorescence emission, including its intensity and behavior, so that normal and cancer tissues may be discriminated after fluorescence analysis. This technique has been used to detect neoplastic tissues in a variety of organ systems, such as the cervix of uterus, colorectum, lungs, and head and neck (Sivabalan et al., 2010; Rajasekaran et al., 2013; Sulfikkarali and Krishnakumar, 2013). These studies suggest the possibility of using autofluorescence spectroscopy in cancer diagnosis.

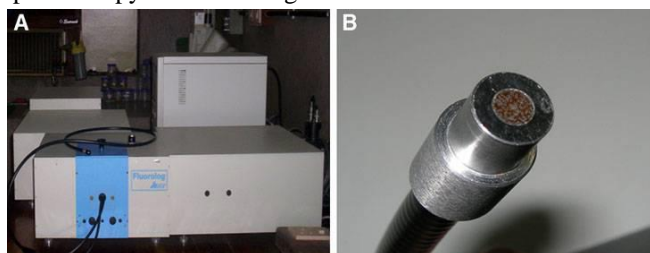


Figure.3. (a) Spectrofluorometer with the fiber optic probe and (b) Fiber optic probe bundle for analysis

3. Review of literature

Kirkpatrick et al., (2005) have used endogenous fluorescence spectroscopy to measure metabolic changes in response to treatment with N-4-(hydroxyphenyl) retinamide (4HPR) in ovarian and bladder cancer cell lines. Fluorescence signals consistent with nicotinamide adenine dinucleotide (NADH), flavin adenine dinucleotide (FAD) and tryptophan were measured to monitor cellular activity through redox status and protein content. The results revealed that redox signal changes depended primarily on changes consistent with NADH fluorescence, whereas the FAD fluorescence remained relatively constant. Further, the results suggest that fluorescence redox values along with changes in tryptophan fluorescence may be used as an endpoint marker for chemopreventive drugs.

Li and Xie, (2005) have investigated the autofluorescence spectroscopic differences in normal and malignant colonic tissues at 280, 340, 380, 460 and 540 nm excitation wavelengths. Malignant tissues showed higher amino acids and endogenous porphyrins and lower NAD(P)H and FAD when compared to the normal tissues. The results suggest that under 340, 380 and 460 excitation wavelength were found to be optimal excitation wavelengths for the diagnosis of colonic cancer.

Skala et al., (2007) have investigated the potential for *in vivo* precancer diagnosis with metabolic imaging via multiphoton fluorescence lifetime imaging microscopy (FLIM) of the endogenous metabolic cofactor, reduced nicotinamide adenine dinucleotide (NADH). The results demonstrated that the protein-bound NADH lifetime decreased with low grade pre-cancers (mild to moderate dysplasia) and high grade pre-cancers (severe dysplasia and carcinoma *in situ* (CIS)) when compared to the normal tissues. Further, they observed that the protein-bound NADH relative to free NADH decreased with low grade pre-cancers *in vivo*. The results suggest that multiphoton FLIM is a powerful tool for the non-invasive characterization and detection of epithelial pre-cancers *in vivo*.

Farwell et al., (2010) have investigated the benefit of using time resolved fluorescence spectroscopy for diagnosing malignant and premalignant lesions of the oral cavity. Spectral intensities and lifetime values at 3 spectral emission bands (spectral bands (SBs); $SB_1=380 \pm 10$ nm; $SB_2=460 \pm 10$ nm and $SB_3=635 \pm 10$ nm) allowed for discrimination among healthy epithelium, dysplasia, carcinoma *in situ* and invasive carcinoma. The lifetime values at SB_2 were the most important when distinguishing the lesions using only time resolved parameters. An algorithm combining spectral fluorescence parameters derived from both spectral and time domain parameters (peak intensities, average fluorescence lifetimes and the Laguerre coefficient [zero-order]) for healthy epithelium, dysplasia, carcinoma *in situ* and invasive carcinoma provided the best diagnostic discrimination, with 100%, 100%, 69.2%, and 76.5% sensitivity and 100%, 92.2%, 97.1% and 96.2% specificity, respectively. The results suggest that time-resolved fluorescence derived parameters significantly improves the capability of fluorescence spectroscopy-based diagnostics in the head and neck cancer.

Shaiju et al., (2011) have carried out autofluorescence spectroscopic screening of normal volunteers with and without lifestyle oral habits and patients with oral submucous fibrosis (OSF). The spectra from different sites of habitués, non-habitués and OSF patients were analyzed using the intensity ratio, redox ratio and linear discriminant analysis (LDA). The spectral disparities among these groups are well demonstrated in the emission regions of collagen and flavin adenine dinucleotide. The results revealed that LDA gives better efficiency of classification than the intensity ratio technique. The results confirms that the clinical application of autofluorescence spectroscopy along with LDA, yields spontaneous screening among individuals, facilitating better patient management for clinicians and better quality of life for patients.

Liu et al., (2013) have studied *ex vivo* autofluorescence (AF) spectra patterns between the normal colon tissue and adenocarcinoma tissues at different excitation wavelength of 337, 375, 405 and 460 nm. They noticed a significant difference in the spectral patterns of the normal and adenocarcinoma tissues. Compared with the other three excitation wavelengths, the AF spectra obtained at 337 nm excitation provided more diagnostic information, but also more sensitive to the trivial change resulted from neoplastic transformation. For discriminated normal from adenocarcinoma tissues, the sensitivity, specificity and accuracy were 88.9%, 80.0% and 83.9%, respectively at 337 nm excitation. The study suggests that the pattern recognition of the multiple excitation AF spectra is an effective algorithm for improving the diagnostic accuracy of adenocarcinoma.

Lin et al., (2012) have investigated the spectral characteristics of the normal and cancerous nasopharyngeal tissues by laser-induced autofluorescence spectroscopy and recorded the autofluorescence excitation emission matrix by *in vitro*. To quantify the changes of collagen and NAD(P)H in cancerous nasopharyngeal tissues peak ratio algorithm ($I_{455} \pm 10 \text{ nm} / I_{380} \pm 10 \text{ nm}$) was used. The results suggest that the excitation wavelength at 340 nm was an excellent diagnostic excitation wavelength for cancerous nasopharyngeal tissues.

Atif et al., (2012) have studied fluorescence emission spectra of normal and malignant lung cells at different excitation wavelengths: 230, 300, 340, and 450 nm, corresponding to the absorption of tyrosine, tryptophan, collagen or elastin, Nicotinamide adenine dinucleotide (NADH) and flavin adeno dinucleotide (FAD). Similarly excitation spectra were also recorded at 340 nm. The emission profiles showed considerable difference between the malignant and normal cells with the malignant cells having more fluorescence intensity than that of normal cells keeping emission at 340 nm. Furthermore, the results suggest the discriminating features between normal and carcinoma cells lines because of higher concentration of tryptophan (1.5 times), NADH (3 times) and flavin (4 times) in carcinoma cell lines.

Shaiju et al., (2013) have reported the efficacy of autofluorescence spectroscopy to serve as a single entity to discriminate tumor tissues from normal ones by analysing the variations in both endogenous fluorophores and chromophores involved. The emissions from prominent fluorophores collagen, flavin adenine dinucleotide, phospholipids and porphyrin were analyzed at 320 and 410 nm excitations. The results conclude that potential of fluorescence spectroscopy as a single entity to evaluate the prominent fluorophores as well as the hemoglobin concentration within normal and tumor brain tissues.

Pu et al., (2013) have investigated the spectral changes of native fluorophores among normal fibroblasts and cancer cell lines of different metastatic ability by fluorescence spectroscopy. The normal (fibroblast), moderately metastatic (DU-145) and advanced metastatic (PC-3) cell lines were each selectively excited at 300 nm, and their fluorescence emission spectra were analysed by PCA to explore the differences of the relative contents of

tryptophan and reduced nicotinamide adenine dinucleotide in those cell lines. The results show that the tryptophan emission featured predominantly in the fluorescence spectra of the advanced metastatic cancer cells when compared with the moderately metastatic cancer and normal cells.

Shah et al., (2014) have investigated the potential of autofluorescence spectrum with metabolic cofactors reduced NADH and FAD for chemotherapeutic response in human head and neck squamous cell carcinoma (HNSCC). The optical redox ratio and fluorescence lifetimes of NADH and FAD resolved a response after 24 hours of treatment with targeted therapies and chemotherapies in HNSCC cells. The results indicated that optical metabolic imaging showed promise to identify effective drug candidates during drug development. Additionally, applying optical metabolic imaging to measure treatment response early has potential to impact quality of life for HNSCC patients.

Udayakumar et al., (2014) have investigated the native fluorescence and time resolved fluorescence spectroscopy of normal and malignant oral tissues under UV excitation. To quantify the spectral differences between normal malignant oral tissues, the two ratio variables ($R_1 = I_{275} / I_{310}$ and $R_2 = I_{310} / I_{328}$) were introduced in the excitation spectra. Among them LDA of ratio variables reveals that R_1 provided 86.4 % specificity and 82.5 % sensitivity. The analysis was further extended to time resolved fluorescence spectroscopy of normal and malignant oral tissues and provided better significance when compared to fractional amplitudes and component lifetimes. The ROC analysis of average lifetime results in 77% sensitivity and 70% specificity with the cut off value of 4.85 ns.

4. Conclusion

In this review an attempt has been made to show that fluorescence spectroscopy can be used to evaluate the antitumor efficacy. This raises the important possibility that fluorescence spectroscopy, in conjunction with PC-LDA, has tremendous potential to monitor or potentially predict response to therapy.

REFERENCES

- [1]. Gillison M.L., 2007. Current topics in the epidemiology of oral cavity and oropharyngeal cancers. *Head Neck*, 29: 779-792.
- [2]. Scott, S., M. McGurk and E. Grunfeld, 2008. Patient delay for potentially malignant oral symptoms. *Eur. J. Oral Sci.*, 116: 141-147.
- [3]. Rogers, S.N., J.S. Brown, J.A. Woolgar, D. Lowe, P. Magennis, R.J. Shaw, D. Sutton, D. Errington and D. Vaughan, 2009. Survival following primary surgery for oral cancer. *Oral Oncol.*, 45: 201-211.
- [4]. Hayat, M.J., N. Howlader, M.E. Reichman and B.K. Edwards, 2007. Cancer statistics, trends, and multiple primary cancer analyses from the surveillance, epidemiology, and end results (SEER) program. *Oncologist*, 12: 20-37.
- [5]. Nair, D.R., R. Pruthy, U. Pawar and P. Chaturvedi, 2012. Oral cancer: premalignant conditions and screening-an update. *J. Can Res Therap.*, 8: s57-s66.
- [6]. Mercadante, V., C. Paderni and G. Campisi, 2012. Novel non-invasive adjunctive techniques for early oral

- cancer diagnosis and oral lesions examination. *Curr Pharm. Des.*, 18: 5442-5451.
- [7]. Sharwani, A., W. Jerjes, V. Salih, A.J.M. Robert, M. El-Maaytah, H.S. Khalil and C. Hopper, 2006. Fluorescence spectroscopy combined with 5-aminolevulinic acid-induced protoporphyrin IX fluorescence in detecting oral premalignancy. *J. Photochem. Photobiol. B.*, 83: 27-33.
- [8]. Liu, Q., 2011. Role of optical spectroscopy using endogenous contrasts in clinical cancer diagnosis. *World J. Clin Oncol.*, 2: 50-63.
- [9]. Liu, W., X.H. Zhang, K.P. Liu, S.D. Zhang and X.Y. Duan, 2013. Laser-induced fluorescence: Progress and prospective for in vivo cancer diagnosis. *Chin Sci Bull.*, 58: 2003-2016.
- [10]. de Veld, D.C., M. Skurichina, M.J. Wities, R.P. Duin, H.J. Sterenberg and J.L. Roodenburg, 2004. Clinical study for classification of benign, dysplastic and malignant oral lesions using autofluorescence spectroscopy. *J. Biomed. Opt.*, 9: 940-950.
- [11]. Li, B.H and S.S. Xie, 2005. Autofluorescence excitation-emission matrices for diagnosis of colonic cancer. *World J. Gastroenterol.*, 11: 3931-3934.
- [12]. Zhang, L., Y. Pu J. Xue, S. Prataveira, B. Xu, S. Achilefu and R.R. Alfano, 2014. Tryptophan as the fingerprint for distinguishing aggressiveness among breast cancer cell lines using native fluorescence spectroscopy. *J. Biomed. Opt.*, 19: 037005.
- [13]. Chang, S.K., M. Follen, A. Malpica, U. Utzinger, G. Staerkel, D. Cox, Atkinson E N, C. MacAulay and R. Richards-Kortum, 2002. Optimal excitation wavelengths for discrimination of cervical neoplasia. *IEEE Trans Biomed Eng.* 49: 1102-1111.
- [14]. Sulfikkarali, N.K and N. Krishnakumar, 2013. Evaluation of the chemopreventive response of naringenin-loaded nanoparticles in experimental oral carcinogenesis using laser-induced autofluorescence spectroscopy. *Laser Phys.*, 23: 045601-1-7.
- [15]. Rajaram, N., J.S. Reichenberg, M.R. Migden, T.H. Nguyen and J.W. Tunnell, 2010. Pilot clinical study for quantitative spectral diagnosis of non-melanoma skin cancer. *Lasers Surg. Med.*, 42: 716-727.
- [16]. Skala, M.C., K.M. Ricking, D.K. Bird, A. Gendron-Fitzpatrick, J. Eickhoff, K.W. Eliceiri, P.J. Keely and N. Ramanujam, 2007. In vivo multiphoton fluorescence lifetime imaging of protein-bound and free nicotinamide adenine dinucleotide in normal and precancerous epithelia. *J. Biomed. Opt.*, 12: 024014.
- [17]. Ostrander, J.H., C.M. McMahon, S. Lem, S.R. Millon, J.Q. Brown, V.L. Seewaldt and N. Ramanujam, 2010. Optical redox ratio differentiates breast cancer cell lines based on estrogen receptor status. *Cancer Res.*, 70: 4759-4766.
- [18]. Shah, A.T., M.D. Beckler, A.J. Walsh, W.P. Jones, P.R. Pohlmann and M.C. Skala, 2014. Optical metabolic imaging of treatment response in human head and neck squamous cell carcinoma. *PLoS One*, 9: e90746.
- [19]. Skala, M.C., K.M. Ricking, D.K. Bird, A. Gendron-Fitzpatrick, J. Eickhoff, K.W. Eliceiri, P.J. Keely and N. Ramanujam, 2007. In vivo multiphoton fluorescence lifetime imaging of protein-bound and free nicotinamide adenine dinucleotide in normal and precancerous epithelia. *J. Biomed. Opt.*, 12: 024014.
- [20]. Nagini, S., P.V. Letchoumy, A. Thangavelu and C.R. Ramachandran, 2009. Of humans and hamsters: a comparative evaluation of carcinogen activation, DNA damage, cell proliferation, apoptosis, invasion, and angiogenesis in oral cancer patients and hamster buccal pouch carcinomas. *Oral Oncol.*, 45: e31-e37.
- [21]. Krishnakumar, N., N.K. Sulfikkarali, S. Manoharan and P. Venkatachalam, 2013. Raman spectroscopic investigation of the chemopreventive response of naringenin and its nanoparticles in DMBA-induced oral carcinogenesis. *Spectrochim. Acta A*, 115: 648-653.
- [22]. Stübel, H., 1911. Die Fluoreszenz tierischer Gewebe in ultraviolettem Licht. *Pflügers Arch Physiol.*, 142: 1-14.
- [23]. Policard, A., 1924. Etude sur les aspects offerts par des tumeurs experimentales examinees a la lumiere de Wood. *CR Soc Biol.* 91: 1423-1424.
- [24]. Westbury, G., K.A. Newton, J.G. Humble, H.T. Ford, D.E. Pegg, and W.F. White, 1962. Recurrent cancer of head and neck. *Br Med J.*, 5287: 1238-1242.
- [25]. Monici, M., 2005. Cell and tissue autofluorescence research and diagnostic applications. *Biotechnology Annual Review*, 11: 227-256.
- [26]. Richards-Kortum, R and E. Sevick-Muraca, 1996. Quantitative optical spectroscopy for tissue diagnosis. *Annu. Rev. Phys. Chem.*, 47: 555-606.
- [27]. Kirkpatrick, N.D., C. Zou, M.A. Brewer, W.R. Brands, R.A. Drezek and U. Utzinger, 2005. Endogenous fluorescence spectroscopy of cell suspensions for chemopreventive drug monitoring. *Photochem. Photobiol.*, 81: 125-134.
- [28]. Pu, Y., J. Xue, W. Wang, B. Xu, Y. Gu, R. Tang, E. Ackerstaff, J.A. Koutcher, S. Achilefu, R.R. Alfano, 2013. Native fluorescence spectroscopy reveals spectral differences among prostate cancer cell lines with different risk levels. *J. Biomed Opt.*, 18: 87002.
- [29]. Farwell, D.G., J.D. Meier, J. Park, Y. Sun, H. Coffman, B. Poirier, J. Phipps, S. Tinling, D.J. Enepekides and L. Marcu, 2010. Time-Resolved fluorescence spectroscopy as a diagnostic technique of oral carcinoma: validation in the hamster buccal pouch model. *Arch. Otolaryngol Head Neck surg.*, 136: 126-133.
- [30]. Lin, L.S., F.W. Yang and S.S. Xie, 2012. Extracting autofluorescence spectral features for diagnosis of nasopharyngeal carcinoma. *Laser Phys.*, 22: 1431-1434.
- [31]. Liu, L., Y. Nie, L. Lin, W. Li, Z. Huang, S. Xie and B. Li, 2013. Pattern recognition of multiple excitation autofluorescence spectra for colon tissue classification. *Photodiagnosis Photodyn. Ther.*, 10: 111-119.
- [32]. Atif, A., M.S. AlSalhi, A.A. AlObiadi, and A.S. Aldwayyan, 2012. Fluorescence spectra of cultured normal and malignant lung cells. *Laser Phys.*, 22: 1353-1357.
- [33]. Shaiju, S. Nazeer, A. Saraswathy, A.K. Gupta and R.S. Jayasree, 2013. Fluorescence spectroscopy as a highly potential single-entity tool to identify chromophores and fluorophores: study on neoplastic human brain lesions. *J. Biomed Opt.*, 18: 067002.
- [34]. Udayakumar, K., M. Yuvaraj, F. Awad, V. Jayanth, P.R. Aruna, D. Koteeswaran, M.B. David, S. Ganesan,

2013. Native fluorescence and time resolved fluorescence spectroscopic characterization of normal and malignant oral tissues under UV excitation-an in vitro study. *J. Fluoresc.*, 24: 613-623.

[35]. Sivabalan, S., P.C. Vedeswari, S. Jayachandran, D. Koteeswaran, C. Pravda, P.R. Aruna and S. Ganesan, 2010. In vivo native fluorescence spectroscopy and nicotinamide adinine dinucleotide/flavin adenine dinucleotide reduction and oxidation states of oral submucous fibrosis for chemopreventive drug monitoring. *J. Biomed. Opt.*, 15: 017010.

[36]. Rajasekaran, R., P. Aruna, D. Koteeswaran, L. Padmanabhan, K. Muthuvelu, R.R. Rai, P. Thamilkumar, C. Murali Krishna and S. Ganesan, 2013. Characterization and diagnosis of cancer by native fluorescence spectroscopy of human urine. *Photochem. Photobiol.*, 89: 483-491.

EFFECT OF METAL OXIDE FILLERS ON THE ELECTRICAL AND ELECTROCHEMICAL PROPERTIES OF PVP:NaNO₃ SOLID POLYMER ELECTROLYTES

M.Vahini¹, M. Muthuvinayagam^{2*}

^{1,2}Department of Physics/Multi-functional Materials Research Laboratory
Kalasalingam Academy of Research and Education, Krishnankoil – 626126

*Corresponding author: mmuthuvinayagam@gmail.com

Abstract

The filler added solid polymer electrolytes (SPE) based on polyvinyl pyrrolidone (PVP):sodium nitrate(NaNO₃) have been prepared by solution casting techniques. The metal oxides (ZnO & TiO₂) are used as fillers which are nanosized particles. The maximum ionic conductivity value of 2.76×10^{-5} S/cm is obtained for PVP:NaNO₃:TiO₂ system. The prepared systems are ionic conductors which are proved by transference number studies. The transport parameters like mobility and diffusion coefficient are also calculated. The prepared films are suitable for electrochemical applications which is confirmed by electrochemical studies.

Keywords: PVP, ionic conductivity, activation energy, mobility, liner sweep voltammetry.

1. Introduction

Energy storage systems are being received extensive attention due to the increasing energy demand and environmental crisis. The overview of current development in electrical energy storage technologies and the application in power system operation is explained by Xing Luo et al [1]. Among the applications, the battery systems can offer a number of high-value opportunities, provided that lower costs can be obtained. Due to the lighter, safer, flexibility and low cost of solid polymer electrolytes (SPE) which is used in electrochemical cell applications. SPEs instead of liquid electrolytes are used in energy storage devices [2]. Most composite electrolytes reported in the literature are formed by dispersing fillers (e.g., Al₂O₃, SiO₂, TiO₂) into high-molecular weight polymers doped with salts [3-7]. The fabrication of efficient energy storage devices depends on development of electrolytes with improved electrical and electrochemical properties [5].

In this present work, the metal oxide dispersed sodium ion conducting polymer electrolytes are prepared by solution casting techniques. The sodium-based batteries could provide an alternative chemistry to lithium batteries. The sodium (4th most abundant element in the earth crust) is the second-lightest and smallest alkali metal next to lithium. Based on the wide availability and low cost of sodium, ambient temperature sodium-based batteries have the potential for meeting large scale grid energy storage needs [8-9]. The synthetic polymer PVP is used as polymer host due to its improved ionic move-

ment compared to other semi-crystalline polymers. Sodium nitrate is doped along with PVP polymer matrix and the metal oxide nanofillers ZnO and TiO₂ are dispersed as fillers in the PVP:NaNO₃ polymer electrolytes. The electrical and electrochemical properties of the prepared systems are discussed.

2. Experimental & Characterization techniques

Using solution casting techniques, different polymer electrolytes are prepared by mixing PVP and NaNO₃ in various ratios and PVP:NaNO₃ (94:06) polymer electrolyte shows maximum ionic conductivity of 1.21×10^{-5} S/cm [10]. Along with the optimized system, the metal oxides MO (ZnO and TiO₂) are added as fillers. Ethanol is used as solvent throughout the work. The polymer PVP (94wt.%) and 6wt.% of NaNO₃ are taken and they are dissolved in 30 ml of ethanol separately at room temperature. The solutions are mixed and stirred constantly until the formation of homogeneous solution. After that, 5mg of metal oxide fillers (ZnO/TiO₂) are added along with the homogeneous solution and it is sonicated for 15 minutes. The resulting solution was poured into Petri dish and dried at room temperature till films are peeled from Petri dish.

Electrical properties of the system are analyzed by HIOKI 3532-50 LCR HITESTER Impedance analyzer. Using the Wagner's dc polarization method, the transference number studies are carried out. The electrochemical properties of the system are analyzed by CHI 6008e electrochemical workstation.

3. Results and Discussion

3.1. Electrical Studies

3.1.1 Cole Cole plot

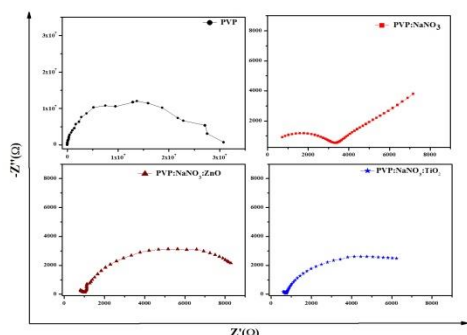


Fig.1 Cole Cole plot of the prepared SPEs

The Cole-cole plot of the system is shown in the Fig.1. The bulk resistances of the SPEs are calculated from Cole-Cole plot by using Z-view software. The pure PVP film has ionic conductivity value of 1.01×10^{-9} S/cm which is enhanced to 1.21×10^{-5} S/cm by addition of 6wt.% of NaNO₃ salt. The ionic conductivity of PVP:NaNO₃ film is enhanced to 1.45×10^{-5} S/cm & 2.76×10^{-5} S/cm by addition of ZnO & TiO₂ nanofillers.

Table.1 Ionic conductivity of the prepared solid polymer electrolytes at different temperature

Temperature	Ionic Conductivity (S/cm)		
	PVP:NaNO ₃ (94:06)	PVP:NaNO ₃ :ZnO (94:06:05)	PVP:NaNO ₃ :TiO ₂ (94:06:05)
303K	1.21×10^{-5}	1.45×10^{-5}	2.76×10^{-5}
313K	1.98×10^{-5}	2.24×10^{-5}	3.70×10^{-5}
323K	3.27×10^{-5}	2.40×10^{-5}	4.55×10^{-5}
333K	7.44×10^{-5}	6.60×10^{-5}	5.62×10^{-5}
343K	1.52×10^{-4}	8.70×10^{-5}	7.41×10^{-5}
353K	2.92×10^{-4}	1.07×10^{-4}	8.96×10^{-5}

The nature of the filler material has an important influence on the conductivity behavior [6]. In Fig.1, the MO dispersed system has a two well defined region: one arc in high frequency region relating to the parallel combination of bulk-resistance & bulk-capacitance of the material and the low frequency spike is attributed to

blocking electrodes.

3.1.2 Dielectric spectrum

The dielectric constant (ϵ') and loss (ϵ'') of the prepared system is shown in the Fig.2. Both dielectric constant and loss have maximum values at low frequency region and relatively constant at high frequency. The large value of ϵ' & ϵ'' is due to the interfacial effects and the motion of the free charge carrier in the materials. At high frequency region there is no hopping of charge carriers and it gets only oscillation without reaching the surface of the electrode. Hence, the $\epsilon'(\omega)$ is constant at high frequency region. Due to the decrease of ion diffusion, $\epsilon''(\omega)$ get constant at high frequency [11].

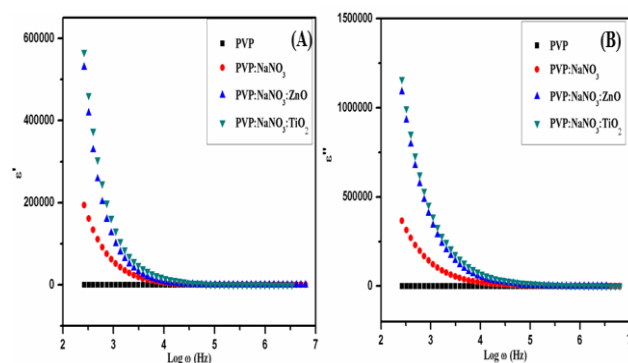


Fig.2 Dielectric spectrum of prepared systems
(A) dielectric constant (B) dielectric loss

The dielectric loss tangent value was calculated from dielectric constant and loss ($\tan \delta = \epsilon'' / \epsilon'$). The relaxation time (table.2) of ions in the system is calculated using the equation $\omega \tau = 1$ (ω - angular frequency, τ -relaxation time). Due to the interfacial polarization mechanism and dipolar relaxation, the dispersive regions are obtained [10]. The low relaxation time is obtained for TiO₂ added system compared to the ZnO added system. It is well matched with ionic conductivity values.

3.1.3 Temperature dependent conductivity

The ionic conductivity of the samples is analyzed in the temperature range from 303K to 353K. The conductivity values of the prepared electrolytes are increased with increase of temperature. The linear increase of ionic conductivity reflects the Arrhenius behavior of the systems. It is used to calculate the activation energy of the systems which is reported in the table.2. The low activation energy (0.21eV) is obtained for PVP:NaNO₃:TiO₂ system [6]. The effect of TiO₂ contributes more than

ZnO to increase the conductivity properties.

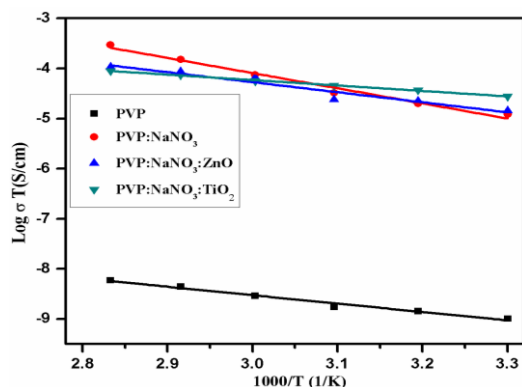


Fig.3 Arrhenius plot of prepared systems

3.2 Transference number studies

Table.2 Transference number parameters of the prepared SPEs

Parameters	Solid polymer electrolytes		
	PVP:NaNO ₃ (94:06)	PVP:NaNO ₃ : ZnO (94:06:05)	PVP:NaNO ₃ : TiO ₂ (94:06:05)
Activation Energy (eV)	0.60	0.39	0.21
Relaxation time (sec)	1.17×10^{-5}	7.94×10^{-6}	4.89×10^{-6}
Transference number (t)	$t_+ = 0.984$ $t_- = 0.015$	$t_+ = 0.999$ $t_- = 0.00012$	$t_+ = 0.999$ $t_- = 3.57 \times 10^{-5}$
Mobility (μ) (cm ² /Vs)	$\mu_+ = 7.77 \times 10^{-8}$ $\mu_- = 1.19 \times 10^{-9}$	$\mu_+ = 9.41 \times 10^{-8}$ $\mu_- = 1.18 \times 10^{-11}$	$\mu_+ = 1.8 \times 10^{-7}$ $\mu_- = 6.42 \times 10^{-12}$
Diffusion coefficient (D)(cm ² /s)	$D_+ = 2.03 \times 10^{-9}$ $D_- = 3.12 \times 10^{-11}$	$D_+ = 2.45 \times 10^{-9}$ $D_- = 3.07 \times 10^{-13}$	$D_+ = 4.69 \times 10^{-9}$ $D_- = 1.68 \times 10^{-13}$

Using Wagner's d.c polarization techniques, the ion transport mechanisms in the prepared systems are analyzed. The variation in the current is observed when constant voltage (1V) is applied to SPE. The maximum current (combination of ionic & electronic current) is obtained at zero time. After that, suddenly current gets to decrease and reaches a constant value for a long polarization time (only electronic current) [10]. The minimum current is obtained at last which proves the system is an ionic conductor. The transference number is increased for filler added systems compared to the filler-free systems. The increase in the transport number is due to the promotion of Na⁺ ion conducting pathways at the filler surface. The mobility and diffusion coefficient of the

ions are also enhanced and it's reported in table.2.

3.3 Electrochemical studies

3.3.1 LSV & CV analysis

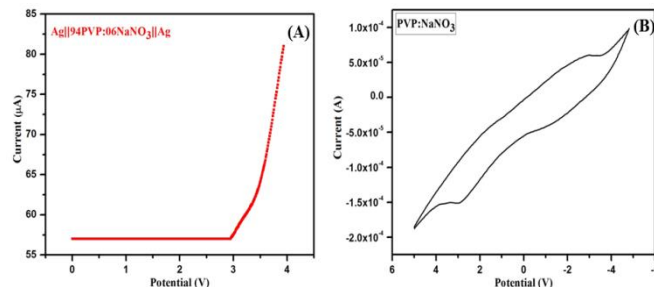


Fig.4 Electrochemical studies of filler free solid polymer electrolyte

The electrochemical performance of the sodium conducting SPE is analyzed in the configuration of Ag|film|Ag cell at room temperature. The reliable potential window of the electrolyte is studied by using LSV for device applications. The current voltage response (Fig.4A) and CV curve (Fig.4B) of filler free polymer electrolyte are shown.

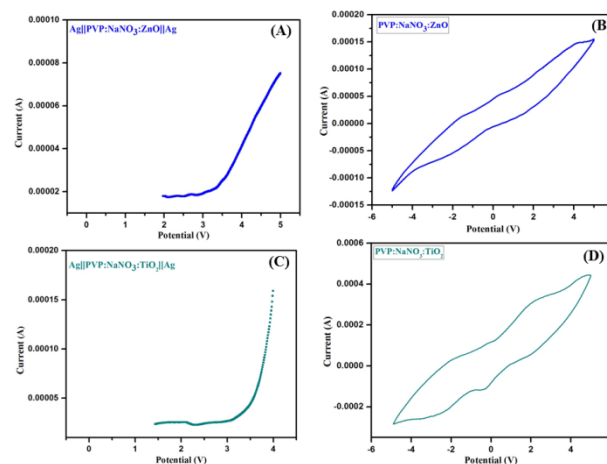


Fig.5 Electrochemical studies of filler added polymer electrolytes

LSV curves of prepared SPEs at room temperature are carried out at 10mV/s. The CV curves of prepared SPEs (303K) are carried out at 100mV/S. Both LSV (Fig.5 A&C) and CV curves (Fig.5 B&D) of filler added systems are shown here. All the systems have a decomposition voltage range above 3V. The current is gradually increasing with increasing applied voltage. The flow of current is small when the voltage is below 3V [12]. A

sudden rise of current value is observed in LSV curve which is varied for all films. The stability of the film is enhanced due to addition of fillers. Among the fillers, TiO₂ improves the stability of film more because of its shape and surface nature which effectively disturbs the order of packing tendency of the polymer chains [5]. The maximum working voltage is observed for TiO₂ added system compared to ZnO added system. The area of the CV curve is increased for filler added systems compared to filler-free system which denotes the enhancement in the electrochemical properties of the film. Hence, all the prepared films are suitable for electrochemical applications. The filler TiO₂ is more suitable than ZnO fillers.

4. Conclusion

The metal oxide filler ZnO and TiO₂ in nanometer range are added to the optimized PVP:NaNO₃ system and they are prepared by solution casting technique using ethanol as solvent. The prepared systems are analyzed by ac impedance studies, transference number analysis and electrochemical studies. The maximum ionic conductivity value of 2.76×10^{-5} S/cm at room temperature is obtained for PVP:NaNO₃:TiO₂ system which has a minimum value of relaxation time (4.89×10^{-6} sec) and activation energy (0.21 eV) compared to the other SPE. All the SPEs are ionic conductors which are proved by transference number studies. The mobility of cations in filler-doped systems are enhanced from 7.77×10^{-8} cm²/Vs to 9.41×10^{-8} cm²/Vs for ZnO doped system and it is improved to 1.8×10^{-7} cm²/Vs for TiO₂ doped system. The effect of fillers in electrochemical properties of the polymer electrolytes are observed from LSV and CV studies. Among all the prepared systems, PVP:NaNO₃:TiO₂ system shows improved properties than others.

5. Acknowledgements

The authors acknowledge the management of Kalasalingam Academy of Research and Education, Krishnankoil-626126, for providing research facilities with research fellowship.

REFERENCES

- [1] Xing Luo, Jihong Wang, Mark Dooner, Jonathan Clarke, Overview of current development in electrical energy storage technologies and the application potential in power system operation, *Applied Energy* 137 (2015) 511–536.
- [2] Martin Winter, Ralph J. Brodd, What Are Batteries, Fuel Cells, and Supercapacitors? *Chem. Rev.* 104 (2004) 4245–4269
- [3] A. H. P. de Oliveira, M. L. F. Nascimento, H. P. de Oliveira, Preparation of KOH-doped PVA/PSSA Solid Polymer Electrolyte for DMFC: The Influence of TiO₂ and PVP on Performance of Membranes, DOI: 10.1002/fuce.201500199 (2016)
- [4] Jian Zhou, Peter S. Fedkiw, Ionic conductivity of composite electrolytes based on oligo (ethylene oxide) and fumed oxides, *Solid State Ionics* 166 (2004) 275–293
- [5] Prasanth Raghavan, Xiaohui Zhao, Jae-Kwang Kim, James Manuel, Ghanshyam S. Chauhan, Jou-Hyeon Ahn, Changwoon Nah, Ionic conductivity and electrochemical properties of nanocomposite polymer electrolytes based on electrospun poly(vinylidene fluoride-co-hexafluoropropylene) with nano-sized ceramic fillers, *Electrochimica Acta* 54 (2008) 228–234
- [6] Peng Chen, Xiaoping Liang, Jun Wang, Di Zhang, Shanmin Yang, Weishan Wu, Wei Zhang, Xiaowei Fan, Dequan Zhang, PEO/PVDF-based gel polymer electrolyte by incorporating nano-TiO₂ for electrochromic glass, *J Sol-Gel Sci Technol* (2017) 81:850–858
- [7] V. Aravindan, P. Vickraman, T. Prem Kumar, ZrO₂ nanofiller incorporated PVC/PVdF blend-based composite polymer electrolytes (CPE) complexed with LiBOB, *Journal of Membrane Science* 305 (2007) 146–151
- [8] Naoaki Yabuuchi, Masataka Kajiyama, Junichi Iwatate, Heisuke Nishikawa, Shuji Hitomi, Ryoichi Okuyama, Ryo Usui, Yasuhiro Yamada and Shinichi Komaba, P2-type Na_x[Fe_{1/2}Mn_{1/2}]O₂ made from earth-abundant elements for rechargeable Na batteries, *Nature Materials* 11 (2012) 512–517
- [9] Alexandre Ponrouch, Elena Marchante, Matthieu Courty, Jean-Marie Tarascon & M.Rosa Palacin, In search of an optimized electrolyte for Na-ion batteries, *Energy Environ. Sci.*, 5 (2012) 8572–8583
- [10] M.Vahini, M.Muthuvinayagam, Synthesis and electrochemical study of sodium ion conducting PVP based solid polymer electrolytes, *Journal of Materials Science: Materials in Electronics* 30 (2019) 10.1007/s10854-019-00854-8 (In press)
- [11] P.Senthil Kumar¹, A.Sakunthala^{1*}, K.Govindan², M.V.Reddy³, M.Prabu⁴, Single crystalline TiO₂ nanorods as effective fillers for lithium ion conducting PVdF-HFP based composite polymer electrolytes, 10.1039/C6RA20649B
- [12] N.Munichandraiah, L.G.Scanlon, R.A.Marsh, B.Kumar, A.K.Sircar, Influence of zeolite on electrochemical and physicochemical properties of polyethylene oxide solid electrolyte, *Journal of Applied Electrochemistry*, 25 (1995) 857–863.

SYNTHESIS, LATTICE ENERGY CALCULATION AND DOCKING STUDIES ON CINNAMOYLPROLINE

M. Venkateshan and J. Suresh

PG and Research Department of Physics, The Madura College, Madurai, Tamilnadu, India.

Email: venkateshan@maduracollege.edu.in

Abstract

Cinnamoylproline was synthesized and the crystal was grown from solution technique by slow evaporation using methanol. The crystal belongs to trigonal crystal system with non-centrosymmetric space group $P3_1$. Lattice energy of the compound was calculated. The lattice energy was found to be -138.4 kJ/mol. Molecular docking studies were done for anti-tuberculosis property of the title compound.

Keywords: Cinnamic acid, proline, PIXEL, Docking, Mycobacterium Tuberculosis.

1. Introduction

The organic molecules inside the crystal have been packed or stabilized by intermolecular interactions like Van der Waals interactions and hydrogen bonding [1]. These interactions take on a significant function in the physical attributes of the molecule. Also, these interactions are very important in drug-receptor interactions. Cinnamic acid derivatives showed some medicinal properties like anti-cancer [2], anti-tuberculosis [3], anti-malarial [4], anti-fungal [5], anti-microbial [6], haemostatic agents [7] and also possess non-linear optical behaviour [8]. In the present work nonlinear optical material of cinnamoylproline (CP) was synthesized and the crystals were grown from solvent evaporation technique and characterized by single crystal X-ray diffraction, lattice energy was calculated using Pixel C and in-silico method was employed to find the molecular drug activity against Mycobacterium Tuberculosis.

2. Experimental

2.1. Synthesis

Cinnamoylproline (CP) was synthesized from the reaction of cinnamoyl chloride (98% purity – Sigma Aldrich) and L-Proline (99% purity - Himedia). 1.2 g of NaOH was dissolved in 10 ml of water and 1.069 g of L-Proline (1.2 M) was dissolved in the solution. To the above mixture 1.666 g of Cinnamoyl chloride (1.5 M) was added in several portions. After the completion of the reaction, the reaction mixture was extracted with diethyl ether and concentrated HCl was added. The formed precipitate was washed with water and diethyl ether twice to get the final desired product. (Yield: 72%). The synthesized CP was dissolved in ethanol and poured into a beaker and covered with a perforated cover and kept in an undisturbed,

dust free environment and allowed to evaporate slowly. After a few days colorless crystals were formed.

2.2. Single crystal XRD studies

A good quality optically clear $0.2 \times 0.21 \times 0.19 \text{ mm}^3$ sized crystal was selected for the intensity data collection using Bruker kappa APEX II diffractometer using the MoK α radiation source. The intensity data were collected at 20°C. Absorption correction was carried out using the SADABS program with multi-scan method. The structure was solved using SHELXS in direct method and refined least squares method using SHELXL embedded in SHELXL-2014 [9,10]. Hydrogen atoms were fixed on the basis of riding model and refined isotropically and all other atoms were refined anisotropically.

2.3. Molecular docking studies

In-silico docking studies were performed using PyRx [11] software. The PDB files of the macromolecules were retrieved from RCSB protein data bank. Docked protein and ligand molecules were visualized using Chimera [12] and PyMol [13] software programs. Macromolecule residue and ligand interaction was visualized using LigPlot+ [14].

3. Results and Discussion

3.1. Single crystal XRD

Cinnamoylproline was crystallized in the trigonal crystal system with non-centrosymmetric space group $P3_1$. Its unit cell values are $a = 15.9976(10)$ Å, $b = 15.9976(10)$ Å, $c = 13.4251(7)$ Å, $\alpha = 90^\circ$, $\beta = 90^\circ$, $\gamma = 120^\circ$ and $V = 2975.5(4)$ Å³. The asymmetric unit contains three molecules of the same (Fig. 1). The crystal is stabilized by C – H ...O and O – H ...O interactions (Table 1). The morphology of the grown crystal was indexed using WinXMorph [15] software by inputting the CIF file. The crystal has twelve well defined planes such as (111) , $(1\bar{1}\bar{1})$, $(2\bar{1}\bar{1})$, $(2\bar{1}\bar{1})$, $(\bar{1}2\bar{1})$, $(\bar{1}2\bar{1})$, $(\bar{1}\bar{1}\bar{1})$, $(\bar{1}\bar{1}\bar{1})$, $(2\bar{1}\bar{1})$, $(2\bar{1}\bar{1})$, $(\bar{1}2\bar{1})$ and $(\bar{1}2\bar{1})$. (Fig. 2)

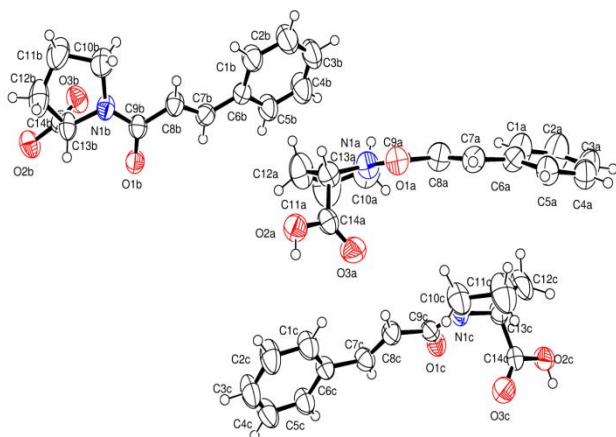


Figure 1. ORTEP diagram of CP with 50% probability

3.2. Lattice energy calculation

PIXEL [16] is a software program used to calculate lattice energy and intermolecular interaction energies, in which the total energy was partitioned into coulombic, polarization, repulsion and dispersion energies. The total lattice energy, calculated using PIXEL was tabulated in Table 2. Among the other energy dispersion energy (-118.0 kJ/mol) contributes the maximum of 85.2 % of the total lattice energy (-138.4 kJ/mol). The crystal is stabilized through the interactions of O(2A) - H(2A1)...O(1A), O(2B) - H(2B1)...O(1B) and O(2C) - H(2C1)...O(1C) with interaction energies of -29.4 kJ/mol, -29.9 kJ/mol and -30.6 kJ/mol respectively. The values of individual energy contributions were listed in Table 3.

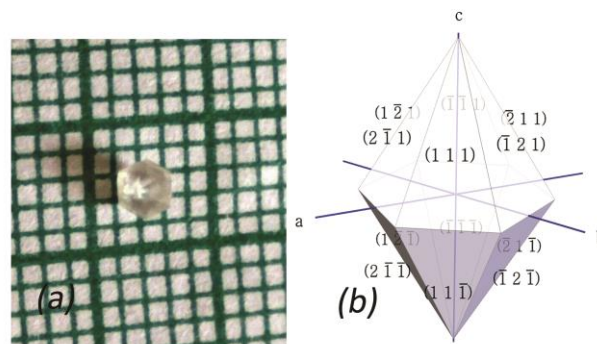


Figure 2. (a) As grown crystal, (b) Crystal morphology of CP.

Table 1: Hydrogen bonds for Cinnamoylproline [Å and °]

D-H...A	d(D-H)	d(H...A)	d(D...A)	<(DHA)
O(2A)-H(2A1)...O(1A)#1	0.82	1.82	2.602(5)	158.0
O(2B)-H(2B1)...O(1B)#2	0.82	1.81	2.596(5)	161.0
O(2C)-H(2C1)...O(1C)#3	0.82	1.83	2.616(5)	159.0
C(2A)-H(2A)...O(3B)#4	0.93	2.47	3.333(7)	154.1
C(8B)-H(8B)...O(3C)#5	0.93	2.45	3.356(6)	165.0

Symmetry transformations used to generate equivalent atoms:

- #1 $-x+y, -x, z-1/3$ #2 $-x+y, -x+1, z-1/3$ #3 $-y+1, x-y, z+1/3$
 #4 $-y+1, x-y+1, z+4/3$ #5 $-y, x-y, z-2/3$

Table 2. Lattice energies (kcal/mol) partitioned into coulombic, polarization dispersion and repulsion contribution using CLP approach

Molecule Name	E_{Coul}	E_{Pol}	E_{Disp}	E_{Rep}	E_{Tot}
Cinnamoylproline	-44.1	-33.4	-118.0	57.0	-138.4

3.3. Molecular docking studies

Molecular docking studies were carried out, in order to find out the in-silico inhibition property of CP against tuberculosis. Mycobacterium Tuberculosis (MTB) are one of the successful pathogen of human, and it is responsible for 2 million deaths in 2008. MTB can survive in the human host for long years, even in hypoxic conditions [17]. But MTB depends on nitrogen for its protein synthesis. Various amino acids like alanine, glycine can provide ammonia nitrogen for this purpose [18]. It is well known that under anaerobic conditions L-Alanine dehydrogenase (Rv 2780) enzyme level was increased in the MTB growth medium [19]. This enzyme catalyzes

the oxidative deamination of L-alanine to pyruvate along with the release of ammonia [17]. In order to control the growth of MTB in hypoxic conditions, it is necessary to control the L-Alanine dehydrogenase enzyme.

Table 3: PIXEL interaction energies (kcal/mol) between molecular pairs related by a symmetry operation and the associated intermolecular interactions in the crystal

E_{Coul}	E_{Pol}	E_{Disp}	E_{Rep}	E_{Tot}	Symmetry operation	Interaction
-20.0	-7.2	-30.2	27.9	-29.4	$-x+y,$ $-x,$ $z-1/3$	O(2A) - H(2A1).. .O(1A)
-19.1	-7.1	-30.0	26.3	-29.9	$-x+y,-$ $x+1,$ $z-1/3$	O(2B) - H(2B1).. .O(1B)
-21.5	-7.3	-30.8	29.0	-30.6	$-y+1,$ $x-y,$ $z+1/3$	O(2C) - H(2C1).. .O(1C)

The PDB file of Rv 2780 (PDB file ID: 2VOE) was downloaded from the PDB databank (www.rcsb.org/). The target protein molecule contains six monomers. Among these, only one monomer was selected for docking studies. Ligand molecule (CP) along with some regular drugs for the treatment of TB was docked using PyRx software in the active site of the molecule Asp 270 and His 96 [20]. The CP showed good binding affinity to the receptor than the regular oral drugs rifampicin and rifabutin with the minimum binding energy of -7.2 kcal/mol. In CP the oxygen atoms of the carboxylic group of pyrrolidine ring were hydrogen bonded to the residues Arg 15 and Asp 270. The interactions were shown in Fig. 3.

4. Conclusion

The optically transparent NLO material of CP was synthesized and grown from slow evaporation technique. FTIR and SXR D studies confirmed the structure of CP. Also SXR D revealed the non-centrosymmetric nature of CP. The twelve well defined crystal planes were indexed. SXR D exposed the presence of O-H...O and C-H...O intermolecular interactions. The lattice energy was measured to be -138.4 kJ/mol. Among other energies dispersion energy contributed a maximum for lattice energy. The six well defined crystal faces were indexed using WinXMorph. In-Silico molecular docking studies shown that, the synthesized compound has a good anti-tuberculosis property with a minimum of -7.2 kcal/mol binding energy.

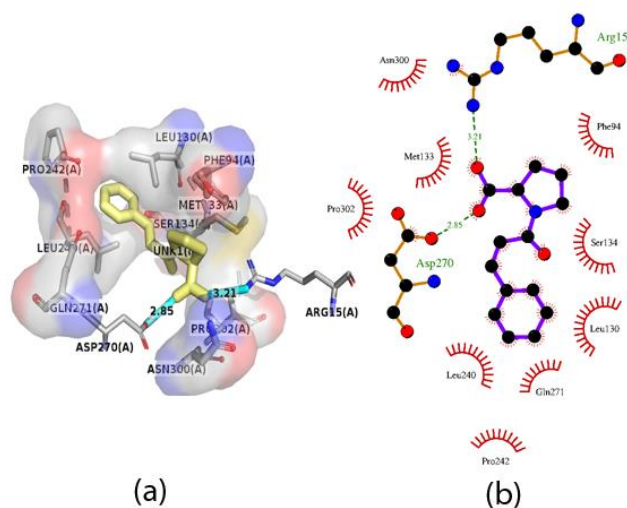


Figure 3: (a) Docking pose of CP in 2VOE (yellow stick represents CP), (b) Docking interaction of CP with protein residues.

5. Acknowledgement

MV and JS thank the management of The Madura College, Madurai for their encouragement and support.

REFERENCES

- [1] A. Bhattacharyya, P. K. Bhaumik, A. Bauza, P. P. Jana, A. Frontera, M. G. B. Drewand S.Chattopadhyay, A combined experimental and computational study of supramolecular assemblies in ternary copper(II) complexes with a tetradentate N4 donor Schiff base and halides, *RSC Adv.*, 4 (2014) 58643-58651.
- [2] P. De, M. Baltas and F. Bedos-Belval, Cinnamic acid derivatives as Anticancer Agents – A review, *Curr .Med. Chem.*, 2011, 18, 1672-1703.
- [3] G. K. Yoya, F. Bedos-Belval, P. Constant, H. Duran, M. Daffe and M. Baltas, Synthesis and evolution of a novel series of pseudo-cinnamic derivatives as antituberculosis agents, *Bioorg. Med. Chem. Lett.*, 2009, 19, 341-343.
- [4] J. Wiesner, A. Mitsch, P. Wißner, H. Jomaa and M. Schliter, Structure–activity relationships of novel anti-malarial agents. Part 2: cinnamic acid derivatives, *Bioorg. Med. Chem. Lett.*, 2001, 11, 423-424.
- [5] S. Tawata, S. Taira, N. Kobamoto, J. Zhu, M. Ishihara and S. Toyama, Synthesis and Antifungal Activity of Cinnamic Acid Esters, *Biosci. Biotechnol. Biochem.*, 1996, 60, 909-910.
- [6] M. Soya, Antioxidant and Antimicrobial Activities of Cinnamic Acid Derivatives, *Mini Rev. Med. Chem.*, 2012, 12, 749-767.
- [7] W. Nong, Z. Anran, J. Wei, X. Lin, L. Wang and C. Lin, Synthesis and biological evaluation of a new series of

- cinnamic acid amide derivatives as potent haemostatic agents containing a 2-aminothiazole substructure, *Bioorg. Med. Chem. Lett.*, 2017, 27, 4506-4511.
- [8] S. Alen, D. Sajan, K. Job Sabu, K. Udaya Lakshmi, V. Veeraiah, K. Chaitanya and V. Bena Jothy, Studies on crystal growth, vibrational, dielectric, electronic, mechanical and thermal properties of new organic nonlinear optical crystal: 3-nitrocinnamic acid, *CrystEngComm.*, 15 (2013) 9176-9188.
- [9] G. M. Sheldrick, SHELXTL Version 2014/7. <http://shelx.uni-ac.gwdg.de/SHELX/index.php>
- [10] G. M. Sheldrick, A short history of SHELX, *Acta Cryst. A.*, 64 (2008) 112-122.
- [11] S. Dallakyan and A. J. Olson, Small-Molecule Library Screening by Docking with PyRx, *Methods Mol. Biol.*, 2015, 1263, 243-250.
- [12] E. F. Pettersen, T. D. Goddard, C. C. Huang, G. S. Couch, D. M. Greenblatt, E. C. Meng and T. E. Ferrin, UCSF Chimera--a visualization system for exploratory research and analysis, *J. Comput. Chem.*, 2004, 25, 1605-1612.
- [13] W. L. DeLano, The PyMOL molecular graphics system, 2002. <http://www.pymol.org>
- [14] A. C. Wallace, R. A. Laskowski and J. M. Thornton, LIGPLOT: A program to generate schematic diagrams of protein-ligand interactions, *Prot. Eng.*, 1995, 8, 127-134.
- [15] W. Kaminsky, WinXMorph: a computer program to draw crystal morphology, growth sectors and cross sections with export files in VRML V2.0 utf8 - virtual reality format, *J. Appl. Cryst.*, 2005, 38, 566-567.
- [16] A. Gavezzotti, Calculation of Intermolecular Interaction Energies by Direct Numerical Integration over Electron Densities. 2. An Improved Polarization Model and the Evaluation of Dispersion and Repulsion Energies, *J. Phys. Chem. B* 2002, 106, 4145-4154.
- [17] W. Wu, D. Wu, W. Cheng, H. Zhang and J. Dai, Syntheses, Crystal Growths, and Nonlinear Optical Properties for 2-Carboxylic acid- 4-nitropyridine- 1-oxide Crystals with Two Different Arrangements of Chromophores, *Cryst. Growth Des.*, 2007, 7, 2316-2323.
- [18] T. Chen, Z. Sun, X. Liu, J. Wang, Y. Zhou, C. Ji, S. Zhang, L. Li, Z. N. Chen and J. Luo, Strong enhancement of second harmonic generation in nonlinear optical crystals: 2-amino-3-nitropyridinium halides (Cl, Br, I), *J. Mater. Chem. C.*, 2014, 2, 8723-8728.
- [19] S. M. Tripathi and R. Ramachandran, Crystal structures of the Mycobacterium tuberculosis secretory antigen alanine dehydrogenase (Rv2780) in apo and ternary complex forms captures "open" and "closed" enzyme conformations, *Proteins.*, 2008, 72, 1089-1095.
- [20] A. Dennis Raj, M. Jeeva, M. Shankar, R. Purusothaman, G. Venkatesa Prabhu and I. Vetha Potheher, Synthesis, growth, optical and DFT calculation of 2-naphthol derived Mannich base organic non linear optical single crystal for frequency conversion applications, *Physica B: Condens. Matter.*, 2016, 501, 45-56.

STRUCTURE AND CHARGE DENSITY ANALYSIS OF (1-x)SrTiO₃-x(Na_{0.5}Bi_{0.5})TiO₃ LEAD FREE CERAMICS

O.V. Saravanan, R. Saravanan, S. Sonai, T. Jayapandi, S. Meenadevi, S. Manimegalai

Research Centre and PG department of Physics, The Madura College, Madurai - 625 011

Email: ovsaravanan2258@gmail.com

Abstract

The (1-x)SrTiO₃-x(Na_{0.5}Bi_{0.5})TiO₃ ((1-x)ST-xNBT) ceramics are promising candidates for environmental friendly material and used in energy storage application. The (1-x)ST-xNBT ceramics were prepared by solid-state reaction method. Structural and charge density distribution studies were investigated using PXRD. Powder profile refinement of X-ray data confirms that the samples crystallized with cubic structure without any additional phase. From the PXRD data the electron density distribution studies were analyzed by maximum entropy method.

Keywords: Charge density, Lead free ceramics, Rietveld refinement, crystal structure, X-ray diffraction, MEM

1. Introduction

Multifunctional materials are becoming increasingly important in technological devices since they enable coupling between electrical, mechanical and optical properties. Lead zirconate titanate Pb(Zr, Ti)O₃ (PZT) and their solid solutions are utilized in a broad variety of devices, such as sensors, actuators, motors, transducers and nonvolatile random access memory chips [1, 2]. However, Pb and PbO were identified as toxic for human health and the environment. Therefore, there has been a growing research interest in developing alternative lead-free materials, which can replace the current lead-based materials. Among various lead-free systems, the Na_{0.5}Bi_{0.5}TiO₃ (NBT) and NBT-based solid solutions are promising compounds. In this work, the lead-free (1-x)SrTiO₃-x(Na_{0.5}Bi_{0.5})TiO₃ ceramics were synthesized using a conventional solid-state reaction technique. Their structure and charge density distribution was analyzed.

2. Experimental

2.1 Preparation

The raw compounds are sodium carbonate (Na₂CO₃ purity 99.99%), strontium carbonate (SrCO₃ purity 99.99%), titanium oxide (TiO₂ purity 99.99%) and bismuth oxide (Bi₂O₃ purity 99.99%) were weight their stoichiometric ratio mixed with the general formula of (1-x)SrTiO₃-x(Na_{0.5}Bi_{0.5})TiO₃. The raw powder was thoroughly mixed in agate mortar on homogeneously for 7 h. The mixed powders were carefully transferred to alumina crucibles. The homogenous mixture was calcined successively at 900 °C for 3 h. The calcined sample was ground again 7 h using agate mortar. Then the sample was transferred in crucibles were kept inside a tubular furnace at final sintering temperature of 1200 °C

for 4 h in a programmable tubular furnace.

2.2 Powder XRD analysis

The crystal structure was analyzed by powder X-ray diffraction (Bruker AXS D8 advance, SAIF, Cochin) in the 2θ range from 5-120° with step size 0.02°. The radiation source is CuKα (λ=1.54056). The Rietveld refinement [3] was done by JANA 2006 [4].

2.3 Charge density distribution

The charge density distribution was analyzed by maximum entropy method [7]. Through the refinement parameter the calculation was carried out PRIMA [5]. The 3D and 2D charge density was show in VESTA [6].

3 Results and Discussion

3.1 Powder X-ray diffraction

Structural characterizations were carried out using powder X-ray data. The phase formations of the prepared (1-x)ST-xNBT samples were analyzed and the prepared (1-x)ST-xNBT systems were well crystallized in cubic structure. No other additional peaks detected from the XRD patterns which clearly indicate the single phase formation of the prepared ceramic systems. The raw XRD profile of the prepared sample is shown in figure 1. The detailed structural studies of the (1-x)ST-xNBT samples were carried out by refining the experimentally observed powder profiles using Rietveld refinement [3] with software JANA 2006 [4]. In the prepared series of BSZT solid solutions with the ABO₃ perovskite structure Sr, Na and Bi ions are occupying A-site while Ti ions are occupying

B-site. The XRD profiles of BSZT were refined by considering the cubic setting with space group $Pm\bar{3}m$ (space group number: 221). The refined profiles (1-x)ST-xNBT are given in figures 2 (a) - (b). The fitted profiles reveal the good matching between the observed and calculated profiles for the two compositions. The refined structural parameters, R_p , R_{obs} and GOF (goodness of fit) values are presented in Table 1.

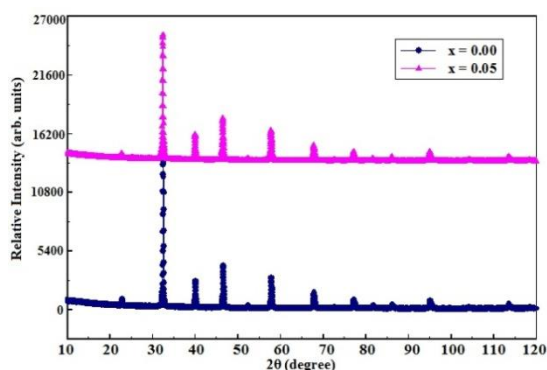


Figure 1. Raw XRD profile for (1-x)ST-xNBT, (a) $x=0.00$, (b) $x=0.05$

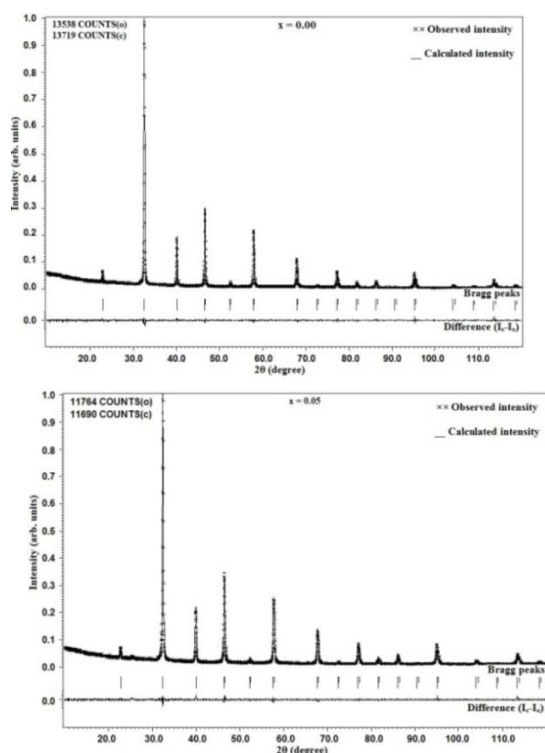


Figure 2. Fitted XRD profile for (1-x)ST-xNBT, (a) $x=0.00$, (b) $x=0.05$

Table 1. Refinement parameters for (1-x)ST-xNBT, $x=0.00$ and $x=0.05$

3.1 Charge density analysis

Parameters	$x=0.00$	$x=0.05$
Space group	$Pm\bar{3}m$	$Pm\bar{3}m$
$a=b=c$ (Å)	3.9041 (4)	3.9096 (3)
$\alpha=\beta=\gamma$ (°)	90	90
Unit cell Volume (Å ³)	59.75 (1)	59.76 (2)
Density (gm/cc)	5.09 (5)	5.13 (5)
R_p (%)	4.96	4.65
R_{obs} (%)	1.63	1.83
GOF	1.14	1.12
$F_{(000)}$	84	84

The electronic structure, charge density distribution and the bonding interactions of the (1-x)ST-xNBT systems were analyzed by maximum entropy method [7] (MEM) using the structure factors obtained from Rietveld refinement [3]. The MEM calculations were carried out successfully by implementing the software PRIMA [5], considering $64 \times 64 \times 64$ pixels per cubic unit cell. The resultant 3D charge density distribution and 2D contour maps were plotted with similar iso-surface level of $1e/\text{Å}^3$, using the visualization software VESTA [6]. The positions of strontium, titanium and oxygen atoms and the electron density distributions in their valence levels are explicitly and clearly seen from the figures 3 and 4 (a). The qualitative analysis of chemical bonding between Sr-O and Ti-O was done by plotting 2D charge density contour maps in the contour range of $0 e/\text{Å}^3$ to $1 e/\text{Å}^3$ and with the contour interval of $0.08 e/\text{Å}^3$ corresponding to two different crystallographic planes (100) shown in figures 3 (b) and (c). The (200) plane is shown in figure 4 (b) and (c). The bond lengths are Sr-O bonds are 2.7644 Å and 2.7646 Å. The bonds lengths are Ti-O bonds are 1.9547 Å and 1.9558 Å. The mid band electron density at bond critical point for Sr-O bonds are 0.3394 and 0.3103 $e/\text{Å}^3$. The mid band electron density at bond critical point for Ti-O bonds are 0.6397 and 0.6102 $e/\text{Å}^3$.

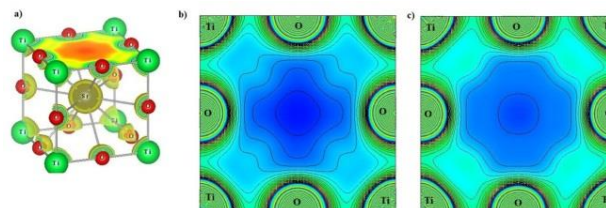


Figure 3. (a) 3D unit cell with (100) plane shaded. 2D electron density distribution on (100) plane (b) $x=0.00$, (c) $x=0.05$

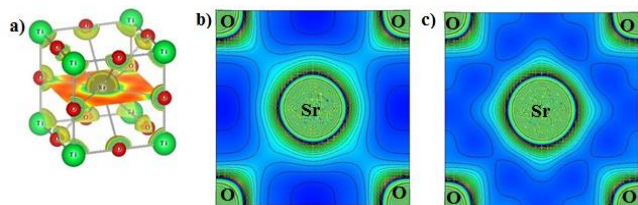


Figure 4. (a) 3D unit cell with (200) plane shaded. 2D electron density distribution on (200) plane (a) $x=0.00$, (b) $x=0.05$

4 Conclusion

The solid solution of lead free ceramics $(1-x)\text{SrTiO}_3-x(\text{Na}_{0.5}\text{Bi}_{0.5})\text{TiO}_3$ were prepared by conventional solid state reaction method. The structure and charge density distribution were investigated with addition of dopant ions. Powder X-ray diffraction confirms the formation of cubic single phase structure without any additional peak. Through Rietveld refinement, the charge density distribution was carried out by maximum entropy method.

5 Acknowledgements

I thank the institution of The Madura College, Madurai for their continuous support for the research activities for

the authors.

REFERENCES

- [1] Lines ME, Glass AM. Principles and applications of ferroelectrics and related materials. Oxford: Clarendon Press; 2001.
- [2] Randall CA, Kelnberger A, Yang GY et al. High strain piezoelectric multilayer actuators—a materials science and engineering challenge. *J Electrocer.*2005;14:177–191.
- [3] Rietveld H M. A profile refinement method for nuclear and magnetic structures. *Journal of Applied Crystallography*, 1969, 2(2): 65–71.
- [4] Petricek V, Dusek M, Palatinus L. The crystallographic computing system JANA 2006: General features. *Zeitschrift für Kristallographie*, 2014, 229(5): 345–352.
- [5] Izumi F, Dilanian R A. Recent Research Developments in Physics, Part II, Vol. 3. Trivandrum, India: Transworld Research Network, 2002
- [6] Momma K, Izumi F. VESTA: a three-dimensional visualization system for electronic and structural analysis. *Journal of Applied Crystallography*, 2008, 41(3): 653–658.
- [7] Collins D M. Electron density images from imperfect data by iterative entropy maximization. *Nature*, 1982, 298(5869): 49–51.

SYNTHESIS, STRUCTURAL INVESTIGATION AND CHARGE DENSITY ANALYSIS OF $(1-x)\text{Na}_{0.5}\text{K}_{0.5}\text{NbO}_3-x\text{SrTiO}_3$ LEAD FREE PIEZOELECTRIC CERAMICS

S. Sonai¹, O.V. Saravanan¹, S. Sasikumar², R. Saravanan¹

¹Research centre and PG department of Physics, The Madura College, Madurai - 625 011, India

²Department of Physics, Kalasalingam Academy of Research and Education, Krishnankoil, Viruthunagar, India
Email: physonai@gmail.com

Abstract

In this work, $(1-x)\text{Na}_{0.5}\text{K}_{0.5}\text{NbO}_3-x\text{SrTiO}_3$ (abbreviated as NKN-ST) lead free piezoelectric ceramics have been synthesized using conventional solid state reaction method. The structural investigation of the synthesized samples have been carried out using Powder X-ray Diffraction (PXRD) technique and analyzed using Rietveld refinement method by matching the observed and calculated profiles of NKN-ST and then the results obtained from the refinement process were used in mapping the electron density distribution using maximum entropy method (MEM) for the charge density analysis of the samples. Based on the studies reported in literature, we expect the modified $(1-x)\text{Na}_{0.5}\text{K}_{0.5}\text{NbO}_3-x\text{SrTiO}_3$ system to become the leading lead-free candidate for piezoelectric components.

Keywords: Lead free ceramics, charge density, crystal structure, X-ray diffraction, MEM

1. Introduction

At present, lead-based piezoelectric materials, represented as $\text{Pb}(\text{Zr}_{1-x}\text{Ti}_x)\text{O}_3$ (PZT), along with PZT-based materials are the most popular one and widely used in transducers, sensors, actuators as well as microelectronic devices owing to their superior electrical properties. However, the use of lead-based materials has caused serious environmental problems owing to the high toxicity of lead oxide. Recent investigations of lead-free piezoelectric materials [1] have been carried out to replace lead-containing materials. Among the various lead-free piezoelectric materials, Sodium potassium niobate $\text{Na}_{0.5}\text{K}_{0.5}\text{NbO}_3$ (abbreviated as NKN) is considered as a promising candidate because hot-pressed NKN ceramics have a high Curie temperature, a high remnant polarization, a large piezoelectric longitudinal response and a high planar coupling coefficient. NKN-based ceramics (e.g., solid solution of NKN- BaTiO_3 , NKN- SrTiO_3 , and NKN- CaTiO_3 [2, 3]) have received considerable attention mainly for two reasons: piezoelectric properties exist over a wide range of temperature and several possibilities for substitution and additions. In this work, the effect of SrTiO_3 on the electrical properties of NKN ceramics has been widely studied.

2. Experimental

2.1. Preparation

The raw materials Na_2CO_3 , K_2CO_3 , Nb_2O_5 , SrCO_3 , and TiO_2 powders (99 % purity) were used to synthesize $(1-x)\text{Na}_{0.5}\text{K}_{0.5}\text{NbO}_3-x\text{SrTiO}_3$ ($x=0.00, 0.01$) samples via the conventional solid-state reaction method. The high purity materials were mixed in stoichiometric ratios and grained into fine powders to prepare the end member NKN-ST using solid state reaction method. The pre-heated starting materials were mixed together in agate mortar pestle for 12 hours. The mixed powders were carefully transferred to thick walled alumina crucibles and calcined at 950°C for 3 hours. Later, the mixture was again grained for 12 hours and then pressed into a pellet with further heating at 1200°C for 3 hours to increase the crystallinity and to remove the binder. The synthesized powders were finally grained and kept for further analysis.

2.1 Powder X-ray diffraction studies

The powder XRD datasets of the synthesized samples were collected using Bruker AXS D8 advance X-ray diffractometer at room temperature with $\text{CuK}\alpha$ monochromatic incident beam ($\lambda=1.54056 \text{ \AA}$) in the 2θ range of 20° - 120° with an interval of 0.02° . The Rietveld refinement [4] was performed for the XRD pattern was done by JANA 2006 [5] software.

2.3 Charge density distribution studies

The charge density distribution of $(1-x)\text{Na}_{0.5}\text{K}_{0.5}\text{NbO}_3-x\text{SrTiO}_3$ ($x=0.00, 0.01$) was analyzed using maximum entropy method (MEM) using the structure factors obtained from X-ray measurements. In the present work, the computation of the charge density is done using the software PRIMA [6] that employs maximum entropy method MEM [7]. The resultant density is plotted with the help of visualization software VESTA [8]. The refined structure factors have been utilized for the electron density mapping using MEM [7].

3. Results and Discussion

3.1 Powder X-ray diffraction analysis

Structural investigation of the synthesized samples was carried out using powder XRD data. The NKN-ST ceramics are composed of orthorhombic NKN and cubic ST. The results reveal that the orthorhombic structure is preserved. In the present work, the raw intensity datasets of sintered samples were refined using Rietveld refinement method [4]. The cell parameters and other structural parameters were refined by JANA 2006 [5]. The fitted profiles for various doping concentrations of the samples using JANA 2006 [5] has been shown in the figures 1 (a) and (b). The least square refinement minimizes the differences between the observed and calculated profiles, rather than individual reflections. The refined structural parameters are given in the Table 1.

3.2 Charge density analysis

Maximum entropy method (MEM) is an accurate technique to deal with the electron density distribution in the unit cell because of its probabilistic approach. Also, it only needs a minimum amount of information from the observed XRD spectra and it yields the least biased information. This method is packaged by the software PRIMA (PRactice Iterative MEM Analyses) [6].

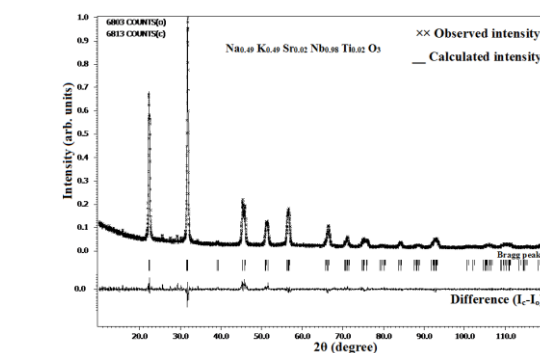
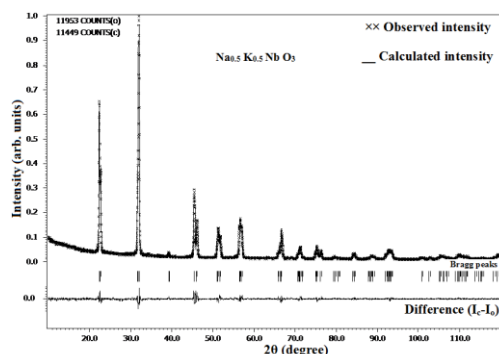


Figure 1. Fitted XRD profile for $(1-x)\text{Na}_{0.5}\text{K}_{0.5}\text{NbO}_3-x\text{SrTiO}_3$ (a) $x=0.00$, (b) 0.01

Table 1. Structural parameters of $(1-x)\text{Na}_{0.5}\text{K}_{0.5}\text{NbO}_3-x\text{SrTiO}_3$ ($x=0.00, 0.01$)

Parameters	$x=0.00$	$x=0.01$
Space group	<i>Amm2</i>	<i>Amm2</i>
a (Å)	3.9538(4)	3.9736(3)
b (Å)	5.6504(1)	5.6663(2)
c (Å)	5.6841(4)	5.6994(3)
$\alpha=\beta=\gamma$ (°)	90	90
Unit cell	126.98(2)	128.33(1)
Volume (Å ³)		
Density (gm/cc)	4.49(4)	4.45(3)
R _p (%)	5.75	5.59
R _{obs} (%)	1.69	2.62
GOF	1.67	1.27
F ₍₀₀₀₎	160	160

The structure factors extracted from the Rietveld refinement technique were used for this study. The electron density distribution in the unit cell was constructed through the PRIMA software.

The MEM [7] calculations for $(1-x)\text{Na}_{0.5}\text{K}_{0.5}\text{NbO}_3-x\text{SrTiO}_3$ ($x=0.00, 0.01$) ceramics were carried out using $64 \times 64 \times 64$ pixels along the a, b and c axes of the orthorhombic and distorted cubic lattice. The results are visualized using the visualization software VESTA (Visualization for Electronic and Structural Analysis) [8]. Previously, a similar technique was applied using the MEM method in other works for charge density analysis. Three-dimensional charge density distributions in the unit cell of $(1-x)\text{Na}_{0.5}\text{K}_{0.5}\text{NbO}_3-x\text{SrTiO}_3$ ($x=0.00, 0.01$)

are constructed with similar iso-surface levels of $1 \text{ e}/\text{\AA}^3$.

The positions of sodium, niobium and oxygen atoms and the electron density distributions in their valence levels are explicitly and clearly seen from the figure 2 (a). The qualitative analysis of chemical bonding between sodium and oxygen and between Niobium and oxygen was done by plotting 2D charge density contour maps in the contour range of $0 \text{ e}/\text{\AA}^3$ to $1 \text{ e}/\text{\AA}^3$ and with the contour interval of $0.08 \text{ e}/\text{\AA}^3$ corresponding to two different crystallographic planes (100) in figures 2 (b) and (c). The (200) plane is shown in figures 3 (b) and (c). The bond lengths for Na-O bonds are 2.8252 \AA and 2.8330 \AA . The bond lengths for Nb-O bonds are 2.9141 \AA and 2.9321 \AA . The mid band electron density at bond critical point for Na-O bonds are 0.2183 and $0.2111 \text{ e}/\text{\AA}^3$. The mid band electron density at bond critical point for Nb-O bonds are 1.0333 and $0.9297 \text{ e}/\text{\AA}^3$.

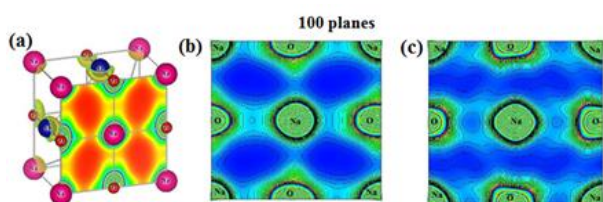


Figure 2. (a) 3D unit cell with (100) plane shaded. 2D electron density distribution on (100) plane (b) $x=0.00$ (c) $x=0.01$

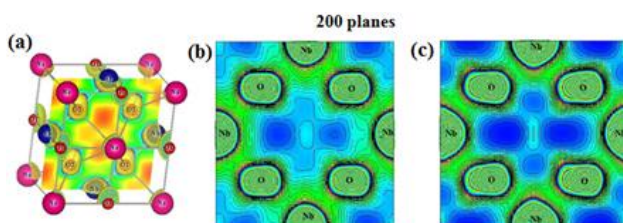


Figure 3. (a) 3D unit cell with (200) plane shaded. 2D electron density distribution on (200) plane (b) $x=0.00$ (c) $x=0.01$

3 Conclusion

$(1-x)\text{Na}_{0.5}\text{K}_{0.5}\text{NbO}_3-x\text{SrTiO}_3$ (abbreviated as NKN-ST) lead free piezoelectric ceramics have been successfully

synthesized using conventional solid state reaction method. The structural investigation of the synthesized samples have been carried out using powder X-ray diffraction technique and analyzed using Rietveld refinement method by matching the observed and calculated profiles of NKN-ST. PXRD analysis reveals that the synthesized samples were in orthorhombic structure and then the results obtained from the refinement process were used in mapping the electron density distribution using maximum entropy method for the charge density analysis of the samples.

4 Acknowledgements

The authorities of the Madura College, Madurai - 625 011 are gratefully acknowledged for their constant encouragement of the research activities of the authors.

REFERENCES

- [1] B. Jaffe, W.R. Cook, H. Jaffe, Piezoelectric Ceramics, Academic press, London, 1971.
- [2] M.R. Yang, C.-S. Hong, C.C. Tsai, and S.Y. Chu, J. Alloys Compd. 488, 169 (2009).
- [3] Z.Y. Shen, J.F. Li, K. Wang, S. Xu, W. Jiang, and Q. Deng, J. Am. Ceram. Soc. 93, 1378 (2010).
- [4] Rietveld H M. A profile refinement method for nuclear and magnetic structures. Journal of Applied Crystallography, 1969, 2(2): 65–71.
- [5] Petricek V, Dusek M, Palatinus L. The crystallographic computing system JANA 2006: General features. Zeitschrift fur Kristallographie, 2014, 229(5): 345–352.
- [6] Izumi F, Dilanian R A. Recent Research Developments in Physics, Part II, Vol. 3. Trivandrum, India: Trans world Research Network, 2002.
- [7] Collins D M. Electron density images from imperfect data by iterative entropy maximization. Nature, 1982, 298(5869): 49–51.
- [8] Momma K, Izumi F. VESTA: a three-dimensional visualization system for electronic and structural analysis. Journal of Applied Crystallography, 2008, 41(3): 653–658.

STUDIES ON NIOBIUM DOPED HYDROXYAPATITE NANOCRYSTALS SYNTHESIZED BY SOL GEL METHOD

V. Kavitha, S. Saranya, M. Prema Rani

Research Centre & PG department of Physics, The Madura College (Autonomous), Madurai -625011

Email: kavitharajan988@gmail.com

Abstract

Niobium doped hydroxyapatite nanocrystals were synthesized by sol gel method for three different concentrations of niobium (2%, 4% & 6%). Structural parameters were analyzed using XRD and the elemental composition was identified by EDS. The average crystallite size synthesized samples were determined as 27 nm from XRD. From XRD data, the space group was determined as P63/m for pure HaP and R3c for niobium doped HaP. Antimicrobial activity taken against *Pseudomonas Aeruginosa* showed that the activity increases with increase in niobium concentration.

Keywords: HaP, XRD, Crystallite size, Interplanar spacing

1. Introduction

Hydroxyapatite ($\text{Ca}_5(\text{PO}_4)_3\text{OH}$) is a bioactive biomaterial. It is also known as bone mineral which crystallizes in hexagonal crystal system. It is used as a filler to replace amputated bone. Modern implant such as hip replacements, dental implants and bone conduction implants are coated with HaP [1,2]. Porous HaP is used for local drug delivery in bone. To repair early lesions in tooth enamel [3,4]. Host reaction against HaP is minimum. Poor mechanical properties, e.g. low strength and toughness, restrict HaP to develop load-bearing parts [5]. One of the ways to increase the fracture toughness is by doping. When niobium is mixed with steel it increases the strength of the steel [6,7]. It is corrosion resistant and used in medical implants [8-10]. It aids osseointegration [11]. It is 34th abundant metal in earth crust and it costs low. It has high melting point [12]. Hence, niobium is chosen as dopant. A number of methods have been used for HaP synthesis [13]. The easiest and cheapest method is solgel. Under controlled pH and temperature the homogeneity of nanocrystal increases [14].

2. Experimental Procedure

Niobium doped hydroxyapatite nanocrystals $\text{Ca}_{10-x}\text{Nb}_x(\text{PO}_4)_{6-x}(\text{HPO}_4)_x(\text{OH})_{2-x}$ where ($x=0, 0.02, 0.04$ & 0.06) were synthesized by sol gel method for three different concentrations of Niobium (2%, 4% & 6%). Diammonium hydrogen phosphate was dissolved in deionized water and stirred in magnetic stirrer at 90°C. Calcium nitrate tetra hydrate and Niobium chloride were dissolved separately in deionized water and added. The above two solutions were added drop wise. pH is maintained at 10 by adding ammonium hydroxide [16]. It was maintained at 90°C for 6 hours. Precipitates were

filtered and washed then dried at 110°C for 22 hours and then calcined at 900°C for 4 hours.

3. Results And Discussion

3.1 Structural Analysis Using XRD

The X-ray powder diffraction measurements were performed at Sophisticated Analytical Instrument Facility (SAIF), Cochin, using $\text{CuK}_{\alpha 1}$ with 2θ ranges from 10° to 120° and step size of 0.02° . The XRD patterns of $\text{Ca}_{10-x}\text{Nb}_x(\text{PO}_4)_{6-x}(\text{HPO}_4)_x(\text{OH})_{2-x}$ ($x= 0.0, 0.02, 0.04, 0.06$) were compared with JCPDS data which confirmed the hexagonal crystal system. The XRD profiles of the pure and niobium doped HaP is shown in figure 15.

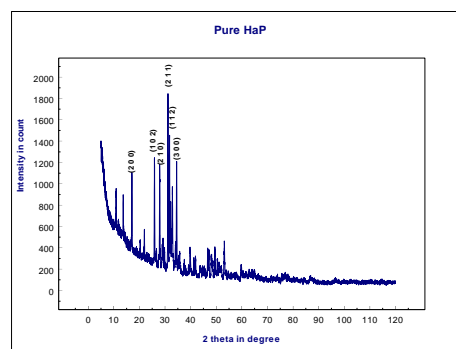


Figure1 XRD profile of pure HaP

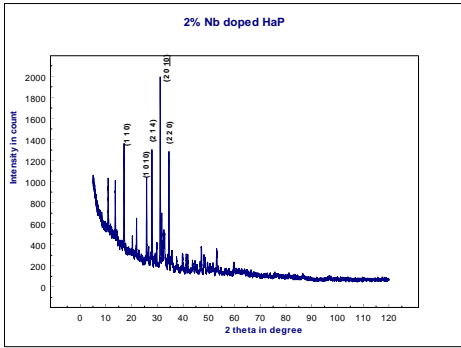


Figure 2 XRD profile of 2%Nb doped HaP

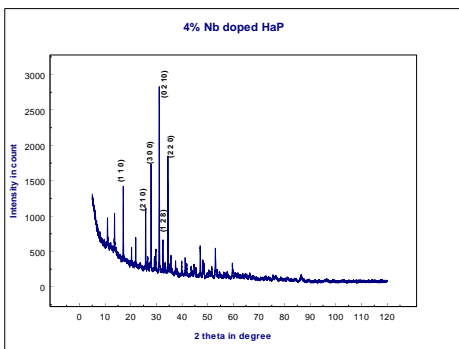


Figure 3 XRD profile of 4% Nb doped HaP

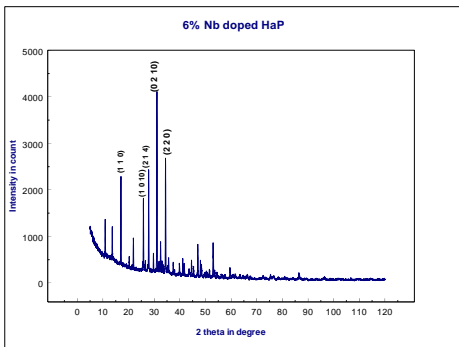


Figure 4 XRD profile of 6% Nb doped HaP

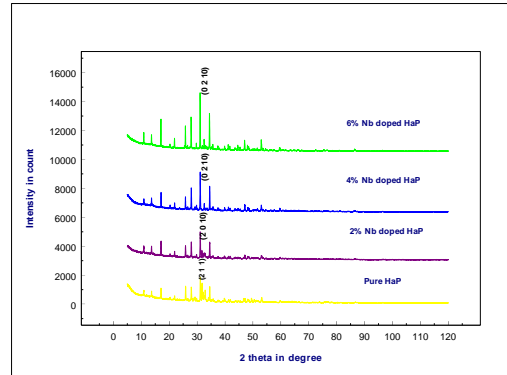


Figure 5 XRD patterns of pure and niobium doped HaP

The shift in main peak is shown in the fig.7

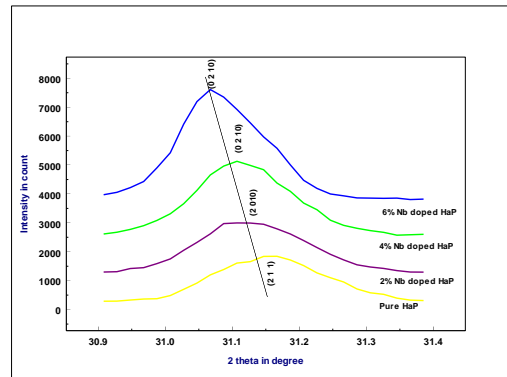


Figure 6 Main peak intensity versus 2theta

Intensity increases with increase in niobium concentration. This shows that the calcium ions are replaced by niobium ions. The Debye Scherrer equation is used in the determinant size of particles of crystals in the form of powder.

Table 1 Crystallite size from XRD

s.no	Sample	D in nm
1	Pure HaP	26.2886
2	2%Nb doped HaP	26.9329
3	4%Nb doped HaP	27.2035
4	6%Nb doped HaP	28.0429

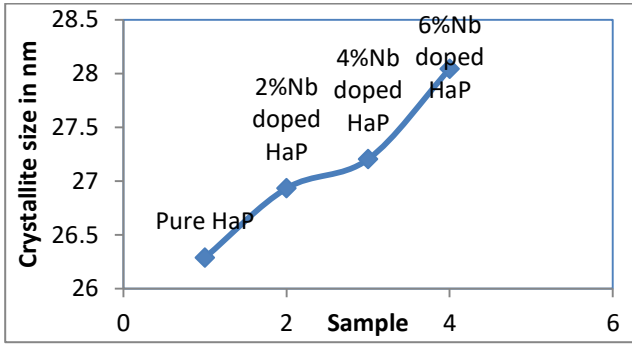


Figure 7 Crystallite size from XRD

Crystallite size, crystallinity degree, lattice parameters and unit cell volume were affected by niobium. The crystallite size increases with increase in niobium concentration. This proves that Nb^{3+} ions replace Ca^{3+} ions in the HaP. Since the ionic radius of niobium (198 pm) is larger than calcium (194 pm).

Table 2 Main peak intensity versus 2θ

S.No	Sample	2θ in degree	d in Å
1	Pure HaP	31.158	2.86901
2	2%Nb doped HaP	31.133	2.87031
3	4%Nb doped HaP	31.117	2.87107
4	6%Nb doped HaP	31.084	2.87513

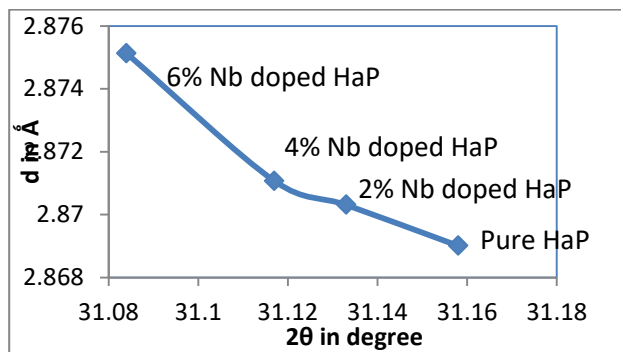


Figure 8 Main peak intensity versus 2θ

By Bragg's law as θ increases the interplanar distance decreases which decrease the lattice parameter. This also proves that the crystallite size increases as 2θ increases with increase in Nb concentration. Space group was determined as P63/m for pure HaP and R3c (161) for Niobium doped HaP [15]. The unit cell volume, density and lattice parameters affected by incorporation of

niobium ions in calcium site. The unit cell volume decreases and density increases with increase in niobium concentration.

3.3 EDX

The chemical characterizations of the samples were done at International Research Centre, Kalasalingam University, Srivilliputhur. Energy Dispersive X-ray spectroscopy (EDS) is an analytical technique used for the elemental analysis of the sample. Figure 13- 16 shows the EDX spectrum of niobium doped HaP.

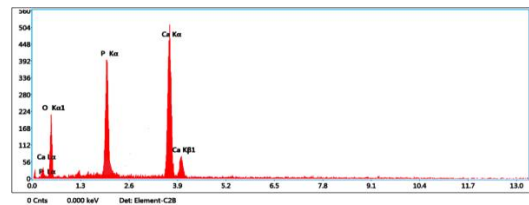


Figure 13 EDX spectrum of pure HaP

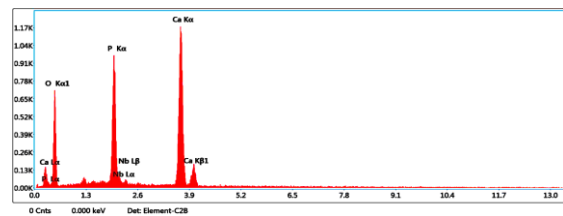


Figure 14 EDX spectrum of 2% Nb doped HaP

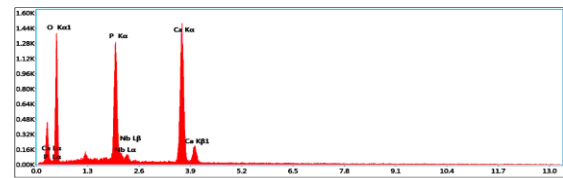


Figure 15 EDX spectrum of 4% Nb doped HaP

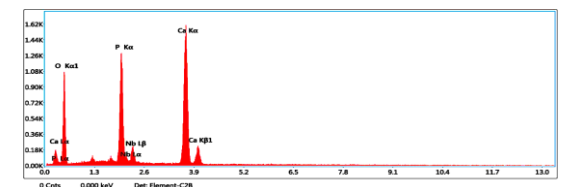


Figure 16 EDX spectrum of 6% Nb doped HaP

4. CONCLUSION

Niobium doped hydroxyapatite nanocrystals were synthesized by sol gel method. Niobium was doped in three different concentrations (2%, 4% & 6%). The

structural characterization was done by XRD. From XRD data the lattice parameters and space group were determined by comparing with JCPDS. By using Debye-Scherrer equation crystallite size was calculated from the FWHM values and 2θ values of peaks in XRD data. The elemental composition was determined by EDX.

REFERENCES

- [1] Sanosh Kunjalukkal Padmanathan, Avinash Balakrishnal, Min Chaol Chu, Young Jin Lee, Taik Nam Kim, Song, Jai Cho, Solgel gel synthesis and characterization of hydroxyapatite nanorods, Particularly, Volume-7, Issue-6, December 2009, pp. 466-470.
- [2] Omer Kaygili, Sergey V. Dorozhkin, Tankut Ates, N. Canan Gursoy, Serhat Keseer, Fahrettin Yakuphanolgu, A. Birkan Selcuk, Structural and dielectric properties of yttrium-substituted hydroxyapatites, *Material Science and Engineering C*, 47 (2015) 333-338.
- [3] Wei G, Ma Px. Structure and properties of nano-hydroxyapatite/polymer composite scaffolds for bone tissue engineering. *Biomaterials*.2004; 25(19): 4749-5
- [4] Biomimetic Synthesis of Calcium deficiency hydroxyapatite in natural hydrogel. *Biomaterials*, volume 27, Issue 26, September 2006, pages 4661-4670.
- [5] www.fluidnova.com
- [6] Gupta, C. K.; Suri, A. K. (1994). *Extractive Metallurgy of Niobium*. CRC Press. pp. 1–16. ISBN 978-0-8493-6071-8.
- [7] Clarke, F. W. (1914). Columbium Versus Niobium. *Science*. 39 (995): 139–140. Bibcode: 1914, Sci. 39, 1, 39C. doi:10.1126/science.39.995.139. JSTOR 1640945. PMID 17780662.
- [8] Mallela, Venkateswara Sarma; Ilankumaran, V.; Srinivasa Rao, N. (1 January 2004). Trends in Cardiac Pacemaker Batteries. *Indian Pacing Electrophysiol J.* 4 (4): 201–212. PMC 1502062. PMID 16943934.
- [9] Vilaplana, J.; Romaguera, C.; Grimalt, F.; Cornellana, F. (1990). New trends in the use of metals in jewellery. *Contact Dermatitis*. 25 (3): 145–148. doi:10.1111/j.1600-0536.1991.tb01819.x. PMID 1782765.
- [10] Vilaplana, J.; Romaguera, C. (1998). New developments in jewellery and dental materials. *Contact Dermatitis*. 39 (2): 55–57. doi:10.1111/j.1600-0536.1998.tb05832.x. PMID 9746182.
- [11] Godley, Reut; Starosvetsky, David; Gotman, Irena (2004). Bonelike apatite formation on niobium metal treated in aqueous NaOH (PDF). *Journal of Materials Science: Materials in Medicine*. 15 (10): 1073–1077. doi:10.1023/B:JMSM.0000046388.07961.81. PMID 15516867.
- [12] <https://en.wikipedia.org/wiki/niobium>.
- [13] Biomimetic Synthesis of Calcium deficiency hydroxyapatite in natural hydrogel. *Biomaterials*, volume 27, Issue 26, September 2006, pages 4661-4670
- [14] https://en.wikipedia.org/wiki/solgel_process.
- [15] Bollinger, R. K.; White, B. D.; Neumeier, J. J.; Sandim, H. R. Z.; Suzuki, Y.; dos Santos, C. A. M.; Avci, R.; Migliori, A.; Betts, J. B. (2011). Observation of a Martensitic Structural Distortion in V, Nb, and Ta. *Physical Review Letters*. 107 (7): 075503. Bibcode: 2011PhRvL.107g5503B. doi:10.1103/PhysRevLett.107.075503. PMID 21902404
- [16] Jarcho M, Bolen C H, Thomas M B, Bobick J, Kay J F, Doremus R H. Hydroxyapatite synthesis and characterization 55 in dense polycrystalline form. *J Mater Sci* 1976; 11: 2027-2035.

A THEORETICAL STUDY OF ELECTRONIC AND REACTIVITY PROPERTIES OF ANTI-HYPERSENSITIVE DRUG HYDROCHLOROTHIAZIDE

R. Niranjana Devi

Assistant professor in Physics, Fatima College, Madurai-625018, Tamil Nadu, India

Email: niranjana.is14@gmail.com

Abstract

In this work, an analysis has been done to describe the structural, electronic and reactivity properties of the potent oral diuretic and antihypertensive drug hydrochlorothiazide. In order to shed light into the intermolecular interactions, the Hirshfeld surface analysis has been done. The information retrieved from the global reactivity descriptors calculation is helpful to understand the molecule's nature of reactivity and site selectivity. The atomic charges which have been obtained from AIM, Mulliken and NBO analysis give better understanding towards the distribution of charges in the molecule. The electrostatic potential assists to pinpoint the sites of electrophilic and nucleophilic attack likely to happen due to the interaction of hydrochlorothiazide with the hypertension drug target. This work throws light into the structural, electrostatic, reactivity properties and drug receptor interaction which further more aids in the outline of novel antihypertensive drugs with improved potential and lower side effects.

Keywords: Charge, reactivity, electrophilicity index, electrophilic region, electrostatic potential

1. Introduction

Hydrochlorothiazide (HCTZ) chemically named (6-chloro-3,4-dihydro-2H-1,2,4-benzothiazine-7-sulfonamide 1,1-dioxide) which is useful in the treatment of several disorders including edema, hypertension and hypoparathyroidism [1]. It is a thiazide diuretic. The investigation on the structural, electronic, nature and reactivity of the HCTZ molecule paves way for not only obtaining better knowledge about the existing drugs but also leads us to design new efficacy drugs with reduced side effects. In that sense this study deals with the structure related things, charges, HOMO(Highest occupied molecular orbital)-LUMO(Lowest unoccupied molecular orbital) analysis, Hirshfeld surface analysis and electrostatic potential in order to obtain better interpretation on the nature and reactivity properties of the HCTZ molecule.

2. Theoretical methodology

2.1. Energy minimization

The optimization and energy minimization for the structure of HCTZ has been done at B3LYP level [2] and (6311G++ (d, p) basis set which also includes diffusion and polarization using DFT theory [3] using GAUSSIAN09 [4] software. The convergence had been reached once the self-consistent field was obtained.

3. Results and discussion

3.1. Structural aspects

The optimization for the molecule HCTZ ($C_7H_8ClN_3O_4S_2$) was converged with the electronic spatial extent value of 5551.40 a.u. The HCTZ molecule has 69 degrees of freedom. The theoretically calculated structural parameters such as bond lengths, bond angles and torsion angles agree well with the previously reported experimental parameters from single crystal XRD. The optimized figure1 shows that delocalization occurred between the carbon bonds of the phenyl ring.

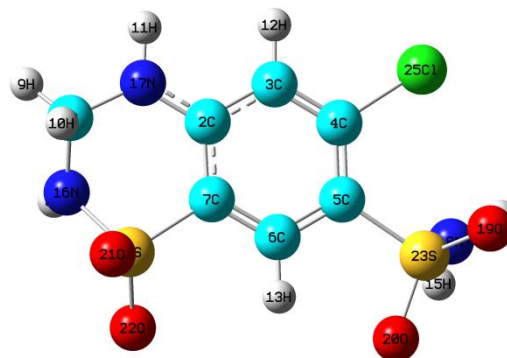


Figure 1: The optimized structure of the HCTZ molecule

3.2. Hirshfeld surface analysis

The Hirshfeld surface analysis shows the strong interactions of the O1, O2 and C11 atoms with the neighboring molecules and the red color indicates the strength of the interactions.

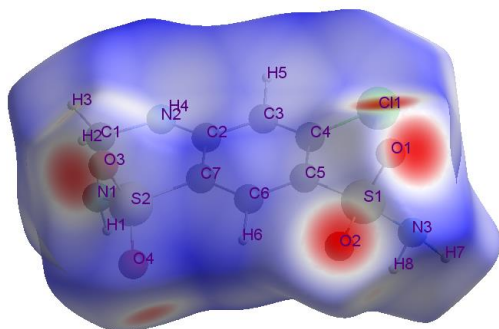


Figure 2: Hirshfeld surface analysis of the HCTZ molecule

3.3. Electronic properties

3.3.1. Charges

In order to know how the charges are distributed in the molecule, an analysis on charges has been done through AIM [5], Mulliken(MPA), and Natural Bond order (NBO) analysis. All the three analysis predict that the charges of S1 and S2 atoms are above 2e (for S1 2.12e (AIM), 2.03e(MPA) 2.08e(NBO); for S2 2.13e (AIM), 2.05e(MPA) 2.09e(NBO)). Similarly, all the Nitrogen atoms, exhibit the highest negative charges in the three schemes.

3.3.2. Reactivity properties

The charge transfer mechanism in a molecule can be explained by HOMO-LUMO analysis and the energy gap between them throws light on the kinetic stability and chemical reactivity of the molecule. Some global reactivity descriptors such as electron affinity [6], ionization potential, hardness[7-9], softness, electronegativity[10] and electrophilicity index[11,12] help us to characterize the nature and reactivity of the molecule. The very low electron affinity (0.083eV) and low ionization potential (0.269eV) shows that the molecule is highly chemically reactive. The very low global hardness (0.093eV) and very high softness (10.75eV) indicates that the molecule is very soft and it actively shares electrons with the neighboring molecule.

The very low electronegativity (0.166eV) shows that the molecule hardly attracts the electrons. Besides the low electrophilicity index (0.086eV) clearly predicts that the molecule has nucleophilic nature and donates electrons while it interacts with the target bio-molecule.

Table 1: Reactivity descriptors of the HCTZ molecule.

Molecular descriptor	Energy(eV)
Electron affinity $A=[-E_{LUMO}]$	0.083
Ionization potential $I=[-E_{HOMO}]$	0.269
Global hardness $\eta=(I-A)/2$	0.093
softness $S=1/\eta$	10.75
Electronegativity $\chi=(I+A)/2$	0.166
Electrophilicity index $\omega=\mu^2/2\eta$	0.086
HOMO energy	-0.269
LUMO energy	-0.083

3.3.3. Electrostatic potential

The electrostatic potential helps us to identify the electrophilic and nucleophilic site and chemical reactivity of the molecules [13]. In this, the nucleophilic regions are found at the vicinity of the O atoms which are prone to electrophilic attack and the electrophilic regions are found near H and S atoms which are prone to nucleophilic attack. The calculated dipole moment value is low and is found to be 11.5Debye which suggests that the molecule is highly polar and is more soluble in water.

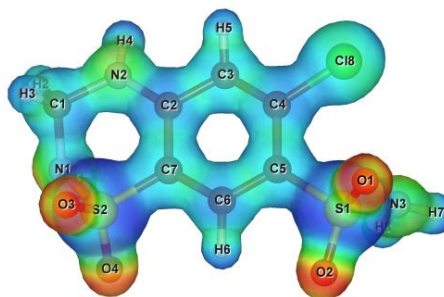


Figure 3: The electrostatic potential map of the molecule HCTZ

4. Conclusion

The analysis on structural, electronic, nature and reactivity of the molecule has been interpreted in detail which supplies better understanding towards the nature and reactivity of the molecule. This study helps us to obtain the chemical characteristic features of the molecule that HCTZ has high chemical reactivity, very soft and it has less attraction towards electrons. Finally

HCTZ qualifies itself as a fast interacting and powerful anti-hypertensive drug which interacts actively with the protein and the nucleophilic region of HCTZ interacts with the electrophilic region of target and the electrophilicity of the new molecule gets modified through the process of electronic charge transfer.

REFERENCES

- [1] R. Tanaka, M. Haramura, N. Hirayama, *Analytical Sciences*, 2004, vol 20.
- [2] C. Lee, W. Yang, R.G. Parr. "Development of the Colle-Salvetti correlation energy formula into a functional of the electron density", *Phys. Rev. B*, 37, 785 (1988).
- [3] A.D. Becke. "Density functional thermochemistry. III. The role of exact exchange", *J. Chem. Phys.*, 98, 5648 (1993).
- [4] Gaussian 09, Revision C.01, M. J. Frisch, G. W. Trucks, H. B. Schlegel, G. E. Scuseria, M.A. Robb, J. R. Cheeseman, G. Scalmani, V. Barone, B. Mennucci, G. A. Petersson, H. Nakatsuji, M. Caricato, X. Li, H. P. Hratchian, A. F. Izmaylov, J. Bloino, G. Zheng, J. L. Sonnenberg, M. Hada, M. Ehara, K. Toyota, R. Fukuda, J. Hasegawa, M. Ishida, T. Nakajima, Y. Honda, O. Kitao, H. Nakai, T. Vreven, J. A. Montgomery, Jr., J. E. Peralta, F. Ogliaro, M. Bearpark, J. J. Heyd, E. Brothers, K. N. Kudin, V. N. Staroverov, T. Keith, R. Kobayashi, J. Normand, K. Raghavachari, A. Rendell, J. C. Burant, S. S. Iyengar, J. Tomasi, M. Cossi, N. Rega, J. M. Millam, M. Klene, J. E. Knox, J. B. Cross, V. Bakken, C. Adamo, J. Jaramillo, R. Gomperts, R.E. Stratmann, O. Yazyev, A. J. Austin, R. Cammi, C. Pomelli, J. W. Ochterski, R. L. Martin, K. Morokuma, V. G. Zakrzewski, G. A. Voth, P. Salvador, J. J. Dannenberg, S. Dapprich, A. D. Daniels, O. Farkas, J. B. Foresman, J. V. Ortiz, J. Cioslowski, and D. J. Fox, Gaussian, Inc., Wallingford CT, 2010.
- [5] R.F.W. Bader, *Chem. Rev.* 91 (1991) 893
- [6] U. Sarkar, J. Padmanabhan, R. Parthasarathi, V. Subramanian, P.K. Chattaraj, *J. Mol. Struct.: THEOCHEM* 758 (2006) 119.
- [7] K.D. Sen, D.M.P. Mingos, *Chemical Hardness: Structure and Binding*, vol. 80, Springer, Berlin, 1993.
- [8] U. Deva Priyakumar, G. Narahari Sastry, *Organometallics* 21 (2002) 1493.
- [9] R. Ghiasi, *J. Organomet. Chem.* 690 (2005) 4761.
- [10] L. Pauling, *The Nature of the Chemical Bond*, second ed., Cornell University Press, Ithaca, NY, 1942.
- [11] R.G. Parr, L.V. Szentpaly, S. Liu, *J. Am. Chem. Soc.* 121 (1999) 1922.
- [12] Kalyan K. Hazarika, Nabin C. Baruah, Ramesh C. Deka, *Struct. Chem.* 20 (2009) 1079.
- [13] M. Da'san, M. Jaradat, S. Mebs, L. Checinska, P. Luger, *Carbohydr. Res.* 342 (2007) 1480.

PREPARATION AND CHARACTERIZATION OF PRISTINE BISMUTH MOLYBDATE BY FACILE SINGLE POT MICROWAVE-COMBUSTION METHOD

A. Shameem¹, P. Devendran¹, V. Siva¹, A. Murugan¹, Shamima Hussain², S. Asath Bahadur^{1*}

¹Department of Physics, International Research Centre, Kalasalingam Academy of Research and Education, Krishnankoil, Tamil Nadu, India – 626126.

²UGC-DAE-CSR Kalpakkam Node, Kokilamedu, Kalpakkam, Tamilnadu, India- 603104.

*Email: s_a_bahadur@yahoo.co.in (Dr. S. Asath Bahadur)

Abstract

The preparation and characterization of highly crystalline orthorhombic bismuth molybdate (Bi_2MoO_6) nanoparticles synthesized by single pot microwave-assisted combustion method. The characterization, XRD pattern confirmed the presence of polycrystalline orthorhombic Bi_2MoO_6 . The surface morphologies of Bi_2MoO_6 with nanosheets and rods are obtained by SEM images. The elemental compositions of the prepared sample have been examined by SEM equipped with EDX analysis system. The formation mechanisms of nanosheet and microrod structures were then discussed. FTIR is used to identify the structural coordination and functional groups of the prepared NPs.

Keywords: Bi_2MoO_6 , microwave-assisted combustion, orthorhombic, nanosheet, microrod.

1. Introduction

Currently, a family of bismuth-based semiconductors has attracted extensive attention due to their photo response in the visible region such as BiOX ($X = \text{Cl}, \text{Br}, \text{I}$) [1-3], BiVO_4 [4], Bi_2O_3 [5], $\text{Bi}_{20}\text{TiO}_{32}$ [6] and BiFeO_3 [7] have been investigated by the scientific community. Among these Bi-containing compounds, Bi_2MoO_6 is a preferable photocatalyst with a smaller band gap (about 2.5–2.8 eV) for employing visible light [8]. It is reported that Bi_2MoO_6 could be utilized in decomposition of organic compounds under visible-light irradiation [9]. As a typical Aurivillius oxide, Bi_2MO_6 ($M = \text{W}, \text{Mo}$) with the layered bismuth oxide family are of unique enthusiasm because of their dielectric, ion-conductive, luminescent, catalytic and synergist properties [10&11]. Developing epic nanostructures by base up systems might be soundly planned.

Solution Combustion synthesis (SCS) is an adaptable, simple and quick procedure, which permits viable production of an assortment of nanosize materials. This procedure includes a self-sustained reaction in the homogeneous arrangement of various oxidizers (e.g., metal nitrates) and fills (e.g., urea, glycine, hydrazides). The microwave-assisted combustion method, a pristine type of SCS synthetic method, conspicuously reduces the time of reaction from days and hours to minutes or even seconds. This method differ from most of conventional methods

with many striking advantages such as enhanced reaction kinetics, selective materials coupling, rapid volumetric heating, high reaction rate, increased product yield, most purity product, low cost, etc. Furthermore, this method can suppress the by-products during synthesis [12]. These advantages could be endorsed to prompt homogeneous nucleation and easy dissolution of the gel. However, only few papers have been published in metal molybdate NPs by microwave assisted combustion method using urea as fuel [13-15].

In this work, Bi_2MoO_6 nanocrystals were synthesized via facile time consuming, eco-friendly, single pot microwave-assisted combustion method. Bi_2MoO_6 NPs expected to have much higher photo and electrochemical activity.

2. Materials and methods

2.1. Materials

Bismuth nitrate pentahydrate ($\text{Bi}(\text{NO}_3)_3 \cdot 5\text{H}_2\text{O}$), Sodium molybdate dehydrate ($\text{Na}_2\text{MoO}_4 \cdot 2\text{H}_2\text{O}$) and Urea ($\text{CO}(\text{NH}_2)_2$) were purchased from Merck, India. All chemicals were analytical grade, and were used without further purification. Double distilled (DD) water was used throughout this study. Ethanol was purchased from Sigma Aldrich, Mumbai, India.

2.2. Synthesis of Bi₂MoO₆

Bi₂MoO₆ NPs was prepared by a simple microwave-assisted combustion method as described earlier by our group [12&13]. Bi(NO₃)₃·5H₂O (1 mmol), Na₂MoO₄·2H₂O (1mmol) and CO(NH₂)₂ (4 mmol) were each dissolved together in 50 mL of DD water under magnetically stirring at room temperature. Later, transferred into domestic microwave oven (IFB-20PG3S) with microwave vitality in a 2.45 GHz multimode cavity at 1000 W for 10minutes. After the reaction, the precipitate was isolated and washed with DD water and ethanol for several times, and dried at oven a night.

2.3. Characterization methods

The crystallinity and phase purity of the samples were characterized by a Bruker D8 advance ECO XRD systems with SSD160 1D Detector X-ray diffractometer. The morphologies and microstructures of the samples were examined with scanning electron microscope (ZEISS EVO 18 Research). Fourier transform infrared spectra (FT-IR) of the prepared powders were engaged in the range of 4000–400 cm⁻¹ by Shimadzu (IR Tracer-100) spectrophotometer by means of KBr pellet technique.

3. Results and Discussion

3.1. X-ray analysis

Fig. 1 depicts the XRD patterns of the Bi₂MoO₆ samples and observed the diffraction peaks between 2θ = 10–80°. As shown in Fig. 1, the diffraction peaks in could be indexed to the γ-Bi₂MoO₆ phase, corresponding to JCPDS Card no.:77-1246. The sharp and intense peaks indicated that the sample have a high degree of crystallinity. It is revealed that all the peaks could be readily indexed to the of primitive lattice γ-bismuth molybdenum oxide, with lattice constants of a=5.482 Å, b=16.19 Å, and c=5.509 Å (JCPDS card no.77-1246). From the structural point of view, NiMoO₄ has a orthorhombic crystal structure and *PCa*₂(29) space group. From the XRD study, no other impurity peak was detected. The prepared nanomaterial is extremely crystalline in nature. The average crystallite size of Bi₂MoO₆ NPs was calculated by Debye Scherrer formula as given below,

$$T = \frac{D\lambda}{\beta \cos\theta} \text{ nm}$$

Where, 'D' is the crystallite size with value 0.9, 'λ' indicate the X-ray wavelength, 'θ' indicate the

Bragg diffraction angle 'β' is the full width at half maximum (FWHM). The average crystallite size was calculated and was found to be around 28.9 nm.

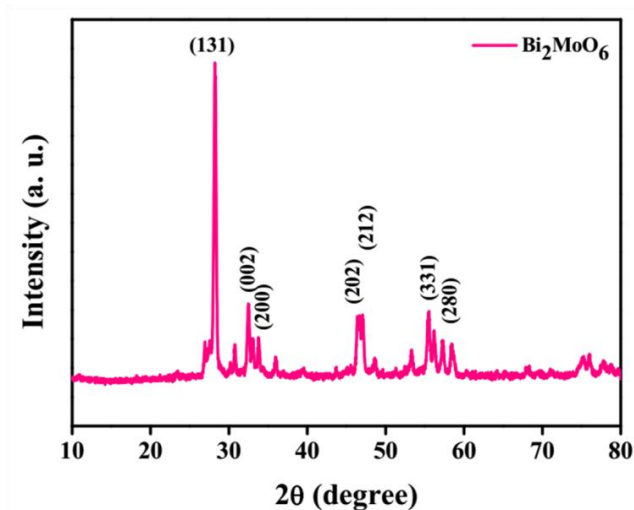
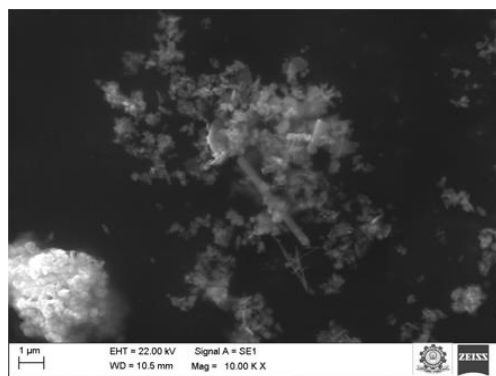


Fig.1. Powder XRD pattern of Bi₂MoO₆ nanostructures.

3.2. SEM



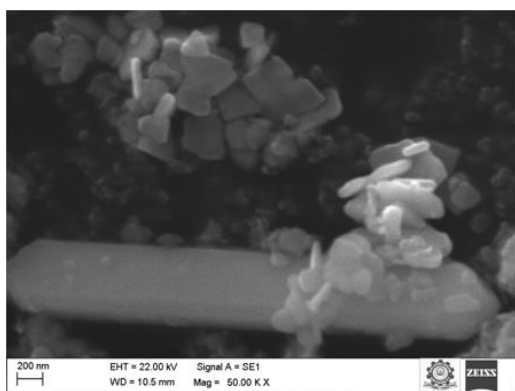


Fig.2. SEM images of as-prepared bismuth molybdate showing nanosheets and microrod like structure morphologies

Generally, the shape determination of the nanocrystals depends on the crystallographic phase of the initial seed during the nucleation processes. The SEM images were used to study the surface morphology of Bi_2MoO_6 NPs. Figure 2 shows the SEM images of Bi_2MoO_6 NPs confirmed that the synthesized NPs having the uniform size nanoplate structure with some microrods. This may be a result of the combination of the NPs with rod-shaped and the growth of unequal crystalline grains for the period of synthesis.

These results clearly illustrates that the formation of microrod like structure, due to the aggregation followed by the agglomeration of NPs. The transformation of the Bi_2MoO_6 morphology from a 2D sheet-like structure to a 1D rod-like has been realized through a facile, time consuming microwave assisted combustion method is visualized through SEM image. Thus Bi_2MoO_6 sample exhibited a photocatalytic activity 12 times higher than that prepared at basic condition for the photodegradation of MB under visible-light irradiation [FTIR].

3.3. EDS and Mapping

Energy-dispersive X-ray spectroscopy (EDS) analyses were carried out for all samples. A fine homogeneity was noticed for the sample $\gamma\text{-Bi}_2\text{MoO}_6$, in accordance with XRD patterns, indicating the presence of $\gamma\text{-Bi}_2\text{MoO}_6$ only. As expected, the Mo stoichiometry was close to the theoretical value of Bi_2MoO_6 . It is worth noting that the presence of Bi, Mo, C and O. The presence of Cu is due to the conductive copper tape used in EDS measurement. The Bi, Mo and O element maps for the samples Bi_2MoO_6 , generated from EDS data collected during SEM imaging of the particles are shown in figures 3(b). The element maps provide addi-

tional insights into the elemental composition and distribution within the Bi_2MoO_6 NPs. Bi, Mo and O in Bi_2MoO_6 are well dispersed throughout the particles, indicating that they can be described as Bi-Mo-O alloys.

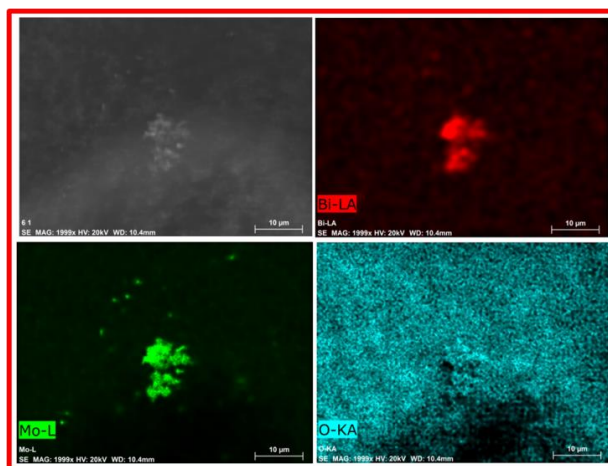
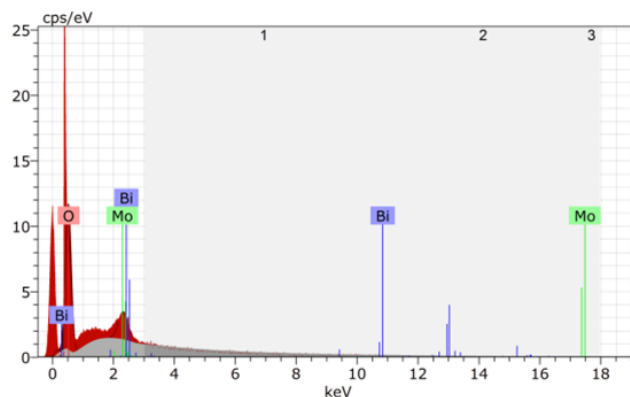


Fig.3. EDS spectrum (a) and elemental mapping (b) of bismuth molybdate NPs

3.3. FTIR Spectroscopy

Fig. 4 shows the FTIR spectra of the prepared Bi_2MoO_6 . A small peak is attributed at 2320 cm^{-1} may be due to CO_2 or nitrile group. The main absorption bands at $400\text{--}900\text{ cm}^{-1}$ are mainly related to Bi-O, Mo-O stretching and Mo-O-Mo bridging stretching modes, which can reflect the variation of structure in crystal [16&17]. The bands at around 845 and 797 cm^{-1} can be assigned as the asymmetric and symmetric stretching mode of MoO_6 involving vibrations of the apical oxygen atoms, respectively. The band at 711 cm^{-1} is attributed to the asymmetric stretching mode of MoO_6 involving vibrations of the equatorial oxygen atoms and the bands at 567 cm^{-1} correspond to the bending vibration of MoO_6 . Furthermore, a small change of the band occurred at 456

cm^{-1} , which is attributed to the stretching and bending vibrations of BiO_6 octahedra, confirming the crystal structure. In orthorhombic Bi_2MoO_6 , the molybdenum cation is located in a distorted MoO_6^{2-} octahedron with different distinct bond lengths, and the bismuth cation is coordinated with the MoO_6^{2-} octahedrons. Consequently, the lone-pair distortion existed in the orthorhombic structure due to the difference in the Bi-O bond lengths around the bismuth cation [16].

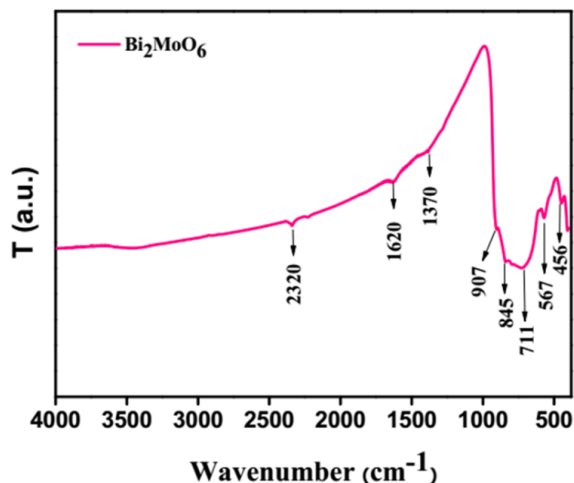


Fig.4. FTIR spectrum of synthesized bismuth molybdate NPs.

4. Conclusion

The bismuth molybdate nanomaterials were successfully synthesized by facile, time-consuming single pot-microwave-assisted combustion method. XRD pattern revealed the presence of orthorhombic primitive Bi_2MoO_6 system structure with average crystallite size of 28.9 nm. The SEM images clearly depict nanosheet and microrods morphology and the presence of relevant elements was exhibited in EDS. The transformation of the Bi_2MoO_6 morphology from a 2D sheet-like structure to a 1D rod-like has been realized through microwave synthetic method expected to have better photocatalytic activity. FTIR spectra were used for the identification of the structural coordination and functional groups. The XRD, FTIR and EDS analyses confirmed the impurity free orthorhombic Bi_2MoO_6 NPs. The microwave-assisted combustion technique presented here seems an economical and easy way for the size and morphology control of such material.

Acknowledgements

Author(s) would like to acknowledge International Research Centre (IRC), Kalasalingam Academy of Research and Education and UGC-DAE-CSR, Kalpakkam Node (Ref.No. CSR-KN/CSR-103/2018-19/1042), Tamil Nadu, India for grants and study support.

References

- [1] C. Huang, J. Hu, S. Cong, Z. Zhao and X. Qiu, *Appl. Catal., B*, 174, (2015) 105.
- [2] W. Zhang, Q. Zhang and F. Dong, *Ind. Eng. Chem. Res.*, 52, (2013) 6740.
- [3] C. Chang, L. Zhu, S. Wang, X. Chu and L. Yue, *ACS Appl. Mater. Interfaces*, 6, (2014) 5083.
- [4] A. Kudo, K. Omori and H. Kato, *J. Am. Chem. Soc.*, 121, (1999) 11459.
- [5] A. Hameed, T. Montini, V. Gombac and P. Fornasiero, *J. Am. Chem. Soc.*, 130, (2008) 9658.
- [6] T. Zhou and J. Hu, *Environ. Sci. Technol.*, 44, (2010) 8698.
- [7] T. J. Park, G. C. Papaehymiou, A. J. Viescas, A. R. Moodenbaugh and S. S. Wong, *Nano Lett.*, 7, (2007) 766.
- [8] J. Zhang, C. Niu, J. Ke, L. Zhou and G. Zeng, *Catal. Commun.*, 59, (2015) 30.
- [9] X. Zhao, J. Qu, H. Liu and C. Hu, *Environ. Sci. Technol.*, 41, (2007) 6802.
- [10] N. Baux, R.N. Vannier, G. Mairesse, G. Nowogrocki, *Solid State Ionics* 91, (1996) 243.
- [11] M.S. Islam, S. Lazure, R.N. Vannier, G. Nowogrocki, G.J. Mairesse, *Mater. Chem.* 8, (1998) 655.
- [12] A. Shameem, P. Devendran, V. Siva, R. Packiaraj, N. Nallamuthu, S. Asath Bahadur *J. Mater. Sci. Mater. Electron.*, (30(4), (2019) 3305.
- [13] K. Seevakan, A. Manikandan, P. Devendran, A. Shameem, T. Alagesan, *Ceram. Int.*, 44, (2018) 13879.
- [14] K. Seevakan, A. Manikandan, P. Devendran, A. Baykal, T. Alagesan, *Ceram. Int.*, 44, (2018) 17735.
- [15] K. Seevakan, A. Manikandan, P. Devendran, Y. Slimani, A. Baykal, T. Alagesan, *Ceram. Int.*, 44, (2018) 20075.
- [16] L. Zhang, T. Xu, X. Zhao, Y. Zhu, *Appl. Catal., B* 98 (2010) 138.
- [17] M. Maczka, W. Paraguassu, A.G. Souza Filho, P.T.C. Freire, J. Mendes Filho, J. Hanuza, *Phys. Rev. B*, 77, (2008) 094137.

PREPARATION AND CHARACTERIZATION OF AMINO ACID ADDED Na⁺ ION CONDUCTING POLYMER BLEND ELECTROLYTE

V. Srividhya Devi¹, S. Shenbagavalli¹, K. Sundaramahalingam², N. Nallamuthu^{2*}, S. Jayanthi^{1*}

¹Department of Physics, The Standard Fireworks Rajaratnam College for Women, Sivakasi – 626 123. Tamil Nadu, India.

²Department of Physics, Kalasalingam Academy of Research and Education, Krishnankoil – 626 126. Tamil Nadu, India.

*E-mail: nnallamuthu@gmail.com; jayanthi-phy@sfrcollege.edu.in

Abstract

Sodium ion conducting polymer blend electrolytes composed of poly(vinyl alcohol) (PVA), poly(vinyl pyrrolidone) (PVP) as polymer hosts, sodium nitrate (NaNO₃) as an electrolyte with different concentrations of L-methionine have been prepared by traditional solvent casting technique. Double distilled water was used as a solvent. The as-prepared samples were subjected to AC impedance spectroscopy in the frequency range of 42 Hz to 1 MHz. Maximum ionic conductivity of 3.12*10⁻⁶ Scm⁻¹ has been obtained for the addition of 2.5 wt. % of L-methionine. Temperature dependent conductivity, Loss tangent spectra analysis, conduction spectra has also been carried out. Increase in ionic conductivity with the increase in temperature has been observed for all the samples and it seems to obey the Arrhenius behaviour.

Keywords: Solution casting technique, L-Methionine, Ionic Conductivity, Dielectric constant, Loss tangent.

1. Introduction

Polymer blending has received a great deal of attention in recent years since it possesses numerous advantages from other techniques like easy preparation and control of their physical properties within the miscibility compositional regime. Based on it, in the present work we have prepared polymer blend electrolytes consisting of poly(vinyl alcohol) (PVA), poly(vinyl pyrrolidone) (PVP) as polymer hosts, sodium nitrate (NaNO₃) as salt and an amino acid, L-methionine as dopant.

2. Experimental

2.1. Materials and Methods

Poly(vinyl alcohol) (PVA) with molecular weight of ~1,25,000 g and poly(vinyl pyrrolidone) (PVP) with molecular weight of ~90,000 g, were purchased from S. D. Fine 5 Chemicals Ltd., and both the polymers were used without further purification. The L-methionine salt (Merck) and sodium Nitrate (NaNO₃) (Merck) are used as raw materials to synthesis the blend polymer electrolyte.

2.2. Preparation of polymer electrolyte

The polymer electrolyte based on the composition of PVA/PVP/L-methionine and NaNO₃ were blended by solution casting technique using double-distilled water (D.D water) as solvent. Stoichiometric quantities of precursor materials, 50wt%PVA/50wt%PVP and 2wt% NaNO₃ dissolved in D.D water separately and the above all solutions were continuously stirred for 1 h at 40 °C to make the transparent solutions. The above PVP/PVA/NaNO₃ transparent solutions were mixed together with stirring until forming homogeneous blend solution. Then, the amino acid, L-methionine with various concentrations was dissolved in double-distilled water with vigorous stirring at room temperature for 24 hours. The obtained homogeneous solution, PVA/PVP/L-methionine/ NaNO₃ blend was poured then into polypropylene dishes and slowly dried at room temperature for 4 days. The obtained blend polymer film is peeled off from dishes for further studies. [1]

3. Results and Discussion

3.1. Ionic Conductivity studies:

The calculated values of ionic conductivity and the activation energy for

PVA/PVP/NaNO₃/L-methionine systems is shown in Figure 1.

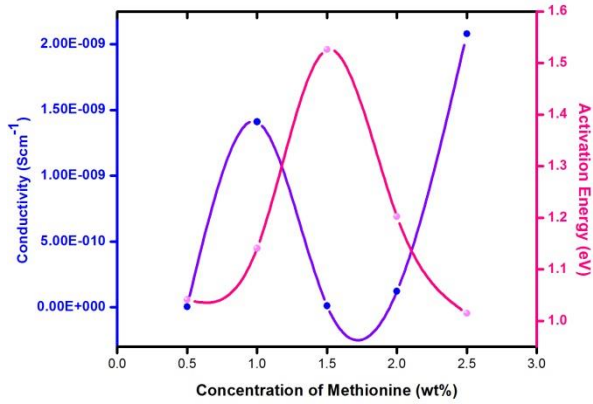


Figure 1 Conductivity Vs Activation energy of L-methionine system.

It is observed from the Figure 1, when the concentration of L-methionine increased from 1.5 wt.% to 2 and 1.5 wt.%, the value of ionic conductivity seems to increase by an order of magnitude. The increase in ionic conductivity is due to the increase in the number of mobile charge carrier and also the nature of the polymer blend electrolyte which reduces the energy carrier, there by facilitating the ion transport. [2]

Concentrations of L-methionine wt%	E_a (eV)
0.5	1.04
1	1.14
1.5	1.52
2	1.20
2.5	1.01

3.2. Temperature dependence of ionic conductivity

The temperature dependence of ionic conductivity for all the prepared system over the temperature 303 K to 363 K is shown in the Figure 2.

Ionic conductivity increases with the temperature for all the samples which implies that it obeys Arrhenius relation given below,

$$\sigma(t) = \sigma_o \exp[-E_a/KT] \dots (1)$$

where, σ_o is the pre-exponential factor, E_a is the activation energy for conduction, and K is the Boltzmann constant.

Arrhenius law states that the moment of the charge carrier from one site to its adjacent site without having acquired much energy.

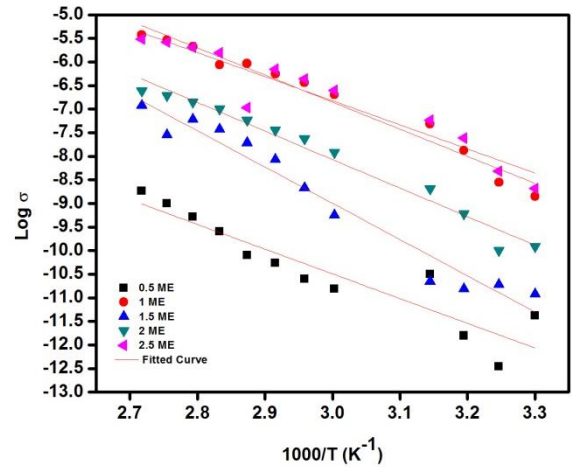


Figure 2 Variation of log σ with increase absolute temperature for PVA/PVP/NaNO₃/ L-methionine system.

The increasing ionic conductivity against the increase of temperature in solid polymer electrolyte enhance the segmental (i.e. polymer chain) motion, which resulting in an increase in the free volume of the system. Thus, the segmental motion either per

mits the ion to hop from one site to another or provides a pathway for ions to move. In other words, the segmental movement of the polymer facilitates, the translation ionic motion. From this, it is clear that the ionic motion is due to translation motion/hopping facilitated by the dynamics segmental motion of the polymer. As the amorphous region increase, the polymer chain acquires faster internal modes in which the bond rotations produced segmental motion to favor inter and intra chain ion hopping, and thus the value of ionic conductivity becomes high. [3] The activation energy (combination of energy for defect formation and the energy for migration of ion) is calculated for all the samples and is given in Figure 1. It can be seen from the figure 1, that the value of E_a of the system is found to low for the sample which possessed maximum ionic conductivity. This is due to the fact, as the temperature increase, it causes the expansion of polymer blend matrix and thus weakness the interaction within the polymer blend matrix. This initiates the decoupling of Na^+ ions from the polymer blend matrix. Besides, as the temperature is increased, the polymeric chain acquires faster internal modes and thus promotes the bond rotation, resulting in faster segmental mobility. Consequently, the intrachain and interchain and interchain ion hopping mechanisms are favorable which in turn result in higher ionic conductivity [3].

3.3. Conduction Spectra:

Conduction spectra for PVA/PVP/ $NaNO_3$ /2.5 wt% of L-methionine system. The conductance spectra can be divided into low frequency dispersion region, a frequency-independent plateau region in the mid frequency range and dispersive region at high frequencies is shown in Figure 3. [4]

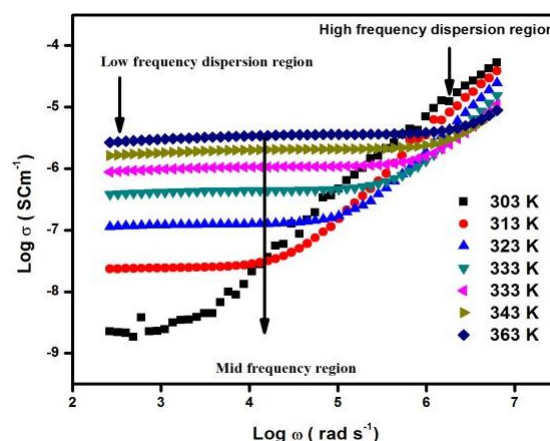


Figure 3 Log ω Vs Log σ for PVA/PVP/ $NaNO_3$ /L-methionine system at various temperatures.

3.4. Loss Tangent Spectra Analysis:

The dielectric loss tangent ($\tan \delta$) can be defined by the equation:

$$\tan \delta = \frac{\epsilon''}{\epsilon'}$$

The variation of $\tan \delta$ with frequency for all the prepared PVA/PVP/ $NaNO_3$ /2.5wt% of L-methionine at different temperatures was represented in Figure 4. It has been observed that $\tan \delta$ increases with increase in frequency and reaches a maximum value and decreases for further increase of frequency as per the Debye equation. [5]

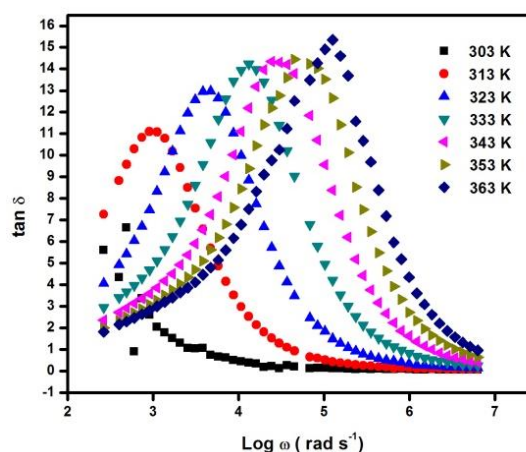


Figure 4: Loss tangent spectra of PVA/PVP $NaNO_3$ /2.5 wt% of L-methionine at various temperatures.

Conclusion

Solid Polymer blend electrolytes comprising of PVA, PVP, NaNO₃ with different concentrations of L-methionine were successfully prepared using solution casting technique. From the AC impedance analysis, maximum ionic conductivity $3.12 \times 10^{-6} \text{ Scm}^{-1}$ was observed for 2.5 wt.% of L- methionine added system. Temperature dependence of ionic conductivity seems to Arrhenius behavior. Low activation energy of 1.01eV was obtained for the sample which possessed maximum ionic conductivity.

REFERENCES

- [1] S. Jayanthi, K. Kulasekarapandian, A. Arulsankar, K. Sankaranarayanan, B. Sundaresan, *Journal of Composite Materials*, 49 (2015) 1035-1045
- [2] V. Parameswaran, N. Nallamuthu, P. Devendran, E.R. Nagarajan, A. Manikandan, *Physica B*, 515 (2017) 89-98.
- [3] D. Vanitha, S. Asath Bahadur, N. Nallamuthu, S. Athimoolam, *Ionics*, doi: 10.1007/s11581-017-2169-8.
- [4] V.Moniha, M.Alagar, S.Selvasekarapandian, B.Sundaresan,R.Hemalatha, G.Boopathi, *Journal of Solid State Electrochemistry*, doi: 10.1007/s10008-018-4028-6.
- [5] S.Gurulakshmi, S.Madewswaran, S.Karthikeyan, S.Selvasekarapandian and S.Monisha, *Recent Trends in Materials Science and Applications*, doi: 10.1007/978-3-319-44890-9_25.s

FUNCTIONAL AND AC IMPEDANCE ANALYSIS OF AMMONIUM THIOCYANATE DOPED PEO/PVP POLYMER BLENDS

K. Sundaramahalingam, M. Muthuvinaygam*, N. Nallamuthu, D. Vanitha

Department of Physics, International Research center
Kalasalingam Academy of Research and Education -626 126, India
*email: mmuthuvinayagam@gmail.com

Abstract

Proton conducting Poly ethylene oxide:Poly vinyl pyrrolidone polymer blend Electrolytes have been prepared by solution casting technique. The prepared solid electrolytes are characterized by FTIR and AC impedance analysis. The FTIR spectrum confirms the complexation between salt and polymers. The conductivity of the samples is analyzed by Impedance spectroscopy technique within the frequency range of 42Hz to 1MHz in the temperature range of 303K to 363K. The conductivity of Polymer electrolytes increases upto 20wt% of Ammonium thiocyanate concentration and the higher conductivity is found to be 2.62×10^{-4} S/cm at room temperature.

Keywords: PEO:PVP; AC impedance; Polymer blending; FTIR;

1. Introduction

In the recent years, polymer electrolytes are broadly considered because of their potential electro-chemical applications in batteries, energy units, super capacitors, electro-chromic sensors [1]. Polymer electrolytes have numerous points of interest such as adaptability, simplicity of processing into thin films, electrochemical strength and sealing nature [2]. There are few procedures used to prepare polymer electrolytes, for example, blending [3], co-polymerization, plasticization, addition of ceramic Nano fillers[4] to enhance the ionic conductivity of Polymer electrolytes.

Polymer blending is one of the viable ways to deal with diminishing the crystalline behaviour and improve the amorphous nature. Polymer blends frequently display properties that are better than the individual component polymers[13]

PEO is one of the semi-crystalline polymers, which has both crystalline and amorphous nature at room temperature[5]. Poor ionic conductivity ($10^{-8} - 10^{-7}$ S/cm) at surrounding temperature [7] and low cation transference number (<0.3) were the two noteworthy downsides acquired for PEO based Solid polymer electrolytes [7]. Yet, in room temperature, the ionic conductivity of PEO based polymer electrolytes are in the order of 10^{-7} to 10^{-8} S/cm [8, 9]. There are different ways to deal with the enhancement of ionic conductivity in PEO based electrolytes [10]. As of late, PEO has been widely contemplated as an electrolyte and separator materials because of its exceptional film forming capacity and good lithium

ion stability. The polymeric chain of PEO is equipped for wrapping around the lithium ion, making coordination bonds [11, 12]. It can solvate a wide assortment of salts even at high salt concentrations.

PVP is a unique one among the conjugated polymers as a result of its high amorphous nature that allows faster ionic mobility. The presence of the carbonyl group (C=O) in PVP leads to form variety of complexes with different inorganic salts and displays high Tg with great environmental, thermal and mechanical stability [14]. PVP is an Organic polymer to blend with polyethylene oxide to enhance the ionic conductivity of polymer electrolytes. It is an extraordinary conjugated polymer, on the grounds that PVP has high amorphous nature at room temperature. The another preferred point of PVP is that the formation of thermally cross connected polymer chain and accordingly, it has extraordinary thermal stability and high mechanical strength of blend materials [15-16]. In the present work, various of ammonium thiocyanate is mixed with PEO and PVP polymers.

2. Experimental

2.1. Preparation

PEO (Molecular weight 4×10^6 g/mol) is purchased from Aldrich chemicals USA, PVP (molecular weight, $M_w = 9 \times 10^5$ g/mol) is purchased from (S-d fine chem-Ltd), India and Ammonium thiocyanate of molecular weight $M_w = 76.117$ g is purchased from Merck, India. The solution casting technique is simple and flexible

method to prepare polymer electrolyte. Double distilled water is used as solvent. PEO, PVP and Ammonium thiocyanate are taken in the ratios of (30:70:5) (30:70:10) (30:70:15) (30:70:20) and (30:70:25). Initially the polymers PEO, PVP and Ammonium thiocyanate are dissolved in distilled water separately. Then it is mixed and stirred well. The resultant homogeneous solution is poured into petri dish and allowed for solvent evaporation.

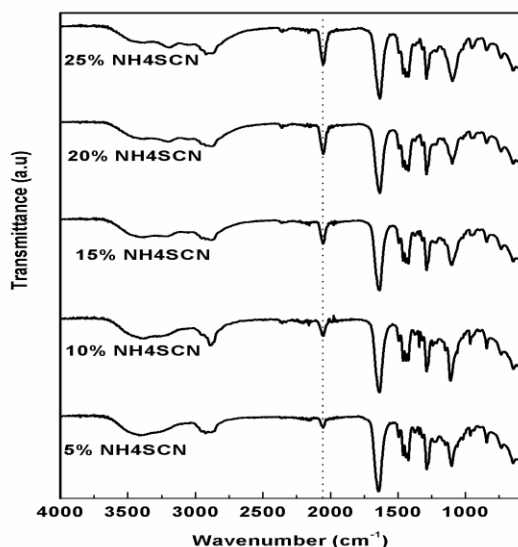
2.2. Characterization

The FTIR Transmittance spectra of the films are recorded using "SHIMADZU IR Tracer 100" Spectrometer with a resolution of 4 cm^{-1} . The spectra are obtained in the wave number range of $400\text{--}4000\text{ cm}^{-1}$. The impedance measurements are done by the computer controlled HIOKI 3532-50 LCR Hi-tester within the frequency range of 42Hz- 1MHz in the temperature range of 303K-363K.

3. Results and Discussion

3.1. FTIR

In the blend polymer electrolyte, there are two possible interactions for the cation (i) electron rich ether group of PEO, (ii) C=O of PVP. By the addition of the salt, the corresponding ion will approach the suitable coordinating site and thereby alter the environment of the polymer chain. From the figure, it is clearly observed



that the C=O shows minor shift and increase in intensity. Figure 1 shows the FTIR graph of different wt% NH_4SCN doped PEO/PVP.

A sharp band observed at 2893 cm^{-1} for pure PEO/PVP is due to the asymmetric CH stretching of CH_2 . The sharp band is decreased in intensity by increasing the concentration of PEO/PVP. The band observed at 1461 cm^{-1} is due to the CH_2 Scissoring mode of PEO. The C-O stretching vibration located at 953 cm^{-1} is associated with PEO with some CH_2 rocking asymmetric vibration. The vibration bands observed at 1282 cm^{-1} , 1348 cm^{-1} , 1461 cm^{-1} are assigned to CH_2 asymmetric twisting, CH_2 bending of PEO and CH_2 wagging, respectively. The band located at 834 cm^{-1} is owing to the CH_2 rocking mode of PVP with little bit contribution from C-O stretching mode of host polymer PEO. The absorption band located near 1461 cm^{-1} belongs to the CH_2 wagging of PVP. Furthermore, PVP presence is verified by the location of two strong absorption bands at 1349 cm^{-1} and 1687 cm^{-1} which corresponds to the C-N stretching and C=O stretching, respectively. FTIR wavenumbers and Corresponding assignments are tabulated in table 1.

Table 1: FTIR Assignments and corresponding wavenumbers

wavenumber	Assignments
956	CH_2 rocking asymmetric vibration
1283	CH_2 asymmetric twisting
1349	CH_2 bending of PEO
1461	CH_2 Scissoring mode of PEO
1639	C=O stretching
2893	asymmetric CH stretching of CH_2

In the present system two interactions are possible for the cation, when salt is added to the polymer blend then it will approach the suitable coordinating site and will alter the environment of the polymer chain. From the Figure 5 it is clearly visible that the C=O shows minor shift and decrease of intensity in peak position. The C-O-C stretching vibration band of PEO shows peak splitting in addition to salt in symmetric an asymmetric C-O-C stretching. Also, the shift in the wavenumber is noticeable which provides us strong evidence that the cation is going to coordinate with the electron-rich ether group of PEO.

3.2. Ac Impedance analysis

3.2.1. Cole-Cole plot:

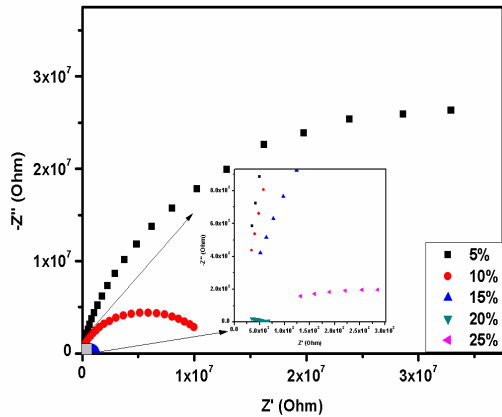


Figure 2. Cole cole plot for Different wt% of NH₄SCN with PEO/PVP polymer matrix.

The impedance plots for PEO/PVP/Xwt% Ammonium thiocyanate (NH₄SCN) polymer electrolytes at room temperature are shown in Figure.4. There is a semicircular portion in all the polymer systems. In the complex impedance representation, by increasing the salt concentration the bulk resistance of the films are decreased and the maximum bulk resistance reduction at 20wt% NH₄SCN added to the films. The semicircle in high frequency region corresponds to the bulk response of the films due to the parallel combination of resistance and a capacitance. The migration of ions and the polarization of immobile polymer chains produce the impedance effect from resistance and capacitance which represent the depressed semicircle [24]. The ionic conductivity is calculated by using the formula,

$$\sigma = l/R_b A \quad \dots \dots 1$$

where l-thickness of the film, A- area of the film and R_b-bulk resistance of the material.

3.2.2. Conductance Spectra

Figure 3, demonstrates the conductance spectra of 30%PEO/70%PVP mixed with different wt% of ammonium thiocyanate. The spectra give the frequencydependence of conductivity of the polymer blend.

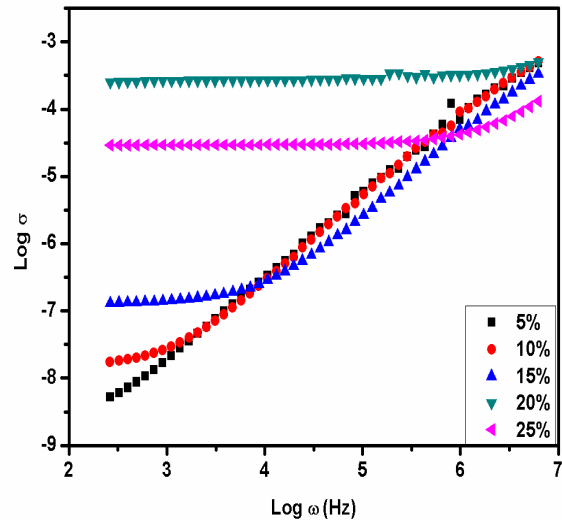


Figure 3. Conductance spectra for various wt% of NH₄SCN doped PEO/PVP polymer matrix.

The Characteristic conductance spectra consist of two distinct regions: the high frequency spike and frequency independent plateau region. The appearance of the spike is due to the bulk relaxation phenomena. The dc conductivity can be connected with the pleateau region. The conductivity can be obtained by extrapolating the plateau region on the log σ axis. For 20 wt% ammonium thiocyanate mixed with polymer electrolyte shows maximum higher conductivity of 2.62×10^{-4} S/cm at room temperature. For 25wt% Ammonium thiocyanate mixed with polymer electrolyte, it may have more voids with lower concentration and hence the conductivity is obtained minimum.

4. Conclusion

PEO/PVP/ammonium thiocyanate polymer electrolytes have beenprepared by solution casting in different compositions. FTIR spectroscopic analysis shows the presence of certain characteristic bands and there is an occurrence of shifting of bands with the increase in the salt concentration and confirm the complexation between polymers and salt. The impedance analysis shows the increase in conductivity with increase in both temperature and the lithium acetate doping level. The polymer electrolyte PEO/PVP/20 Wt% Ammonium thiocyanate has showed the higher conductivity of 2.62×10^{-4} S/cm. From the Conductance spectra, it is confirmed that the maximum conductivity is obtained for 20wt% NH₄SCN doped PEO/PVP.

5. Acknowledgements

The authors thank the management of Kalasalingam Academy of Research and Education for Providing facilities and fellowships to carry out the research.

REFERENCES

- [1] S. Ramesh, Geok Bee The, Rong-FuhLouh, Yong Kong Hou, Pung Yen Sin and Lim Jing Yi, Preparation and characterization of plasticized high molecular weight PVC based polymer electrolytes, Indian Academy of Sciences 35, (2010) 87-95,.
- [2] P. Santhosh, T. Vasudevan, A. Gopalan, and K. P. Lee, Preparation and properties of new cross-linked polyurethane acrylate electrolytes for lithium batteries, J. Power Sources, 160, (2006) 609-620.
- [3] S. Rajendran, R. Kannan and O. Mahendran, An electrochemical investigation on PMMA/PVdF blend-based polymer electrolytes, Mater Lett., 49, (2001) 172-179.
- [4] M. Sundar and S. Selladurai, "Effect of Fillers on MagnesiumPoly (Ethylene Oxide) Solid Polymer Electrolyte", Ionics, 12, (2006) 281- 286.
- [5] F.M. Gray, Solid Polymer Electrolytes, VCH, New York, 1991.
- [6] D.E. Fenton, J.M. Parker, P.V. Wright, Complexes of alkali metal ions with poly (ethylene oxide), Polymer 14, (1973) 589.
- [7] K. Kesavan&Chithra M. Mathew & S. Rajendran& C. Subbu& M. Ulaganathan, Solid Polymer Blend Electrolyte Based on Poly (ethylene oxide) and Poly (vinyl pyrrolidone) for Lithium Secondary Batteries, Braz J Phys 45, (2015) 19-27.
- [8] M Kovac, M Gaberscek, J Grdadolnik, The effect of plasticizer on the microstructural and electrochemical properties of a (PEO)_nLiAl(SO₃Cl)₄ system, ElectrochimActa 44, (1998) 863.
- [9] Ghosh A, Kofinas P ECS Trans 11 (2008) 131.
- [10] Z. Ahmad, N.A. Al-Awadi, F. Al-Sagheer, Morphology, thermal stability and visco-elastic properties of polystyrene-poly(vinyl chloride) blends, PolymDegrad Stab 92 (2007) 1025,.
- [11] P.G. Bruce, Solid state electrochemistry (Cambridge University Press, Cambridge, pp. 344, 1995.
- [12] Y.G. Andreev, P.G. Bruce, Polymer electrolyte structure and its implications, Electrochim. Acta 45, (2000) 1417.
- [13] D.A.J. Rand, J. Power Sources 4, (1979) 01.
- [14] K. KiranKumar, M. Ravi, Y. Pavani, S. Bhavani, A.K. Sharma, V.V.R. NarasimhaRao, Investigations on the effect of complexation of NaF salt with polymer blend (PEO/PVP) electrolytes on ionic conductivity and optical energy band gaps, Phys. B 406, (2011) 1706.
- [15] J.J. Zieba, Y. Zhang, P.N. Prasad, Sol-gel-processed inorganic oxides: organic polymer composites for second-order nonlinear optical applications, Sol-Gel optics II 1758, (1992) 287.
- [16] Hew-Der Wu, I-Der Wu, Feng-Chih Chang, the interaction behavior of polymer electrolytes composed of poly (vinyl pyrrolidone) and lithium perchlorate (LiClO₄), Polymer 42 (2001) 555.

ELECTRICAL IMPEDANCE STUDIES OF PVA-PVP- Na_2SO_4 POLYMER ELECTROLYTES FOR SOLID STATE BATTERY APPLICATION

B. J. Gogoi¹, K. Sundaramahalingam², N. Nallamuthu², A. Murugan^{1*}

¹Department of Chemistry, North Eastern Regional Institute of Science and Technology, Nirjuli, Arunachal Pradesh, India.

²Department of Physics, School of Advanced Sciences, Kalasalingam Academy of Research and Education, Krishnankoil, Srivilliputtur, Tamilnadu, India.

*Corresponding author. E-mail: amu@nerist.ac.in

Abstract

Sodium (Na) based rechargeable batteries (SIBs) have now captured much attention due to its environmentally friendly nature, non-toxic and moreover low cost and abundant materials. PVA and PVP blended polymer doped with different concentrations of sodium sulphate (Na_2SO_4) have been prepared by the solution casting method. Cole-cole plot showed the depressed semicircles. Electrical impedance and conductivity studies are also analyzed to sodium sulphate mixed blend polymer matrices. The highest conductivity is observed as $2.4 \times 10^{-7} \text{Scm}^{-1}$ for 8% Na_2SO_4 doped PVA-PVP polymer sample.

Keywords: polymer blend, solution casting method, PVA/PVP, ac impedance, sodium sulphate.

1. Introduction

Access to energy is a key pillar for human wellbeing, economic development and poverty alleviation[1]. However, our present energy systems have important environmental impacts. If we are to meet our global climate targets and avoid dangerous climate change, the world needs a significant transition to an environmental friendly energy sources. Among various environment friendly energy sources, solid state batteries (SSBs) have become one of the strong candidates for energy source.

Solid state batteries (SSBs) uses solid electrolytes have attracted great importance throughout the world for last several years[2,3]. The conventional liquid electrolyte based batteries have various inherent disadvantages like limited life time, time consuming charging-discharging, limitation of the temperatures and vibrations resulting in potential dangerous leakages, flammable and toxic [4,5]. The SSBs not only eliminate the above limitations of liquid electrolyte based batteries, but also having maximum energy density. SSBs can be scalable and have the potential to be ultra-small in size with high density – enabling them to store twice as much energy as liquid electrolyte based battery in the same area. Solid-state battery technology is not only used for faster recharging for electric vehicles and consumer electronics but also grid energy storage, medical devices and avionics.

Recent work on rechargeable, all-solid-state alkali-metal batteries has advanced the technology to a point

where applications through the whole battery product range can be envisaged. Although significant progresses have been achieved in the field of lithium ion batteries (LIBs) as a promising energy storage device [6,7,8], their high cost, less abundance, environmental impact and safety limitations impede the widespread implementation of lithium insertion materials in future battery technologies[9-11]. Therefore, there is urgent necessity to search for alternative energy storage system technology capable of complementing the current Li-ion battery technology. Amongst the accessible battery chemistries, sodium (Na) based rechargeable batteries (SIBs) have now captured much attention due to its environmentally friendly nature, non-toxic and moreover low cost and abundant materials [12,13] and thus can be used in large or medium scale industries.

The electrolyte cum separator between two electrodes is an essential component of the battery plays a significant role in the transportation of ions during charging and discharging processes, so it must be in stable form during battery operation. Solid polymer electrolytes (SPEs) have attracted great scientific interest during the last two decades because of their numerous potential applications in various advanced devices including solid-state batteries, fuel cells, electrochemical display devices/smart windows, photo-electrochemical cells etc.[14-16], due to their high conductivity, high energy density, wide electrochemical stability and easy processibility[17]. SPEs exhibits various advantages like easy to prepare, light weight, easy to handle, flexible in shape and size, good mechanical strength, shows good

electrode-electrolyte contact and do not show any signs of electrode corrosion[18-20].

Poly vinyl alcohol (PVA) is a semicrystalline polymer studied extensively because of its many interesting physical properties which arise from the hydrogen bond formation due to the presence of $-OH$ groups. Poly vinyl pyrrolidone (PVP) is a biopolymer with higher order of amorphosity, deserves a special attention among the conjugated polymers because of its good environmental stability, easy processability and moderate electrical conductivity. The semicrystalline nature of PVA at room temperature, subsequently limits its ionic conductivity. One of the alternate way to enhance the amorphous nature of PVA based electrolyte systems is to blend with amorphous PVP polymer[21]. The interactions between PVA and PVP is expected to occur through interhydrogen bonding between the carbonyl($C = O$) group of PVP and the hydroxyl ($-OH$) group of PVA. In the present study, PVA and PVP blended polymer doped with different concentrations of sodium sulphate (Na_2SO_4) have been prepared by the solution casting method. Electrical Impedance and conductivity studies are analysed to Sodium sulphate mixed blend polymer matrices.

2. Experimental Methods and Characterisation

Solution casting method is the easiest method to prepare the PVA and PVP blended gel matrices. Analytical grade of Polyvinyl alcohol, polyvinyl pyrrolidone and sodium sulphate are acting as a precursor to make the polymer film through solution casting method. Stoichiometric amount of PVA, PVP and Sodium sulphate were dissolved in double distilled (DD) water in separate beakers. Initially aqueous solutions of PVA and PVP were mixed. After half an hour string the previous mixed solution, sodium sulphate solution was added into the above solution drop wise at room temperature. After the complete addition, solution was stirred constantly for 5 hours. The solution was converted into gel. The gel was dried at $80^\circ C$ to form transparent film. Electrical impedance and conductivities have studied for solid state battery applications.

3. Results and discussion

3.1. Electrical Impedance

Impedance spectroscopy is used to analyse the microstructure of the blend polymer samples. The cole –cole plot showed the semicircles as displayed in the figure. The obtained depressed semicircles are attributed to the parallel combination of resistance and capacitance.

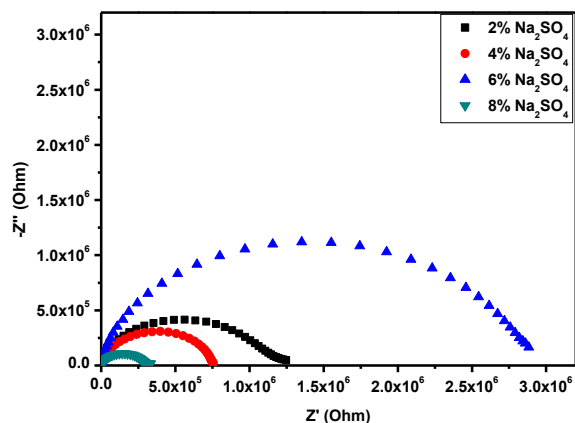


Fig. 1 cole-cole plot of Na_2SO_4 doped PVA-PVP polymer sample

The lower impedance is observed for 8% Na_2SO_4 doped PVA-PVP polymer sample. The electrical conductivity is calculated using measured impedance data by the following equation

$$\sigma = l/RA$$

Where R - measured impedance, l - thickness of the materials and A – cross sectional area of the sample. The electrical conductivity is calculated as $2.4 \times 10^{-7} Scm^{-1}$ for 8% Na_2SO_4 doped PVA-PVP polymer sample.

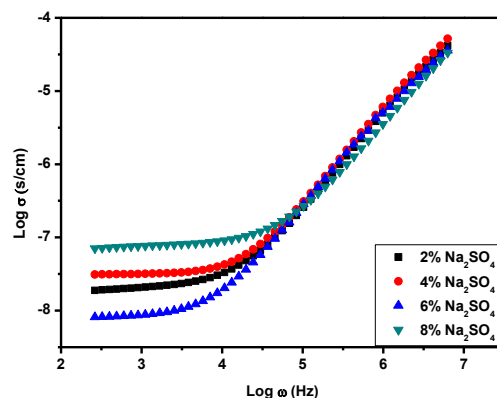


Fig. 2. Frequency dependent conductivity of Na_2SO_4 doped PVA-PVP polymer sample

Fig. 2. Shows the frequency dependent conductivity of Na_2SO_4 doped PVA-PVP polymer sample. It showed plateau region at lower frequency and dispersion region at higher frequency. The dc conductivity observed at lower frequency is highest for 8% Na_2SO_4 doped PVA-PVP polymer sample.

The ionic polarization is involved in the blend polymer sample. The sodium ions are mobilised inside

the materials and accumulated at the interfacial region of the materials. Hence, the dielectric constant is high at lower frequency due to space charge polarization of the materials. In the modulus spectra, the space charge polarization is suppressed and the curve is formed in the electric modulus which is related to the ionic relaxation of the materials.

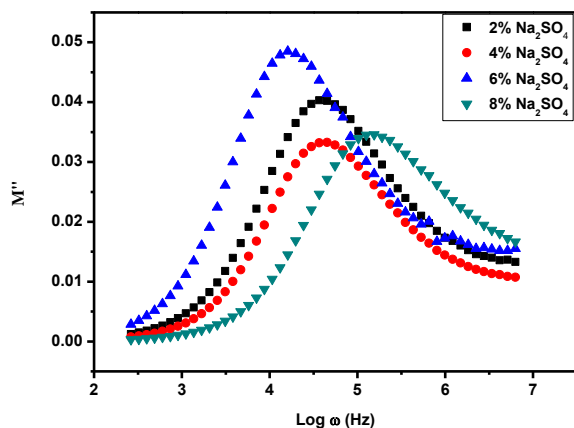


Fig. 3. Frequency dependent electric modulus of Na_2SO_4 doped PVA-PVP polymer sample

4. Conclusion

The solid polymers at various composition of Na_2SO_4 doped PVA-PVP polymer sample are prepared by solution casting method. After the polymer samples are confirmed by several characterizations, the electrical impedance and conductivities are analyzed. The highest conductivity is observed as $2.4 \times 10^{-7} \text{ Scm}^{-1}$ for 8% Na_2SO_4 doped PVA-PVP polymer sample. This 8% Na_2SO_4 doped PVA-PVP polymer is applicable for fabrication of solid state battery.

5. Acknowledgements

Authors would like to gratefully acknowledge Kalasalingam Academy of Research and Education (KARE) for constant support to this research work.

REFERENCES

- [1] Panos E, Densing M, Volkart K (2016) Access to electricity in the World Energy Council's global energy scenarios: An outlook for developing regions until 2030. *Energy Strategy Reviews* **9** 28-49.
- [2] Reisch Marc S (20 November 2017) Solid-state batteries inch their way toward commercialization. *Chemical & Engineering News* **95** 46 19-21
- [3] Vandervell Andy (26 September 2017) What is a solid-state battery? The benefits explained. *Wired UK*. Retrieved 7 January 2018.
- [4] A Manuel Stephan, K S Nahm (2006) *Polymer* **47** 5952-5964.
- [5] A R Kulkarni (2002) *Solid State Ionics, Proc. Asian Conf.*, 8th, 273-282
- [6] Boschini A, Johansson P (2015) *Electrochimica Acta* **175** 124
- [7] Yoshino A (2012) *Angew Chemie-International Ed.* **51** 5798
- [8] Zhou G, Li F F, Cheng H M (2014) *Energy Environ. Sci.* **7** 1307
- [9] Vikström H, Davidsson S, Hook M (2013) *Appl. Energy* **110** 252
- [10] Palomares V, Serras P, Villaluenga I, Hueso K B, Carretero-Gonzalez J, Rojo T (2012) *Energy Environ. Sci.* **5** 5884
- [11] Vignaroban K, Kushagra R, Elango A, Badami P, Mellander B.-E, Xu X, Tucker T G, Nam C, Kannan A M (2016) *International Journal of Hydrogen Energy* **41** 2829
- [12] Ni'mah Y L, Cheng M Y, Cheng J H, Rick J, Hwang B J (2015) *J. Power Sources* **278** 375
- [13] Wang L, Lu Y, Liu J, Xu M, Cheng J, Zhang D, Goodenough J B (2013) *Angew. Chem.* **52** 1964
- [14] Yang X F, Wang G C, Wang R Y, Li X W (2010) *Electrochim Acta* **55** 5414-5419.
- [15] Wright PV (1975) *Polymer* **7** 319-326
- [16] Armand MB, (1983) *Solid State Ionics* **9** 745-751
- [17] Takada N, Koyama T, Suzuki M, Kimura M, Hanabusa K, Shirai H, Miyata S (2002) *Polymer* **43** 2031
- [18]. Scrosati B (1993) In: Scrosati B (ed) *Applications of electroactive polymers*. Chapman and Hall, London, pp. 354-360
- [19]. Sekhon S S, Kumar M (2002) Plasticized proton conducting polymer electrolytes based on polyethylene oxide and ammonium salts NH_4X : $\text{X} = \text{F}^-$, BF_4^- . *Proceedings of 8th Asian Conference on Solid State Ionics - Trends in the New Millennium*, pp. 377-384, World Scientific Singapore
- [20]. Kuila T, Achaya H, Srivastava SK, Samantaray BK, Kureti S (2007) *Mater Sci and Engg B* **137** 217-224
- [21] Kim D W, Park J K and Rhee H W 1996 *Solid State Ion.* **83** 49

SYNTHESIS OF SURFACE MODIFIED TiO₂ NANO CRYSTALLITES WITH Ag NANOPARTICLE

S.Babu, Rajajeyaganthan Ramanathan

Department of Chemistry, Kalasalingam Academy of Research and Education, Krishnankoil, TN, India – 626 126

Email: rajajeyaganthan.r@klu.ac.in

Abstract

Surface modification is a group of techniques to modify the surface of the cheap bulk material and to bring the desired properties on its surface. Lot of surface modification methods is followed to change the surface properties of the bulk material. In this study, the surface of TiO₂ nano crystallites was modified with Ag by direct reduction of AgNO₃ using NaBH₄. Different concentration of reduced Ag nano particles was used to modify the surface of the TiO₂ nano crystallites. The loading concentration of Ag nano particles on TiO₂ nano crystallites, imparts different color on TiO₂ nano crystallites. This kind of surface modified TiO₂ nano crystallites finds many applications in solar cells and photocatalytic activity.

Keywords: Anatase, Nano crystallites, TiO₂, Ag

1. Introduction

The anatase phase TiO₂ most used in solar cells due to its high activity in UV region of solar spectrum, high stability, low toxicity and low cost. Researches have proved that the doping of transition metals can modify the band gap and leads to tuning of its performance when used in photovoltaic cells.[1-4] Among the other noble metals, silver ions are attracted particularly as dopant in DSSC applications due to their electron transport effects, easy preparation and low cost [5,6]. Silver (Ag) is used to modify the surface of anatase TiO₂ and originate the defects in the Ti lattice, such as oxygen vacancies and surface related defects which enable an efficient charge separation [7, 8]. This work is to synthesis of surface modified TiO₂ nano crystallites with Ag nanoparticle of different concentration which can be used for solar cell and photocatalytic activities.

2. Experimental

2.1. Preparation of Ag coated TiO₂ nano crystallites:

Ag coated TiO₂ nano crystallites were prepared by reducing silver nitrate to silver using sodium borohydride on TiO₂ nano crystallites. About 0.2 g of TiO₂ nano crystallites (Aeroxide P25, 99.5% pure and 21 nm particle size) was slowly added to 50 ml of freshly prepared sodium borohydride solution (1.58 x 10⁻² M) taken in a round bottom flask. The addition of TiO₂ nano crystallites to sodium borohydride solution was carried out while stirring and it was stirred continuously throughout

the experiment. For the preparation of Ag coated TiO₂ nano crystallites, the round bottom flask was kept in an ice bath and silver nitrate solution (7.06 x 10⁻² M) was added slowly at the rate of 1 drop per 5 seconds with continuous stirring. The color change was observed depends on the amount of silver nitrate solution added to the TiO₂ – sodium borohydride solution. The solution was stirred for about 12 hours and the Ag coated TiO₂ nano crystallites were separated from the solution by centrifugation. The centrifuged Ag coated TiO₂ nano crystallites were washed thrice with de-ionized water to make it free from sodium borohydride solution. The washed Ag coated TiO₂ nano crystallites was air dried initially and finally dried at 60°C for an hour. Four different samples of Ag coated TiO₂ nano crystallites were prepared of using this methodology. The percentage of silver on four different samples of Ag coated TiO₂ nano crystallites was 1 %, 2 %, 3 %, 4 % and 15%, respectively.

2.2. Characterization techniques:

The powder X-ray diffraction was performed (SEIFERT JSO-2002) using Cu-K_{α1} radiation with the diffraction angle 2θ of 20°–80° and analyzed with XRDA 3.1 software. To understand the presence of functional groups in the prepared samples, Fourier transform infrared spectra (FT-IR, PERKIN ELMER SPECTRUM1) was recorded in the range of 450-4000 cm⁻¹.

2.3. Structural analysis: X-ray diffraction

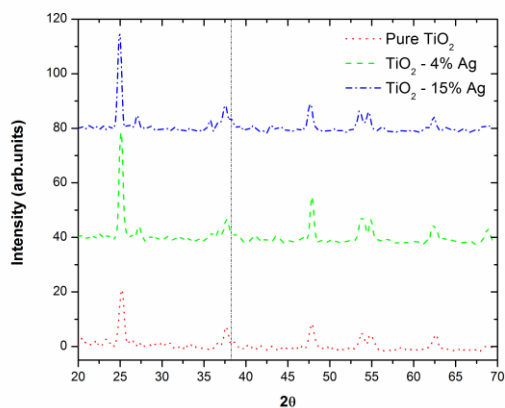


Figure 1. XRD pattern of TiO₂ nano crystallites and Ag:TiO₂ nano crystallites

2.4. Functional group analysis: FT-IR

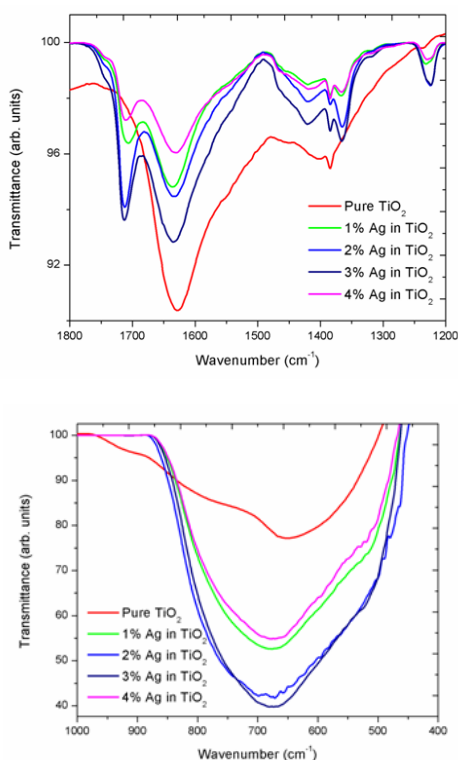


Figure 2. FT-IR spectra of TiO₂ nano crystallites and Ag:TiO₂ nano crystallites

3. Results and Discussion

To investigate the effect of Ag surface doping on the crystal structure of TiO₂ were analyzed by XRD, and the results are shown in figure 1. The diffraction peaks at $2\theta = 25.28^\circ, 37.80^\circ, 48.05^\circ, 53.89^\circ$ and 55.06° assigned to anatase phase of TiO₂ (JCPDS: 21-1272) for both pure and Ag-doped samples. The additional peaks appeared at $27.47^\circ, 36.02^\circ, 41.20^\circ$ and 54.32° corresponds to rutile phase (JCPDS: 065-1119) of TiO₂ which found to be more in Ag doped TiO₂. The characteristic peak for metallic silver was not found in 1%, 2% and 3% Ag surface doped samples owing to low Ag concentration in TiO₂ matrix. But, 4% and 15% Ag surface doped samples showed diffraction peak at 38.08° peak of (111) plane. The FTIR spectrum of pure and Ag:TiO₂ nanoparticles were given in figure 2. It is well known that the broad band centred at $500\text{--}650\text{ cm}^{-1}$ confirms the presence of metal oxide (Ti–O–Ti) bonding. The peaks of Ag:TiO₂ is deviated to 1630 cm^{-1} and the peak intensity at 3450 cm^{-1} becomes slightly smaller after surface doping with Ag nanoparticles compared with pure TiO₂.

4. Conclusion

Ag surface doped TiO₂ nanoparticles were prepared by sodium borohydride assisted simple reduction method. The color changes from white (pure TiO₂) to pale yellow, yellow, brown, red and dark red for 1%, 2%, 3%, 4% and 15%, respectively for surface loading of Ag on TiO₂. The maximum efficient loading of Ag is upto 3% and after that the loading is not possible due to agglomeration of Ag nanoparticles and turn to grayish black color on storage.

REFERENCES

- [1] Lei X F *et al* 2014 *Appl. Surf. Sci.* **321** 396
- [2] Grover I S *et al* 2013 *Appl. Surf. Sci.* **280** 366
- [3] Junlabhuth P *et al* 2016 *Surf. Coat. Technol.* **306** 262
- [4] Arun Kumar D *et al* 2012 *Appl. Nanosci.* **2** 429
- [5] Nainani R *et al* 2012 *J. Mater. Sci. Eng.* **2** 52
- [6] Lee M S *et al* 2005 *J. Mol. Catal. A: Chem.* **242** 135
- [7] López Ortiz A *et al* 2015 *Int. J. Hydrog. Energy* **40** 17308
- [8] Roose B *et al* 2015 *Chem. Soc. Rev.* **44** 8326

INVESTIGATION OF Mn₃O₄ NANOPARTICLES DECORATED ON CARBON SPHERES BY HYDROTHERMAL METHOD

V. Selva barathi, S. Saraswathi, M. Sindukavi, S. Ezhilarasi, R. Ranjith kumar, C.Sambathkumar, A. Arivarasan, N. Nallamuthu, S. Asath Bahadur, P. Devendran*

Department of Physics, International Research Center, Kalasalingam Academy of Research and Education, Krishnankoil - 626 126, Tamilnadu, India.

Email: pdevavenmani@gmail.com

Abstract

Pure carbon sphere (CS) and Mn₃O₄ nanoparticles (NPs) decorated on uniform carbon spheres were synthesized by facile hydrothermal method. The prepared sample was studied with structural, functional groups, and morphological properties by XRD, FTIR and SEM analysis respectively. The average particles size and morphology of both bare CS and Mn₃O₄ NPs coated carbon spheres were determined through XRD and SEM analysis. This carbon based Mn₃O₄ nanocomposites may lead to enhanced electrochemical activities due to high porous nature.

Keywords: Mn₃O₄, Mn₃O₄@CS, Hydrothermal, Carbon Spheres, nanocomposites.

1. Introduction

There is a growing interest in the field of nanotechnology and nanomaterials in past few decades. Among various segregations, the transition metal oxides were of significant interest for the researches as it contains an excellent physico-chemical property that paves way for various applications [1, 2]. The preparation of nanomaterials in the few nanometric sizes would enhance the additional properties that are possessed by the material. The various form of carbon derivatives is getting much interest among researchers working on nanotechnology field [3, 4]. Carbon sphere is the recently discovered material that contains unique physical properties and outstanding mechanical properties [5]. A wide range of potential for technological applications including electron field emitters, gas sensor, nano-electronic devices, energy storage devices such as supercapacitor have been demonstrated [6]. Carbon sphere can be synthesized by various methods such as arc discharge, laser ablation chemical vapor deposition methods, and hydrothermal respectively [7, 8]. Comparing all other techniques, the hydrothermal synthesis is simple user-friendly method.

In this present work, the both pure CS and Mn₃O₄ NPs coated on the uniform size and shaped carbon spheres were prepared through hydrothermal technique. The prepared material was undergone few analytical techniques to study the basic properties. With the help of powder XRD the structural parameters is determined. The molecular and atomic bond interactions such as bending, stretching vibrations is studied using FTIR spectral analysis. The appearance, sphere size and surface morphology of the pure CS and Mn₃O₄ wrapped carbon sphere were

examined through SEM analysis.

2. Experimental

2.1. Materials

Glucose, MnCl₂, NaOH and ethanol were purchased from Sisco Research Laboratories (SRL) Pvt. Ltd., Mumbai, India. Analytical grade chemicals with high purity of 99% were used. Ultra-pure Millipore deionized (DI) water was used as a solvent for whole reaction.

2.2. Preparation

The bare carbon sphere was synthesized using 1M of glucose. It was dissolved in 125 ml of DI water and continuously stirred until the reaction mixture gets saturated. Then the solution was transferred into the 150 ml autoclave and kept undisturbed in oven at about 180° C for 12h. The obtained bare carbon sphere was cleaned and washed by centrifuging with DI water and ethanol for several times to remove extra additives. Following this, the sample was dried overnight in hot air oven at 80° C. The Mn₃O₄ coated carbon sphere was prepared by taking prepared bare carbon sphere and MnCl₂ in the equimolar ratio of 0.05M in 125 ml DI water. The reaction mixture was kept in magnetic stirring for about 30 min. After complete dispersion and dissolution of bare carbon sphere and MnCl₂ in the solvent, 1 M of NaOH was added. Then the same procedure was carried out as like as the bare carbon sphere.

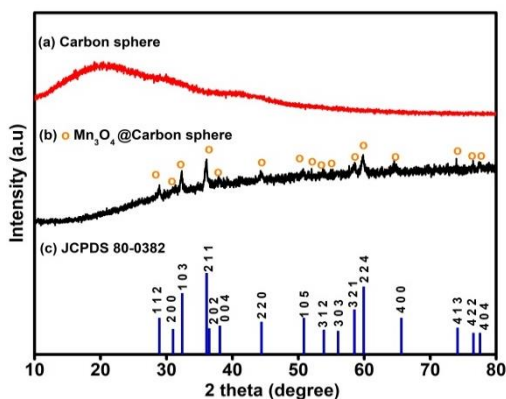
2.3. Structural characterization

Powder X-ray diffraction analysis using Bruker X-ray diffractometer (D8 advance ECO) with monochromatic Cu-K α radiation containing 1.5406 Å wavelengths, the crystal structure was determined. To study functional groups of the prepared sample Fourier transform infrared spectrometer (FTIR) were employed using a Shimadzu (IR Tracer-100) spectrophotometer within the range of 4000–400 cm $^{-1}$ using KBr pellet system. Bare CS and Mn $_3$ O $_4$ covered carbon sphere formation was confirmed through the morphological using Scanning Electron Microscope (SEM, ZEISS-EVO 18 Research, Japan).

3. Results and Discussion

3.1. Powder XRD analysis

Figure 1 shows the powder XRD pattern of prepared (a) bare carbon sphere (b) Mn $_3$ O $_4$ covered carbon sphere. The PXRD pattern of carbon sphere was observed as a hump at 2 theta value of 20° shown in figure 1(a). The 2 theta values were fixed between 10–80°. The crystalline peaks of Mn $_3$ O $_4$ were perfectly matched with the standard JCPDS card number 80-0382 depicted in figure 1(b). Tetragonal structure with space group I41/amd (141) was obtained. The maximum diffraction peaks were observed in 32.3, 36.0, 58.5, 59.9, 65.6° with corresponding hkl indices (211), (103), (224), (400), (112). The crystallite size of prepared bare and Mn $_3$ O $_4$ coated carbon sphere were calculated



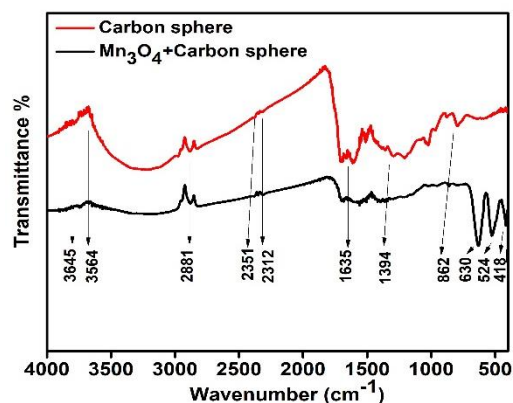
through Scherrer formula and was found to be ~30 nm.

Figure 1. XRD patterns of (a) bare carbon sphere and (b) Mn $_3$ O $_4$ coated carbon sphere

3.2. FTIR analysis

The presence of functional groups metal ions interactions with bending and stretching vibrations between the molecules were examined using FTIR analysis. The figure 2 reveals the FTIR spectra of

(a) bare carbon sphere (b) Mn $_3$ O $_4$ covered carbon sphere. In finger print region, the metal oxide interactions i.e., Mn-O bond vibrations were observed in peaks 630, 524, and 418 cm $^{-1}$. In the wavenumber between 2881 cm $^{-1}$ the C-H bond stretch were seen. The triple bond formation of carbon-carbon atom was observed in peaks 2351



and 2312 cm $^{-1}$. C=C, C=O bond interactions were noted in peaks 1635 and 1394 cm $^{-1}$.

Figure 2. FTIR spectra of (a) bare carbon sphere and (b) Mn $_3$ O $_4$ NPs coated on carbon sphere

3.3. SEM analysis

The figure 3 reveals the (a) bare carbon sphere (b) Mn $_3$ O $_4$ coated carbon sphere. The spherical formation of carbon sphere was witnessed from this image 3 (a). The Mn $_3$ O $_4$ coating was clearly observed on the surface of the carbon sphere in the figure 3 (b). The result clearly state that the sphere shaped particles were formed and the Mn $_3$ O $_4$ nanoparticles were wrapped as the outer cover uniformly.

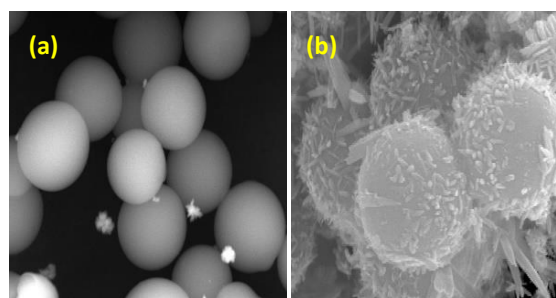


Figure 3. SEM images of (a) pure carbon sphere and (b) Mn $_3$ O $_4$ NPs coated on carbon sphere

4. Conclusion

In summary, the carbon sphere both bare and Mn $_3$ O $_4$ coated carbon sphere were prepared by facile hydrothermal method. The crystal structure of prepared Mn $_3$ O $_4$ material was found to be tetragonal structure that has wrapped on the surface of the

carbon sphere were confirmed through SEM analysis. The diameter of both bare and Mn_3O_4 wrapped carbon sphere were found to have slight difference which further proved the coating of nanomaterial on the outer surface of carbon sphere. The functional groups with C-C and metal oxide bond interactions were clearly observed through FTIR analytical technique.

5. Acknowledgements

The authors show their gratitude to IRC, Kalasalingam Academy of Research and Education (KARE) for providing research facilities and thankful for funding under the University Research Fellowship (URF) scheme.

REFERENCES

- [1] Jason F. Weaver, Surface Chemistry of Late Transition Metal Oxides, *Chem. Rev.*, 2013, 113 (6), pp 4164–4215. DOI: 10.1021/cr300323w
- [2] Yan Wang, Jin Guo, Tingfeng Wang, Junfeng Shao, Dong Wang and Ying-Wei Yang, Review Mesoporous Transition Metal Oxides for Supercapacitors, *Nanomaterials* 2015, 5, 1667-1689; doi:10.3390/nano5041667
- [3] Shinae Jun, Sang Hoon Joo, Ryong Ryoo, Michal Kruk, Mietek Jaroniec, Zheng Liu, Tetsu Ohsuna, and Osamu Terasaki, Synthesis of New, Nanoporous Carbon with Hexagonally Ordered Mesostructure, *J. Am. Chem. Soc.*, 2000, 122 (43), pp 10712–10713.
- [4] Li Li Zhang and X. S. Zhao, Carbon-based materials as supercapacitor electrodes, *Chem. Soc. Rev.*, 2009, 38, 2520–2531
- [5] Z H Han, B Yang, S H Kim and M R Zachariah, Application of hybrid sphere/carbon nanotube particles in nanofluids, *Nanotechnology* 18 (2007) 105701 (4pp). doi:10.1088/0957-4484/18/10/105701
- [6] Yuanzhu Mi, Weibing Hu, Youmeng Dan, Yingliang Liu, Synthesis of carbon micro-spheres by a glucose hydrothermal method, *Materials Letters* 62 (2008) 1194–1196.
- [7] G. Wu, Y. Cheng, Y. Ren, Y. Wang, Z. Wang, H. Wu, Synthesis and characterization of $\gamma\text{-Fe}_2\text{O}_3\text{/C}$ nanorod-carbon sphere composite and its application as microwave absorbing material, *Journal of Alloys and Compounds* (2015), doi: 10.1016/j.jallcom.2015.08.236.
- [8] N. Q. Lich, P. Q. Pho, L. H. Bac, and N. H. Lam, Structural characterization of carbon spheres and carbon nanotubes, Proceedings of the 1 IWOFN-3 IWONN Conference, Halong, Vietnam, December 6-9, 2006.

STRUCTURAL AND IMPEDANCE STUDIES ON POLYVINYL ALCOHOL AND CORNSTARCH BLEND POLYMER ELECTROLYTES

M. AnandhaJothi, D. Vanitha*, S. AsathBahadur

Department of Physics, Kalasalingam Academy of Research and Education, Krishnankoil, Tamil Nadu, India

*Email: vanibala2003@gmail.com

Abstract

Biopolymer based Solid polymer blend electrolytes have been prepared using Poly vinyl alcohol (PVA) and Corn Starch (CS) by solution casting technique. The prepared electrolytes are characterized by XRD, FTIR and Impedance analysis. The structural characteristic of PVA and CS blend Polymer Electrolytes (PEs) are analysed by XRD. The interaction between PVA and Corn Starch is studied by FTIR analysis. The prepared samples are analysed by using the Impedance spectroscopy in the frequency range of 40Hz-1MHz. The combination of 60wt% PVA and 40wt% Corn Starch is having the high conductivity ($1.5 \times 10^{-9} \text{ S cm}^{-1}$) and low activation energy. The variations in conductivity with temperature follow the Arrhenius behaviour.

Keywords: PVA, Corn Starch, XRD, FTIR and Conductivity studies

1. Introduction

In recent times, biodegradable materials have been growing in importance, particularly for the protection of the environment from ever-increasing plastic waste. Biodegradable polymers play an increasingly significant role in plastic engineering by replacing commodity, non-degradable and non-renewable petrol-based polymers [1]. Since last decades, many attempts have been focused on grafting or blending of plastic materials with cheap and biodegradable natural biopolymers, such as starch, cellulose, and phylum to create new materials with desired properties. These biopolymers, especially starch, are abundant, inexpensive and also degradable. Research on starch plastic composites began in the 1970s [2] and several different technologies are currently being studied. Polyvinyl alcohol (PVA) is a water soluble, cost effective biodegradable polymer with excellent film forming capacity. There are some strict limitations to the development of starch- based products, due to its poor mechanical properties and high sensitivity to moisture. However, pure starch is brittle and rapidly degrades when exposed to water. In efforts to overcome this disadvantage, there have been many attempts to combine starch with synthetic polymers. Raw, granular starch comes from a variety of sources, including corn, wheat, rice, and potatoes. Corn starch (CS) is preferred because it has the smallest particle size and provides better dispersions in blends with thermoplastic polymer. CS is one of the natural polymers which are non-toxic, biodegradable, available in abundance and soluble in water. However, most of natural polymer such as CS formed very low thin film conductivity [3]. The CS polymer is composed of a mixture of linear amylase and branched amylopectin polysaccharide chain [4]. Blending of PVA with

Corn starch is effective in overcoming retro gradation which is a common problem in Starch based systems. The miscibility of Starch and PVA is promoted by the formation of hydrogen bonds. In the present paper, Corn starch-PVA blend has been investigated as a new material for biodegradable solid polymer electrolytes.

2. Materials and Preparation method

Polyvinyl alcohol with linear formula of $\text{C}_2\text{H}_4\text{O}$ was obtained from Sd fine- chem (SDFCL). Corn starch with a linear formula of $\text{C}_6\text{H}_{10}\text{O}_5$ was obtained from SRL chemicals (Sisco Research Laboratories Pvt. Ltd).

For sample preparation, different wt % of CS was dissolved in 50 ml of distilled water and heated at 75°C for 30 minutes. After the solutions cooled to room temperature and then various wt % of PVA were added to the solution. Then solution was stirred for 24 hours until they became homogenous. The formed homogenous solutions were transferred to Polypropylene Petri dishes and the solvent was permitted to evaporate gradually at room temperature. Three days later, the prepared PVA-CS blend electrolytes were expelled from Petri dish for further analysis. The average thickness of dry films was about 0.15 mm. All samples were stored airtight under room temperature. The composition and coding of the prepared films are as follows

Composition Ratio(PVA: CS)	Sample Code
0:100	VA-00
20:80	VA-20
40:60	VA-40
60:40	VA-60
80:20	VA-80

3. Characterization

All the samples were subjected to x-ray diffraction (XRD), Fourier transform infrared spectroscopy (FTIR) and ac-impedance spectroscopy. The structural properties of the biodegradable PEs were investigated via XRD study using Bruker make X-Ray diffractometer having Cu-K α radiation ($\lambda = 1.540 \text{ \AA}$) with scanning rate 5° per minute in the range of $2\theta = 10^\circ\text{--}60^\circ$. To determine the complexation between polymer blends, FTIR transmittance spectra were traced using "SHIMADZU IR Tracer 100" spectrometer in the wave number region between 400 cm^{-1} and 4000 cm^{-1} . The prepared samples were subjected to ac-impedance spectroscopy. The thickness of the samples was measured by using a screw gauge. The ionic conductivities of the prepared solid polymer electrolytes (SPE) were determined by HIOKI 3532-50 LCR HI-TESTER over the frequency range of 42 Hz to 1 MHz.

4. Results and Discussion

4.1. XRD Analysis

Figure 1 exemplifies the XRD patterns for different wt% composition of PVA and CS. The presence of small humps at $2\theta = 14.8^\circ, 16.8^\circ, 19.8^\circ, 23.2^\circ$ and 30.8° are due to presence of in VA-00.

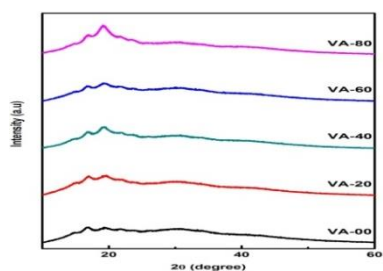


Figure 1: X-ray diffractograms for different compositions of PVA/CS

By increasing the concentration of PVA with CS, the hump present at 19.8° increases in intensity indicating the complete complexation of the polymer blend [5]. For VA-60, the intensity of the hump decreases denoting the increase in amorphous nature of the prepared polymer blend. Beyond the concentration, the intensity of the hump increases and thereby the crystalline nature of the polymer blend has been improved.

4.2. FTIR Analysis

The infrared spectra depict the occurrence, complexation, and interactions between various constitutions which vary according to the compositions of blend PEs. Figure 2 shows the FTIR spectra for various blend ratios of PVA and CS PEs. When two or more polymers are mixed, characteristic spectra peaks will change to reflect the interactions between physical blends and chemical reactions [6]. CS has several --OH groups, therefore FTIR spectra for VA-00 shows the strong and broad absorption in the hydroxyl band region. The broad band observed at 3285 cm^{-1} is due to the OH stretching of intermolecular hydroxyl groups of PVA. The band at 2927 cm^{-1} is due to the C-H stretching of PVA. The band observed at 1638 cm^{-1} is due to the C-O stretching of Corn starch. The intensity of the band changes by increasing the concentration of PVA. The band appeared at $1437 \text{ cm}^{-1}, 1339 \text{ cm}^{-1}, 839 \text{ cm}^{-1}$ [7] is mainly due to the starch and also used to monitor the starch content in the polymer blend. The band at 1019 cm^{-1} occurs mainly due to the C-O stretching of C-O-C group of glucose unit of starch in the blend. The band at 980 cm^{-1} is due to the C-C stretching of PVA which disappears beyond VA-60. Some bands assignments of PEs are listed in table 1

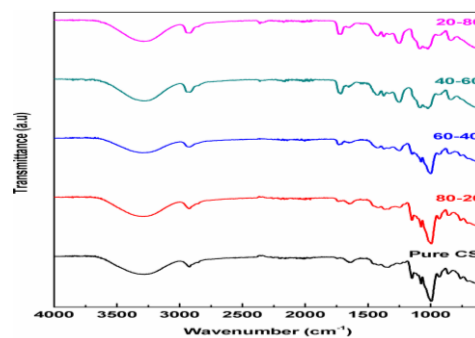


Figure 2: FTIR for VA-00, VA-20, VA-40, VA-60 and VA-80

Table 1: Functional groups and mode of vibration from FTIR spectra of CS/PVA blend PEs

Assignment	Observed wavelength (cm^{-1})
CO stretching	926, 1008, 1077, 1149
CH stretching	2927
CH deformation	1334
CH_2 bending	1425
CH_2 bending	2927
C-C stretching	840

4.3 AC impedance studies

4.3.1 Cole-Cole plot/ Nyquist plot

A typical Nyquist plot of complex impedance of VA-00 to VA-80 is depicted in Figure 3a. The Semicircle obtained for all polymer electrolytes is equivalent to the parallel combination of the constant phase element and a resistor. The effect of constant phase element and the resistor arises due to the immobile and mobile ion in the polymer matrix. The bulk resistance can be obtained from interception of the semicircle on the x-axis in Nyquist plot. The conductivity is calculated by using the formula, $\sigma = l / R_b A$ in S/cm where l is the thickness of the PE in cm, R_b is bulk resistance of PE in Ω , and A is the surface area of PE film or silver electrode in cm^2 . Table 2 shows the conductivity of different wt% ratio of PVA and CS blend PEs at ambient temperature.

Table 2: Conductivity of CS/PVA blend polymer electrolytes

Sample Code	σ (S/cm)
VA-00	2.3×10^{-10}
VA-20	1.4×10^{-10}
VA-40	1.8×10^{-10}
VA-60	1.5×10^{-9}
VA-80	6.7×10^{-10}

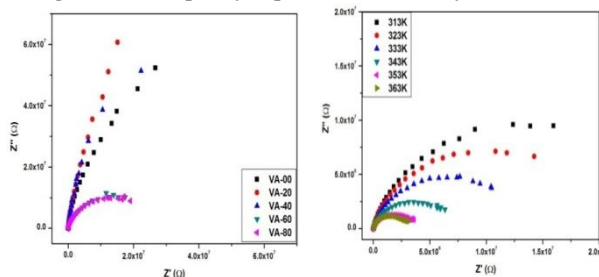
The higher conductivity at ambient temperature is found to be $1.5 \times 10^{-9} \text{ S cm}^{-1}$ for the composition of VA-60. The amorphous nature observed for the composition in the XRD is in agreement with the conductivity value. In the sample VA-60, the mobile charge carriers easily move in polymer matrix to increase the conductivity. The variation conductivity with temperature for the higher conductivity polymer electrolyte is depicted in figure 4b. The conductivity of the polymer electrolyte increases with the rise in temperature. The conductivity of the VA-60 PE has been increased to reach the value $4.93 \times 10^{-9} \text{ S cm}^{-1}$ at 363K. This rise in conductivity values arises due to the increase in flexibility of the polymer electrolyte [8] and the inter- and intra chain hopping from chain bonding rotations and thereby increasing the number of density and mobility of ions [9].

Figure 3(a): Cole-Cole plot for different compositions of PVA/CS at ambient temperature(b) Cole-Cole Plot for VA-80 with different temperature from ambient temperature to 363K

4.3.2 Conductance spectra

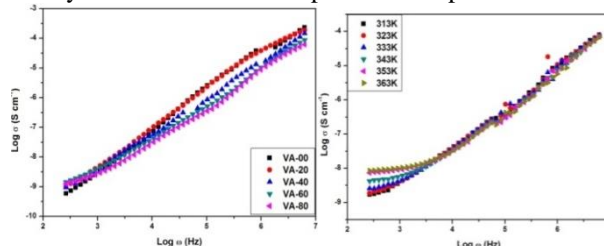
In frequency dependence conductance spectra is helpful for know about the ion dynamics and conductance behaviour in the SPEs at lower frequency to higher frequency.

Figure 4(a): Frequency-dependent conductivity for VA-0, VA-2,



VA-4, VA-6 and VA-8 at ambient temperature (b) Frequency-dependent conductivity for VA-8 with various temperatures (303-373K)

Variation of conductivity as a function of frequency for samples VA-00, VA-20, VA-40, VA-60 and VA-80 has been shown in Figure 4a. The ionic conductivity improvement may be due to the enhancement of the ionic mobility and the large number of carrier ions being introduced into the complex. From 303K to 363K, conductivity variations in all composition samples are observed



particularly at low frequency as clearly shown in figure 4b. The conductance spectra consist of two regions. The extrapolations of plateau region to meet along y-axis is used for determine the dc value of conductivity. At higher frequencies the ion exchange process occurs more effectively. But in the higher frequency there is no variations are observed in ionic conductivity from Figure 5b because, dipoles of the molecules are oriented in the direction of applied field due to the orientation or dipole polarization.

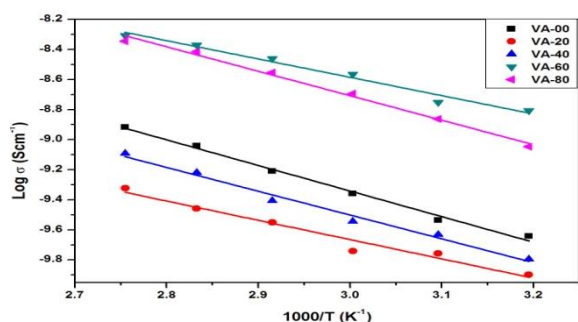
4.3.3 Temperature dependence–ionic conductivity studies

The temperature dependent conductivities of PVA-CS polymer electrolyte system investigated at temperature range of 313 to 363K as shown in figure 5. When the

temperature increases from ambient temperature to higher temperature, the polymer matrices have been expanded to form the free volume and unoccupied spaces for migration of ions. In this way conductivity of ions in PEs have been improved with increasing temperatures according to ion hopping mechanism [10]. The conductivities are linearly increased by rising temperature in all the PE samples to obey the Arrhenius behaviour as shows in figure 4. Using linear fitting to the curves from $\log \sigma$ versus $1000/T$ graph, then found the slope value from this plot. This slope value used for the calculation of activation energy E_a for the PEs. Activation energy E_a was calculated using the Arrhenius rule, as given below

$$\sigma(T) = \sigma_0 \exp\left(\frac{-E_a}{KT}\right)$$

where $\sigma(T)$ denote the temperature dependent conductivity ($S\ cm^{-1}$), σ_0 is the pre-exponential factor, E_a is the activation energy (eV), K is the Boltzmann constant ($J\ K^{-1}$) and T is absolute temperature (K). High conducting



sample VA-60 has low activation energy of 0.23eV.

Figure 5: Arrhenius plot for samples VA-00, VA-20, VA-40, VA-60 and VA-80

5. Conclusion

Different compositions of PVA and corn starch blend polymer electrolytes have been prepared by solution casting method using distilled water as solvent. From the XRD results, 60 wt% PVA + 40 wt% cornstarch was found to be the most suitable ratio to serve as the polymer blend due to the increase in amorphous nature. FTIR

reveals the complexation of PVA and CS was confirmed by the presence of carbonyl groups, C-H deformation, C-H wagging. The higher conductivity at ambient temperature is found to be $1.5 \times 10^{-9}\ S\ cm^{-1}$ for the composition of VA-60. The plot of conductivity versus temperature shows that all electrolytes obeyed the Arrhenius rule. High conducting sample VA-60 has low activation energy of 0.23eV.

6. Acknowledgements

This research work was supported by International Research centre (IRC), Kalasalingam Academy of Research and Education for university research fellowship.

REFERENCES

- [1] Park JS, Yang JH, Kim DH, Lee DH. Degradability of expanded starch/PVA blends prepared using calcium carbonate as the expanding inhibitor. *J Appl Polym Sci* 2004; 93:911-919.
- [2] Griffin GJL. Starch polymer blends. *Polymer Degrad Stability* 1994; 45:241-247.
- [3] C. Liew and S. Ramesh, "Electrical, structural, thermal and electrochemical properties of corn starch-based biopolymer electrolytes," *Carbohydr. Polym.*, vol. 124, pp. 222–228, 2015.
- [4] Pawlicka A, Sabadini AC, Raphael E, Dragunski DC (2008) *Mol Cryst Liq Cryst* 485:56–68
- [5] Rahul V. Manek, Philip F. Builders, William M. Kolling, Martins Emeje, and Olobayo O. Kunle, *AAPS PharmSciTech*, Vol. 13, No. 2, June 2012, DOI: 10.1208/s12249-012-9761-z
- [6] Yin Y J, Yao K D, Cheng G X and Ma J B 1999 *Polym. Int.* 48 429–33
- [7] Lee, J.; Isobe, T.; Senna, M. J. *Colloid Interface Sci.* 1996, 177, 490–494. doi:10.1006/jcis.1996.0062
- [8] Harun N I, Ali R M, Ali A M M and Yahya M Z A 2011 *Mater. Res. Innov.* 15 S168–72
- [9] Rajendran S, Sivakumar M and Subadevib R 2004 *Mater. Lett.* 58 641–9
- [10] C.-W. Liew, S. Ramesh, K. Ramesh, A.K. Arof, J. *Solid State Electrochem.* 16 (2012) 1869–187

STRUCTURAL AND OPTICAL STUDIES ON A NEW THIRD ORDER NONLINEAR OPTICAL CRYSTAL: β - ALANINIUM p -TOLUENESULFONATE

M. Suresh^{1*}, S. Asath Bahadur² and S. Athimoolam³

¹Department of Physics, Er. Perumal Manimekalai College of Engineering, Hosur, Tamilnadu - 635117, India.

²Department of Physics, Kalasalingam Academy of Research and Education, Krishnakoil, Tamilnadu - 626 190, India.

³Department of Physics, University College of Engineering, Nagercoil, Tamilnadu - 629 004, India.
Email: sureshmuthu23@yahoo.com

Abstract

In the present work, a new third order nonlinear optical crystal: β -alaninium p-toluenesulfonate (BAPT) is reported. BAPT is crystallized in orthorhombic system with the space group of Pbca. The crystal exhibits very good optical properties includes wide optical transparency in region 210 – 1100 nm and the ultraviolet wavelength emission ($\lambda = 289$ nm) and large third order susceptibility value ($\chi^3 = 7.3721 \times 10^{-11}$ esu) indicate the suitability for favorable optoelectronics and optical limiting applications.

Keywords: Crystal structure, Crystal growth, Optical Material, third order harmonics

1 Introduction

Organic NLO materials with high optical nonlinearity and synthetic flexibility which favours the wide range of possibility to fine tune their optical properties through molecular engineering and chemical synthesis [1]. The important goal for designing the molecules with large third order nonlinearities is to incorporate them into devices used in the optical signals processing [2, 3]. Recent studies on organic NLO systems show that p-conjugated organic systems have been attracting candidate used in the synthesis of efficient NLO materials due to its quick response with the enhanced properties with low dielectric constant at higher frequencies [4]. Owing to the interesting properties of amino acids and p- toluenesulfonic acid monohydrate, a series of amino acid and p- toluenesulfonic acid complexes are reported already from our group (5-8). In this series, a newly synthesized p- toluenesulfonic acid amino acid complex, β - alaninium p- toluenesulfonate (BAPT) is reported here.

2 Material Synthesis and crystallization

β - alaninium p-toluenesulfonate (BAPT) salt is synthesized from β -alanine and p-toluenesulfonic acid monohydrate taken in the equimolar ratio (1:1) from aqueous solution. The precursor chemicals were dissolved in de-ionized water and stirred well for an 1 hour. The reaction was allowed to happen as in the scheme (Fig. 1a) in room temperature. Slow evaporation solution growth method was used to grow

the single crystals of BAPT using saturated solution prepared from synthesized salt. The filtered solution was kept undisturbed for crystal growth and the grown crystals were harvested in 15 days. Bulk crystal growth is attempted by submerged seed solution growth method by immersing the seed crystal inside the prepared supersaturated solution. The bulk crystal of characteristic size and shape is obtained in the period of 20 days and shown in Fig. 1b.

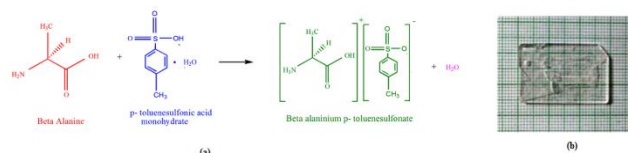


Fig. 1 (a) Reaction scheme (b) Photograph of the crystal

3 Results and discussion

X-Ray data collection was done by ENRAF NONIUS CAD4-F single crystal X-ray diffractometer (graphite-monochromated, Mo $K_{\alpha} = 0.71073(\text{\AA})$). BAPT (empirical formula $C_3H_8NO_2^+ \cdot C_7H_7SO_3^-$) is crystallized in orthorhombic system, space group Pbca with the unit cell parameters of $a = 10.350(7) \text{ \AA}$, $b = 8.361(4) \text{ \AA}$, $c = 28.7516(2) \text{ \AA}$, Volume $V = 2488.2(3) \text{ \AA}^3$ and $Z = 8$. The structure was solved and refined with the SHELXL -14 programmes [9] and complete data is deposited with CCDC (CCDC No: CCCD1476185). All the atoms except H atoms were refined anisotropically. All the H atoms except

hydrogen atoms participating in classical hydrogen bonds were positioned geometrically and refined using riding model with $C-H=0.93 - 0.96\text{\AA}$, and $U_{iso}(H)= 1.2-1.5U_{eq}(C)$. The H atoms which are involved in the hydrogen bonds were located from electron density map and refined isotropically. The convergence of the structure is confirmed from the R-factor [4.73% for $I > 2\sigma(I)$]. The observed absolute structure parameters (Flack parameter) of the compounds confirm the chiral nature of the compound. The asymmetric part of the crystal (Fig. 2a) consists of β -alaninium cation and *p*-toluenesulfonate anion. The C–O bond lengths [1.305 (4) & 1.202 (4) \AA] of the carboxyl group in cation clearly indicates the presence of COOH group. The protonation of the N site is confirmed from the lengthened C–N bond distance [1.479 (4) \AA], respectively. Fig. 2a shows the ORTEP view of the molecules [BAPT] drawn at 50% probability thermal displacement ellipsoids with the atom numbering scheme.

The crystal structure of compound is stabilized through a three dimensional hydrogen bonding network formed through N–H...O and O–H...O hydrogen bonds. The N atom of cation and O atom from the carboxyl group are connected through N–H...O intermolecular hydrogen bond to form chain $C(6)$ motif running along the *a*-axis of the unit cell. Another chain $C_2^2(10)$ motif is formed through O–H...O intermolecular hydrogen bond extending along the same axis. These two chain motifs are interlinked with each other to form ring $R_3^3(10)$ motif. These chain and ring motifs lead to the hydrophilic layers at $z = 0, 1/2$ and 1 which is sandwiched between the hydrophobic layers at $x = 1/4$ and $3/4$ (Fig. 2b). Symmetry transformations used to generate equivalent atoms are #1- $x+1/2, y+1/2, z$ #2 $x+1/2, -y+1/2, -z+1$ #3 $x-1/2, -y+1/2, -z+1$ and #4 $x-1, y, z$. It is noted that the hydrogen bonds are a kind of NLO functional bonds in the crystallographic frame as highlighted by Xue et al[10-12].

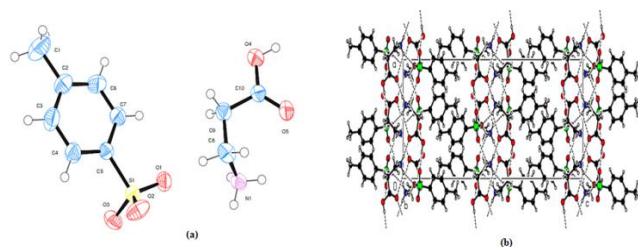


Fig. 2 (a) ORTEP diagram (b) Packing diagram of BAPT viewed down the *b*-axis of the unit cell

The UV-Vis- NIR absorption analyses were carried out between 200 and 1100 nm covering the entire ultraviolet and visible regions using the UV-1700 Shimadzu spectrometer with the resolution of 1nm. Well polished single crystal of 1 mm thickness was used and the result is shown in Fig. 3a. In the spectrum, there is no significant absorption observed in the visible and NIR region and the

cut-off wavelength is found 294 nm, which suggested that BAPT might be a suitable material for efficient optoelectronic applications.

The emission spectrum of title compound was recorded in the wavelength range from 280 to 500 nm with 280 nm as excitation wavelength using Cary eclipse spectrophotometer. The recorded spectrum is shown in Fig. 3b. The sharp intense peak occurred around at 289 nm due to the intraband transition ($n \rightarrow \pi^*$) between amino and C–O group of the compound. The peak around 289 nm also indicates that the grown crystal has ultraviolet emission and it suggest the usefulness of the compound in ultraviolet region.

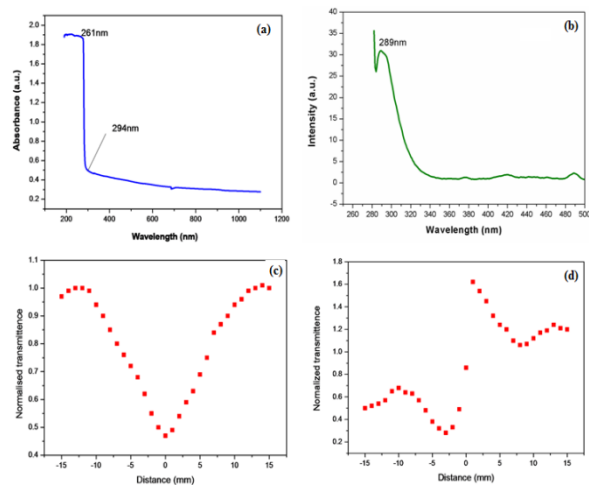


Fig. 3 (a) UV- Vis- NIR absorbance spectrum, (b) Emission spectrum, (c) Normalized transmittance Vs Distance-Open aperture mode and (d) Normalized transmittance Vs Distance-Closed aperture mode

The NLO behavior of BAPT was analyzed by *Z*-scan method. The parameters such as the nonlinear absorption coefficient, third order susceptibility and nonlinear refractive index of grown crystals were investigated by employing the He - Ne laser source of wavelength 632.8nm with the beam radius of 12 μm . The Gaussian input laser beam generated by focusing via Gaussian filter was projected through a convex lens placed at a focal length of 30mm transverse mode operation. Beam radius of the aperture (W_a) and aperture radius (r_a) used are 3.3mm and 2mm respectively. The Sample thickness (*l*) used is 0.6mm. BAPT crystal was moved across +*Z* to -*Z* axial direction and the plot between normalized transmittances and position for open and closed aperture were plotted (Fig. 3c & 3d). The open aperture curve demonstrates a nonlinear absorption and the characteristic pattern of the curve indicates the reverse saturation absorption as the nonlinear absorption by BAPT. For closed aperture scan, the observed peak and valley is due to the nonlinear phase shift of the compound and the positive phase shift, positive nonlinear index (n_2) confirms the self focusing effect of BAPT.

From the values of non linear absorption coefficient ($\beta = 2.3295 \times 10^{-02} \text{ m/w}$) and non linear refractive index ($n_2 = 6.9822 \times 10^{-09} \text{ m}^2/\text{w}$) and the real and imaginary part of the third order susceptibility (χ^3) of compounds were calculated using the equations in the literature [13]. The real and imaginary part of the third order nonlinear susceptibility was determined to be $7.27010 \times 10^{-11} \text{ esu}$ and $1.2220 \times 10^{-11} \text{ esu}$, respectively. The measured values of n_2 and third order nonlinear susceptibility (χ^3) of BAPT is found higher than the KDP ($n_2 = 2.34 \times 10^{-13} \text{ esu}$ and $\chi^3 7.3721 \times 10^{-11} \text{ esu}$) [13]. The calculated positive value of nonlinear absorption coefficient (β) confirms the two – photon absorption process occurred in compound. The high value of real part reveals that the third order nonlinear property of BAPT at 632.8 nm is highly influenced by the nonlinear refraction rather than nonlinear absorption. The coupling factor (ρ) is calculated from the ratio of imaginary part to real part of third-order nonlinear susceptibility and found equal to 0.16. The observed value of ρ is less than 1/3, indicates that the nonlinearity is electronic in origin. The two – photon absorption nature and self focusing effect concluded that the crystal could be a potential candidate for optical limiting applications and optical modulation.

4. Conclusion

In the present work, an organic third order nonlinear optical material BAPT was crystallized in orthorhombic space group of Pbcu. The crystal structure of BAPT shows excessive hydrogen bonds which may enhances the NLO activity of the material. The linear optical studies demonstrated wide optical transparency in the region 210 - 1100 nm and the lower cut-off wavelength of 294 nm. The emission peak at 289 nm is the evident for the material's fluorescence property in the ultraviolet wavelength region. Z-scan study revealed good third order nonlinear optical susceptibility, nonlinear refractive index and non-linear absorption coefficient. The wide optical transparency and high third order nonlinear

optical response suggest that BAPT crystal as a potential candidate for optical limiting, optoelectronic and optical switching applications.

REFERENCES

- [1] A. Datta, and S.K. Pati, *J. Chem. Phys.* 118 (2003)8420.
- [2] M. Somac, A. Somac, B.L. Davies, M.G. Humphery, M.S. Wong, *Opt. Mater.* 21 (2002) 485- 488.
- [3] J.G. Breitzar, D.D. Diott, L.K. Iwaki, S.M. Kirkpatrick, T.B. Rauchturs, *J. Phys. Chem.* A103 (1999) 6930-6937.
- [4] R.P. Jebin, T. Suthan, N.P. Rajesh, G. Vinitha, U. Madhusoodhanan, *Spectrochim. Acta.* A 135 (2015) 959 - 964.
- [5] M. Suresh, S. Asath Bahadur, S. Athimoolam, *Optik.* 126 (2015) 5452–5455M. Suresh, S. Asath Bahadur, S. Athimoolam, *J. Mater. Sci: Mater. Electron.* 27(5) (2016) 4578–4589.
- [6] M. Suresh, S. Asath Bahadur, S. Athimoolam, *J. Mol. Struct.* 1112 (2016) 71-80.
- [7] M. Suresh, S. Asath Bahadur, S. Athimoolam, *J. Mater. Sci: Mater. Electron.* 28(1) (2017) 661–672.
- [8] G. M. Sheldrick, *Acta Cryst.* **C71** (2015) 3-8
- [9] D. Xue, S. Zhang, *J. Solid State Chem.* **135** (1) (1998) 121- 126.
- [10] D. Xue, S. Zhang, *Chem. Phys. Lett.* **301** (1999), 449 – 452.
- [11] D. Xue, H. Ratajczak, *J. Mol. Struct. (Theochem).*, **716** (1-2) (2005), 207-210.
- [12] R.A.Ganeev, I.A. Kulagin., A.I. Ryasnyansky, R.I. Tugushev, T. Usmanov, *Opt. Commun.* **229** (2004) 403–412.
- [13] S. Seetharam, G. Umesh, K. Chandrasekharan, B. K. Sarojini, *Opt. Mater.* **30** (2008) 1297.

SENSITIVITY ENHANCEMENT OF SURFACE PLASMON RESONANCE SENSOR WITH 2D MATERIAL COVERED NOBLE AND MAGNETIC MATERIAL (NI)

A. Nisha¹, P. Maheswari³, P. M. Anbarasan¹, K. B. Rajesh^{2*}, Z. Jaroszewicz⁴

¹Department of physics, Periyar University, Salem, Tamil Nadu, India.

³Department of physics, PSGR Krishnammal College for Women, Coimbatore

^{2*}Department of Physics, Chikkanna Government Arts College, Tirupur, Tamil Nadu, India.

⁴Institute of Applied Optics, Department of Physical Optics, Warsaw, Poland.

Email id: rajeskb@gmail.com

Abstract

In this paper, surface plasmon resonance (SPR) sensor on 2D materials such as MoS₂ and graphene on Au and magnetic material Ni in Kretschmann configuration is analyzed using transfer matrix method. Here we noted that by sandwiching the MoS₂ layer between the Au and Ni film and adding graphene over Ni film improved the sensitivity as high as 229°/RIU. We also noted that the sensitivity of the proposed sensor changes with the addition of no. of layers of graphene and MoS₂. We expect that such a high sensitivity SPR sensor could find optional application in chemical examination, medical diagnostic and biological detections.

Keywords Surface plasmon resonance · Sensitivity · Biosensor · Grapheme · MoS₂

1. Introduction

The results show that the addition of materials Last two decays SPR sensors have drawn great attention in sensing technology due to their distinctive benefits such as their enormous sensing properties, label free detection and bio-compatibility [1]. They took important part in many investigations such as bimolecular detection, bimolecular interaction, sensing technology[2], food safety, environmental changes detection[3] and so on. It is possible to use SPR sensor in earlier disaster or disability diagnostic analysis, when increasing its sensitivity as high as possible and hence to develop a good sensor with a superior sensitivity is of great interest. In common, there are two quite different detection techniques have been used so far for SPR sensors, namely angle interrogation and wavelength interrogation. The angle interrogation method working under the kretschmann configuration it requires only monochromatic light to produce surface plasmons (SPs), however the wavelength inter-rogation needs a polychromatic light beams to yield SPs. Here we have chosen the angle interrogation technique namely the kretschmann configuration for our theoretical analysis since the kretschmann configuration is found to have the advantages of attaining a higher signal to noise ratio and other parameters with a single light source. Here the metal layer is coated directly on the top of the prism where as in Otto's configuration an air gap is maintained between the prism and the metal

film. In the conventional SPR biosensor configuration, metals such as Au (Gold), Ag (Silver), Cu (Copper), and Al (Aluminum) [4,5,6] are commonly used and each of this metal layers have its own merits and demerits. Au is preferably chosen as a metal layer apart from all these metals because it possesses excellent resistant capability from oxidation and corrosion in all kind of environments [7,8,9,10], Moreover gold shows larger shift in the resonance angle corresponding to the changes in refractive index of the sensing medium, which provides a high sensitivity In this paper we have designed a new sensing configuration consisting of 2D materials, Au and Magnetic material Ni. Here the 2D material such as graphene and -MoS₂ are employed to improve the light absorption capacity of the sensor [11,12,13], which is much beneficial to get higher sensitivity. The reflectance curve, resonance angle, sensitivity are analyzed theoretically using Fresnel equation and transfer matrix method. such as MoS₂ and graphene on magnetic material Ni shows a higher sensitivity than the traditional sensor.

2. Theory

The proposed SPR sensor has six different layers based on the kretschmann configuration as shown in Fig. 1. Here we assumed the excitation of SPs with 633 nm wavelength laser source [14]. The first layer is BK7 prism and its refractive index is $n_1 = 1.5151$. The second and fourth layers are Au and Ni metal films with MoS₂ layer in between them with thickness $d_2 = M \times 0.65$ nm where M is the no of MoS₂ layer. The complex refractive index of MoS₂ at 633 nm wavelength is $5.0805 + 1.1723i$. Here we fixed the thickness of Au film d_2 as 30 nm and the Ni film d_4 as 10 nm. The complex refractive indexes of the Au and Ni films are calculated according to the Drude formula[15,16]

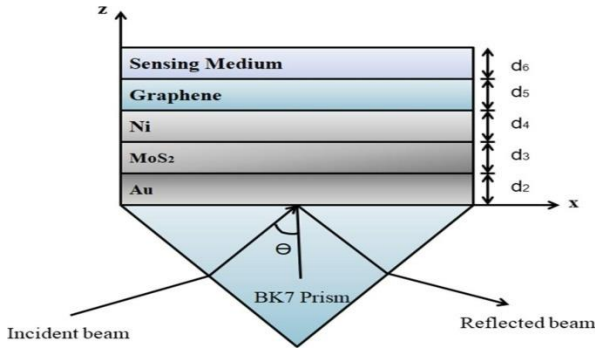


Fig. 1 Schematic diagram of proposed SPR biosensor

Sensitivity of the proposed SPR biosensor is measured as the ratio of little difference in the refractive index of cover region Δn_c to the change in resonance condition $\Delta\theta_{res}$ in the reflectance curve, consequently the sensitivity is given as [17]

$$S = \frac{\Delta\theta_{res}}{\Delta n_c}$$

3. Results and discussion

Figure 2a shows the reflectance spectra obtained for the configuration without Graphene ($L = 0$) and MoS₂ ($M = 0$) layers. We observed that for the above mentioned configuration, the change in resonance angle $\delta\theta_{res}$ is found to be 0.92° and the corresponding sensitivity of the biosensor is calculated as $183^\circ/\text{RIU}$ according to the equation no (7). Figure 2b shows the same plot with the consideration of $L = 0$ and $M = 1$. In this case the shift in resonance angle is found to be 1.0318 and the corresponding sensitivity is calculated as $206^\circ/\text{RIU}$. It is clearly observed that the sensitivity and shift in resonance angle are found to be higher than the

previous case when adding the single layer of MoS₂. Figure 2c shows the situation of reflectance spectra versus angle of incidence when the proposed sensor is considered with $L = 1$ and absent of MoS₂ $M = 0$, in this case, $\delta\theta_{res}$ is 0.98° and the sensitivity is calculated as $194^\circ/\text{RIU}$. The sensitivity obtained is found to be less than the previous case of $L = 0$ and $M = 1$. Hence it is noted that MoS₂ is better material than the graphene to increase the sensitivity of the biosensor. Figure 2d shows the reflectance spectra obtained for the proposed sensor considered with the presence of both MoS₂ $M = 1$ and Graphene $L = 1$ layer. Here the shift in resonance angle is found to be much increased as 1.0891° and the sensitivity improved as $217^\circ/\text{RIU}$. Since sensitivity depends up on the absorption of the different layers of the sensor, we noted that the configuration with single layer of graphene and MoS₂ shows better absorption and hence the better sensitivity. Fig. 3a. It is noted that the increasing of $\delta\theta_{res}$ varies for different types of layers used. It is observed that the resonance angle shifts from 76.81° to 80.99° for the configuration without graphene and MoS₂ ($M = 0$ and $L = 0$) whereas, it increased to 77.38° to 81.85° for the configuration with single layer of graphene ($M = 0$ and $L = 1$) due to the good absorption property of graphene. It is also noted that further increase in $\delta\theta_{res}$ around 78.24° to 82.94° is obtained for the configuration with single layer of MoS₂ ($M = 1$ and $L = 0$) which shows that better absorption property of MoS₂ than graphene. It is further noted that the shift in resonance angle is found to very much improved to 78.93° to 83.86° for the configuration with both graphene and MoS₂ ($M = 1$ and $L = 1$). Figure 3b shows the plot of sensitivity versus refractive index for the proposed configuration with and without graphene and MoS₂ layers obtained by keeping the other parameters constant. We noted that for the configuration without MoS₂ and graphene layers, the sensitivity increased from $183^\circ/\text{RIU}$ to $240^\circ/\text{RIU}$ ($M = 0$ and $L = 0$). However adding a single graphene layer of graphene ($M = 0$ and $L = 1$), the sensitivity is found to improved from $183^\circ/\text{RIU}$ to $252^\circ/\text{RIU}$ whereas it is found to further improved from $194^\circ/\text{RIU}$ to $275^\circ/\text{RIU}$ ($M = 1$ and $L = 0$) for the configuration with single layer of MoS₂. Figure 4a shows the reflectance curve obtained for single layer of graphene with increasing no. of MoS₂ layers by keeping the other parameters same as before. It is observed from the figure, that increasing the number of MoS₂ layer, shifts the reflectance dip to larger incident angle which implies that the sensitivity of the biosensor can be enhanced by manipulating the number of MoS₂ layer. We also noted that similar trend is observed with the increase of graphene layer in the presence of single layer of

-MoS₂ and areshown in Fig. 4b. However, we noted that though the shift in resonance angle is larger for the addition of -MoS₂ layer when compared to the addition of graphene layer, the reflectance curve becomes wider and the minimum reflectance goes to higher values for the addition of MoS₂ layer, when compared to the addition of graphene layer. This implies that addition of more MoS₂ and graphene layers.

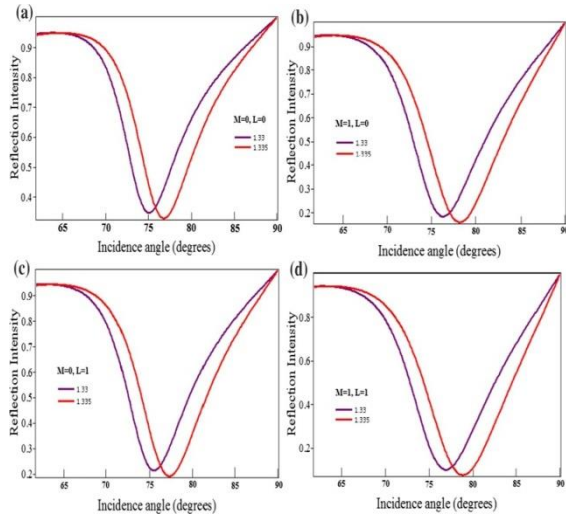


Fig 2a. Reflectance curve of M=0 L=0 b. M=1 L=0 c. M=0 L=1 d. M=1 L=1

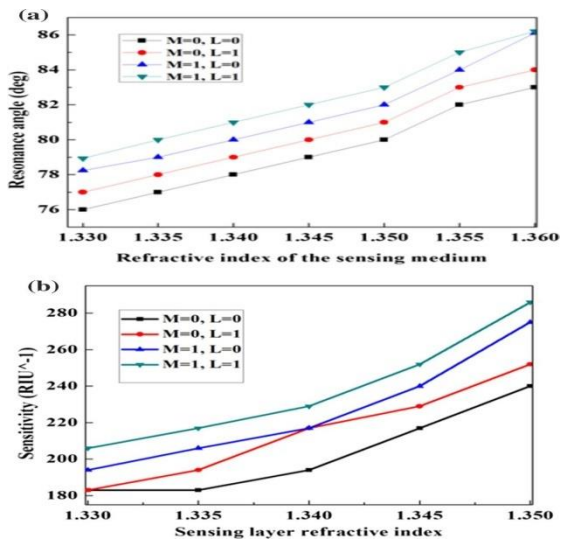


fig3 a. Resonance angle b. Sensitivity versus sensing layer refractive index

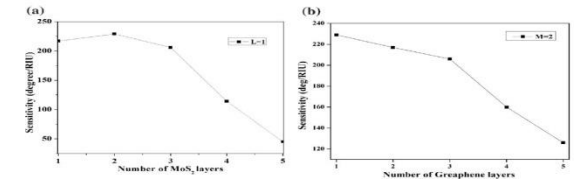
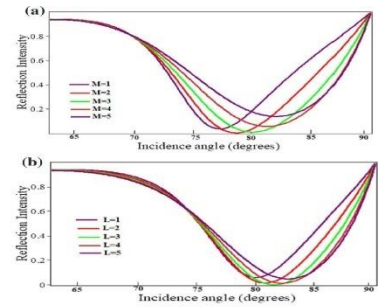


Fig. 4a,b Reflectivity versus angle of incidence varying a number of MoS₂ layers with single layer of graphene b. number of graphene layers with single layers of MoS₂

Fig. 5a. Number of -MoS₂ layer for single layer of graphene, b. number of graphene layers for the optimized two layers of MoS₂

Hence in order to optimize the number of -MoS₂ and graphene layer, we calculated sensitivity corresponding to different layers of MoS₂ and graphene. Figure 5a depicts the variation of sensitivity with respect to number of -MoS₂ layer with a single layer of graphene keeping the other parameters same as before. We can find that the sensitivity of SPR bio-sensor initially increase as the number of -MoS₂ layer increases from 1 to 2 and later it starts decreasing sharply as the number of MoS₂ layer is further increases from 3 to 5. This is because of decreasing of light utilization rate with the increasing the -MoS₂ layer. The maximum sensitivity of 229°/RIU is obtained for M = 2 and hence, the two layer of -MoS₂ is optimized for best performance of the SPR biosensor. Figure 5b shows that the variation of sensitivity with respect to number of graphene layer with optimized two layer of -MoS₂ (M = 2). It is noted from Fig. 5b, while on increasing the number of graphene layers, the sensitivity of biosensor is decreasing and it is clearly shows that the maximum sensitivity of 229°/RIU is obtained for single layer of graphene. Hence a single layer of graphene is optimized for the excellent performance of the SPR biosensor. On a whole, it is optimized that the proposed biosensor with structure of 30 nm thick Au,

2 layer of MoS₂, 10 nm thick Ni and 1 layer of graphene can produce large shift of resonance angle ($\delta\theta = 1.14^\circ$) of the SPR curve within a small change of the refractive index of sensing medium ($\delta n_s = 0.005$), which result in the highest sensitivity of 229°/RIU. The sensitivity obtained for the pro-posed sensor is found to be much higher than all the recently reported SPR sensor schemes and are compared in Table 1. We believe that the proposed scheme with high sensitivity could find more significance in chemical examination, medical diagnosis and biological applications.

4. Conclusion

In this work, sensitivity enhanced SPR sensor configuration employing 2D material such as MoS₂ sandwiched between Au and Ni layer of fixed thickness and graphene layer over Ni is analyzed theoretically using Fresnel equation and transfer matrix method. We observed that the proposed sensor exhibits enhanced sensitivity compared to the conventional gold film based SPR sensor. It is observed that for the optimized no. of -MoS₂ and graphene layers, the sensitivity as high as 229°/RIU in angular interrogation method is obtained.

REFERENCES

- [1] B. Rothenhauser, W. Knoll, Surface plasmon microscopy, *Nature* **332**, 615-617, (1988).
- [2] Y.A. Akimov, W.S. Koh, Resonant and nonresonant plasmon nanoparticle enhancement for thin-film silicon solar cells, *Nanotechnology*, **21**, 235201, (2010).
- [3] Y.A. Akimov, K. Ostrikov, E.P. Li, Surface plasmon enhancement of optical absorption in thin-film silicon solar cells, *Plasmonics*, **4**, 107-11, (2009).
- [4] S. Zheng, G. Masoud, J.P. Ou, Photonic crystal fiber long-period grating absorption gas sensor based on a tunable erbium-doped fiber ring laser, *Sensors Actuators B*, **223**, 324–32, (2016). [5] S. Zheng, Y.N. Zhu, S. Krishnaswamy, Fiber humidity sensors with high sensitivity and selectivity based on interior nanofilm-coated photonic crystal fiber long-period gratings, *Sensors Actuators B*, **176**, 264–74, (2013).
- [6] S.J. Qiu, Z. Zhou, X. Feng, F. Xu, Y.Q. Lu, Lead silicate fiber-based, refractive index-independent temperature sensor, *J. Mod. Opt.*, **60**, 851–3, (2013).
- [7] A. Otto, Excitation of nanoradiative surface plasmon waves in silver by the method of frustrated total reflection, *Zeitschrift fur physic*, **216**, 398-410, (1968).
- [8] E. Kretschmann, H. Raether, Radiative decay of non-radiative surface plasmon excited by light, *Zeitschrift Fur Naturforschung*, **23A** 2135-2136, (1968).
- [9] B. Liedberg, C. Nylander, I. Lundstrom, Surface plasmon resonance for gas detection and biosensing, *Sens Actuators*, **4**, 299-304, (1983).
- [10] S.A. Alexander, *Plasmonics: Fundamentals and Applications*, Springer, (2007).
- [11] Raether, H, *Surface plasmons on smooth and rough surfaces and on Gratings*, Springer-Verlag, (1998).
- [12] E. Hutter, J.H. Fendler, Exploitation of localized surface plasmon resonance, *Adv. Mater*, **16(19)**, 1685-1706, (2004).
- [13] H.S. Chu, W.B. Ewe, W.S. Koh, E.P. Li, Remarkable influence of the number of nanowires on plasmonic behaviors of the coupled metallic nanowire chain, *Appl. Phys. Lett*, **92(10)** 103103, (2008).
- [14] Y.A. Akimov, W.B. Koh, K. Ostrikov, Enhancement of optical absorption in thin-film solar cells through the excitation of higher-order nanoparticle plasmon modes, *Opt. Express*, **17(12)** 10195-10205, (2009).
- [15] Y.A. Akimov, W.B. Koh, S.Y. Sian, S. Ren, Nanoparticle-enhanced thin film solar cells: metallic or dielectric nano particles?, *Appl. Phys. Lett*, **96(7)**, 073111, (2010).
- [16] L. Wu, H. Chu, W.B. Koh, E.P. Li, Highly sensitive graphene biosensors based on surface plasmon resonance, *Opt. Express*, **18**, 14395–14400, (2010).
- [17] R.P.H. Kooyman, *Handbook of Surface Plasmon Resonance*, (eds Schasfoort, R. B and Tudos, A. J.) Royal Society of Chemistry, Ch. **2**, 15-34, (2008).

QUANTUM CHEMICAL INVESTIGATION ON STRUCTURAL, MOLECULAR ORBITAL AND POPULATION ANALYSIS OF GUANIDINIUM P- TOLUENESULFONATE: A NONLINEAR OPTICAL MATERIAL

V. Siva^a, S. Asath Bahadur^{a*}, A. Shameem^a, A. Murugan^a, S. Athimoolam^b

^aDepartment of Physics, International Research Centre, Kalasalingam Academy of Research and Education, Krishnankoil- 626 126, India.

^bDepartment of Physics, University College of Engineering Nagercoil, Anna University, Nagercoil- 629 004, India.

Corresponding Author: s_a_bahadur@yahoo.co.in

Abstract

Quantum chemical studies of Guanidinium p- toluenesulfonate have been investigated by Density Functional Theory with 6-311++G(d,p) basis set. Mulliken charge analysis demonstrates the accumulation of positive and negative charge on atoms and their participation in hydrogen bonding interactions. Furthermore, the molecular orbital calculations such as HOMO–LUMO energy gap and Mapped molecular electrostatic potential (MEP) surfaces were also performed with the same level of DFT. The frontier orbital has lower band gap value, which indicates the possible optical activity of the molecule. Frontier molecular Orbital analysis clearly depicts the occurrence of intermolecular N-H...O hydrogen bond influencing the charge transfer in the system. Molecular Electrostatic Potential study predicts the possible sites for hydrogen bonding nucleophilic and electrophilic interactions. The calculated polarizability and first order hyperpolarizability values show that the compound is good candidate for NLO applications.

Keywords Density Functional Theory, HOMO–LUMO, Mulliken charge, MEP, Nonlinear optical (NLO)

1. Introduction

Guanidinium complexes are biologically important due to their presence as a functional group in amino acids [1-3]. Its physical properties are of considerable interest with regard to the variety of applications in the field of nonlinear optics, ferroelectricity, biotechnology, medicine, etc. Guanidine [CNH(NH₂)₂] readily reacts with all types of organic acids to give salts with good crystallinity, largely because of the presence of five potential donor sites for hydrogen bonding interactions. Due to the strong base character of guanidine, it can be considered as a super-base that readily undergoes protonation to generate a resonance-stabilized guanidinium cation. The conjugation π -electron moiety provides a pathway for the entire length of conjugation under the perturbation of an external electric field. Organic molecules containing conjugate systems have some advantages over inorganic materials owing to the possibility of highly enhanced electronic nonlinear optical polarization responses [4]. Fictionalization of

both ends of the π bond systems with appropriate electron donor and acceptor group can increase the asymmetric electronic distribution in either the ground state or excited state or both thus leading to an increased optical nonlinearity [5]. In the present work, guanidinium p-toluenesulfonate has been characterized to study its structural, population analysis and nonlinear response by quantum chemical calculations.

2. Computational details

The computational calculation of the compound GPTS is performed from the crystallographic data with Density Functional Theory methods at 6-311++G(d,p) basis set, using GAUSSIAN 09W software package [6]. Frontier molecular orbital (FMO) analysis based on DFT calculation was another approach to investigate the charge transfer at a molecular level. The charge transfer reactions consisted of a charge movement between the relevant orbitals, in which the interactions between the occupied and unoccupied orbitals played a vital role.

Finally, the results viewed through the GAUSSVIEW program [7]. Also, the hyperpolarizability and Molecular electrostatic potential (MEP) calculations were carried out with same basis sets.

3. Results and Discussion

3.1 Mulliken charge Distribution analysis

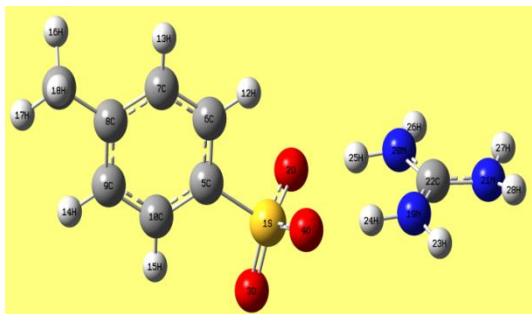


Figure 1 Optimized structure of GPTS

Fig. 1 shows that the optimized molecular geometry and atomic numbering scheme of GPTS. The Mulliken atomic charge distribution was analyzed by DFT/B3LYP level with 6-311++G(d,p) basis set. The atomic charges are plotted in Fig. 2. The carbon atom (C8) in p-tolunesulfonate was more electropositive ($0.647e$), this carbon atom was enclosed by three electronegative carbon atoms (C7, C9 and C11). The carbon atoms have a both positive and negative charge which shows that they are highly influenced by their substituent. Also, Nitrogen (N19) atom has more electro negativity ($-0.528e$). The presence of negative charge on nitrogen and oxygen atoms and net positive charge on hydrogen atoms may suggest the formation of intra-molecular interaction in solid forms.

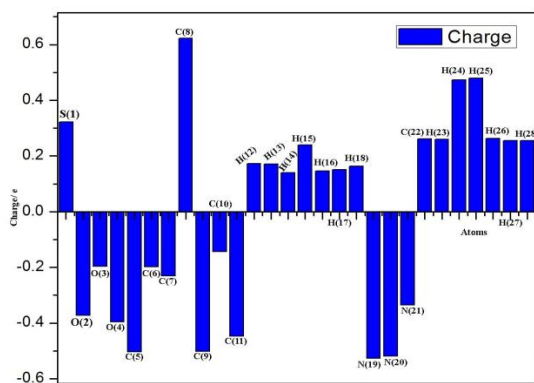


Figure 2 Mulliken charge distribution of GPTS

3.2 Frontier Molecular orbital calculations

Organic molecules that contain conjugated π -electrons characterized as hyper-polarizabilities analyzed by means of vibrational spectroscopy, electronic spectroscopy and quantum mechanical

calculation [8]. The highest occupied molecular orbital (HOMO) and lowest unoccupied molecular orbital (LUMO) are called as frontier molecular orbitals. Energy level diagram of molecular orbits of GPTS is shown in Fig.3. Energy difference between HOMO and LUMO analysis is called as band-gap which is an important parameter to indicate the stability of the structure. The HOMO–LUMO analysis has also been used to elucidate the charge transfer phenomena within the molecule. The calculated energy values of HOMO and LUMO for the compound are 6.017 eV and 1.417. The frontier molecular orbital energy gap value is 4.6 eV. These results show that the molecule has small frontier energy gap. This lowest energy gap is connected with the high chemical reactivity and occurrence of charge transfer within the molecule [9].

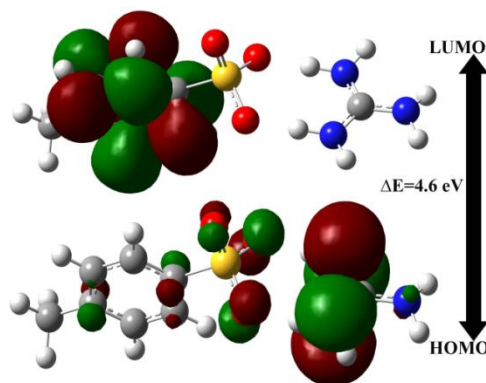


Figure 3 Energy level diagram of molecular orbits

3.3 Molecular electrostatic potential Surface

The Molecular Electrostatic Potential (MEP) is the most useful electrostatic property to study the relation between structure and activity. The MEP maps of the title molecule of conformers are shown in Fig.3, whereas electrophilic attack is presented by negative (red) regions, nucleophilic reactivity is shown by the positive (blue) regions of MEP map of GPTS. As seen from the Fig.3, the red region is mainly localized on the oxygen atoms of Sulfonate, whereas the nucleophilic reactivity of the molecule is mainly localized on the surface of H atoms bound to amine group and also H atoms in guanidinium cation.

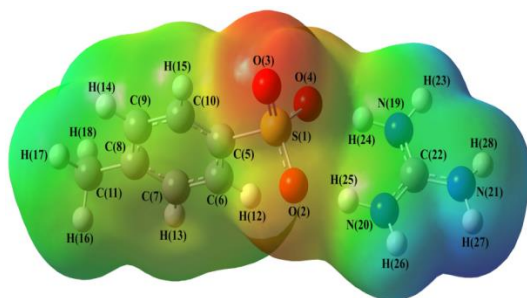


Figure 4 MEP maps GPTS

3.4 Nonlinear optical analysis

Based on the finite-field approach, NLO parameters such as electronic dipole moment, molecular polarizability, anisotropy of polarizability and molecular first hyperpolarizability of present compound were investigated given in Table 1. The large value of first-order hyperpolarizability, which is the measure of the nonlinear optical activity of the molecular system, is associated with the intermolecular charge transfer, resulting from the electron cloud movement through the π -conjugated framework from the electron donor to electron acceptor groups. The first order hyperpolarizability was calculated for the GPTS structure is 8.699×10^{-36} esu, which is nearly 6 times greater than standard urea [10]. The above results show that the present molecule is a promising material for the third order NLO applications.

4. Conclusion

The optimized molecular structure, Frontier molecular Orbital, Mulliken charge distribution and NLO analysis of guanidinium p-toluenesulfonate were investigated by quantum chemical calculations with DFT / B3LYP methods invoking 6-311++G (d, p) basis sets. The Mulliken charge analysis confirms the charge distribution occurs between the molecules. The HOMO and LUMO energies study give the information of electron affinity, ionization potential, chemical hardness and chemical potential of the molecule. The first order hyperpolarizability value is

nearly 6 times greater than that of urea and which shows that the GPTS is a promising material for optoelectronic applications.

Table 1 Non linear optical parameters of GPTS

Parameter	a.u	esu($\times 10^{-24}$)	Parameter	a.u	esu $\times 10^{-33}$)
μ_x	-25.861		β_{xxx}	-	-8136.59
μ_y	-2.002		β_{xxy}	-	-892.746
μ_z	-0.596		β_{xyy}	-69.372	-613.183
μ	25.945		β_{yyy}	-9.412	-83.191
α_{xx}	12.781	1.894	β_{xxz}	24.168	213.622
α_{xy}	-1.904	-0.282	β_{xyz}	-20.227	-178.786
α_{yy}	-120.076	-17.795	β_{yyz}	-41.731	-368.859
α_{xz}	5.083	0.753	β_{xzz}	14.812	130.923
α_{yz}	3.262	0.483	β_{yzz}	5.586	49.371
α_{zz}	-132.073	-19.573	β_{zzz}	-0.037	-0.3270
α	-79.789	-11.825	β_0	980.869	8699.33
$\Delta\alpha$	267.843	39.694			

Acknowledgement

The author V. Siva is grateful to Kalasalingam Academy of Research and Education, Krishnankoil, India for providing financial support as the Post Doctoral Fellowship. Also, financial assistance from Council of Scientific and Industrial Research, India through the Minor Research Project (No. 03 (1276)/13/EMR-II) is gratefully acknowledged by V. Siva and S. Asath Bahadur.

REFERENCES

- [1] Ishikawa T., Isobe T., Modified Guanidines as Chiral Auxiliaries, *Chem. Eur. J.*, 8 (2002), 552–557.
- [2] Ward M.D., Fagan P.J., Calabrese J.C., Johnson D.C., Electrostatic structural enforcement in low-dimensional solids. Synthesis, structure, and electronic properties of polycationic ruthenium complexes with polycyanoanions, *J. Am. Chem. Soc.*, **111** (1989), 1719.
- [3] Hoong-Kun Fun, Suhana Arshad, Dinesha, Sandeep Laxmeshwar, G.K. Nagaraja Bis(4-fluoroanilinium) sulfate *Acta Cryst. E67*: (2011) 2408–2417.
- [4] V. Siva, A. Shameem, S. Suresh Kumar, M. Raja, S. Athimoolam, S. Asath Bahadur (2017) Structural, spectral, Quantum chemical and thermal studies on a new NLO crystal: Guanidinium Cinnamate, *J. Mat. Sci: Mat. Electr.* 28:12484–12496.
- [5] Bryndal, Ledoux-Rak I, Lis T, Ratajczak H (2014) Search for molecular crystals with NLO properties: 5-Sulfosalicylic acid with nicotinamide and isonicotinamide, *J. Mol. Struct.* 1068:77-83.
- [6] M.J. Frisch et al, Gaussian Inc., Wallingford, CT, (2009).
- [7] R. Dennington, T. Keith, J. Millam. Gauss View, Version 5.0.8 Semicem Inc., Shawnee Mission KS. (2013).
- [8] D. Sajan, IH. Joe, VS. Jayakumar, J. Zaleski, *J. Mol. Struct.* 785 (2006) 43–53.
- [9] K. Parimala, V. Balachandran, Structural study, NCA, FT-IR, FT-Raman spectral investigations, NBO analysis and thermodynamic properties of 2,4-difluoroacetophenone by HF and DFT calculations, *Spectrochimica Acta Part A: Molecular and Biomolecular Spectroscopy* 110 (2013) 269–284
- [10] Siva V, Suresh Kumar S, Suresh M, Raja M, Athimoolam M, Asath Bahadur S N–H···O hydrogen bonded novel nonlinear optical semiorganic crystal (4-methoxyanilinium trifluoroacetate) studied through theoretical and experimental methods, *J. Mol. Struct.* (2017) 1133:163-171,

INVESTIGATION ON CRYSTAL GROWTH AND SOLID STATE PROPERTIES OF NONLINEAR OPTICAL SINGLE CRYSTAL: 2-AMINOPYRIDINIUM PHTHALATE

M. Ajay, A. Ajaykumar, M. Ajitha, V. Siva, S. Asath Bahadur*

Department of Physics, International Research Centre, Kalasalingam Academy of Research and Education, Krishnankoil- 626 126, India.

Corresponding Author: s_a_bahadur@yahoo.co.in

Abstract

Single crystals of 2-aminopyridinium phthalate (2APP) were grown by the slow evaporation method. The unit cell dimensions were determined from single crystal X-ray diffraction analysis. The X-ray diffraction measurements showed that the crystal belongs to non-centrosymmetric space group $P2_1$ of monoclinic system. Dielectric constant and dielectric loss of 2APP crystal were evaluated for the frequency range 1 kHz–1 MHz in the temperature region 303K–363K. The mechanical properties of the grown crystals have been analyzed by Vickers microhardness method. UV–vis–NIR studies reveal that 2-aminopyridinium phthalate has UV cutoff wavelength at 340 nm. Its SHG efficiency has been tested by Kurtz powder method.

Keywords Optical materials, Organic crystal, X-ray diffraction, Mayer index, Non-linear optics

1. Introduction

In modern society the organic nonlinear optical materials are playing vital role due to their potential application in optical switches, modulators, optical limiters, and optical data storage [1,2] and also they have greater optical susceptibilities, and higher optical thresholds for laser power compared to inorganic materials, as well as inherent ultrafast response times. Organic molecules containing conjugate systems have some advantages over inorganic materials because of the possibility of highly enhanced electronic nonlinear optical polarization responses. Organic crystal exhibiting nonlinear optical effects have been explored with a view to developing optical devices, for example optical modulators and frequency-doubling devices [3-5]. In continuation to this, the present work investigates the second order NLO response of 2-aminopyridinium phthalate single crystal to explore its possible applications in nonlinear optics. The crystals grown by slow solvent evaporation have been characterized by single crystal XRD, Dielectric, Vicker's microhardness, UV-Visible and Kurtz perry technique.

2. Experimental

2.1 Crystal growth and characterization

2-aminopyridinium phthalate crystals were grown by dissolving equimolar ratio of both 2-aminopyridine and phthalic acid in methanol as a polar solvent. The whole solution was prepared by stirring for 3 h using a magnetic stirrer to obtain a homogeneous mixture. The completely dissolved solution was filtered using filter paper to remove the suspended impurities and allowed to crystallize by slow evaporation of solvent. After 10 days, transparent single crystals of 2APP were obtained. The Photograph of the grown crystal is given in Figure 1.

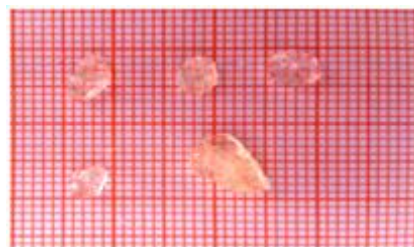


Figure 1 Photograph of 2APP crystal

The unit cell dimensions of the grown single crystal were determined from single crystal XRD by ENRAF NONIUS CAD4-F single crystal X-ray diffractometer (graphite-monochromated, $\text{MoK}\alpha=0.71073\text{\AA}$). Microhardness measurements on GPTS crystal were carried out using a Leitz Wetzlar Vicker's microhardness tester attached with an optical microscope. Measurements of dielectric loss and dielectric constant were carried out for the crystals using HIOKI LCR HITESTER 3532-50. The UV-Vis-NIR transmittance spectrum is recorded in the wavelength range of 200-1100 nm. UV-Vis NIR transmittance analysis was carried out between 200 and 1100 nm covering the entire ultraviolet and visible regions using the UV-1700 Shimadzu spectrometer.

3. Results and Discussion

3.1 Structural and Mechanical analysis

The XRD analysis showed that the crystal belonged to the monoclinic crystal system with space group $P2_1$. The cell parameters are $a = 5.159(3)\text{ \AA}$, $b = 8.612(4)\text{ \AA}$, $c = 13.574(5)\text{ \AA}$, $\alpha = 90^\circ$, $\beta = 97(3)^\circ$ and $\gamma = 90^\circ$. The strength of the materials for device fabrication is explicitly dependent on an important parameter called hardness. Hardness is one of the most significant mechanical properties which direct the strength of the material and is mostly related with the crystal structure and molecular bonding. Mechanical strength of the grown crystal is examined by using a Vickers microhardness tester. Loads of different magnitudes (25 g, 50 g, and 100 g) are applied on the crystal for the fixed interval of indentation time of 10 s. To find the Vickers hardness, several indentations are made on the (1 0 0) face of the crystal. The vickers microhardness number H_v of the crystal is calculated using,

$$H_v = 1.8544P/d^2$$

Where P is the applied load in gram and d is diagonal length in micrometer. Fig. 2 (a) shows the variation of microhardness number with applied load and it is noted that hardness value increases with the increase of load. Hardness is found to be increasing with load such that when the load attains the maximum value of 100 g, the harness is found to be 86.42 kg/mm^2 . Fig. 2(b) shows the plot variation of $\log P$ with $\log d$. The slope of the graph gives Mayer's index (n) and it is calculated to be 3.2. Mayer's index value comes out to be 1 to 1.6 for hard materials and greater than 1.6 for soft materials [6]. For that reason, 2APP crystal is identified to be soft material category.

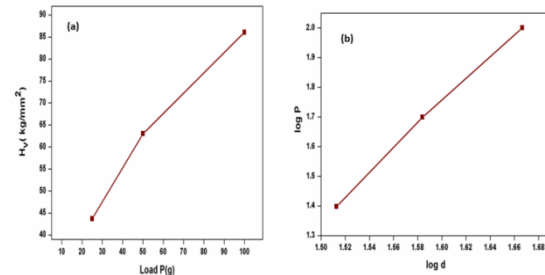


Figure 2 (a) Hardness Number (H_v) vs Load (P)
(b) Variation of $\log P$ with $\log d$

3.2 Dielectric analysis

The study of the dielectric constant of a material gives an outline about the nature of atoms, ions and their bonding in the material. The space charge polarization will depend on the purity and perfection of the material. [7]. Fig 3 and Fig. 4 shows that the dielectric constant and the dielectric loss variation with different temperatures.

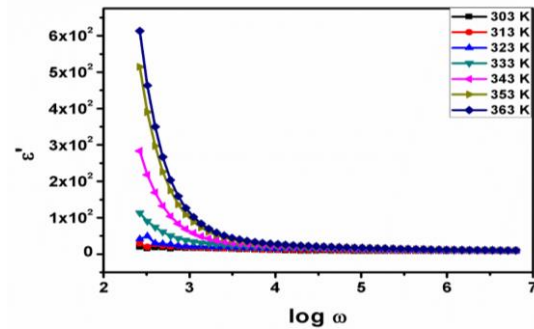


Figure 3 Variation of dielectric constant with frequency

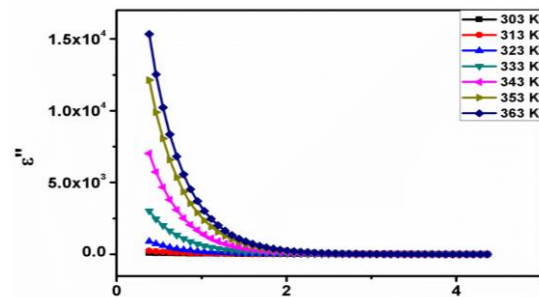


Figure 4 Variation of dielectric loss with frequency

Dielectric study is observed in the high frequency region, in which ϵ' and ϵ'' decreases slightly with increasing frequency. By increasing the frequency,

the space charge polarization cannot be sustained at a point and comply with the external field. This action gives only the diminishing values of dielectric constant. It is observed that the dielectric constant is increasing with temperature due to the orientation of dipoles which facilitate the increase in permittivity at higher temperature [8]. The characteristic of low dielectric loss at high frequencies for a given sample suggested that the sample possesses an enhanced optical quality with lesser defects and this parameter play a vital role in the fabrication of optical devices [9].

3.3 Optical and Nonlinear response

The optical absorbance spectral analysis is an important study for any nonlinear optical material because a nonlinear optical material can be of practical use only if it has wide transparency window without any strong absorptions in the ultraviolet, visible and infrared regions. The obtained optical transmission spectrum of 2APP is shown in Fig.5. The results specify that the grown crystal presents an excellent transparency from 340 nm to 1100 nm and its UV transparency cutoff occurs at 340 nm. The optical transmittance of the material is in the wavelength range from 300 nm to 1100 nm. Such a broad transparency window is a basic requirement for nonlinear optical applications [10].

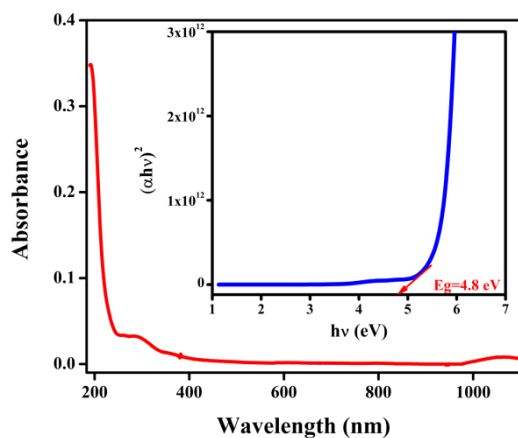


Figure 5 optical transmission spectrum of 2APP

The band gap of the grown crystal was estimated by plotting $(\alpha h\nu)^2$ versus $h\nu$ (eV) as shown in Fig. 5 and extrapolating the linear portion near the onset of absorption edge to the energy axis. The band gap value of the grown crystal was found to be 4.8 eV.

Kurtz and Perry powder technique was used to study the NLO behavior of the 2APP crystal. The grown 2APP crystals have shown a non-centrosymmetric space group $P2_1$, which is the prerequisite for the NLO activity. The Nd:YAG laser beam of wavelength 1064 nm and energy 2.7 mJ/pulse was incident on the crystalline powder of crystal with uniform particle size of 63 μ m. KDP crystalline powder of identical size of 63 μ m was used as reference for the conversion efficiency of the SHG measurement. The output SHG power intensity of 2APP is 1.5 times greater than of the KDP.

Conclusion

Hydrogen bonded NLO crystal of 2-Aminopyridinium phthalate has been grown by slow solvent evaporation technique at room temperature. The molecular structure of the grown crystal was determined by single crystal diffraction technique. The absence of significant absorption in the entire visible region and lower cut-off wavelength and wide band gap indicates the suitability of 2APP for optical applications. The band gap of the grown crystal is found to be 4.8 eV. The SHG efficiency of 2APP was demonstrated for the first time and it is found to be 1.5 times greater than that of well-known KDP material. All the above findings revealed that the title compound is a potential candidate for the NLO application.

Acknowledgements

The authors thank the management of Kalasalingam Academy of Research and Education for providing facilities to carry out the research.

REFERENCES

- [1] Siva Vadivel, Asath Bahadur Sultan, Shameem Abdul Samad, Athimoolam Shunmuganarayanan, Raja Muthu, Synthesis, structural elucidation, thermal, mechanical, linear and nonlinear optical properties of hydrogen bonded organic single crystal guanidinium propionate for optoelectronic device application *Chemical Physics Letters* 707: 165–171, 2018.
- [2] Suresh M, Asath Bahadur S, Athimoolam S, Synthesis, growth and characterization of a new hydrogen bonded organic tosylate crystal: 1-alaninium p-toluenesulfonate for second order nonlinear optical applications, *Journal of Materials Science: Materials in Electronics* 27(5):4578–4589, 2016.
- [3] Siva V, Shameem A, Suresh Kumar S, Raja M, Athimoolam S, Asath Bahadur S. Structural, spectral, Quantum chemical and thermal studies on a new NLO crystal: Guanidinium Cinnamate, *Journal of Material Science: Materials in Electronics* 28(17): 12484–12496, 2017.
- [4] R.T. Bailey, G. Bourhill, F.R. Cruickshank, D. Pugh, J.N. Sherwood, and G.S. Simpson, The Linear and Nonlinear Optical Properties of the Organic Nonlinear Material 4-Nitro-4-Methylbenzylidene Aniline. *J. Appl. Phy*, 73 (1993) 1591-1597.
- [5] A. Priyadharshini, S. Kalainathan, Bulk crystal growth, spectral, optical, thermal, electrical and third-order NLO properties of benzylidene malononitrile derivative single crystal: a promising material for nonlinear optical device applications, *J Mater Sci: Mater Electron*. 29,(2018) 2698–2708.
- [6] E.M. Onitsch, *Über die Mikrohartigkeit der Metal. Mikroskopie*, 2 (1947) 131–151.
- [7] R. Dhanjayan, S. Gunasekaran, S. Srinivasan, Synthesis, crystal structure, optical, thermal and dielectric studies of a potential novel organic material: L-histidinium fumarate Fumaric acid monohydrate single crystal *Mat. Lett.*, 206 (2017) 221-224
- [8] Karthiga Devi P, Venkatachalam K, Growth, spectroscopic, optical, thermal, dielectric and DFT studies of ammonium picrate: a nonlinear optical crystal, *Journal of Material Science: Materials in Electronics*. 27(8):8590–8598, 2016.
- [9] V. Vijayalakshmi, P. Dhanasekaran, N.M. Ganesan, Influence of rare earth gadolinium nitrate addition on structural, dielectric, linear and nonlinear optical properties of glycine single crystals, *J. Cryst. Growth*, 493 (2018) 30-33
- [10] A. Mosset, M. Bagieu-Beucher, A. Lecchi, R. Masse, J. Zaccaro, Crystal engineering strategy of thiocyanates for quadratic nonlinear optics. $\text{Hg}_3\text{CdCl}_2(\text{SCN})_6$ and $\text{Hg}_4\text{CdBr}_4(\text{SCN})_6$, *Solid State Sci.* 4 (2002) 827.

EFFECT OF EUROPIUM CONCENTRATIONS ON LUMINESCENCE PROPERTIES OF Dy³⁺ DOPED BORATE GLASSES FOR WHITE LEDS

M.Vijayakumar^{1,*}, S.K. Tiwary¹, K.Marimuthu²

¹Department of Applied Physics, Jabalpur Engineering College, Jabalpur - 482 011, M.P., India

²Department of Physics, Gandhigram Rural University, Gandhigram- 624 302, TN, India

*Email: mvijayakumarcnp@gmail.com

Abstract

A novel Dy³⁺:Eu³⁺ co-doped borate glasses have been prepared and their spectroscopic behaviors were characterized through absorption, luminescence and decay spectral measurements. The effect of Eu³⁺ ions on the Dy³⁺ luminescence, yellow to blue (Y/B) intensity ratio and the chromaticity color coordinates were measured to obtain the white emission. The lifetimes of the ⁴F_{9/2} excited level were found to decrease with the increase in Eu³⁺ ion concentration due to the occurrence of resonant energy transfer between Dy³⁺-Eu³⁺ ions. The non-exponential behavior of the decay curves were fitted with Inokuti-Hirayama (IH) model thus suggests that the interaction between donor and acceptor ions in the energy transfer process is of dipole-dipole nature.

1. Introduction

In the recent years larger attention is focused on rare earth (RE) doped glasses to fabricate the next generation solid state devices namely white light-emitting diodes (W-LEDs) due to their applications in LCD, automotive displays and solid state lighting sources [1]. One of the most common methods to develop the WLEDs is to combine the blue emitting LEDs with a frequency converting phosphors with organic resins as an affixing material. These conventional WLEDs possess shorter lifetime due to ageing and heating effect that affects the organic resins [2]. To overcome these drawbacks, RE³⁺ doped glasses have proven themselves as the better choice for WLED applications due to its advantages like longevity, high brightness, low power consumption and no ageing effects. Generally spectroscopic properties of the RE-doped glasses depend on the environment around the RE ions which are useful to modify the spectroscopic properties by choosing different chemical composition [2]. Addition of heavy metal oxides into the borate glasses are found to increase the chemical durability, thermal and mechanical stability of the glass materials and further increases the radiative transition rates of the rare-earth (RE³⁺) ions which in turn lead to have higher luminescence yield [2]. Among the RE ions, Dy³⁺ ions are most suitable to stimulate the white light emission due to its ⁴F_{9/2}→⁶H_{15/2} and ⁴F_{9/2}→⁶H_{13/2} intense emission peaks corresponding to the blue and yellow region respectively. In order to increase the red component of the emission spectra, the Eu³⁺ ions were co-doped with Dy³⁺ ions in different host matrices. Usually the Dy³⁺ ions act as a sensitizer to the Eu³⁺ ions because the metastable state of the Dy³⁺ ion is having higher energy than the metastable state of the Eu³⁺ ions [2]. In the present work, Dy³⁺:Eu³⁺ co-

doped borate glasses have been prepared and their spectroscopic and energy transfer behavior were studied and reported.

2. Experimental

Borate glasses were prepared by following melt quenching technique with the composition 60B₂O₃+10Al₂O₃+10PbO+20ZnF₂+0.5Dy₂O₃+xEu₂O₃ (where x=0.05, 0.1, 0.25, 0.5, 1.0 and 2.0 in wt%). The 15 gm batch of each chemical composition were weighed and thoroughly mixed in an agate mortar. The homogenous mixture was taken into a porcelain crucible and kept in the electrical furnace at around 1050 °C for 1.30 hours. The molten flux was air quenched by pouring it on to a preheated brass plate keeping at 375 °C and annealed for 8 hours. The prepared glasses were slowly brought to the room temperature and polished on both sides. Excitation and emission spectra were recorded in the spectral region 400–700 nm using the Perkin Elmer Lambda-55 spectrophotometer by exciting at 391 nm. The lifetime measurements were made using a digital storage oscilloscope (Tektronix TDS1001B) interfaced to a personal computer that records and averages the signal.

3. Results and discussion

3.1. Excitation and Emission spectra

Figure 2 shows the excitation spectra of the AZFBD 0.5E glass monitoring the emission wavelengths at 575 nm and 616 nm corresponding to the ⁴F_{9/2}→⁶H_{13/2} transition of Dy³⁺ ion and ⁵D₀→⁷F₂ transition of Eu³⁺ ion respectively. The

excitation spectra exhibit seven excitation bands from the ⁶H_{15/2} ground state to the various excited

states of the Dy³⁺ ions similar to the reported Dy³⁺ glasses [1].

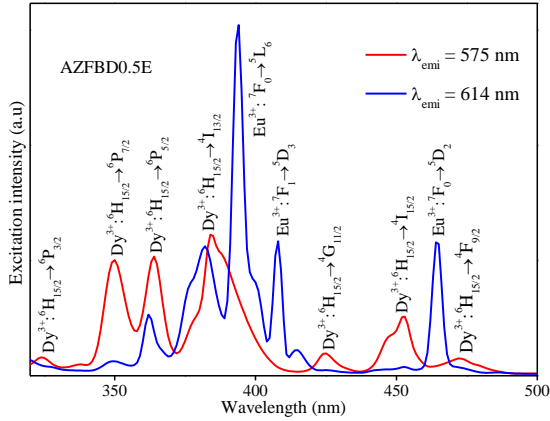


Figure 1: Excitation spectra of the Dy³⁺:Eu³⁺ co-doped AZFBD0.5E glasses

It is observed from figure 1 that, the additional band of Eu³⁺ ions originates from the ⁷F₀ ground state of Eu³⁺ ion to the various excited states have also been observed along with the various excited state of Dy³⁺ ions in the prepared glasses, thus indicate the interaction between Dy³⁺, Eu³⁺ ions. The maximum overlapping of the Dy³⁺ and Eu³⁺ ions excitation bands are observed at 391 nm and this excitation wavelength has been chosen to record the luminescence spectra of the present Dy³⁺:Eu³⁺ co-doped AZFBDxE glasses. The emission spectra of the Eu³⁺ co-doped Dy³⁺: borate glasses were recorded in the wavelength region 400–720 nm by monitoring an excitation at 391 nm. The prepared glasses exhibit both Dy³⁺ ion emission transitions such as ⁴F_{9/2} → ⁶H_{15/2}, ⁴F_{9/2} → ⁶H_{13/2} and ⁴F_{9/2} → ⁶H_{11/2} corresponding to the band positions at 484, 575 and 666 nm and Eu³⁺ ion emission transitions at 592, 612, 653 and 702 nm due to the ⁵D₀ → ⁷F₂, ⁵D₀ → ⁷F₁, ⁵D₀ → ⁷F₀ and ⁵D₀ → ⁷F₃ transitions of the Eu³⁺ ion and thus indicate the energy transfer process takes place in the Dy³⁺:Eu³⁺ co-doped glasses [5]. The Y/B ratio is more sensitive to the host environment around the Dy³⁺ ion and their values are found to be around ‘2’ in all the prepared glasses and the Y/B values confirm the ionic nature of the Dy³⁺ metal-ligand bond.

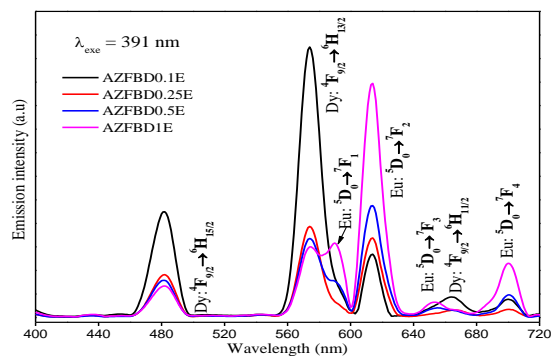


Figure 2: Emission spectra of the AZFBDxE glasses

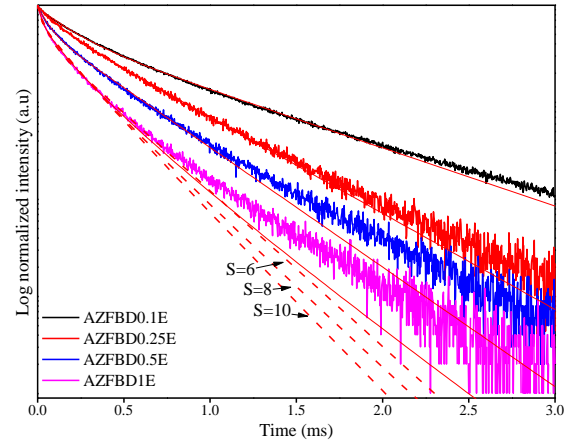


Figure 3: Decay profile of the AZFBDxE glasses

Table 1: The values of τ_{exp} (ms), (x,y) color coordinates, CCT (K), R₀ (nm), Q, C_{DA}($\times 10^{-43}$ cm⁶/s) of the Dy³⁺:Eu³⁺ co-doped of the AZFBDxE glasses

Parameter	AZFBD 0.1E	AZFBD 0.25E	AZFBD 0.5E	AZFB D1E
τ_{exp}	0.737	0.512	0.425	0.357
x	0.35	0.34	0.36	0.41
y	0.38	0.36	0.39	0.38
CCT	4436	4573	3979	3184
R ₀	84.9	76.1	57.4	49.5
Q	0.427	0.965	1.281	2.113
C _{DA}	1.53	2.84	5.62	9.73

The decay curves pertaining to the ⁴F_{9/2} excited level of the Dy³⁺ ions were measured by fixing the exciting at 391 nm and emission at 575 nm for all the prepared glasses and the same is shown in figure 3. The lifetime pertaining to the ⁴F_{9/2} excited level of the Dy³⁺ ions were calculated by taking the first e-fold of the decay curves and the calculated lifetime values are presented in table 1. It is observed from table 1 that, the lifetime values are found to decrease with the increase in Eu³⁺ ion concentration in the prepared borate glasses which confirms the dominant energy transfer between Dy³⁺ and Eu³⁺ ions takes place through non-radiatively. All the decay curves are found to be non-exponential and these behaviors further increases with the addition of Eu³⁺ ions in the prepared glasses. The non-exponential behavior is due to the resonant or nearly resonant energy transfer from the Dy³⁺ ion in an excited ⁴F_{9/2} state to a nearby Eu³⁺ ions ground state (⁷F₀) and the same is shown in figure 4. The possible resonance energy transfer among the Dy³⁺–Eu³⁺ ions is mainly

attributed to the $^4I_{15/2} \rightarrow ^6H_{15/2}$, $^4F_{9/2} \rightarrow ^6H_{15/2}$ and $^7F_0 \rightarrow ^5D_2$, $^7F_0 \rightarrow ^5D_0$ transitions. In order to identify the nature of the non-exponential behavior, the decay curves are fitted within the frame of IH model [6] together with the three possible interaction mechanism including $s=6$, $s=8$ and $s=10$ namely dipole-dipole, dipole-quaropole and quaropole-quaropole, respectively. The interaction parameter C_{DA} , critical distance R_0 and the dipole-dipole energy transfer parameter Q values were calculated and presented in table 1. The decay curves were well fitted with $s=6$ thus indicate that the cross-relaxation energy transfer is caused by the dominant electric dipole-dipole interaction mechanism among the Dy^{3+} - Eu^{3+} ions which is responsible for the non-exponential behavior.

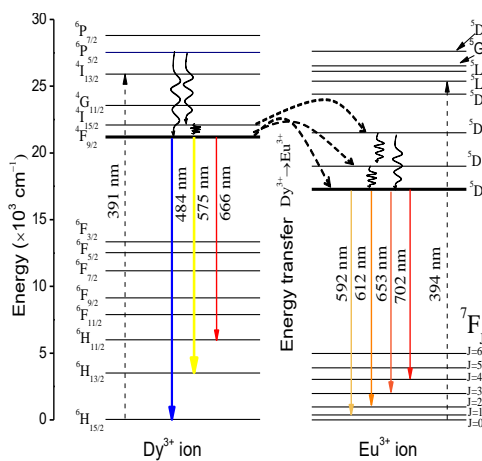


Figure 4: Partial energy level diagram of the $Dy^{3+}:Eu^{3+}$ co-doped AZFBDe glasses

coordinates (x,y) are presented in table 1 along with the color correlated temperature values. It is observed from figure 5 that, all the glasses possess the capacity to produce white light. Among the prepared glasses, AZFBDe.25E glass exhibits (x,y) values as (0.35, 0.36) closer to the standard white light illumination (x=0.33, y=0.33) and also have a CCT value closer to the day light and hence suggested for WLED applications.

REFERENCES

- [1] A.M.Babu, B.C.Jamalaiah, J.S.Kumar, T. Sasikala and L.R.Moorthy, *J.Alloys Compds.* **509**, 457 (2011).
- [2] K. Linganna, Ch. Srinivasa Rao, C.K.Jayasankar, *J. Quan. Spect. Radiative. Trans.* **118**, 40 (2013).
- [3] R. Vijayakumar, K. Maheshvaran, V. Sudarsan, K. Marimuthu, *J. Lumin.* **154**, 160 (2014).
- [4] T. Chengaiah, C.K. Jayasankar, A.M. Babu, L.R. Moorthy, *Mater. Exp.* **4(2)**, 153 (2014).
- [5] K.V. Krishnaiah, K.U.Kumar, C.K. Jayasankar, *Mater. Exp.* **3(1)**, 61 (2013).
- [6] B. C. Jamalaiah, M. V. Vijaya Kumar, K. Rama Gopal, *Opt. Mater.* **33**, 1643 (2011).

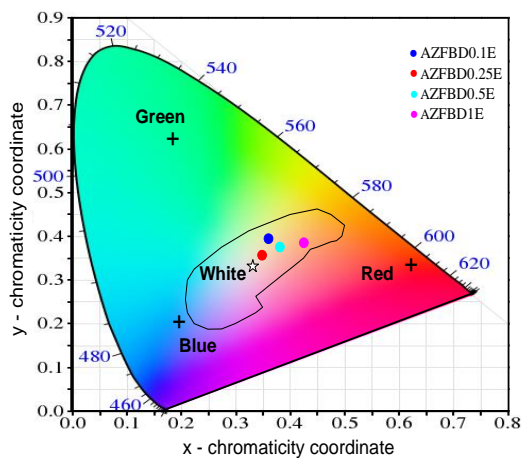


Figure 5: The CIE chromaticity diagram for the AZFBDe glasses

3.4. White light stimulation

Figure 5 shows the CIE 1931 chromaticity diagram of the title glasses and the calculated color

STRUCTURAL, MORPHOLOGICAL AND OPTICAL ANALYSIS OF PVP ASSISTED HEMATITE NANOPARTICLES BY CHEMICAL SYNTHESIS METHOD

P. Pandiselvi, K. Pavithra, S. Ezhil Arasi, S. Arunpandiyar, R. Ranjithkumar, P. Devendran, A. Arivarasan*

Department of Physics, International Research Center, Kalasalingam Academy of Research and Education, Krishnankoil- 626 126, Tamilnadu, India.
Email:arivarasan.nanotech@gmail.com

Abstract

Fe₂O₃ nanoparticles were prepared by simple chemical route. The structural, optical, morphological properties of prepared nanoparticles were obtained by Powder X-ray Diffraction analysis, UV-Visible spectroscopy, and Scanning Electron Microscopy analysis respectively. The average grain size of the prepared nanoparticles was calculated using the Scherrer formula. The absorption maximum of the prepared nanoparticles was obtained at 404 nm.

Keywords: Nanoparticles, Fe₂O₃, XRD, UV-Visible, SEM.

1. Introduction

In past few decades, the role of transition metal oxides has been enormously increasing for their excellent optical and electrical properties which made it for utilizing in various applications such as energy storage devices, catalysis, photodegradation etc, [1,2]. The nanoparticles with magnetic properties have attracted many researchers for their typical physical and chemical properties. By modifying the structure of nanoparticles the properties and applications can be varied. Among various magnetic materials, hematite (Fe₂O₃) nanoparticles has been widely synthesized and used in many applications [2,3]. Also it is an ecofriendly material that is more stable and neutral in all alkaline solutions.

In general, the hematite nanoparticles can be prepared by various techniques such as combustion method, sol-gel technique, hydrothermal, etc., Of all these methods, simple chemical technique is the most common among many researchers as it is done in ordinary room temperature with mild conditions. Iron oxides exhibits variety of nanostructures [4]. Though various structures were available, the quasi spheres like structure exhibits better electrochemical behavior. The iron oxide nanoparticles show excellent theoretical capacitance of about 382.7mF/cm² at 0.5 mA/cm² [5,6]

In this study, the magnetic Fe₂O₃ nanoparticles were prepared through a cost-effective chemical method and

characterized by PXRD, UV-Visible and SEM analysis from which the crystal structure, optical behavior and surface morphology were examined. This work can be further preceded to various electrochemical applications [7].

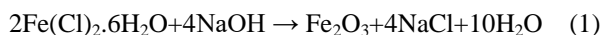
2. Experimental section

2.1. Chemicals

Analytical grade Iron (III) chloride hexa hydrate Fe(Cl)₂.6H₂O, was used as the starting material, polyvinylpyrrolidone ((C₆H₉NO)_n), PVP), sodium hydroxide (NaOH) and ethanol were purchased from Sisco Research Laboratories Pvt. Ltd., Mumbai, India. All chemicals with analytical grade were used as purchased. The entire reaction and electrolyte solutions were freshly prepared with deionized (DI) water. All the synthesis procedures were carried out in room temperature.

2.2. Preparation of Fe₂O₃ nanoparticles

Facile Fe₂O₃ nanoparticles was prepared using Iron (III) chloride hexa hydrate Fe(Cl)₂.6H₂O as precursor material. Stoichiometric amount of Fe(Cl)₂.6H₂O was dissolved in 100 ml DI water. Aqueous solution of NaOH was added drop-wise in order to maintain the pH of reaction mixture at 7. The reaction mechanism was given in equation (1).



In addition, 0.2 g weight % of PVP was added in the resultant solution as surfactant and allowed to constant stir up to 1h. The precipitate obtained was centrifuged several times with DI water and ethanol to remove the un-reactant materials or additives present in the sample. Thus the acquired precipitate was further air dried at ambient temperature then, calcinated at 300°C for 3 h to improve the crystallinity of sample.

2.3. Material characterizations

The prepared hematite nanoparticles were characterized by powder X-ray diffraction analysis, Crystalline nature of prepared Fe_2O_3 nanoparticles were confirmed by powder X-ray diffraction analysis (PXRD) using Bruker X-ray diffractometer (D8 advance ECO) with monochromatic Cu-K_α radiation ($\lambda = 1.5406 \text{ \AA}$). UV-Vis absorption spectrum was recorded by Shimadzu UV 1800 spectrophotometer to examine optical properties of prepared nanoparticles. Surface morphology of Fe_2O_3 nanoparticles was analyzed using ZEISS-EVO 18 Research, Japan, and Scanning Electron Microscope (SEM).

3. Results and Discussion

3.1. XRD

The crystalline structure of prepared PVP assisted Fe_2O_3 nanoparticles were analyzed by powder X-ray diffraction analysis. The PXRD pattern of prepared PVP assisted Fe_2O_3 nanoparticles were shown in figure 1. The range was fixed between 10-80°. The peaks were in good accordance with the bulk Fe_2O_3 (JCPDS card number #89-8104). Eight different maximum peaks were observed in prepared PVP assisted Fe_2O_3 nanoparticles. The 2θ values and their corresponding hkl indices were 24.213° (012), 33.255° (104), 35.722° (110), 40.973° (113), 49.602° (024), 54.232° (116), 62.615° (214), 64.178° (300) respectively. Broader peak suggests that the prepared sample were in nano size with rhombohedral crystal structure. The space group of prepared PVP assisted Fe_2O_3 nanoparticles was found to be R3c(167) with cell parameters $a=5.023 \text{ \AA}$, $c=13.708 \text{ \AA}$. The average crystallite size of prepared PVP assisted Fe_2O_3 nanoparticles were ~12 nm.

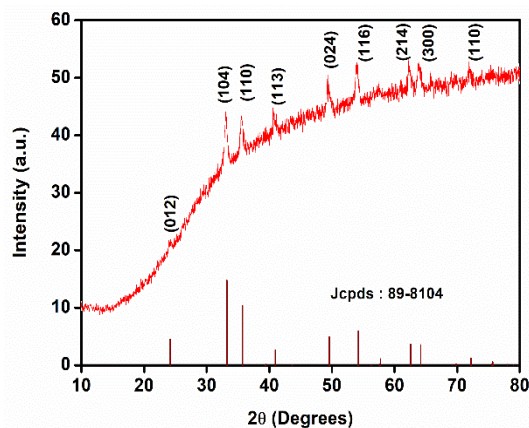


Figure 1. XRD patterns of PVP assisted Fe_2O_3 nanoparticles

3.2. UV-Visible

Figure 2 shows the UV-Vis absorption spectra of prepared PVP assisted Fe_2O_3 nanoparticles. From the UV-Visible absorption spectroscopy analysis, band gap of prepared Fe_2O_3 nanoparticles were obtained. The absorption maximum values were found to be in 404 nm. The peak clearly suggests that the nanoparticles were in nano regime.

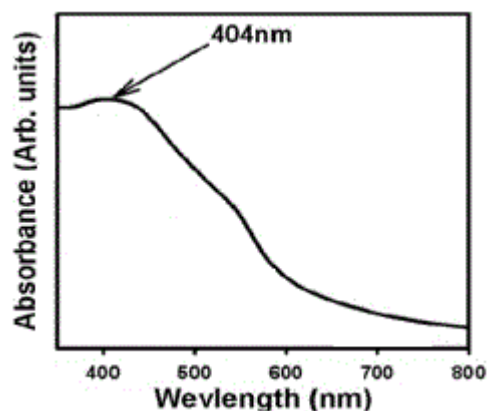


Figure 2. UV-Vis absorption spectrum of PVP assisted Fe_2O_3 nanoparticles

3.3. SEM

Figures 3 (a & b) shows the SEM images of PVP assisted Fe_2O_3 nanoparticles. The morphology of the Fe_2O_3 nanoparticles shows fine particles. The absence of agglomerate reveals the effect of surfactant molecules in

the preparation procedure. The particle size was found to be 100-200 nm. SEM images also show the morphologies of agglomerated particles and surface of the nanocrystalline structures.

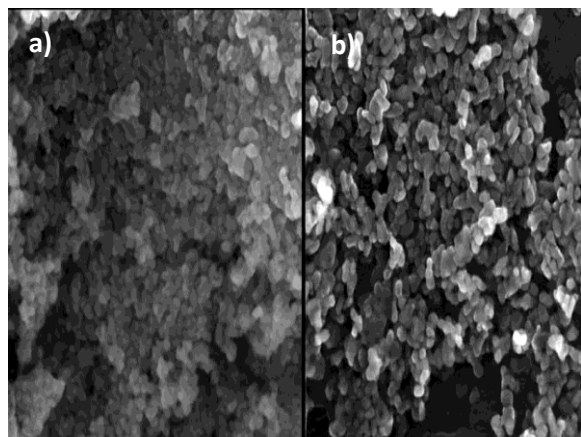


Figure 3. SEM images of PVP assisted Fe_2O_3 nanoparticles

4. Conclusion

Iron oxide nanoparticles were successfully prepared by chemical route. The average crystallite size of the prepared nanoparticles was found to be ~ 12 nm. The XRD studies revealed that that the prepared nanoparticles have the rhombohedral structure. The absorption maximum values of prepared Fe_2O_3 nanoparticles were of about 404 nm. This work can be further carried out with electrochemical studies for energy storage or conversion applications.

5. Acknowledgements

The authors show their gratitude to IRC, Kalasalingam Academy of Research and Education (KARE) for providing research facilities and owe thankful for fund-

ing under the University Research Fellowship (URF) scheme.

REFERENCES

- [1] Eunice Aparecida Campos, Denise Villela Barcza Stockler Pinto, José Irineu Sampaio de Oliveira, Elizabeth da Costa Mattos, Rita de Cássia Lazzarini Dutra, Synthesis, Characterization and Applications of Iron Oxide Nanoparticles – a Short Review, *J. Aerosp. Technol. Manag.*, Vol.7, No 3, 2015, pp. 267-276.
- [2] Young Soo Kang, Subhash Risbud, John F. Rabolt, and Pieter Stroeve, Synthesis and Characterization of Nanometer-Size Fe_3O_4 and $\gamma\text{-Fe}_2\text{O}_3$ Particles, *Chem. Mater.* 1996, 8, 2209-2211.
- [3] Q. Ma, X. Zhang, R. Guo, H. Zhang, Q. Cheng, M. Xie, X. Cheng, Persulfate activation by magnetic $\gamma\text{-Fe}_2\text{O}_3/\text{Mn}_3\text{O}_4$ nanocomposites for degradation of organic pollutants, *Separation and Purification Technology* (2018), doi: <https://doi.org/10.1016/j.seppur.2018.06.060>.
- [4] Fang Yang, Kaibing Xu, Junqing Hu, Construction of $\text{Co}_3\text{O}_4@ \text{Fe}_2\text{O}_3$ core-shell nanowire arrays electrode for supercapacitors, *Journal of Alloys and Compounds*, 729 (2017) 1172-1176.
- [5] Shunli Yin, Xiaomei Wang, Zhigang Mou, Yijie Wu, Hui Huang, Mingshan Zhu, Yukou Dua and Ping Yang, Synergistic contributions by decreasing overpotential and enhancing charge-transfer in $\alpha\text{-Fe}_2\text{O}_3/\text{Mn}_3\text{O}_4/\text{graphene}$ catalysts with heterostructures for photocatalytic water oxidation, *Phys.Chem.Chem.Phys.*, 2014, 16, 11289.
- [6] Yu Liu, Le Yu, Yong Hu, Changfa Guo, Fumin Zhang and Xiong Wen (David) Lou, A magnetically separable photocatalyst based on nest-like $\text{g-Fe}_2\text{O}_3/\text{ZnO}$ double-shelled hollow structures with enhanced photocatalytic activity, *Nanoscale*, 2012, 4, 183.
- [7] Bonil Koo, Hui Xiong, Michael D. Slater, Vitali B. Prakapenka, Mahalingam Balasubramanian, Paul Podsiadlo, Christopher S. Johnson, Tijana Rajh, and Elena V. Shevchenko, Hollow Iron Oxide Nanoparticles for Application in Lithium Ion Batteries, *Nano Lett.* 2012, 12, 2429–2435

STRUCTURAL, MORPHOLOGICAL AND OPTICAL PROPERTIES OF Cu_2CdS_3 THIN FILMS FOR SOLAR CELL APPLICATION

S. Abirami, M. Gayathri, S. Asath Bahadur*

Department of Physics, International Research Centre,
Kalasalingam Academy of Research and Education, Krishnankoil 626 126.

*Corresponding Author: s_a_bahadur@yahoo.co.in

Abstract

The Cu_2CdS_3 thin film was deposited on glass substrate by successive ionic layer adsorption and reaction method. The sample was characterized for structural, morphological and optical properties. The powder X-ray diffraction pattern result showed that the deposited film has Cu_2CdS_3 phase with hexagonal structure. The SEM study reveals that the deposited film is rough and compact without any visible cracks or pores. The film has high absorbance in the visible range and energy band gap of 1.67 eV. This makes the material as a good candidate for low cost and environment friendly thin film solar cells.

Keywords: Cu_2CdS_3 ; SILAR; PXRD; UV-Vis;

1. Introduction

In recent years, there is a great deal of interest in research on chalcopyrite semiconductors due to their suitable optical bandgap and high optical absorption coefficient for potential application in thin film solar cells [1]. The copper based compound semiconductor materials are used as absorber materials in photovoltaic technology. Also, in recent years, importance is given to nontoxic semiconductors from both the fundamental and technological point of view.

The CuCdS_2 thin film exhibited hexagonal structure with an optical band gap of 1.42 eV, it is a p-type semiconductor and suitable candidate for photovoltaic cells. They augmented the crystallinity of CuCdS_2 thin films and explored that the nature of electrical conductivity could be tuned between n-type and p-type [2]. It is also observed, a decreasing trend in the optical band gap of $\text{Cu}_{(1-x)}\text{Cd}_x\text{S}_2$ thin films from 2.45 eV to 2.2 eV with the increase in copper concentration. The synthesized zinc blend CuCdS nanocrystals prepared by single step synthesis has the application in tunable color LEDs [3]. The concentration of copper strongly influences on the optical and electrical properties of copper sulphide and consequently decides the application [4].

The Cu_2CdS_3 thin film has been synthesized by non-vacuum chemical method of successive ionic layer adsorption and reaction (SILAR) [5]. SILAR technique, compared to other chemical methods is a simple, less

expensive and less time consuming method for the deposition of semiconducting thin films. It is also relevant in the deposition of large area thin films. In SILAR method, substrate is successively dipped into the precursor solution during the deposition process and has easy control on film thickness by varying number of deposition cycles.

In this method, deposition cycles and dipping time are important parameters for preparation of nano-size Cu_2CdS_3 thin films. Sufficient reaction time favors the complete chemical reaction and hence produces pure phase compounds without secondary phases. The present work reports the synthesis of Cu_2CdS_3 thin film deposited on to glass substrate by SILAR method and its characterization for structural, morphological and optical properties.

2. Experimental

2.1 Materials and Methods

All chemicals purchased for the present work are of analytical grade and used without any further purification. Copper Chloride pentahydrate ($\text{CuCl}_2 \cdot 5\text{H}_2\text{O}$), Cadmium Chloride hydrate ($\text{CdCl}_2 \cdot \text{H}_2\text{O}$) and Thiourea ($\text{CH}_4\text{N}_2\text{S}$) were used as precursors, double distilled water, acetone as solvent and micro slide glass as substrate.

Prior to the film deposition process, the substrates (2.5mm × 7mm) were cleaned in soap oil solution, boiled chromic acid for 60 minutes, and then sequentially rinsed in double distilled water. The rinsed glass substrates are vertically immersed in dilute HF for 2 minutes

to etch the depositing substrates and finally the substrates were cleaned using ultrasonic water bath for 30 minutes, in order to eliminate surface dust particles and organic impurities present if any.

To deposit the nano-scale Cu_2CdS_3 thin film by a simple SILAR method, the following baths were prepared. The cationic and anionic precursor solutions were 0.1 M CuCl_2 , 0.05 M CdCl_2 and 0.15 M $\text{CH}_4\text{N}_2\text{S}$ dissolved in 50 ml of double distilled water respectively. The one cycle of deposition of Cu_2CdS_3 thin films by SILAR method involves the following steps.

(i) Immersion of the cleaned substrate in cationic precursor solution for 40 seconds. where cations were adsorbed on the surface of the substrate.

(ii) Thus the substrate was rinsed for 10 seconds in double distilled water placed on magnetic stirrer, maintained at 65°C to remove the loosely bound cations.

(iii) The substrate was then immersed in the anionic precursor solution for 40 seconds. The sulfide ions reacted with adsorbed cationic ions on the active center of the substrate surface.

(iv) Finally, the substrate was rinsed for 10 s in double distilled water placed on magnetic stirrer, maintained at 65°C , to remove loosely bound unreacted ions present on the substrate.

The thin films taken for the present work is prepared with 40 cycles.

Further the prepared film was dried at 60°C under the oven for 1h and annealed at 300°C for 1h in muffle furnace to increase the crystallinity. In SILAR method concentration, temperature of precursor solutions, dipping time and number of cycles are important parameters to get a good film

2.2 Materials characterization

The structural properties of Cu_2CdS_3 films were studied using high resolution powder X-ray diffractometer with $\text{CuK}\alpha$ radiation (1.54056 \AA). The surface morphology and compositional study of films were carried out using scanning electron microscopy (SEM), (JEOL, JSM-6360, Japan) attached with an energy dispersive X-ray (EDAX) analyzer. Optical absorption studies of the films deposited on glass substrates were carried out in the wavelength range of 300–1100 nm using UV–vis spectrophotometer (Shimadzu-1800, Japan).

3. Results and Discussion

3.1 Structural analysis

Powder X-ray diffraction (XRD) is a useful tool to analyze the crystalline phase of the deposited film. The XRD pattern of the annealed sample is shown in Fig. 1. The film shows improved crystallinity after annealing. The major X-ray diffraction peaks appeared at $2\theta = 24.9, 26.5, 28.2, 36.6, 43.8, 47.9, 51.9, 54.98$ and 59.4° were indexed as (100), (002), (101), (102), (110), (103), (112), (004) and (202) planes respectively of Cu_2CdS_3 (JCPDS No. 80-0006). The crystallite size (D) of the sample can be estimated according to the Scherrer's equation as follows [6].

$$D = \frac{k\lambda}{\beta \cos\theta}$$

Where k is a structural constant (0.9), λ the X-ray wavelength by the source of $\text{CuK}\alpha$, β - full width at half maximum and θ the Bragg diffraction angle. Thus, the crystallite size of the sample calculated using the high intensity peak corresponding to the plane of (002) is about 17 nm.

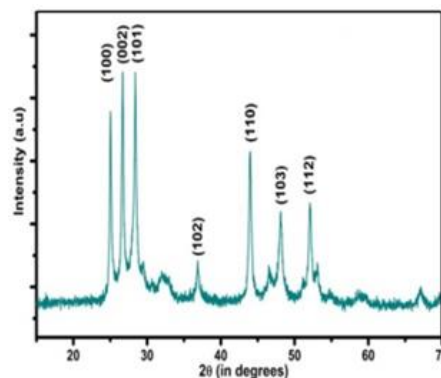


Figure 1 Powder XRD pattern of Cu_2CdS_3 thin film

3.2 Morphology

The film surface morphology of the annealed layer on glass substrate was taken by SEM is shown in Figure 2. According to this micrograph, it is evident that the surface has got well deposited and without any visible cracks or holes. However, the sample surface is covered partially by spherical shape micro-crystallites with various diameters ranging from 99 to 200 nm.

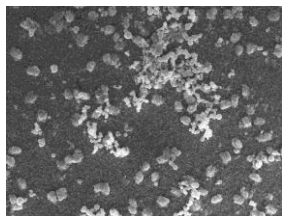


Figure 2 SEM image of the Cu_2CdS_3 thin film

3.3 Optical properties

Figure 3 shows the UV-Vis absorbance spectra of Cu_2CdS_3 film. It is seen that the film shows good absorbance in the entire visible spectrum ranges of 400 to 800 nm confirm this is a good candidate for low cost and environment friendly solar cell absorber layer and has suitable band gap for thin film solar cell. The band gap of the material formed in the deposits is calculated from the absorbance data using the Tauc's relation [7].

$$\alpha = \frac{A(E - E_g)^n}{E}$$

From equation α is the absorption coefficient, E is the photon energy in eV, E_g is the band gap energy in eV. The superscript n , is a constant which is assigned values 1/2, 3/2 and 3 for direct allowed, indirect forbidden and indirect allowed materials respectively. Figure 4 shows the Tauc's plots for the annealed Cu_2CdS_3 film. The optical energy band gap of the Cu_2CdS_3 film is calculated as 1.67 eV.

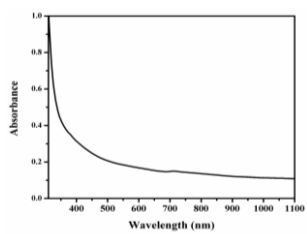


Figure 3 UV-Vis absorbance spectrum of Cu_2CdS_3 thin film

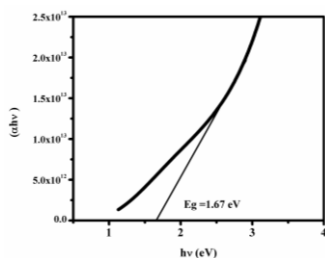


Figure 4 Tauc plot of Cu_2CdS_3 thin film

4. Conclusion

The Cu_2CdS_3 thin films were deposited on micro glass slide by successive ionic layer adsorption and reaction method. Powder XRD shows good crystalline nature and grain size of the Cu_2CdS_3 thin film evaluated by Scherrer's equation as 17 nm. The morphology of annealed film shows spherical particles on the substrate with diameter size as 99 nm and well uniformly deposited without any crack. Optical property of the film shows good absorbance in visible wavelength it is suitable for solar cell absorber material because the optical energy band gap is 1.67 eV respectively.

Acknowledgements

The authors thank the Tamilnadu State Council for Science and Technology, Tamilnadu, for the financial support (Lr. No.: TNSCST/SPS/AR/2018-19).

REFERENCES

- [1] J. Tang, S. Hinds, S. Kelley, E. Sargent, *Chem. Mater.*, 20(2008)6906–6910.
- [2] V. Nirmal Kumar, R. Suryakarthick, S. Karuppusamy, M. Gupta, Y. Hayakawa, R. Gopalakrishnan, *RSC Adv.*, 5 (2015) 23015–23021.
- [3] A.H. Khan, A. Dalui, S. Mukherjee, C.U. Segre, D.D. Sarma, S. Acharya, *Angew. Chem.* 127 (2015) 2681–2686.
- [4] Z. Fang, C. Wang, F. Fan, S. Hao, L. Long, Y. Song, T., *Chin. J. Chem.* 31 (2013) 1015–1021.
- [5] A. Shameem, P. Devendran, V. Siva, M. Raja, S. AsathBahadur, A. Manikandan, *J Inorg Organomet Polym*, 27(3) (2017) 692-699.
- [6] S Das, K Sa, P C Mahakul, J Raiguru, I Alam, BVRS Subramanyam, P Mahanandia., doi:10.1088/1757-899X/338/1/012062
- [7] R. Sani, R. Manivannan, S.N. Victoria, *Chalcogenide Lett.*, 14 (5) (2017)165–170.

INVESTIGATION OF NANOCRYSTALLINE $\text{Cu}_2\text{ZnSnS}_4$ THIN FILM ABSORBER LAYER FOR PHOTOVOLTAIC APPLICATION

A. Murugan, V. Siva, A. Shameem, S. Asath Bahadur*

Department of Physics, International Research centre,
Kalasalingam Academy of Research and Education, Krishnankoil-626 126, India.

*Corresponding Author: s_a_bahadur@yahoo.co.in

Abstract

$\text{Cu}_2\text{ZnSnS}_4$ thin films have been deposited on to glass substrate by successive ionic layer adsorption and reaction method. The annealing films were characterized by structural, morphological and optical property has been studied. The powder X-ray diffraction studies revealed the formation of polycrystalline $\text{Cu}_2\text{ZnSnS}_4$ films and confirmed tetragonal structure, grain size, and dislocation density was calculated. Scanning electron microscope images showed smooth, compact and uniform film formation after annealing. The UV-Vis spectroscopy data show that the films have a high optical absorption coefficient in the visible region.

Keywords: $\text{Cu}_2\text{ZnSnS}_4$, SILAR, PXRD, SEM, Optical property

1. Introduction

Solar energy one of the renewable energies, is most abundant, clean, and readily available throughout the year. Photovoltaic devices/solar cells are one of the most effective ways to harvest the solar energy and convert it into electricity for various applications. The CuInGaSe_2 (CIGS) has been identified to be suitable for sustainable high efficiency solar cells and used as a photo electro-chemical (PEC) photocathode [1, 2]. Owing to the insufficiency and high cost of In and Ga elements in CIGS a suitable alternative is required. The $\text{Cu}_2\text{ZnSnS}_4$ (CZTS) is the material suitable alternative for CIGS with a similar structure, has attracted intense emphasis as good visible light absorber material, both photovoltaic and PEC applications and as a low cost, earth-abundant environmental-friendly material.

The CZTS compound is a p-type semiconductor which belongs to the $\text{I}_2\text{-II-IV-VI}_4$ family. It can be used as a potential absorber layer in thin film solar cells. Due to high optical absorption coefficient and ideal direct band gap of 1.4 to 1.5eV [3] hence used as an absorbing material in solar cells. CZTS thin films were generally deposited by physical or chemical deposition (under vacuum or non-vacuum) methods. Various non-vacuum methods have now been developed for low cost preparation of thin films such as Electro-deposition[4], sol-gel, spin coating [5], chemical bath deposition [7], spray pyrolysis [8], and successive ionic layer adsorption reaction method [6] etc.

The successive ionic layer adsorption and reaction (SILAR) method is particularly unique because of its simplicity, inexpensive, homogenous deposition and less time method for the deposition of quaternary semiconducting thin films [9]. It is also applicable in the deposition of large and complicated area of substrates, low temperature thin films. In this work, the preparation of CZTS thin films by SILAR method and their characterization in terms of structural, optical, and morphological properties have been carried out.

2. Experimental section and methods

In the present work, all the chemicals used are in A.R. grade, such as copper sulphate pentahydrate ($\text{CuSO}_4 \cdot 5\text{H}_2\text{O}$), zinc sulphate heptahydrate ($\text{ZnSO}_4 \cdot 7\text{H}_2\text{O}$), tin sulphate (SnSO_4), thiourea ($\text{CH}_4\text{N}_2\text{S}$) and double distilled water, without further purification. The substrate was of commercially available microscopic glass slides of dimensions is 26 mm \times 76 mm \times 1 mm. The quality and quantity of thin film mainly depends on well cleaned substrate. Hence, the glass substrates were cleaned with chromic acid rinsed with double distilled water, acetone and finally substrate was ultrasonically cleaned with Double distilled water bath for 30 minutes.

The deposition of CZTS film on glass slides by SILAR method includes different parameters viz., precursor concentration, dipping time and number of cycles. For synthesis of CZTS film, mixture of cationic precursors 0.1 M CuSO_4 , 0.05 M ZnSO_4 and 0.05 M SnSO_4

were dissolved in 50 ml of double distilled water. The anionic precursor solution was prepared by dissolving 0.2 M $\text{CH}_4\text{N}_2\text{S}$ in 50 ml double distilled water. First, the pre-cleaned substrates were immersed in the composite cationic solution for 40 seconds to adsorb Cu^{2+} , Zn^{2+} and Sn^{2+} ions. Then the substrate was rinsed in distilled water for 20 seconds to remove the loosely adsorbed ions if any. After, that the substrate was immersed in the anion solution (S^{2-}) for 40 seconds where the chemical reaction takes place between anions and cations to form CZTS. The substrate is again rinsed in distilled water for 20 s to remove the powdery precipitate if any. The above four steps forms one SILAR cycle and it was optimized. Similarly, 40 cycles were employed to obtain homogeneous CZTS film. The deposited films were annealed at 400 °C for 1h in an air atmosphere.

2.1. Characterization

The structural characteristics of CZTS film was analyzed by using X-ray diffraction (XRD) patterns recorded [using Bruker- D8 advance ECO XRD systems with SSD160 1D, Detector] in the span of angle 10° to 80° with Cu-K α radiation [wavelength of 1.5406 Å]. The surface morphology of the CZTS film was carried out by using Scanning Electron Microscopy (SEM) Model: ZEISS-EVO 18 Research, equipped with Energy dispersive X-Ray spectrometer (EDAX) (BRUKER-X Flash 6130). The optical absorption spectrum was recorded using UV-Vis absorption spectrophotometer and recorded in the range of 400-1100 nm, (Shimadzu-1800).

3. Results and Discussion

3.1. Structural analysis

Figure 1 shows the powder XRD pattern of the deposited film and the patterns are well matched with wurtzite and kesterite phase of CZTS thin films. The high crystallite peak obtained at 2 θ value 26.7°, and 51.6° are attributed to (002), and (103) planes respectively of wurtzite and 2 θ at 33.94° can be attributed to (200) planes of kesterite phase of CZTS film. The observations are in good agreement with the previous literature [10, 11]. The parameters such as grain size, and dislocation density are calculated from the powder XRD pattern.

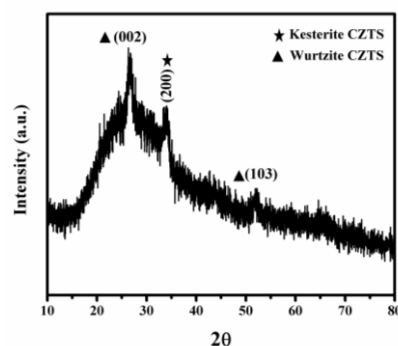


Figure 1 XRD pattern of CZTS thin films

The average grain size is calculated by Scherrers formula

$$D = \frac{0.9 \lambda}{\beta \cos \theta}$$

where β is full width at half maximum (FWHM), λ is the wavelength of the X-ray source, θ is the Bragg angle. The calculated grain size is 17.4 nm.

The dislocation density of the prepared films can be calculated from the following relation.

$$\varepsilon = \frac{1}{D^2}$$

where ε dislocation density(line/m²) and D is grain size(nm). The calculated dislocation density value is 3.3×10^{15} line/m².

3.2 Morphology of the film

The morphological features of the CZTS sample was investigated by SEM. Figure 2 shows the SEM surface micrograph for annealed CZTS thin films, that shows a relatively uniform, densely packed surface, without cracks or holes and well covered on to the glass substrate.

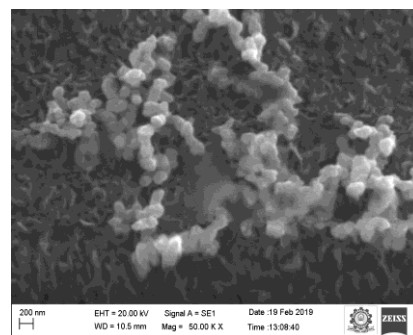


Figure 2 Morphology of the CZTS thin film

3.3 Analyses of optical properties

UV-Visible absorption studies of the deposited thin films are used to study the visible light absorption properties and to estimate the band gap of the material. The absorbance spectrum of the annealed CZTS thin film recorded in the wavelength range of 400–1100 nm is shown in Figure 3. The mixed phase of CZTS film exhibit a broad absorption peak in the visible. The energy band gap is calculated by tauc's plot (Figure 4) drawn between $h\nu$ versus $(\alpha h\nu)^2$ (α = absorbance, h = Planck's constant and ν = frequency). The calculated energy band gap is 1.48 eV and its value is close to that of thin film solar cell.

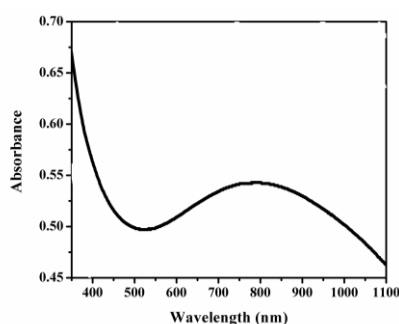


Figure 3 UV-Vis absorbance spectrum

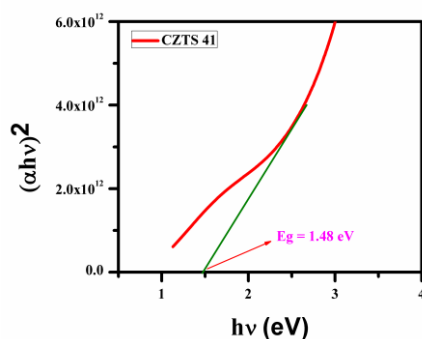


Figure 4 Tauc plot of CZTS thin film

4. Conclusion

CZTS thin films were deposited by SILAR method. Powder XRD pattern confirmed the crystalline nature of the film with tetragonal structure. The morphology of film shows a spherical like particles present

at range of 200 nm and average particle diameter is 120nm. The UV-Vis spectroscopy shows that the film have a good optical absorption coefficient in the visible region and its estimated optical band gap is 1.48 eV confirm the suitability of this material for solar cell application.

4. Acknowledgements

The authors A. Murugan and S. Asath Bahadur are thankful to Department of Science and Technology, Science and Engineering Research Board (DST-SERB) - New Delhi, for the financial support (No : EMR/2016/006874).

REFERENCES

- [1] K. Woo, Y. Kim and J. Moon, Energy Environ. Sci, 5 (2012) 5340.
- [2] H. Ye, H. S. Park, V. A. Akhavan, B. W. Goodfellow, M. G. Panthani, B. A. Korgel and A. J. Bard, J. Phys. Chem. C, 115 (2010) 234.
- [3] N.M. Shinde, P.R. Deshmukh, S.V. Patil, C.D. Lokhande, J. Materials Research Bulletin, 48 (2013) 1760–1766.
- [4] P. Wang, T. Minegishi, G. Ma, K. Takanebe, Y. Satou, S. Maekawa, Y. Kobori, J. Kubota and K. Domen, J. Am. Chem. Soc., 134 (2012) 2469.
- [5] K. Tanaka, N. Moritake and H. Uchiki, Sol. Energy Mater. Sol. Cells, 91 (2007) 1199.
- [6] N. M. Shinde, D. P. Dubal, D. S. Dhawale, C. D. Lokhande, J. H. Kim and J. H. Moon, Mater. Res. Bull., 47 (2012) 302.
- [7] M. Ortega, G. Santana, A.M. Acevedo, Solid State Electron., 44 (2000) 1769.
- [8] C.H. Bhosale, A.V. Kambale, A.V. Kokate, K.Y. Rajpure, Mater. Sci. Eng. B, 122 (2005) 67.
- [9] A. Shameem, P. Devendran, V. Siva, M. Raja, S. Asath Bahadur, A. Manikandan, J Inorg Organomet Polym, 27(3) (2017) 692-699.
- [10] Xiaotang Lu, Zhongbin Zhuang, Qing Peng and Yadong Li., Chem. Commun., 47 (2011) 3141–3143.
- [11] Mei Li, Wen-Hui Zhou, Jie Guo, Yan-Li Zhou, Ze-Liang Hou, Jie Jiao, Zheng-Ji Zhou, Zu-Liang Du, Si-Xin Wu., J. Phys. Chem. C, DOI:10.1021/jp307346k.

STRUCTURAL CHARACTERIZATION STUDIES OF ZnO/NiO NANOCOMPOSITE, SYNTHESISED BY GEL COMBUSTION METHOD

M.Raveena¹, R. Packiaraj¹, N. Nallamuthu¹, K .S.Venkatesh^{1*}

¹Department of Physics, School of Advanced Sciences, Kalasalingam Academy of Research and Education, Krishnankoil, Srivilliputtur – 626 126, Tamilnadu, India.

*Corresponding author. E-mail: venkatesh10685@gmail.com

Abstract

Energy demand is being a major concern around the globe. Electrochemical supercapacitors are one among various alternative and green energy devices. The performance of supercapacitors depends mainly on the enhanced properties of electrode materials. In the present work, ZnO/NiO nanoparticles have been successfully synthesized by a simple and facile citrate-based gel combustion procedure. The crystal structure, phase identification and morphology of the samples were confirmed by X-ray diffraction (XRD) pattern, Fourier-transform infrared spectroscopy (FTIR) and scanning electron microscope (SEM) respectively. It has been observed in X-ray diffraction pattern that the crystalline peaks are broader and confirmed the presence of ZnO/NiO nanoparticles. The mean size of the particle is found to be ~25 nm.

Keywords: ZnO/NiO, gel combustion method, supercapacitors, XRD, FTIR, SEM.

1. Introduction

Supercapacitors have received substantial attentions as an energy storage device in recent years. Compared with secondary batteries, supercapacitors have the advantages such as ultrafast charging–discharging rate, wide operation temperature range and very long cycle life [1-3]. Nevertheless, supercapacitors suffer from low specific capacitance and thus low energy density. Such drawbacks limit their potential applications in energy storage area. In order to overcome these drawbacks, researchers have put a lot of works on the development of new types of electrode materials with high performances. In recent years, transition metal oxides have been widely used as supercapacitor electrode materials. The working principle of transition metal oxides for supercapacitors is based on the fast faradaic redox reactions [4-6]. Compared with carbon materials which work on electrical double layer mechanism, transition metal oxides can provide higher specific capacitance and thus higher energy density. Apart from single metal oxides, many binary metal oxides have been well studied due to their richer redox reactions and synergistic effects of the different metal ions. For example, Xiang et al. reported the fabrication of NiCo₂O₄ microstructures with different morphologies and their application as electrode materials for supercapacitors [7]. Che and co-workers have reported flower-like MnCo₂O₄ microstructures for supercapacitor applications [8]. Shen et al. reported a flexible supercapacitor based on ZnCo₂O₄ nanorods grown on nickel wires [9]. Wang et al. reported the growth of ZnCo₂O₄ nanorod arrays on Ni foam and

their utility as supercapacitor electrodes [10]. Although binary metal oxides have drawn intense attentions in the field of supercapacitor, up to now, only spinel structured binary metal oxides are well studied. In this work, synthesized NiO/ZnO nanocomposites were prepared through a Gel-combustion method and subsequent calcination. XRD analysis shows the coexistence of both cubic NiO and hexagonal ZnO. FTIR spectrum conforms the pure ZnO/NiO was formed. SEM observation shows the sphere like morphology.

2. Experimental Methods and Characterisation

Citrate-based gel combustion method is adopted to obtain ZnO/NiO nanocomposite. Analytical grade of zinc nitrate, nickel nitrate are acting as a precursor and citric acid were used as a gelling agent in the gel combustion method. Appropriate amount of zinc nitrate, nickel nitrate and citric acid (2:6 molar ratio) were dissolved in double distilled (DD) water in separate beakers. Initially zinc nitrate and nickel nitrate precursors were dissolved in DD water. The citric acid solution was added into above solution drop wise at 80 °C. After the complete addition, the temperature is increased to 130 °C. Then, solution was kept overnight to convert into gel and dried gel was formed. The dried gel was calcined at 500 °C for 3 hrs. The samples were well characterized by means of XRD, FTIR, and SEM and the electrochemical studies are performed for supercapacitor applications.

2. Results and discussion

3.1. XRD

XRD pattern of the ZnO/NiO nanocomposite is displayed in Fig. 1. In the crystal structure, ZnO and NiO are hexagonal and cubic geometry, respectively.

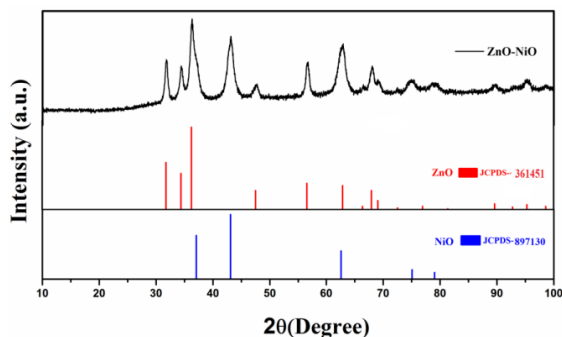


Fig. 1 XRD pattern of ZnO/NiO

Fig. 1b shows XRD pattern of the calcinated sample, all the diffraction peaks could be indexed to hexagonal ZnO (JCPDS No. 361451) and cubic NiO (JCPDS No. 897130)[11]. No diffraction peaks belonging to impurities could be found, indicating that the precursor was completely transformed into ZnO/NiO mixed metal oxides. The particle size was found using Scherrer's equation. Scherrer's equation can be written as:

$$D = k\lambda / \beta \cos\theta \quad (1)$$

D-Particle size, k- Boltzmann constant, λ - Wavelength of X-ray source, β - Full width and half maximum, θ - diffraction angle. The average size of the particle is found to be ~25 nm.

3.2. FTIR

FTIR spectra of ZnO/NiO nanocomposites, heated for 3h at 500 °C is shown in fig. 2. Four new peaks were found to be observed at 1602, 1478, 1100 and 417 cm^{-1} [12]. A broad band around 3346 cm^{-1} corresponds to stretching mode of OH group which is contributed by adsorbed water molecules. The peak around 2367 cm^{-1} can be attributed due to presence of C-O bond. Band formed at 1602 cm^{-1} can be contributed due to OH group in the sample. IR band at 1478 cm^{-1} is obtained corresponds to asymmetric stretching of C=O bond and at 1100 cm^{-1} are obtained due to C-O bonding. IR peak at 417 cm^{-1} is observed due to confirm the presence of crystalline Ni-O

bond formation [13].

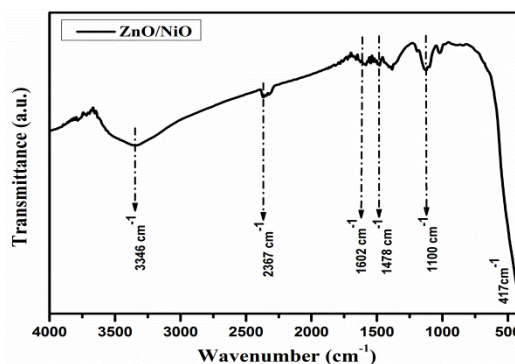


Fig. 2 FTIR-ZnO/NiO

3.3. SEM

The morphologies of the ZnO/NiO composite are observed by SEM. SEM images of the ZnO/NiO composite are presented as shown in Fig. 3. It display that the sample is composed of nano sphere like agglomerated particles. The average size of the particles is measured as ~61 nm.

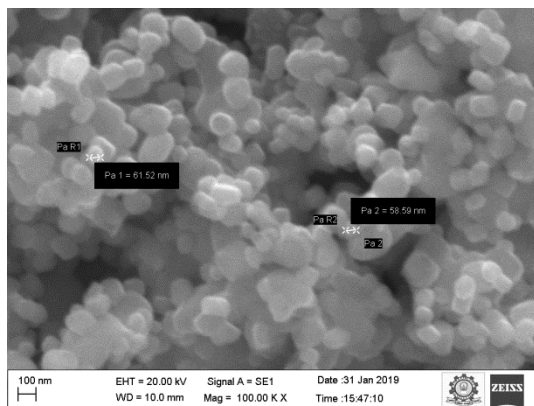


Fig. SEM-ZnO/NiO

4. Conclusion

ZnO/NiO nanocomposite has been successfully synthesized by Gel-combustion process. The XRD revealed the mixed phases of ZnO/NiO nanocomposite. The FTIR spectrum confirmed the formation pure metal oxides ZnO/NiO. The SEM study divulged sphere like particles. This type of composite material is probably used for supercapacitor application.

5. Acknowledgements

Authors would like to gratefully acknowledge Kalasalaingam Academy of Research and Education (KARE) for constant supporting to this research work.

REFERENCES

- [1]. Conway, B. E.. Transition from “supercapacitor” to “battery” behavior in electrochemical energy storage. *Journal of the Electrochemical Society*, 138(6), 1539-1548 (1991).
- [2]. Conway, B. E., Birss, V., Wojtowicz, J.. The role and utilization of pseudocapacitance for energy storage by supercapacitors. *Journal of power sources*, 66(1-2), 1-14 (1997).
- [3]. Arico, A. S., Bruce, P., Scrosati, B., Tarascon, J. M., Van Schalkwijk, W, Nanostructured materials for advanced energy conversion and storage devices. *Review Articles from Nature Publishing Group* (pp. 148-159) (2011).
- [4]. Cui, L., Huang, L., Ji, M., Wang, Y., Shi, H., Zuo, Y., Kang, S.. High-performance MgCo_2O_4 nanocone arrays grown on three-dimensional nickel foams: preparation and application as binder-free electrode for pseudo-supercapacitor. *Journal of Power Sources*, 333, 118-124 (2016).
- [5]. Meng, G., Yang, Q., Wu, X., Wan, P., Li, Y., Lei, X., Liu, J, Hierarchical mesoporous NiO nanoarrays with ultrahigh capacitance for aqueous hybrid supercapacitor. *Nano Energy*, 30, 831-839 (2016).
- [6]. Zhang, L., Zheng, W., Jiu, H., Ni, C., Chang, J., & Qi, G.. The synthesis of NiO and NiCo_2O_4 nanosheets by a new method and their excellent capacitive performance for asymmetric supercapacitor. *Electrochimica Acta*, 215, 212-222 (2016).
- [7]. Xiang, N., Ni, Y., & Ma, X.. Shape-Controlled Synthesis of NiCo_2O_4 Microstructures and Their Application in Supercapacitors. *Chemistry–An Asian Journal*, 10(9), 1972-1978 (2015).
- [8]. Che, H., Wang, Y., & Mao, Y.. Novel flower-like MnCo_2O_4 microstructure self-assembled by ultrathin nanoflakes on the microspheres for high-performance supercapacitors. *Journal of Alloys and Compounds*, 680, 586-594 (2016).
- [9]. Liu, B., Liu, B., Wang, Q., Wang, X., Xiang, Q., Chen, D., & Shen, G, New energy storage option: toward ZnCo_2O_4 nanorods/nickel foam architectures for high-performance supercapacitors. *ACS applied materials & interfaces*, 5(20), 10011-10017 (2013).
- [10]. Wang, S., Pu, J., Tong, Y., Cheng, Y., Gao, Y., & Wang, Z, ZnCo_2O_4 nanowire arrays grown on nickel foam for high-performance pseudocapacitors. *Journal of Materials Chemistry A*, 2(15), 5434-5440 (2014).
- [11]. Zhu, D., & Shao, Y, NiO/ZnO Nanocomposite as Electrode Material for Supercapacitors. *International Journal Of Electrochemical Science*, 13(4), 3601-3612 (2018).
- [12]. Malik, R., Chaudhary, V., Tomer, V. K., Rana, P. S., Nehra, S. P., & Duhan, S. (2016). Visible light-driven mesoporous Au– $\text{TiO}_2/\text{SiO}_2$ photocatalysts for advanced oxidation process. *Ceramics International*, 42(9), 10892-10901.
- [13]. Sharma, A., & Pallavi, S. K. (2012). Synthesis and Characterization of NiO-ZnO Nano Composite.

SYNTHESIS AND CHARACTERIZATION OF A NON-LINEAR OPTICAL CRYSTAL 2-AMINOPYRIDINIUM TRICHLOROACETATE

R. Arunkumar, S. Kamala Sri, S. Sruthi, M. Venkateshan and R. Vishnu Priya

PG and Research Department of Physics, The Madura College, Madurai, Tamilnadu, India.

Email: mailsofarun1997@gmail.com

Abstract

The main aspect of this paper is to study the properties of the 2-Aminopyridinium Trichloroacetate. An organic material of 2-Aminopyridinium trichloroacetate single crystal was grown using the slow evaporation method. The obtained crystals were transparent and slightly yellowish in color. UV-Vis optical studies shown that, the grown crystals have wide optical transparency in the entire visible region. The grown crystal was subjected to Single crystal XRD analysis, confirming the monoclinic nature of the crystal and the optical behavior of the grown crystal was analyzed by PL studies. FTIR analysis confirmed the presence of the functional groups.

Keywords: Crystal growth, trichloroacetic acid, 2-aminopyridine, UV-visible, Photoluminescence.

1. Introduction

NLO property may be used for the application of ultra-fast optical switching and high density storage devices. Property also plays a major role in the field of telecommunications. NLO materials have technological information and industry based applications. This can be essentially traced to the improvement of the performances of the NLO materials. The easy understanding of the nonlinear polarization mechanisms and their relation to the structural characteristics of the materials have been essentially developed. The aim is to develop materials presenting large nonlinear properties and satisfying at the same time, all the technological requirements for applications of wide transparency range, fast response, and high damage threshold. The earlier studies show that the trichloroacetic acid derivatives L-proliniumtrichloroacetate [1] and L-glyciniumtrichloroacetate have NLO property also 2-aminopyridine derivatives 2-aminopyridine potassium dihydrogen orthophosphate lithium chloride [2] and 2-aminopyridinium trifluoroacetate [3] possesses NLO responses. So that, we have been chosen trichloroacetic acid and 2-aminopyridine to grow 2-aminopyridiniumtrichloroacetate.

2. Experimental

2.1. Preparation

Single crystals were grown from saturated aqueous solution containing 2-aminopyridine and trichloroacetic acid in anequimolar ratio. The mixture was stirred at about 50°C for bringing a homogeneous solution. After stirring process, the saturated solution is filtered and

poured into a beaker and covered with a perforated cover and kept in an undisturbed, dust free environment and allowed to evaporate slowly. After a few days slightly yellowish crystals were formed. The grown crystal was shown in Figure. 1.

2.2. Single crystal XRD studies

A good quality optically clear 0.2 x 0.21 x 0.19 mm³ sized crystal was selected for the unit cell measurement using Bruker kappa APEX II diffractometer using the MoK α radiation source. The intensity data were collected at 20°C.

2.3. FTIR analysis

The FTIR spectrum shows the functional groups present in the synthesized crystal. The FTIR spectrum of synthesized crystal was recorded using SHIMADZU FTIR spectrum RXI spectrometer by KBr pellet technique in the range 400–4000 cm⁻¹. The recorded FTIR spectrum was shown in Figure. 2. The frequency assignments were tabulated as Table. 1.

2.4. Optical Studies

Linear optical properties of synthesized crystals were studied using a UV-1700 series spectrophotometer in the region 200–800 nm.

3. Results and Discussion

3.1. Single crystal XRD

2-aminopyridinium trichloroacetate was crystallized in the monoclinic crystal system with the space group $P2_1/c$. Its unit cell values are $a = 8.67(10) \text{ \AA}$, $b = 11.43(10) \text{ \AA}$, $c = 11.10(7) \text{ \AA}$, $\alpha = 90^\circ$, $\beta = 102.49^\circ$, $\gamma = 90^\circ$ and $V = 1074(4) \text{ \AA}^3$.

Table 1: FTIR spectral data of 2 APTC.

Absorption wavenumbers	Bond
3343	N-H stretching
1669	Stretching mode of carboxylate anion
1637	C-C stretching
1484	C-N stretching
1426	C-H in-plane bending
1379, 1327	C-NH ₂ stretching
1163, 993, 624	C-H out-of-plane bending
1055	C-N stretching in the ring
931	CCC in-plane bending
824	Anti-symmetric stretching of CCl ₃
680, 430	COO

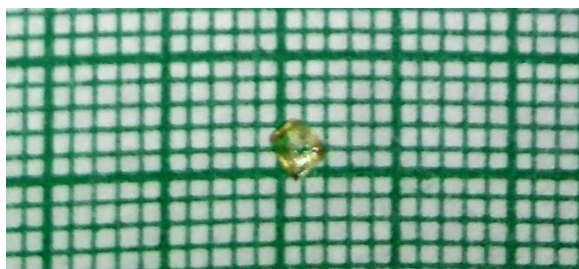


Figure 1: Photograph of as grown Crystal

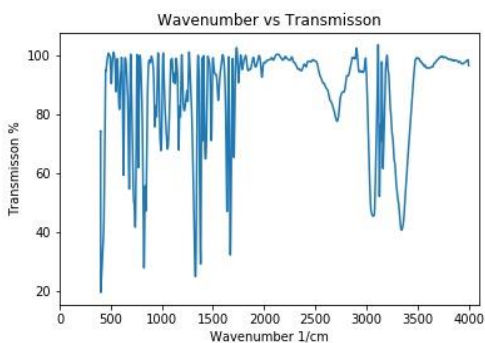


Figure 2: FTIR Spectrum

3.2. FTIR spectral analysis

The observed vibrational frequencies and their tentative

assignments are given in Table 1. The strong band at 824 cm^{-1} is due to antisymmetric stretching type vibrations of CCl_3 group. The strong peak observed at 734 cm^{-1} is corresponds to the in-plane deformation modes of COO group derived from trichloroacetic ions. The analogous strong infrared band is present at 745 cm^{-1} in the spectrum of melaminiumtrichloroacetate [4].

3.3. UV-Visible analysis

The recorded UV-Visible spectrum was shown in figure. 3. The spectra show that the title compound has a characteristic absorption at 314 nm leading to an electronic transition. The compound has a lower cut-off wavelength at 354 nm after this the compound shows transmission in the entire visible range. This is an important property of a NLO material.

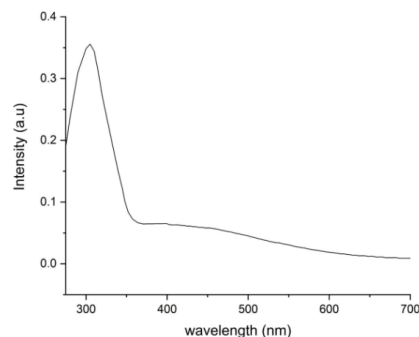


Figure 3: Absorption spectrum

3.4. Photoluminescence

The materials with π conjugated systems exhibit photoluminescence property. The title compound was subjected to photoluminescence with the excitation wavelength of 373 nm and an emission of 378 nm was recorded. The PL spectrum was shown in figure. 4.

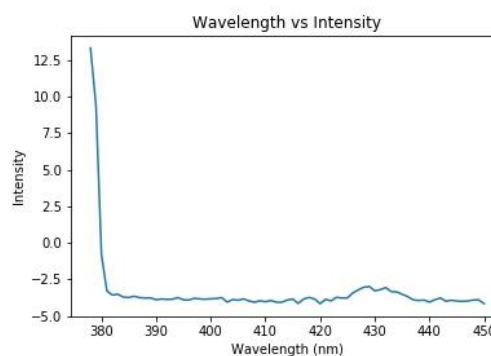


Figure 4: Photoluminescence spectrum

4. CONCLUSIONS

The single crystals of 2-aminopyridinium trichloroacetate were grown from slow evaporation technique. The unit cell parameters of the crystal were measured using single crystal XRD. This confirmed that the grown crystal belongs to monoclinic crystal system. The functional group analysis was performed from FTIR analysis. The frequency assignments were done. This proves the existence of both carboxylic acid and amine groups present in the structure. The grown crystal was subjected to optical studies. The UV-visible spectrum confirmed the wide band transmission in the entire visible region. This is an important property for a material to be a good NLO material. The PL spectrum confirmed the emission at 378 nm.

5. Acknowledgements

The authors thank the management of The Madura College, Madurai for their support and encouragement.

REFERENCES

- [1] D. Kalaiselvi and R. Jayavel, Synthesis, growth and characterization of L-proliniumtrichloroacetate single crystal for nonlinear optical applications, *Optoelectron. Adv. Mat.*, 4 (2010) 1400-1403.
- [2] D. Sivavishnu, R. Srineevasan and J. Johnson, Synthesis, growth, optical, band gap energy and mechanical properties of semiorganic nonlinear optical material: 2-Aminopyridine potassium dihydrogen orthophosphate lithium chloride (2APKDPL) crystal, *Mat. Sci. Ener. Tech.*, 1 (2018) 205-214.
- [3] P. V. Dhanaraj and N. P. Rajesh, Investigations on Nonlinear Optical 2-Aminopyridine Derivative Single Crystals, *Adv. Mat. Res.*, 685 (2013) 211-215.
- [4] S. Debrus, M.K. Marchewka, M. Drozd, H. Ratajczak, Vibrational, calorimetric and nonlinear optical studies of melaminium-bis(trichloroacetate) monohydrate molecular-ionic crystal, *Opt. Mater.*, 29 (2007) 1058-1062.

PREPARATION AND CHARACTERIZATION OF RUBIDIUM DOPED NiO THIN FILMS

S. Sebastian¹, I. Kulandaisamy¹, S. Valanarasu², S. Saravanakumar³, P. Diana³

^{1,2}PG& Research Department of Physics, Arul Anandar College, Karumathur, India – 625 514

³Department of Physics, Kalasalingam University, Krishnankoil - 626 126, Virudhunagar, Tamil Nadu, India

E-mail: speedseba@yahoo.co.in

Abstract

Here we report the effect of Rb doped NiO in thin film form. Rubidium doped cuprous oxide thin films are prepared on glass substrates. Thin films Rb doped NiO are deposited on the glass substrate by Nebulizer spray technique (NST) at different doping percentage of concentration (0%, 2.5wt. % and 5wt. %). X-ray diffraction, SEM, and optical measurements were performed to investigate the properties of the material. XRD study reveals oriented growth of the film along the [111] direction. Tauc's plot is used to determine the optical band gap of NiO and Rb doped NiO films. The values of the direct band gap for NiO are found to be 3.48-3.10 eV, respectively

Keywords: Nebulized Spray Pyrolysis, NiO thin film, Rubidium doping, structural, optical properties.

1. Introduction

The NiO, a transition metal oxide, has attracted considerable interest because of its special electrical, optical and magnetic properties. NiO adopts NaCl structure and is an antiferromagnetic insulator at room temperature [1]. Stoichiometric NiO is a Mott insulator, but one can increase its p type conductivity by introducing Ni²⁺ vacancies or by doping with cations [2]. Electrical and magnetic properties of the NiO in thin film form strongly depend upon the deposition parameters like substrate temperature and oxygen content during the deposition. Therefore, selection of the proper substrate, growth condition and deposition technique play crucial role in the synthesis of NiO in thin film form. In the past, NiO thin films have been fabricated on a variety of substrates by various deposition techniques like pulsed laser deposition, sputtering, chemical methods, spray pyrolysis methods etc [3-5]. It has been reported that as compared to other substrates, film has grown on insulating substrates like TiO₂, SrTiO₃ and Al₂O₃ is more likely to be epitaxial in nature and contain less surface defects [6]. The NiO thin films find various scientific and technological applications. It can also be used as an exchange biased layer. One of its most important uses could be its applicability for spintronics application by doping with a suitable impurity.

Experimental

1.1. Preparation

NiO thin Films were deposited using the nebulizer spray technique. It consists of a base plate, in which a heater coil is embedded to facilitate heating, upon which the substrates for film deposition are to be placed. Substrate temperature (T_s) was maintained with the help of a feedback circuit which controls the heater supply. Temperature of the substrate can be varied from room temperature to 400°C. During the spray, temperature of the substrate was kept constant with an accuracy of ±5°C. Many trials were conducted for optimizing the deposition parameters to good quality ferric nitrate thin film. Ferric nitrate thin films were deposited using spray pyrolysis deposition method. The deposition of the NiO films, we took 10 ml of 0.1 mol of Nickel chloride and dissolved in de-ionized water. The deposition was takes on glass substrate and the substrate temperature maintained at 400°C for varies pressure 1.5 Kg/cm² using nebulizer setup. Distance between the substrate and nebulizer gun is fixed at 5cm, the compressed air acts as a gas carrier the air flow rate controlled by the suitable flow controller. And the same solution we adding 2.5.wt. % of rare earth metal Rb to the same solution Rb doped NiO thin film deposited. Again we adding 5 wt. % of rare earth metal Rb to the same solution Rb doped NiO thin film is deposited.

To study the structural properties of the grown thin film X-ray diffraction (XRD) was performed in Θ -2 Θ geometry using Cu K α source. Magnetic behavior of the thin film was recorded using SQID vibration magnetometer from Quantum Design.

1.2. XRD studies

Fig 1. Shows the X-ray diffraction patterns of pure and NiO:Rb thin films were deposited with different doping concentration (0%, 2.5 wt.%, and 5wt.%) at 400°C using nebulizer spray pyrolysis method. The XRD pattern gave one dominant peaks at $2\theta = 37.267^\circ$ assigned to the (1 1 1) crystal planes and less intense peaks were recorded at 43.286° and 62.933° assigned to (2 0 0) and (2 2 0) crystal planes respectively. The observed lattice spacings (d) are similar to standard Bunsenite (NiO) peaks identified by JCPDS with file No. 78–0643. Strong peak intensity shows a highly crystallinity of the phase. The grain diameter (D), micro-strain (ϵ), dislocation-density (δ) and a number of crystallites (n_c) calculated using Debye-Scherer’s equation are summarized in table 1.

$$D = \frac{K\lambda}{\beta \cos\theta} \text{----- (1)}$$

$$\epsilon = \frac{\beta \cos\theta}{4} \text{----- (2)} \quad \delta = \frac{1}{D^2} \text{----- (3)} \quad n_c = \frac{t}{D^3} \text{----- (4)}$$

Table 1. Micro structural parameters of pure and Rubidium doped NiO thin films of (111) plane

Samples	Crystallite size D (nm)	Dislocation density (δ) $\times 10^{15}$ (lines/m ²)	Micro strain (ϵ) $\times 10^{-3}$ (lines ² m ⁴)	Number of crystallites (n_c) $\times 10^{17}$ (lines/m ²)	Thic kness (nm)
Pure NiO	19.14	2.729	1.790	0.416	292
NiO: Rb (2.5wt. %)	28.35	1.243	1.208	0.140	319
NiO: Rb (5 Wt. %)	30.91	1.046	1.108	0.109	323

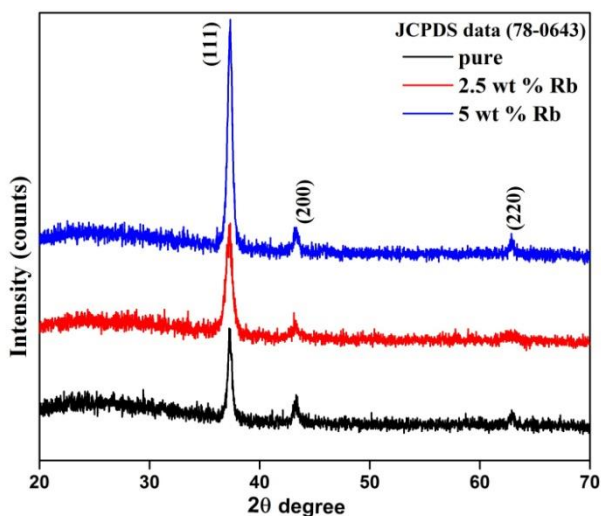


Figure 1. X-ray diffraction patterns of pure and NiO:Rb thin films.

1.3. SEM studies

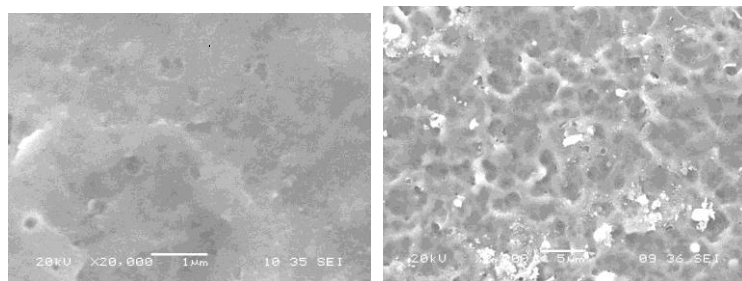


Figure 2. SEM images of pure and 5%Rubidium doped NiO thin films

The surface morphology of the films was studied by Scanning electron microscopy (SEM). Fig. 2(c) 5wt.% Rb shows the topography images of the deposited of pure and Rubidium doped nickel oxide thin film with different doping concentration of (0%, 2.5 wt.% and 5wt.%). The grain size is varied at different doping percentage of Rb. This is depicted in Table 1. The structural analysis confirmed cubic polycrystalline nickel oxide. The surface morphology revealed a porous surface with inhomogeneous randomly shaped heaps.

1.4 .Optical studies

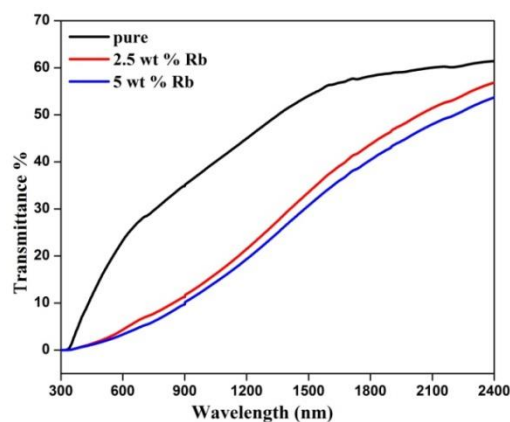


Figure 3: The total transmittance of pure and Rb doped NiO thin films

The spectrum was recorded for the films as wavelength range from 300 – 2400 nm. In Fig.4 shows that the overall total optical transmittance is found to decrease when the wavelength of incident increases. It is mainly correspond to the thickness of the film in which the transmittance is reduced. Finally the transmittance mainly influenced by doping percentage which affects the film optical properties

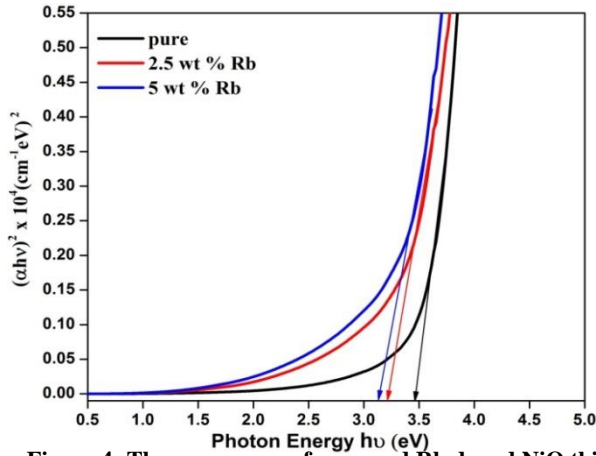


Figure 4: The energy gap of pure and Rb doped NiO thin films

The energy gap value E_g is to be calculated to understand the absorption edge of the material, and it can be obtained in Fig. 6 from the following equation.

$$(\alpha h\nu)^n = A(h\nu - E_g) \quad (5)$$

The wide band gap of the material can be determined by extrapolating the linear region of the graph to photon energy. The optical band gap was found to decrease from 3.48, 3.22 and 3.10 eV for the pure and NiO:Rb thin films for (0%, 2.5%, and 5%) respectively. Calculated optical band gap of the prepared NiO:Rb thin film was found to be 3.10 eV, which is well agrees with the reported band gap values of NiO films. It was observed the band gap decreases with increasing Rb doping percent-

age; this is due to the variation of thickness of the deposited films.

4. Conclusion

NiO:Rb thin film was prepared by NSP method. The films produced are strongly adherent. The XRD pattern revealed the formation of NiO. Crystallite size has been calculated using XRD. It also shows that the deposited film showed well-covered entire substrate surface. The structure and morphology of the film were studied using SEM. Grain size has been calculated using SEM. Further, the Optical transmission study revealed wide band gap nature is found to be of the order of 3.1eV.

We concluded that the obtained NiO:Rb thin films were optical quality in nature suitable for thin films solar cell. So this NSP method is the simple technique to prepare the thin film materials. The prepared NiO:Rb film is suitable material for photovoltaic application

REFERENCES

- [1] Fujii E, Tomozawa A, Torii H and Takayama R 1996 Japan. J. Appl. Phys 35 L328.
- [2] Wu J, Nan C W, Lin Y and Deng Y 2002 Phys. Rev. Lett. 89 217601
- [3] Nandy S, Goswami K S and Chattopadhyay K 2010 Appl Surf Sci 256 3142
- [4] Wang H, Wang Y and Wang X 2012 Electrochem Commun 18 92
- [5] Xia X, Tu J, Zahang J, Wang X, Zahang W and Huang H 2008 Sol Energy Mater Sol Cells 92 628
- [6] Lee Ju Ho, Kwon Yong Hun, Kong Bo Hyun, Lee Jeong Yong and Cho Hyung Koun 2012 Cryst Growth Des. 12 2495

GREEN SYNTHESIS OF SILVER SOL USING PHYLLANTHUS RETICULATUS*

M.S.Revathy¹, S. Gnanalakshmi¹, D. Gudavathi¹, R. Archana¹, K. Viswanathan^{1*}

¹Department of Physics, Kalasalingam Academy of Research and Education, Krishnankoil
Email: kvnooty@gmail.com

Abstract

In this present work *Phyllanthus reticulatus* is used as an active ingredient renowned for its medicinal uses. *Phyllanthus reticulatus* has been proved to show antidiabetic, antiviral, anticancer, antiplasmodial, hepatoprotective, antibacterial and anti-inflammatory activities. The plant contains tannic acid, terpenoids, flavonoids, phenolic compounds and steroids as main chemical constituents. This article aims to provide a simple green synthesis of silver sol for further investigation of phytochemical and pharmacological aspects of this plant.

Keywords: *Phyllanthus reticulatus*, Silver sol

1. Introduction

In traditional culture medicinal plants are used all over the world and they are becoming increasingly popular in modern society as natural alternatives to synthetic chemicals *Phyllanthus reticulatus* (Family – Euphorbiaceae) commonly known as pancoli or karineli, (Synonym: *Kirganelia reticulata* Poir.) is a large glabrous or pubescent shrub with smooth or lenticellate branches growing from 8-10 ft in height. The plant is widely present in Tropical Africa, Srilanka, South East Asia, China, Malaysia and throughout India, mostly in hedges or waste places. Fruiting and flowering season of plant is from July to March. Leaves of the plant contain tannic acid and gum. Fruit of the plant becomes purplish black when ripe[1].

2. Experimental

2.1. Materials

Silver Nitrate (AgNO₃, 99% purity, Merck Products), *Phyllanthus reticulatus*(*Neeroli*) leaves collected from Kerala.

2.2. Preparation of the extract

The leaves of *Phyllanthus reticulatus* plant were collected from the local garden and then washed thoroughly with tap water to remove the dust and dirt. The leaves were then dried under shade for about five days and then finely powdered using mortar. About 2 grams of the powder was taken and mixed with distilled water and stirred for 30 minutes. The obtained aqueous leaf extract was then filtered using whatman filter paper. The pale green colour extract was further utilized as reducing and capping agents in silver sol synthesis.

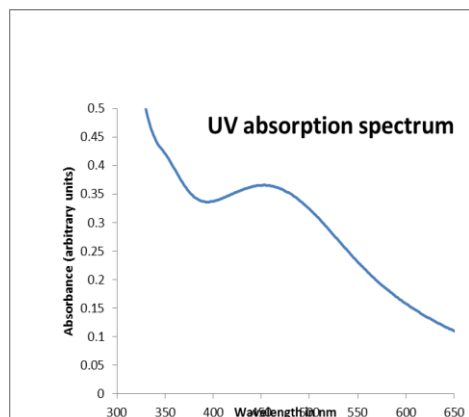
2.3. Preparation of Silver Nitrate Solution

0.125g of Silver nitrate was added into 100ml of distilled water and stirred continuously for 1-2min to get Silver Nitrate solution.

2.4. Silver Sol synthesis

The best volume of plant extract were added to the best molarity of AgNO₃ solution at room temperature and stirred continuously for ten minutes using Magnetic Stirrer. Slow reduction took place and kept for 24 hours to obtain the colour change. After 24 hours pale green colour changes to red colour, which indicate the formation of silver nano particle. The UV absorption spectrum of the sol was taken which is shown in Fig. 2. The peak at around 450 nm shows the formation of silver nano particles.





3. Conclusion

A simple green synthesis of stable silver sol using *Phyllanthus reticulatus* at room temperature was reported in this study. The synthesis was found to be efficient in terms of reaction time as well as stability of synthesised sol which excluded chemical agents. The green synthesis of silver sol method provides a simple environmental ecofriendly and cost effective route for the synthesis of silver nanoparticle. The formation of nanoparticle was identified by the change of colour of the solution. This is confirmed by the observation of the UV absorption peak at around 450 nm. This sol can be used for the study of SERS of some sample.

4. Acknowledgements

The Authors thank the International Research Centre, Kalasalingam Academy of Research and Education for providing facilities to carry out the research work.

REFERENCES

- [1] Shalini Sharma and Sunil Kumar, "*Phyllanthus Reticulatus* Poir. – An Important Medicinal Plant: A Review Of Its Phytochemistry, Traditional Uses And Pharmacological Properties," *IJPSR*, 2013; Vol. 4(7): 2528-2534
- [2] T. Hu and J. P. Desai, "Soft-Tissue Material Properties under Large Deformation: Strain Rate Effect," *Proceedings of the 26th Annual International Conference of the IEEE EMBS*, San Francisco, 1-5 September 2004, pp. 2758-2761.
- [3] A. S. Prasad, "Clinical and Biochemical Spectrum of Zinc Deficiency in Human Subjects," In: A. S. Prasad, Ed., *Clinical, Biochemical and Nutritional Aspects of Trace Elements*, Alan R. Liss, Inc., New York, 1982, pp. 5-15.
- [4] J. K. Wu, "Two Problems of Computer Mechanics Program System," *Proceedings of Finite Element Analysis and CAD*, Peking University Press, Beijing, 1994, pp. 9-15.
- [5] L. Honeycutt, "Communication and Design Course," 1998. <http://dcr.rpi.edu/commdesign/class1.html>
- [6] R. Hauptmann, M. Kondo, S. Kitagawa, *Z. Kristallogr. New Cryst. Struct.* 215, (2000) 169–172.
- [7] M. Luo, M. J. Jedrzejewski, S. Singh, C. L. White, W. J. Brouillette, G. M. Air, W. G. Laver, *Acta Cryst.* D51, (1995) 504-510.
- [8] O. Wright and W. Wright, "Flying-Machine," US Patent No. 821393, 1906.

ELECTROCHEMICAL ANALYSIS OF CUO NPS FOR SUPERCAPACITOR APPLICATION

R. Packiaraj¹, P.Devendran¹, K .S.Venkatesh¹, S. Asath Bahadur¹, N. Nallamuthu^{1*}

¹Department of Physics, School of Advanced Sciences, Kalasalingam Academy of Research and Education, Krishnankoil, Srivilliputtur, Tamilnadu, India.

*Corresponding author. E-mail: nnallamuthu@gmail.com

Abstract

Facile and simple gel combustion method has been used to synthesis copper oxide (CuO) nanostructures. The structural, morphological and electrochemical properties of the CuO has been studied and reported. X-ray diffraction pattern confirms the formation of monoclinic CuO at 500 °C. Electrochemical investigation indicates that the CuO nanostructures prepared at 500°C reveals a maximum specific capacitance of 435 Fg⁻¹ at 0.5mA/cm². Electrochemical study shows that the obtained CuO supercapacitor properties in 2.0 M KOH solution. This work demonstrates that the construction of binary oxide nanocomposites is a strategy to develop high performance supercapacitor electrode materials.

Keywords: CuO, gel combustion method, supercapacitors, XRD and SEM.

1. Introduction

Global warming, as well as the increasing price and decreasing availability of fossil fuels, all highlight need to move towards a sustainable development, where it is critical to preserve the environment and to build highly efficient renewable energy storage/conversion systems. Supercapacitors, as a new class of energy storage device, are specialized form of capacitors with an exceedingly high level of capacitance. They have received significant attention in recent years because they can achieve higher energy density than conventional capacitors and offer better power performance than batteries [1, 2]. Based on the charge storage mechanism, supercapacitors are classified as electric double layer capacitors (EDLC) and pseudo-capacitors or ultracapacitors. EDLCs, which store charges electrostatically, through reversible ion adsorption at the electrode/electrolyte interface, commonly use carbon-based electrode materials with high surface area, high conductivity, electrochemical stability and open porosity. In contrast, pseudocapacitors are fabricated based on transition metal oxides (TMO) where charge storage occurs through electrochemical redox reactions [3]. Among the TMOs, RuO₂ has been widely investigated because of its high conductivity, remarkable specific capacitance and distinct oxidation states. Although RuO₂ can offer excellent charge storage performance, the high cost and toxicity of RuO₂ hinders its use in practical applications. More cost-effective transition metal oxides such as MnO₂, Fe₃O₄, V₂O₅, NiO etc., owing to their hallmark properties such as tuneable morphology, lesser toxicity and multiple valences are widely exploited towards supercapacitor electrode applications but the poor electronic conductivity of these oxides de-

ters their use in high power applications. Nevertheless, nanostructures of these metal oxides possess better electronic conductivity, higher specific capacitance and enhanced cycling stability [4, 5]. Recently, CuO nanostructures have attracted considerable interest with regard to battery and bio-sensing applications due to their low cost and environmental friendly nature [6]. Synthesizing unique nanostructures of Cu based oxides could mitigate with poor cyclic stability and lower conductivity because nanostructures may endow additional pathways for electrolyte penetration and maintain the sustainability of the crystal structure during cycling. Simple fabrication procedure and cost effectiveness of nanostructured materials are much favoured for mass production and commercialization. In this study, we report, a simple and inexpensive procedure based on gel combustion technique to synthesized CuO nanostructures and studied their potential towards supercapacitor electrode applications.

2. Experimental Section

Analytical grade copper nitrate (Cu (NO₃)₂.3H₂O), citric acid (C₆H₈O₇) were purchased from Sigma Alrich, India. All reagents were utilized as such without further purification process.

2.1. Synthesis of CuO nanostructures

Citric acid assisted gel combustion method is adopted to obtain CuO nanoparticles. Analytical grade of copper nitrate as a precursor and citric acid a gelling agent were used in the gel combustion method. Appropriate amount of copper nitrate and citric acid (1:3 molar ratio) were

dissolved in double distilled water in separate beakers. The citric acid solution was added into copper nitrate solution drop wise at 80 °C. After the complete addition, the temperature is increased to 130 °C. Then, solution was kept in oven for 12 hours to convert into gel and dried gel was formed. The dried gel was calcined at 500 °C for 3 hrs. The samples were well characterized by means of XRD, FTIR, and SEM. The electrochemical studies are performed for supercapacitor applications.

2.2. Fabrication of electrodes for supercapacitor applications

Electrochemical studies of CuO samples were performed using a three-electrode cell set up, consists of CuO nanostructures as working electrode, platinum wire as counter electrode, and Ag/AgCl as the reference electrode. The electrode material (1 mg) was prepared using 80 wt% sample, 15wt% activated carbon and 5 wt% Polyvinylidene fluoride (Pvdf). This mixture was coated on a nickel foam surface which was dried at 80 °C for 10 hr. The electrochemical tests were performed in 2.0 M KOH aqueous electrolyte solution at room temperature.

3. Results and discussion

3.1. Structural and Morphological studies

The X-ray diffraction patterns of CuO annealed at 500 °C for 3 hr is shown in Fig.1. The diffraction peaks matches well with the JCPDS (card no. 89-5896) data for CuO. Moreover, CuO nanostructures exhibit monoclinic symmetry (C_2/C space group) and lattice parameters such as $a = 4.683$ nm, $b = 3.424$ nm and $c = 5.129$ nm: $\beta = 99.44^\circ$. All the diffraction peaks were perfectly matched with JCPDS data. Further, the absence of any collateral peaks in the XRD pattern indicates the high purity of the prepared CuO samples [7].

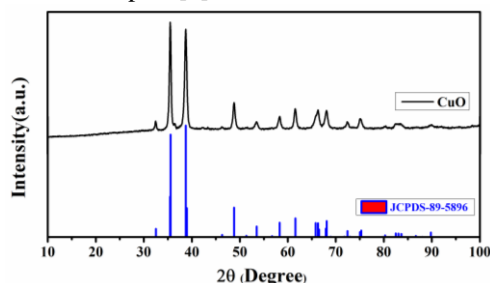


Fig. 1: X-ray diffraction pattern of CuO NPs

From fig.2 shows the scanning electron microscopy (SEM) image of CuO NPs sample. The image demonstrated the formation of particles with spherical shape having uniform size. The homogeneous distribution of the obtained particles emphasizes the advantage of method adopted. The size of the particle is measured from the image and it is roughly about 65 nm.

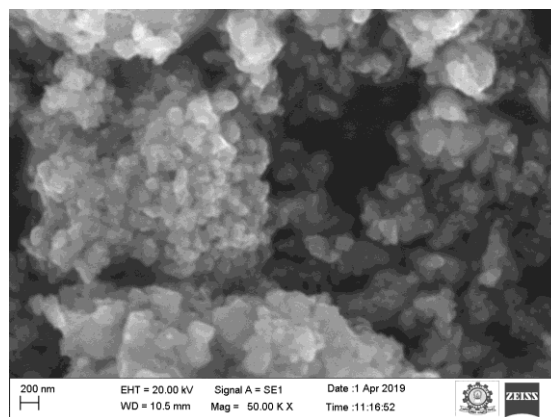


Fig. 2 Scanning electron microscope image of CuO NPs

3.2. Electrochemical Studies

3.2.1. Cyclic Voltammetry analysis

To study the cyclic Voltammetry performance, the prepared CuO NPs was employed as the working electrode and tested using 2 M KOH electrolyte solution. Fig. 3 shows the CV curves of CuO nanostructures at different scan rates. The CV curves of the sample CuO confirms the presence of redox peaks in their cathodic and respective anodic scan indicates the significant share of pseudocapacitance in the electrochemical process. The specific capacitance of CuO nanostructures were calculated using the following equation (1),

$$C_{sp} = \frac{\int idv}{s \cdot m \cdot \Delta V} \text{ Fg}^{-1} \quad (1)$$

Where, C_{sp} (Fg^{-1}) is the specific capacitance, $\int idv$ area of the under CV curve, m (mg) is the mass of the active material, s is the scan rate (mV) and ΔV (V) is the potential window.

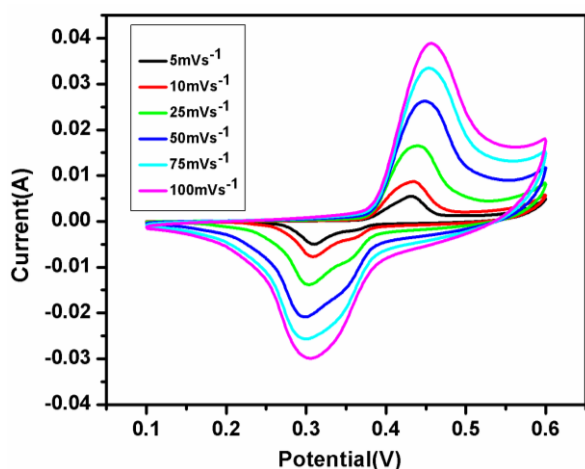


Fig. 3 Cyclic Voltammetry curves of CuO NPs

The specific capacitance values are calculated from CV curve, the equation (1) is used to find the values at various scan rates such as 5, 10, 25, 50, 75 and 100 mV/s, respectively. The values are shown in table.1. The increase of scan rate weakens the specific capacitance significantly due to the inability of electrolyte ions to access the interior parts of the electrode active materials at higher scan rates [8].

Table.1

S.No	Scan rates mV/s	Specific capacitance of different Scan rates Fg^{-1}
1	5	305
2	10	279
3	25	234
4	50	218
5	75	180
6	100	120

3.3. Galvanostatic charge discharge analysis

To explore the electrochemical richness of CuO nanostructures and to determine the discharge specific capacitance, the galvanostatic charge and discharge (GCD) measurements were carried out using 2.0 M KOH. Fig. 4 presents the GCD profiles of CuO at various current densities such as 0.5, 1, 2, 3, 4 and 5 mA/cm^2 , respectively. The specific capacitance values are determined from GCD curves based on the following relation (2),

$$C_{sp} = I * \Delta t / m * \Delta V \text{ Fg}^{-1} \quad (2)$$

Where, I (mA), Δt (s), ΔV (V) and m (mg) are the discharging current, discharge time, potential window and mass loading of the active material in the electrode. The calculated discharge specific capacitance of CuO is 435 Fg^{-1} at 0.5 mA/cm^2 . In the present work CuO nanospheres exhibit higher specific capacitance, when compared with aforesaid work.

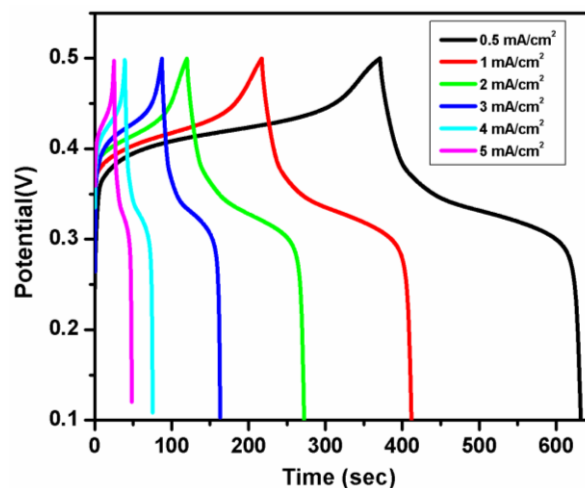


Fig. 4 Charge discharge profile of CuO NPs

4. Conclusion

Simple and cost effective method has been used to synthesis CuO nanospheres. The XRD analysis showed the poly crystalline nature with monoclinic symmetry structure. The sphere like morphology of CuO NPs was confirmed through SEM analysis. A CuO nanostructure revealed higher specific capacitance (435 Fg^{-1}) at 0.5 mA/cm^2 . These electrochemical studies suggested that the CuO nanosphere electrode is considered to be one of the promising electrode candidates for supercapacitor applications.

5. Acknowledgements

Authors would like to gratefully acknowledge Kalasalingam Academy of Research and Education (KARE) for constant supporting to this research work.

REFERENCES

- [1] Simon, Patrice, and Yury Gogotsi. "Materials for electrochemical capacitors." In Nanoscience and

- Technology: A Collection of Reviews from Nature Journals, pp. 320-329. 2010.
- [2] Su, Yu-Zhi, Kang Xiao, Nan Li, Zhao-Qing Liu, and Shi-Zhang Qiao. "Amorphous Ni (OH)₂@ three-dimensional Ni core-shell nanostructures for high capacitance pseudocapacitors and asymmetric supercapacitors." *Journal of Materials Chemistry A* 2, no. 34 (2014): 13845-13853.
- [3] Zhang, Chuanfang, Yingbo Xie, Mengqiang Zhao, Amanda E. Pentecost, Zheng Ling, Jitong Wang, Donghui Long, Licheng Ling, and Wenming Qiao. "Enhanced electrochemical performance of hydrous RuO₂/mesoporous carbon nanocomposites via nitrogen doping." *ACS applied materials & interfaces* 6, no. 12 (2014): 9751-9759.
- [4] Lang, Xingyou, Akihiko Hirata, Takeshi Fujita, and Mingwei Chen. "Nanoporous metal/oxide hybrid electrodes for electrochemical supercapacitors." *Nature nanotechnology* 6, no. 4 (2011): 232.
- [5] Guan, Cao, Jinping Liu, Chuanwei Cheng, Hongxing Li, Xianglin Li, Weiwei Zhou, Hua Zhang, and Hong Jin Fan. "Hybrid structure of cobalt monoxide nanowire@ nickel hydroxidenitrate nanoflake aligned on nickel foam for high-rate supercapacitor." *Energy & Environmental Science* 4, no. 11 (2011): 4496-4499.
- [6] Cain, Matthew F., Russell P. Hughes, David S. Glueck, James A. Golen, Curtis E. Moore, and Arnold L. Rheingold. "Synthesis and Structure of Intermediates in Copper-Catalyzed Alkylation of Diphenylphosphine." *Inorganic chemistry* 49, no. 17 (2010): 7650-7662.
- [7] Suresh, R., K. Tamilarasan, and D. Senthil Vadivu. "Synthesis and characterization of copper oxide nanostructures for supercapacitor electrode applications." *Journal of Ovonic Research* 12, no. 4 (2016): 215-223.
- [8] Wee, Grace, Huan Zhong Soh, Yan Ling Cheah, Subodh G. Mhaisalkar, and Madhavi Srinivasan. "Synthesis and electrochemical properties of electrospun V₂O₅ nanofibers as supercapacitor electrodes." *Journal of Materials Chemistry* 20, no. 32 (2010): 6720-6725.

IMPROVED SUPERCAPACITOR PERFORMANCE OF MnO₂ NANORODS BY REDOX-ACTIVE ELECTROLYTE

C. Selvameenakshi¹, S. Arunpandiyan¹, S. Ezhil Arasi¹, A. Arivarasan^{1*}

¹Multifunctional Materials Laboratory, Department of Physics, International Research Centre, Kalasalingam Academy of Research and Higher Education, Krishnankoil, Tamil Nadu 626126, India

*Email: arivarasan.nanotech@gmail.com

Abstract

Pure MnO₂ nanorods were successfully synthesized by one step hydrothermal method and characterized with different techniques to analyze their crystalline nature, surface morphology, functional groups, and optical properties. Electro-chemical performance of the prepared MnO₂ nanorods was studied by the addition of 0.1M K₄[Fe(CN)₆] redox additives into 1M KOH electrolyte. The maximum specific capacitance of the prepared nanorods using 1M KOH electrolyte is 89 Fg⁻¹ and it is greatly enhanced by the addition of redox additives (634 Fg⁻¹).

Keywords: MnO₂ nanorods, Supercapacitor, Redox-active electrolyte, SEM, CV.

1. Introduction

Supercapacitors, a kind of energy storage devices with high power density, fast charge and discharge rate, long service life and wide operating temperature, fill the gap between conventional dielectric capacitors and batteries [1]. Furthermore, it has broad application prospects in national defense, aerospace, automotive, consumer electronics, telecommunications, electric vehicles, railways, etc., [2]. The electrode material is known to be vital for their charge storage performances. Carbon derivatives, metal oxides and conducting polymers are usually used as electrode materials. Metal oxides with unique electrochemical pseudocapacitive behavior can carry out fully reversible redox reactions and adsorption/desorption processes repeatedly. It is a research hotspot at present.

Common metal oxides used for supercapacitor are RuO₂ [3], MnO₂ [4], Co₃O₄ [5], NiO [6], TiO₂ [7], etc. Manganese dioxide (MnO₂), with its high specific capacitance, low-cost and environmental compatibility, has attracted more attention as a pseudocapacitor electrode material [8]. Normally, 1-D nanorods are possessing a high surface area than other types of nanomaterials and it is key component to achieve high specific capacitance. Recently, redox active electrolytes are used to improve the performance of supercapacitor electrode materials by enhancing faradaic redox reactions inside the

electrolyte. From previous reports, the addition of 0.1M K₄[Fe(CN)₆] to the usual KOH electrolyte will enhance the specific capacitance tremendously [9]. In this work, we have synthesized 1-D MnO₂ nanorods with high surface area through one-step hydrothermal method and achieved high supercapacitor performance by adding 0.1M K₄[Fe(CN)₆] redox additive to the 1M KOH electrolyte solution.

2. Experimental

2.1. Preparation

All the precursors were purchased in analytical grade and used without further purification. In which Manganese sulfate monohydrate (MnSO₄.H₂O) and (KMnO₄) potassium permanganate were used as starting materials for the synthesis of MnO₂ nanorods and procured from SRL chemicals, India. Potassium hydroxide (KOH) and potassium ferrocyanide (K₄[Fe(CN)₆]) was purchased from Reachem chemicals, India. They are used for electrolyte preparation.

2.2. Synthesis of MnO₂ Nanorods

In a typical synthesis, 0.05 M of MnSO₄.H₂O solution was prepared in 120 ml of Millipore water. One gram of KMnO₄ was added with the above solution under constant stirring. The resultant solution was transferred into 150 ml Teflon lined autoclave and reacted for 24 h at 160°C. The

resultant solution was filtered and extensively washed using distilled water followed by ethanol and dried at 80°C for overnight. Then the impurities were removed by calcination at 300°C for 3 h.

2.3. Electrode Preparation and Evaluation

The calcinated sample was well ground and mixed with activated carbon (for enhancing the conductivity) in 85:15 weight ratio. Then, an appropriate amount of Nafion solution (binder) was added dropwise to the above mixture to make a slurry. And the obtained slurry was pasted on to the Ni-foil (1 cm²) and dried in the air oven at 80°C for overnight. The total active mass pasted on to the substrate is about 1 mg/cm². The electrochemical performances of the as-prepared modified working electrode were evaluated by the three-electrode system. Here, the platinum wire and Ag/AgCl is used as a counter and reference electrodes respectively. And 1M KOH with 0.1M K₄(Fe(CN)₆) is used as a redox additive based electrolyte solution for enhanced supercapacitor performance. The potential window is optimized and set into 0 to 0.6 V and Cyclic Voltammetry (CV) measurements are carried out at different scanning rate of 5, 10, 15, 25, 50, 75 and 100 mVs⁻¹. Galvanostatic Charge Discharge (GCD) measurements were performed at different current densities to check the charge storage capacity of the electrode. Electrochemical Impedance Spectroscopy (EIS) techniques were performed to study the ionic movement between the electrodes through the electrolyte. The EIS measurements were carried out in the frequency range between 1Hz to 100 KHz.

2.4. Characterization Techniques

The prepared samples were characterized by X-Ray diffractometer (BRUKER-D8 Advance Eco XRCD) systems with SSD 160 1D Detector, Scanning Electron Microscope (EVO18 CARL ZEISS), Fourier Transform Infra-red Spectrophotometer (IR Tracer 100) recorded from 400 to 4000 cm⁻¹, UV-VIS-NIR double beam spectrophotometer (Varian Cary 5000 scan-Diffuse reflection), CH instrument CHI6008e, USA.

3. Results and Discussion

3.1. XRD Analysis

The X-ray diffraction (XRD) pattern of calcinated MnO₂ nanorods was as shown in **figure 1**. The diffraction peaks were observed at (2θ) 12.78, 18.10, 28.84, 37.52, 39.01, 41.96,

49.86, 56.37, 60.27, 65.10, 69.71, 72.71° corresponding to the crystalline planes 110, 200, 310, 211, 330, 301, 411, 600, 521, 002, 541, 312 respectively. They (peaks) can be indexed to tetragonal α-MnO₂ in bulk form (JCPDS No. 44-0141) with lattice constants a = b = 9.785 Å, c = 2.863 Å. A sharp diffraction peak at 37.3° demonstrated that MnO₂ sample was well crystallized in the lattice plane. There are no impurity peaks were observed, which indicates that the sample prepared MnO₂ nanorods was of high purity.

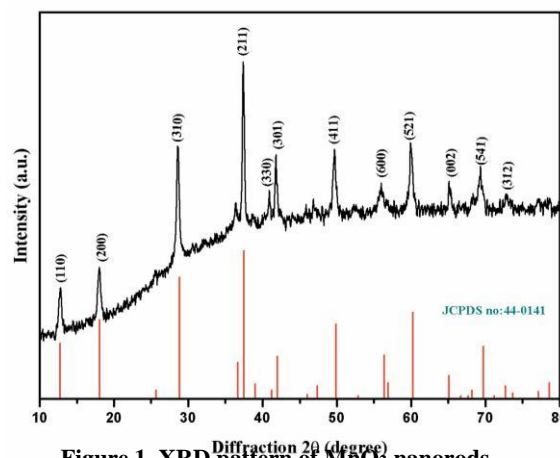


Figure 1. XRD pattern of MnO₂ nanorods

3.2. SEM analysis

The surface morphology of the MnO₂ Nanorods were examined by SEM analysis. The **figure 2 (a, b)** shows the SEM images of MnO₂ at different magnifications. The result showed that the obtained products have a rod like morphology. The EDAX spectrum as shown in **figure 2(c)** shows the peak for only Mn, O elements, which confirms there is no impurities were present in the sample. The mapping of Mn and O elements were shown in **figure 2(e, f)**. The overall mapping shown in **figure 2(d)** reveals, more than 40% oxygen was present in the surface of the MnO₂ nanorods.

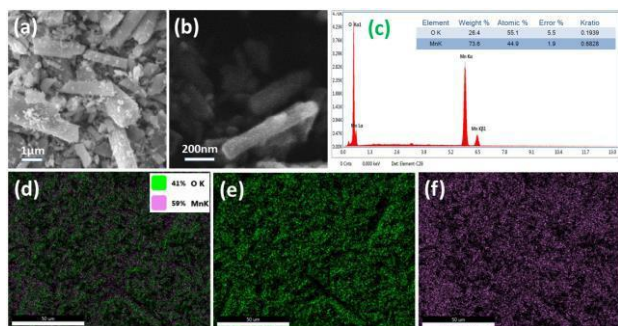


Figure 2. (a, b) SEM images at different magnifications, (c) EDAX spectrum, (d) overall mapping and (e, f) mapping of O, Mn

3.3. FTIR analysis

The FTIR was performed to study the presence of functional groups and metal-oxygen vibrations of the prepared nanorods. The FTIR spectrum was shown in figure 3. The peaks wavenumber and corresponding vibrations are listed in table 1.

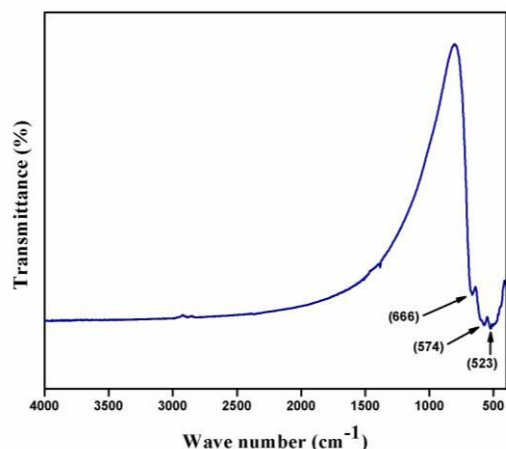


Figure 3. FTIR spectrum of MnO₂ nanorods

Table 1. Functional group

Functional groups	Transmittance (cm ⁻¹)
(Mn-O) mode of stretching	523,574
C-OH Stretching vibration	666

3.4. UV-Vis Analysis

The optical properties of prepared samples were studied by UV-Vis spectrometer. Figure 4(a) show the absorption spectra of MnO₂ nanorods. UV-Vis spectra were recorded in absorption mode and it can be clearly seen that there is no

visible absorption. The spectrum illustrates that a sharp peak occurs at ~ 305 nm, which is the effect of quantum confinement and broad absorption peak observed at ~ 450 nm corresponding to the MnO₂ nanorods. The bandgap energy was calculated by tauc plot using equation 1 as shown figure 4(b). The average band gap energy calculated is about 2.36 eV.

$$E = hc/\lambda \text{ (eV)} \quad (1)$$

where, h is Planck's constant (6.626×10⁻³⁴J.s) c is velocity of light (3×10⁸ m s⁻¹) λ is the wavelength corresponding to the sharp absorbance

3.5. Cyclic voltammetry

The cyclic voltammogram were performed using two different electrolytes (1M KOH and 1M KOH with 0.1M K₄(Fe[CN]₆)) are shown in figure 5 (a, b).

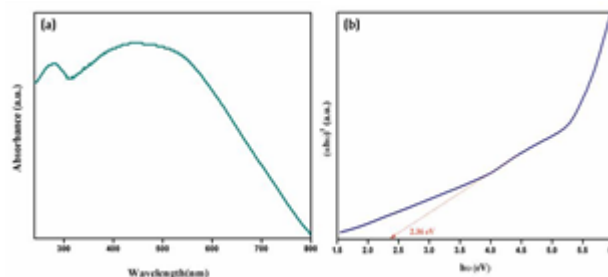


Figure 4. (a) UV-Vis absorption spectrum of MnO₂ nanorods (b) Tauc plot for band gap determination

The integral area of current over the CV curve for redox electrolyte shows, there is improvement in specific capacitances as shown in figure 5(c, d). It reveals that there is a small potential drop was observed for 1M KOH and it was expanding after addition of redox additive to the electrolyte. The specific capacitance achieved for each electrolyte at various scan rates was displayed in figure 6. The maximum specific capacitance achieved for redox active electrolyte was about 634 Fg⁻¹. The EIS spectrum for both electrolytes was displayed in figure 7. For 1M KOH, it possessing a straight line which is related to the pure capacitive behavior. The EIS spectrum observed for 1M KOH electrolyte was exhibiting a broad semi-circle like curve from high frequency region to

low frequency region, which shows the parallel combination of capacitor and re-sistor behavior. In the case of redox active electrolyte, there is no semicircle were noted, this is because of reduced electrolyte resistivity and pure capacitive behaviour.

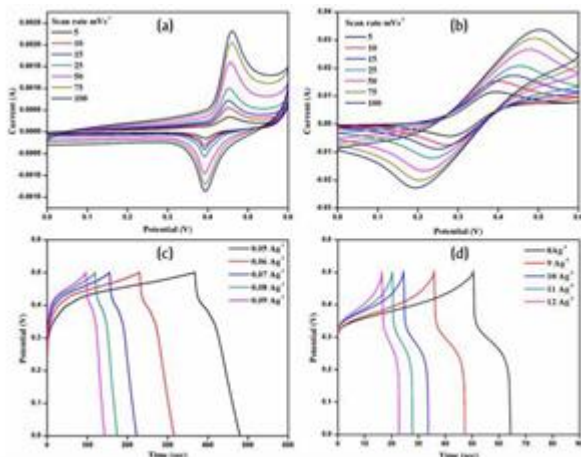


Figure 5. (a, b) Cyclic Voltammogram and (c, d) Galvanostatic charge discharge

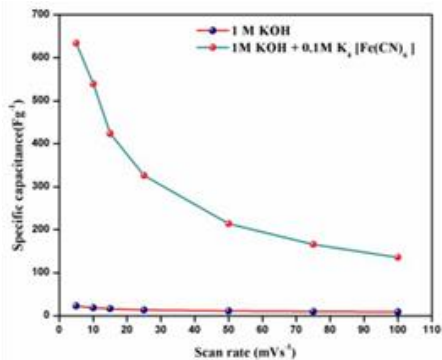


Figure 6. Specific capacitance at different scan rates

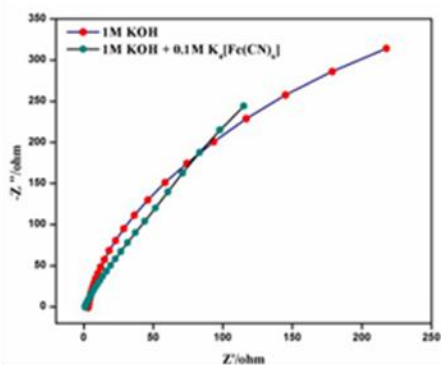


Figure 7. Electrochemical Impedance Spectrum

4. Conclusion

Pure MnO_2 nanorods was successfully synthesized using one step hydrothermal method. Tetragonal structure of the prepared MnO_2 nanorods was con-firmed by the XRD analysis and the presence of na-norods was confirmed by the SEM analysis. The spe-cific capacitance values are increased by adding 0.1M $K_4[Fe(CN)_6]$ into the 1M KOH electrolyte. By en-hancing redox reactions in electrode and electrolytes, the supercapacitor performance was comparatively increased. The resistivity of the electrolyte also reduced after the ad-dition of redox additive.

5. Acknowledgements

Authors are great fully acknowledged to Kalasalingam Academy of Research and Education for providing research facilities.

REFERENCES

- [1] D.L. Ji, J.H. Li, L.M. Chen, D. Zhang, T. Liu, N. Zhang, R.Z. Ma, G.Z. Qiu, X.H. Liu, Needle-like CoO nanowires grown on carbon cloth for enhanced electrochemical prop-erties in supercapacitors, RSC Adv. 5 (2015) 41627– 41630.
- [2] Y. Zhang, G.Y. Li, Y. Lv, L.Z. Wang, A.Q. Zhang, Y.H. Song, B.L. Huang, Electrochemical investigation of MnO_2 electrode material for supercapacitors, Int. J. Hydrogen Energy 36 (2011) 11760–11766.
- [3] X.F. Wang, Y.J. Yin, X.Y. Li, Z. You, Fabrication of a symmetric micro supercapacitor based on tubular ruthenium oxide on silicon 3D microstructures, J. Power Sources 252 (2014) 64–72.
- [4] H. Xia, C.Y. Hong, X.Q. Shi, B. Li, G.L. Yuan, Q.F. Yao, J.P. Xie, Hierarchical heterostructures of Ag nanoparticles decorated MnO_2 nanowires as promising electrodes for su-percapacitors, J. Mater. Chem. A 3 (2015) 1216–1221.
- [5] J.C. Deng, L.T. Kang, G.L. Bai, Y. Li, P.Y. Li, X.G. Liu, Y.Z. Yang, F. Gao, W. Liang, Solution combustion syn-thesis of cobalt oxides (Co_3O_4 and Co_3O_4/CoO) nanoparti-cles as supercapacitor electrode materials, Electrochim. Acta 132 (2014) 127–135.

- [6] C.Y. Chen, C.Q. Chen, P.P. Huang, F.F. Duan, S.C. Zhao, P. Li, J.C. Fan, W.G. Song, Y. Qin, NiO/nanoporous gra-phene composites with excellent supercapacitive perfor-mance produced by atomic layer deposition, *Nanotechnol-ogy* 25 (2014) 504001.
- [7] D.L. Yu, X.F. Zhu, Z. Xu, X.M. Zhong, Q.F. Gui, Y. Song, S.Y. Zhang, X.Y. Chen, D.D. Li, Facile method to enhance the adhesion of TiO₂ nanotube arrays to Ti substrate, *ACS Appl. Mater. Inter.* 6 (2014) 8001–8005.
- [8] M.S. Song, K.M. Lee, Y.R. Lee, I.Y. Kim, T.W. Kim, J.L. Gunjaker, S.J. Hwang, Porously assembled 2D nanosheets of alkali metal manganese oxides with highly reversible pseudocapacitance behaviors, *J. Phys. Chem. C* 114 (2010) 22134–22140.
- [9] S. Maiti, A. Pramanik, S. Mahanty, ChemComm organic framework derived nanostructured cerium, *Chem. Com-mun.* 50 (2014) 11717–11720. doi:10.1039/C4CC05363J.

CHARGE TRANSFER CONTRIBUTIONS NON-LINEAR OPTICAL PROPERTY OF 2-AMINOPYRIDINIUM DI-HYDROGEN PHOSPHATE BASED ON *AB-INITIO* HF AND DFT CALCULATIONS

G. Sivaraj^a, N. Jayamani^{b*}, V. Siva^c

^aDepartment of Physics, Periyar University, Salem-636 011, India.

^bDepartment of Physics, Government Arts College Salem-636 007, India.

^cDepartment of Physics, International Research centre, Kalasalingam Academy of Research and Education, Krishnankoil-626 126, India.

*Corresponding Author: drnjayamani@gmail.com

Abstract

2-Aminopyridinium Dihydrogen Phosphate (2APDP) were optimized using HF/DFT(B3LYP) 6-311++G(d,p) basis set. The values of polarizability and hyperpolarizabilities were calculated and discussed. The HOMO-LUMO plot reveals the charge transfer possibilities in the molecules. The chemical hardness, electronegativity, chemical potential and electrophilicity index of 2APDP were found along with the HOMO-LUMO values. The lower band gap value obtained from the Frontier Molecular Orbital (FMO) analysis reiterates the NLO activity of the compound. Using MEP plot the electrophilic nucleophilic regions are identified.

Keywords: DFT;HOMO-LUMO; Non-linear optics; MEP.

1. Introduction

In recent years, the search of new nonlinear optical materials (NLO) includes organic compounds due to their advantages over inorganic compounds. Organic molecules exhibit the large second order nonlinearity, and hence they are widely used in many applications like optical communication, information storage, optical switching, etc., Density functional theory (DFT) has been extensively used in theoretical modeling. The development of better exchange correlation functionals has made it possible to calculate many molecular properties with comparable accuracies to traditionally correlated *ab-initio* methods, with more favorable computational costs [4]. Literature survey has revealed that the DFT has a great accuracy in reproducing the experimental values in geometry, dipole moment, etc. [5–9].

Many investigations are being carried out to synthesize new organic materials with large second-order optical nonlinearities in order to satisfy day to day technological requirements [6,7]. Organic nonlinear materials have larger optical susceptibilities, inherent ultrafast response times and high optical thresholds for laser power compared to inorganic materials [8]. It is well known for organic materials that large delocalization of electrons induces electrooptic effects and produces large nonlinear optical responses [9].

2. Computational details

The entire calculations was performed at HF and DFT (B3LYP) levels with the standard basis set 6-311++g(d,p) on personal computer using GAUSSIAN 09W [10] program package, invoking gradient geometry

optimization. The global minimum energy conformer is used in the vibrational wavenumber calculation at the HF and DFT(B3LYP) with using 6-311++g(d,p) level. Gauss View 05 [11] was utilized to envision the optimized structure

3 Results and discussion

3.1 Optimized molecular geometry

The molecular structure along with the numbering of atoms of title compound is obtained from Gaussian 09 programs. The geometry optimized by HF/DFT(B3LYP) with 6-311++g(d,p) basis set along with numbering scheme has been figured out in Fig. 1 (a) and (b). The comparative important geometrical parameters such as bond lengths and bond angles are presented in Table 1. The optimized C–N bond lengths are 1.337, 1.3192 and 1.3493 Å for HF/6-311++G(d,p) method and 1.3601, 1.3340 and 1.3519 Å for DFT(B3LYP)/ 6-311++G(d,p) method. N–H···O interactions 1.56072 Å in HF and 1.71001 Å in DFT methods.

3.2 Mulliken atomic charges

The atomic charge in molecules is fundamental to chemistry. Mulliken charge [12] atomic charge calculation has an important role for the application of quantum chemical

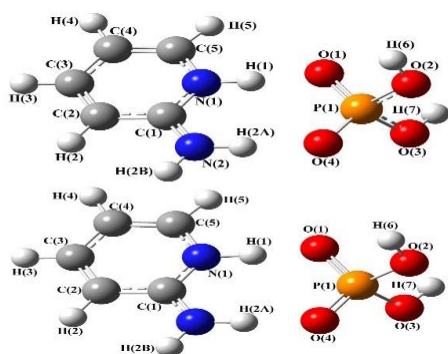


Figure 1. Optimized molecular geometry and atomic numbering scheme of the 2APDP by (a) HF/6-311++G(d,p) and (b) DFT/6-311++G(d,p) levels.

Table 1 Bond length and Mulliken atomic charges.

Bond length(Å)	HF	DFT	Atom	Charge	
				HF	DFT
C(1)–C(2)	1.42	1.42			
C(1)–N(1)	1.34	1.36	C(1)	-0.10	-0.42
C(1)–N(2)	1.32	1.33	C(2)	0.51	0.67
C(2)–C(3)	1.36	1.37	C(3)	-0.51	-0.55
C(2)–H(2)	1.07	1.08	C(4)	-0.33	-0.06
C(3)–C(4)	1.42	1.41	C(5)	-0.09	-0.24
C(4)–C(5)	1.35	1.37	N(1)	-0.46	-0.29
C(4)–H(4)	1.07	1.08	N(2)	-0.60	-0.42
C(5)–N(1)	1.35	1.35	H(2)	0.23	0.19
C(5)–H(5)	1.07	1.08	H(3)	0.23	0.18
N(1)–H(1)	1.05	1.11	H(4)	0.23	0.19
N(2)–H(2A)	1.02	1.05	H(5)	0.24	0.19
N(2)–H(2B)	0.99	1.01	H(1)	0.72	0.63
P(1)–O(1)	1.50	1.53	H(2A)	0.54	0.45
P(1)–O(2)	1.60	1.63	H(2B)	0.31	0.27
P(1)–O(3)	1.59	1.62	P(1)	0.97	0.56
P(1)–O(4)	1.47	1.50	O(1)	-0.84	-0.66
O(2)–H(6)	0.94	0.96	O(2)	-0.49	-0.39
O(3)–H(7)	0.94	0.96	O(3)	-0.44	-0.34
O(1)···H(1)	1.56	1.45	O(4)	-0.69	-0.52
O(4)···H(2A)	1.71	1.64	H(6)	0.30	0.28
			H(7)	0.29	0.28

calculations of the molecular system. For instance, atomic charge has been used to describe the processes of electronegativity equalization and charge transfer in chemical reactions [13,14] and to model the electrostatic potential outside molecular surfaces [15-17]. And atomic

charge affects dipole moment, polarizability, electronic structure and other molecular properties as the system. The calculated Mulliken charge (e) value of 2APDP are listed in table 1. It is worthy to mention that C(1), C(3), C(4) and C(5) atoms of 2APDP exhibit negative charge, while C(2) atom exhibit positive charge and C(3) has maximum negative charge value about -0.512036(HF)/-0.552028(DFT).

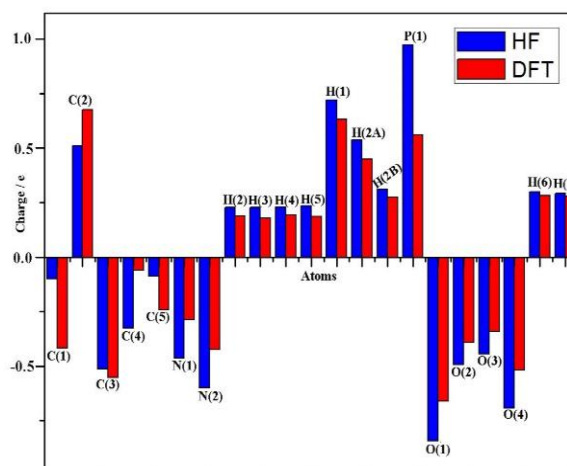


Figure 2 Mulliken charges of the optimized molecular structure for 2APDP

3.3 Nonlinear optical (NLO) effects

The simplest polarizability, characterizes the ability of an electric field to distort the electronic distribution of a molecule. Higher order polarizability (hyperpolarizabilities β , γ , etc.) which describe the non-linear response of atoms and molecules are related to a wide range of phenomena from non-linear optics to intermolecular forces, such as the stability of chemical bonds, as well as, the conformation of molecules and molecular aggregates [18, 19]. The large value of first hyperpolarizability, which is the measure of the NLO activity of the molecular system, is associated with the resulting from the electron cloud movement through π conjugated frame work from electron donor to electron acceptor groups. These studies led to the fact that *ab-initio* calculations of polarizabilities and hyperpolarizabilities have become available through the strong theoretical basis for analyzing molecular interactions.

In the present study, the electronic dipole moment, molecular polarizability, anisotropy of polarizability and molecular first hyperpolarizability of present compound were investigated. The polarizability and hyperpolarizability tensors (α_{xx} , α_{yy} , α_{zz} , α_{xy} , α_{xz} , α_{yz} , β_{xxx} , β_{yyy} , β_{zzz} , β_{xyy} , β_{xxy} , β_{xxz} , β_{xzz} , β_{yzz} , β_{yyz} , β_{xyz}) can be obtained by a frequency job output file of Gaussian. However, α and β values of Gaussian output are in atomic units (a.u.) so

they have been converted into electronic units (esu). The mean polarizability (α_0), anisotropy of polarizability (α) and the average value of the first hyperpolarizability (β_{total}) can be calculated using the equations

The total static dipole moment is

$$\mu = \mu_x^2 + \mu_y^2 + \mu_z^2$$

The isotropic polarizability is

$$\alpha_0 = \frac{\alpha_{xx} + \alpha_{yy} + \alpha_{zz}}{3}$$

The anisotropy polarizability is

$$\Delta\alpha = \left[\frac{(\alpha_{xx} - \alpha_{yy})^2 + (\alpha_{yy} - \alpha_{zz})^2 + (\alpha_{zz} - \alpha_{xx})^2}{2} \right]^{\frac{1}{2}}$$

The mean first-order hyperpolarizability is

$$\beta_0 = \sqrt{(\beta_x^2 + \beta_y^2 + \beta_z^2)}$$

Table 2 Molecular properties and NLO parameters

Molecular Properties	Energy	
	HF	DFT
HOMO	-0.35058	-0.33059
LUMO	0.02193	-0.19786
$\Delta(E_{\text{HOMO}}-E_{\text{LUMO}})(a.u)$	0.37251	0.13273
$\Delta(E_{\text{HOMO}}-E_{\text{LUMO}})$ eV	10.14754	3.61570
Ionization Potential (I)	0.35058	0.33059
Electron Affinity (A)	-0.02193	0.19786
Global Hardness (η)	0.18626	0.06637
Global Softness (ν)	5.36898	15.06818
Electro negativity(χ)	0.16433	0.26423
Chemical potential (μ)	-0.16433	-0.26423
Global Electrophilicity (ω)	0.07249	0.52599

Parameters	values	
	HF	DFT
μ	9.72	8.2
α	-71.87	-52.35
$\Delta\alpha$	8.35	64.85
β_{tot} (a.u.)	71.28	59.85
$\beta_{\text{tot}} \times 10^{-30}$ (e.s.u)	0.62	0.52

In table 2 part-II, the calculated parameters described above and electronic dipole moment $\{\mu_i$ ($i = x, y, z$) and total dipole moment $\mu\}$ for title compound are listed. It is well known that the higher values of dipole moment, molecular polarizability, and hyperpolarizability are important for more active NLO properties. The calculated dipole moment is equal to 9.7174(HF)/ 8.2013(DFT) Debye (D). The highest value of dipole moment is observed for component μ_x . In this direction, this value is equal to 9.5831(HF)/ 8.0628(DFT). The calculated po-

larizability α_{ij} have non-zero values and was dominated by the diagonal components. Total anisotropy of polarizability (α) are calculated as -71.87(HF)/ -52.35(DFT) D Å. The first hyperpolarizability value β_{total} of the title compound is equal to 71.28(HF)/ 59.85(DFT) a.u. The hyperpolarizability β dominated by the longitudinal components of β_{xxx} . Domination of particular component indicated on substantial delocalization of charges in this direction. Total dipole moment of title molecule is equal to 0.62×10^{-30} e.s.u (HF)/ 0.52×10^{-30} e.s.u (DFT). That is to say, the title compound can be used as a good candidate of NLO materials.

3.4 Molecular electrostatic potential

For investigating chemical reactivity of the molecule, molecular electrostatic potential (MEP) surface is plotted over the optimized electronic structure of 2APDP using density functional HF and DFT (B3LYP) method with 6-311++G(d,p) basis set. The MEP generated in space around a molecule by the charge distribution is very helpful in understanding the reactive sites for nucleophilic and electrophilic attack in hydrogen bonding interactions [20]. In hydrogen bonded systems, the study of interacting behavior of various constituents of the molecule has great importance. Because the computationally observed MEP surface is directly provide information about the electrophilic (electronegative charge region) and nucleophilic (most positive charge region) regions. Fig. 3 shows the computationally observed MEP contour map.

The various values of the electrostatic potential at the surface are represented by various colors. The color scheme for the MEP surface is red electron rich, partially negative charge (electrophilic reactive center); blue-electron deficient, partially positive charge; light blueslightly electron deficient region (nucleophilic reactive center); yellow-slightly electron rich region; green-neutral, respectively. The potential increases in the order red < orange < yellow < green < cyan < blue. It can be seen that the negative regions are mainly over the O(1), O(2), O(3) and O(4) atoms. Negative (red color) and positive (blue) regions of electrostatic potential are associated with electrophilic and nucleophilic reactivity. The majority of light green region MEP surface resemble a potential halfway between two extremes red and dark blue color. The negative molecular electrostatic potential resembles an attraction of the proton by the evaluate electron density in the molecule (shades of red), the positive electrostatic potential corresponds to the repulsion of the protons by the atomic nuclei (shades of blue). According to these calculated results, the MEP map illustrates that the negative potential sites are on oxygen and nitrogen atoms and the positive potential sites as well are around the hydrogen atoms. These active sites found to

be clear evidence of biological activity in the title compound.

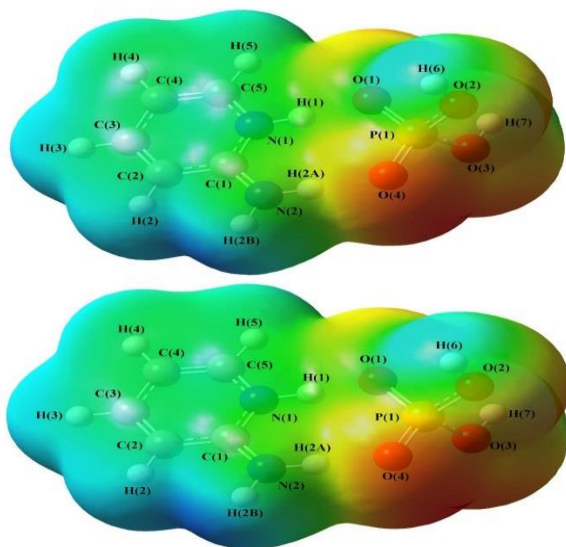


Figure 3. Molecular electrostatic potential (MEP) surface map of 2APDP a) HF and b) DFT(B3LYP)

3.5 Frontier molecular orbital's (FMOs)

The most important orbital's in molecule is the frontier molecular orbital's, called highest occupied molecular orbital (HOMO) and lowest unoccupied molecular orbital (LUMO). These orbitals determine the way of molecule interacts with other species. The frontier molecular energy gap helps to characterize the chemical reactivity and kinetic stability of the molecule. Generally, the energy gap between the HOMO and LUMO decreases, it is easier for the electrons of the HOMO to be excited. The higher energy of HOMO, the easier it is for HOMO to donate electrons whereas it is easier for LUMO to accept electrons when the energy of LUMO is low. Commonly, the atom occupied by more densities of HOMO should have stronger ability to detach an electron whereas; the atom with more occupation of LUMO should have ability to gain an electron. For 2APDP molecule, the HOMO orbital of π type is lying at -0.35058 (HF)/ -0.33059 (DFT) a.u. while the LUMO orbitals are π^* in type is lying at 0.02193 (HF)/ -0.19786 (DFT) a.u. As a result, a very small energy gap is observed between HOMO and LUMO molecular orbitals of 2APDP and the energy gap calculated at HF/DFT(B3LYP) and 6-311++G(d,p) basis set is 10.14 (HF)/ 3.61 (DFT) eV. Hence the probability of $\pi \rightarrow \pi^*$ proton transition is highly possible in between HOMO and LUMO orbitals for the 2APDP. The chemical hardness and softness of a molecule is a good indicator of the chemical stability of a molecule. From the HOMO– LUMO energy gap, one can find whether the molecule is hard or soft. The molecules having large

energy gap are known as hard and molecules having a small energy gap are known as soft molecules. The soft molecules are more polarizable than the hard ones because they need small energy to excitation.

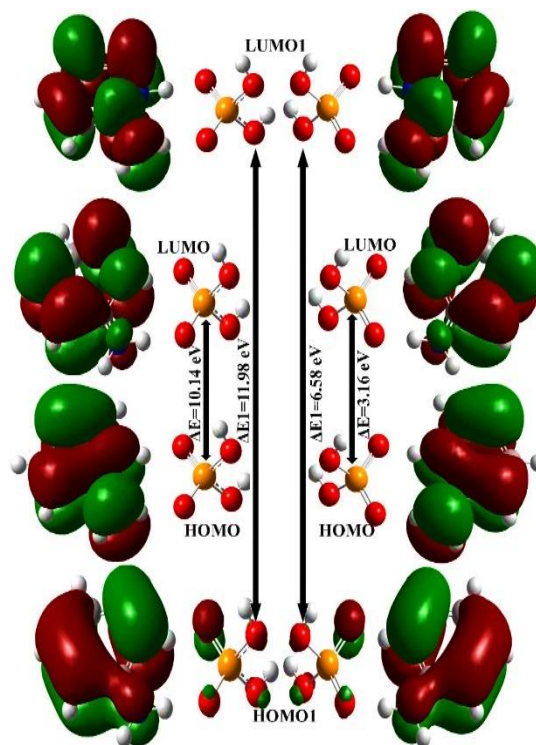


Figure 4 HOMO-LUMO plot

Conclusion

The geometrical parameters were optimized by HF and DFT(B3LYP) with 6-311++G(d,p) basis set. Total dipole moment of title molecule is equal to 0.62×10^{-30} e.s.u (HF)/ 0.52×10^{-30} e.s.u (DFT), this values 1.65 times greater than that of urea(urea $\mu=1.3732$ debye, $\beta=0.37289 \times 10^{-30}$ esu). That is to say, the title compound can be used as a good candidate of NLO materials. The MEP map illustrates that the negative potential sites are on oxygen and nitrogen atoms and the positive potential sites as well are around the hydrogen atoms. These active sites found to be clear evidence of biological activity in the title compound. Mulliken atomic charges also calculated.

REFERENCE

- [1] F.D. Proft, P. Geerlings, Chem. Rev. 101 (2001) 1451–1464.
- [2] H. Tanak, J. Phys. Chem. A 115 (47) (2011) 13865–13876.

- [3] H. Tanak, *Int. J. Quantum Chem.* 112 (2012) 2392–2402.
- [4] H. Tanak, *Comput. Theor. Chem.* 967 (2011) 93–101.
- [5] G. Fitzgerald, J. Andzelm, *J. Phys. Chem.* 95 (1991) 10531–10534.
- [6] J. Andzelm, E. Wimmer, *J. Chem. Phys.* 96 (1992) 1280–1303.
- [7] U. Meir, M. Bosch, C. Boshard, P. Gunter, DAST a high optical nonlinearity organic crystal, *Synth. Met.* 109 (2000) 19.
- [8] R. Siddheswaran, R. Sankar, M. Rathnakumari, P. Murugakoothan, R. Jayavel, P. Suresh Kumar, Growth and characterization of a new semi-organic non-linear optical crystal l-arginine hydrochlorofluoride monohydrate (lahclf), *Surf. Rev. Lett.* 13 (2006) 803.
- [9] T. Pal, T. Kar, G. Bocelli, L. Rigi, Synthesis, growth, and characterization of l-arginine acetate crystal: a potential NLO material, *Cryst. Growth Des.* 3 (2003) 13.
- [10] A. Natansohn, P. Rochon, The versatility of azobenzene polymers, *Can. J. Chem.* 79 (2001) 1093.
- [11] M. J. Frisch et al, Gaussian, Inc., Wallingford CT, 2013.
- [12] D.C. Young, *Computational Chemistry a Practical Guide for Applying Techniquesto Real-world Problems (Electronics)*, John Wiley and Sons, New York, 2001.
- [13] R.S Mulliken, *J. Chem. Phys.* 23(1955) 1833-1840.
- [14] D.M. Burland, R.D. Miller, C.A. Walsh, *Chem. Rev.* 94 (1994) 31.
- [15] S. Yazoco, C. Albayrak, I. Gumrukcuoglu, I. Senel, O. Buyukungor, *J. Mol. Struct.* 985 (2011) 292–298.
- [16] S. Gunasekaran, R.A. Balaji, S. Kumaresan, G. Anand, S. Srinivasan, *Can. J. Anal. Sci. Spectrosc.* 53 (2008) 149–162.
- [17] P. Politzer, P.R. Laurence, K. Jayasuriya, *Environ. Health Perspect.* 61 (1985) 191–202.
- [18] I. Fleming, *Frontier Orbitals and Organic Chemical reactions*, JohnWiley& Sons, New York, 1976.
- [19] R.P. Iczkowski, J.V. Margrave, *J. Am. Chem. Soc.* 83 (1961) 3547–3551.
- [20] L. Larabi, Y. Harek, O. Benali, S. Ghalam, *Prog. Org. Coat.* 54 (2005) 256–262.
- [21] I. Lukovits, I. Bako, A. Shaban, E. Kalman, *Electrochim. Acta* 43 (1998) 131–136.
- [22] R.G. Parr, L.V. Szentpaly, S. Liu, *J. Am. Chem. Soc.* 121 (1999) 1922–1924.

COPPER VESSEL EFFICIENCY AGAINST DIFFERENT DRINKING WATERS

A. Vinothkumar, S. Mugeshkumar, V. Vanitha, Naidu Dhanpal Jayram*

Department of physics, Kalasalingam Academy of Research and Education

Email:dhanpal@klu.ac.in

Abstract

Storage of water in copper vessels is traditionally followed in past and many reports have been published about the antibacterial growth in copper vessel. It is essential to determine the water purity for drinking purposes in daily life through low cost approach. In the present work an attempt has been made to investigate the effect of storage of different drinking water in copper vessel for one week. The corresponding values of pH and TDS meter for different waters were recorded and analyzed. The optical properties such as UV-Vis and Raman studies along with physio parameters like pH and TDS were analyzed for a week against different water sources kept in copper vessel. The Raman and SERS spectra provide information for trace. Similarly the UV-Vis spectroscopy provide the peak variation for different waters, however the effect of days and copper concentration analysis are in investigation. The overall Results obtained in this study reveals that water stored in copper vessel reduces the TDS level of bore water and maintains pH for all kinds of water in-between 7.0 to 8.0 for one week.

Keywords: Copper vessel, TDS, pH and Different water types

1. Introduction

The continued rapid growth in human population demands for water resources in large quantity. Worldwide, more than one million deaths occur due to water-borne diarrheal diseases [1-2]. Diseases related to contamination of drinking water constitute a major burden on human health. It is estimated that approximately 780 million people lack access to an improved water source. In India, there are additional problems due to the disruption of piped water supplies in rural and urban areas, resulting in a need to store water for drinking, food preparation and bathing purposes [3-5]. Drinking water may be contaminated at the source or during storage. Even though, storage of water has been recommended as method of water purification, contamination of treated or disinfected water can also occur during storage due to improper handling. Traditionally, vessels made up of copper and its alloys and earthenware pots have been used in India for storing drinking water. Previous reports on surfaces containing at least 55%-70% copper reduces many pathogenic seeded microorganisms, *Escherichia coli*, fungi such as *Candida albicans*, viruses such as influenza viruses or the human immunodeficiency virus (HIV) and bacteria such as *Staphylococcus aureus*, [6-9]. The present study proposed to resolve the effect of different water storage in copper vessel for a week. The corresponding values of pH and TDS meter for different waters were recorded and analyzed. As this work is in initial stage the UV-Vis and Raman studies will be extended for further investigation.

Experimental

Copper glasses were purchased through local shop and pH and TDS meter were purchased online. For the study, 3 drinking sample were collected among which 2 were bore water from different districts of Tamil nadu and remaining one was regular drinking water present in our university.

1.1. Observation Table

1.2. Table 1. TDS and pH readings

Copper Effect	TDS and pH reading					
	Bore well 1		Bore well 2		Drinking water (univ)	
Day	pH	TDS	pH	TDS	pH	TDS
1 st	8.4	116	7.7	894	7.5	30
2 nd	8.2	142	8.2	900	8	31
3 rd	8.4	122	8.1	820	7.4	40
4 th	8	115	8	796	7	35
5 th	7.9	104	8	740	7	36
6 th	8.1	104	8	172	7	40

Different Water pH vs No of days in copper vessel

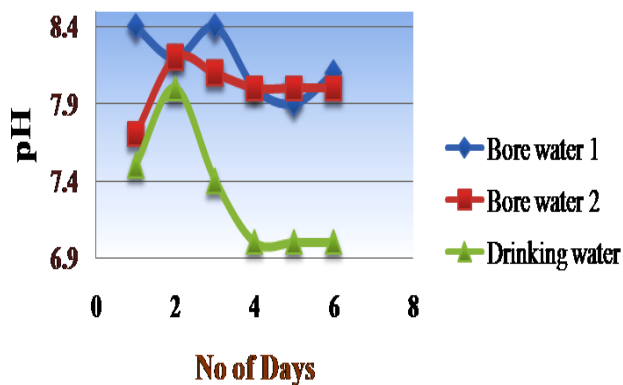


Figure 1: Different water pH levels against the no of days in copper vessel

TDS Vs No of days

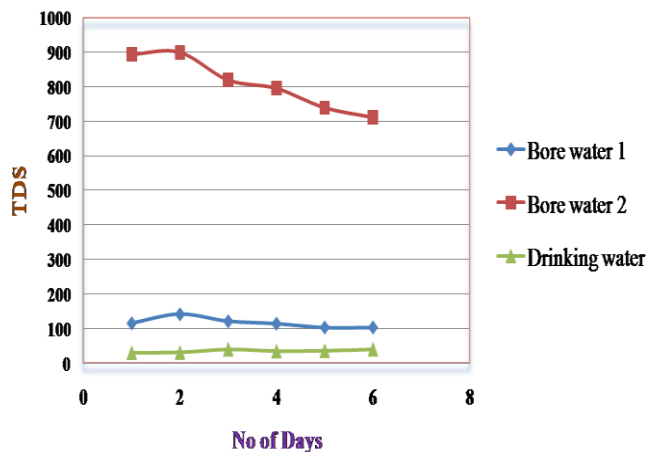


Figure2: Total dissolved salts in copper vessel for different waters

2. Results and Discussion

2.1. pH analysis

Water with pH value more than 9 or less than 4.5 become unsuitable for most life forms and also for other uses. The desirable pH range for drinking water is 6.5-8.0 pH. In our experiments stored water ranges in between 7.0 to 8.4 as shown in figure 1. High pH is observed for bore well water 2, while the pH for drinking water in our university shows low pH value of 7.0. copper has greater efficiency towards the pH water level

and sometimes it make water more alkaline when its pH is low. But in our experiment the drinking water available in university doesn't showed any variation in pH but the pH of bore water 1 drastically decreases from 8.5 to 8.0, similarly for bore water 1 also its shows decrease in pH. This can be due to ability of absorption of minerals through copper vessels [6-8]

2.2. TDS analysis

TDS is an important indicator of overall water quality. TDS helps in understanding the level of turbidity and hardness of water It is a measure of inorganic and organic materials dissolved in water. High TDS concentration may cause a bad odour or taste to drinking water, as well as cause scaling of pipes and corrosion. Waters can be classified based on the concentrations of TDS [4] as given below.

- Up to 450mg/L-Desirable for drinking
- Up to980mg/L-Permissible for drinking
- Up to2000mg/L- Useful for irrigation
- Up to3000mg/L-Not useful for drinking and irrigation.

In the present work the initial TDS of bore water 1 was 894 ppm and keeping iin copper for one week its drastically changes to 712 ppm, while Bore well water 2 is found to be 115ppm and remains constant even after one week. Similarly in case of university drinking water the TDS shows constant reading value of 36ppm

3. Conclusion

The obtained TDS and pH are suitable for drinking purposes well matches with WHO reports. Drinking water kept in copper vessel for one week shows a good change for bore well water 2, as the TDS and pH decreases continuously. In the case of bore well water 1, TDS remains constant and shows the value of 104ppm even after week. The university drinking water from the beginning of analysis maintained pH value of 7.4 and TDS of 35ppm and doesn't show any variation throughout the week. Overall results concluded that copper can be used effectively for drinking storage purpose up to one week and maintains pH and TDS without any bacterial growth. Uv-Vis and Raman studies are in investigation. Copper vessels can be used for drinking purposes as conventional resources especially in rural areas when the facilities for purifier not available.

4. Acknowledgements

All authors want to thank Kalasalingam Academy of Research and Education for providing characterization

facilities at International Research Centre (IRC). On behalf of all authors, the corresponding author states that there is no conflict of interest.

REFERENCES

- [1] V.B.Preethisudha,S.Ganesan,G.P.Pazhani,T.Ramamurthy G.B.Nair and P.Venkatasubramanian "Storing Drinking-water in Copper pots Kills Contaminating Diarrhoeagenic Bacteria", March 2012 Journal of Health Population and Nutrition 30(1):17-21.DOI:10.3329/jhpn.v30i1.1127.
- [2] Department of Microbiology, St. Pious X Degree and P.G College"Effect of storage of water in different metal vessels on coliforms"ISSN: 2319-7706 Volume 2 Number 11 (2013) pp. 24-29.
- [3] M.S.S.Abujazara, S.Fatihah, A.E.Kabeel, S.Sharil and S.S.Abuamr "Evaluation quality of desalinated water derived from inclined copper-stepped solar still" 131 (2018) 83–95November.doi: 10.5004/dwt.2018.22958
- [4] C.E.Santo, E.W.Lam, C.G.Elowsky, D.Quaranta, D.W.Domaille, C.J.Jhang and G. Grass, "Bacterial killing by dry metallic copper surfaces",(2011) Applied and Environmental Microbiology, 77 (3), pp. 794-802,DOI: 10.1128/AEM.01599-10.
- [5] V.B.P.Sudha, K.O.Singh, S.RPrasad and P.Venkatasubramaia"Killing of enteric bacteria in drinking water by a copper device for use in the home",(2009) Transactions of the Royal Society of Tropical Medicine and Hygiene, 103 (8), pp. 819-822,DOI: 10.1016/j.trstmh.2009.01.019.
- [6] J.O'Gorman and H.Humphreys,"Application of copper to prevent and control infection. Where are we now",(2012) Journal of Hospital Infection, 81 (4), pp. 217-223,DOI: 10.1016/j.jhin.2012.05.
- [7] D.R.Thomas, B.Sunil, C.Latha and B.Chacko,"Microbiological Quality of Water Stored in Copper,Earthenware and Stainless Steel Vessels",Citation: IJAEB: 7(1): 25-28 March 2014,DOI 10.5958/j.2230-732X.7.1.004.
- [8] N.Mohanan,E.K. Manju and S.Jacob,"The Effect of Different Types of Storage Vessels on Water Quality",Vol. 6, Issue 10, October 2017,DOI:10.15680/IJIRSET.2017.0610119.
- [9] RajaniShrestha, Dev Raj Joshi, Jyotsna Gopali and Sujan Piya,"Oligodynamic Action of Silver, Copper and Brass onEnteric Bacteria Isolated from water of Kathmandu-ValleyWater",Nepal Journal of Science and Technology 10 (2009) 189-193

PREPARATION AND CHARACTERIZATION OF Zn DOPED TiO₂ NANOPARTICLES FOR PHOTO CATALYTIC ACTIVITY

N. Nithya*¹, P. Maheswari¹, G. Bhoopathi², G. Magesh²

¹PG and Research Department of Physics, PSGR Krishnammal College for Women, Coimbatore 641004, India

²PG and Research Department of Physics, PSG College of Arts and Science, Coimbatore-641014, India.

Corresponding Author Email: n.nithya@psgrkcw.ac.in.

Abstract:

The current work emphasis on the preparation, characterization and the photo catalytic activity of Zn doped TiO₂ nanoparticle. The structural, morphological and optical properties of Zn doped TiO₂ nanoparticle were studied by XRD, UV, PL, FTIR, FESEM, EDAX and TEM analysis. The XRD analysis showed that the TiO₂ and Zn doped TiO₂ nanoparticle with various molar concentration (0.5mM, 1mM, 1.5mM and 2mM) nanoparticle contains tetragonal anatase phase. The average crystallite size was found to be 13-11 nm. The band gap energy of TiO₂ nanoparticle and Zn doped TiO₂ nanoparticles were found in the range 3.56-3.52 eV. The intensity of prepared samples decreases and new green emission peaks were formed in the photoluminescence spectra. FTIR studies confirmed the presence of vibrational modes of chemical substance present in the sample. The grain size and surface morphology of the samples were analysed by FESEM and TEM-SAED analysis. The elemental compositions of the prepared samples were detected by energy dispersive X-ray analysis (EDAX). The effect of Zn concentrations on TiO₂ nanoparticle was studied for Methylene Blue and Congo red dye under UV irradiation.

Keywords: TiO₂ nanoparticle, Zn doped TiO₂ nanoparticle, Structural properties, Optical properties, Photo catalytic activity.

1. INTRODUCTION

TiO₂ is one of the most studied semiconducting materials in the last couple of decades because of its excellent physical and chemical properties, high stability, non-toxic, low cost and photosensitivity etc. TiO₂ is an important semiconductor with mainly three allotropies, namely anatase (3.2eV), brookite (1.9eV) and rutile (3eV). Each phase plays an important role in antibacterial, photocatalyst, solar cell and gas sensing applications [6,7]. The phase transformation of titania nanoparticle is particularly important in high temperature application and processes such as porous separation membrane and gas sensors [8]. It has widespread applications such as toxic gas removal, organic compound degradation, dye sensitized solar cell, biomedical application and photo dynamic therapy [9].

2. RESULTS AND DISCUSSION

2.1. XRD Analysis of Pure TiO₂ and Zn doped TiO₂ Nanoparticles

XRD study was performed by explore the crystal structure and preferred orientation of the crystallites. XRD Pattern of the Pure TiO₂ and Zn doped TiO₂ nanoparticles were shown in fig 1.

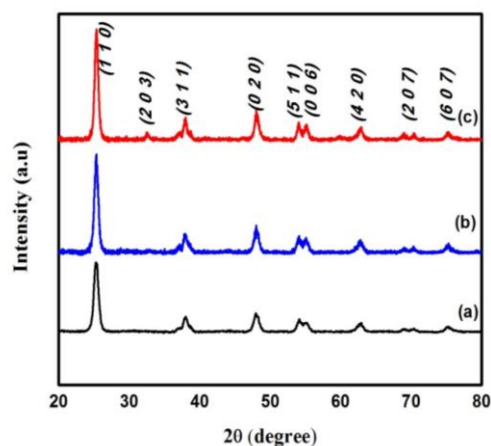


Fig 1 (a) XRD Analysis of pure TiO₂ nanoparticle (b) doped TiO₂ 0.2 wt% and (c) Zn doped TiO₂ nanoparticle (0.8 wt.%)

All samples were composed of mainly anatase phase. The peaks at angles $2\theta = 25.35^\circ, 32.32^\circ, 37.60^\circ, 48.35^\circ, 54.09^\circ, 55.12^\circ, 62.26^\circ, 68.44^\circ$ and 75.25° corresponds to the reflections from (1 1 0), (2 0 3), (3 1 1), (0 2 0), (5 1 1), (0 0 6), (4 2 0), (2 0 7) and (6 0 5) crystal planes of the tetragonal structure of TiO₂ nanoparticles. All the diffraction peaks agreed with the reported JCPDS Card no. 82-1127. The average particle size was found to be in the range 11.4 nm to 15.2 nm.

2.2 UV - visible analysis of pure TiO₂ and Zn doped TiO₂ nanoparticles

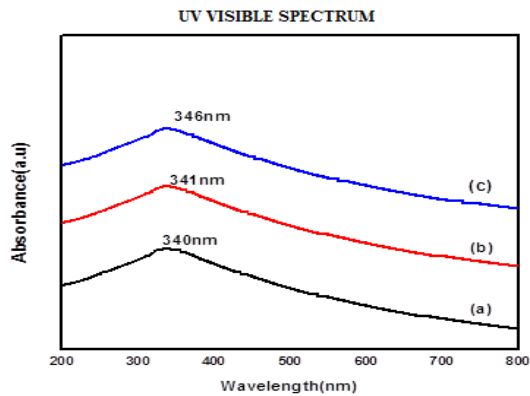


Fig 2 UV –Visible spectrum of (a) Pure TiO₂ (b) Zn/TiO₂ (0.2 wt%) and (c) Zn/TiO₂ Nanoparticles (0.8wt%)

Optical absorption spectra of pure TiO₂ and Zn doped TiO₂ nanoparticles in the wavelength range of 200nm-800nm are shown in the fig.5.2. It can be seen that the optical absorption of all samples starts up to 340nm indicates the semiconducting feature with direct bandgap of the samples. The absorption spectra showed a narrow absorption band at 340nm for pure TiO₂ nanoparticles. The absorption peak red shifted from 340nm for pure TiO₂ nanoparticles to 341nm, 346nm for various weightage of Zn doped TiO₂ nanoparticles.

2.3 FT-IR Analysis of Pure TiO₂ and Zn doped TiO₂ Nanoparticles

FTIR analysis was used to detect the various characteristic functional group associated with the nanoparticles. The fig.5.3 (a) shows the FTIR spectrum of pure TiO₂ and Zn doped TiO₂ nanoparticles was in the range of 500-4000cm⁻¹. The peaks indicates the characteristic functional group present in the synthesized nanoparticles.

The strong absorption bands observed at 699cm⁻¹ confirms the titanium nanoparticles. The absorption bands shifted from 699cm⁻¹ to 735cm⁻¹ and 742cm⁻¹ for Zn doped TiO₂ nanoparticles. By using FTIR analysis the removal of unwanted ions, phase formation, organic impurities that can be removed at the time of preparation was confirmed. The typical vibration absorption peaks at 1629cm⁻¹ may be related to hydroxyl (bending) groups of molecular water. The absorption range around 3364cm⁻¹ indicates the presence of hydroxyl stretching which is probably due to that spectra were recorded in sites and some re adsorption of water from the ambient atmosphere has occurred.

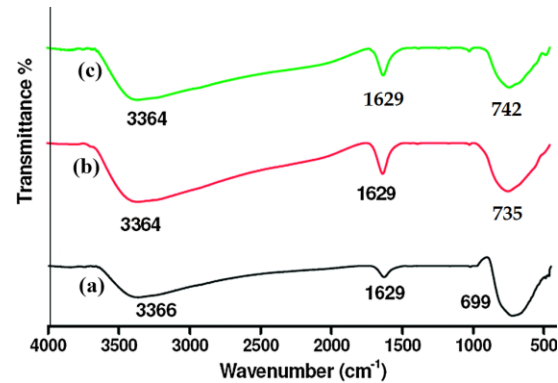


Fig 3 FTIR spectrum of pure TiO₂ and Zn doped TiO₂ Nanoparticles

(a) Pure TiO₂ (b) 0.2 wt% of Zn/TiO₂ (c) 0.8 wt% of Zn/TiO₂

3. CONCLUSION

Pure TiO₂ and Zn doped TiO₂ nanoparticles were synthesized by simple Solgel method. The prepared samples were characterized by UV, FTIR, XRD, FESEM. In UV analysis, wavelength increases and bandgap decreases. In FTIR analysis, functional group confirms the presence of TiO₂ nanoparticle. In XRD analysis, crystallite size increases when increasing the concentration of Zn. In FESEM analysis, particles are spherical in shape. In future work, pure and Zn doped TiO₂ nanoparticles were investigated for antibacterial and photocatalytic activity

REFERENCE

- [1] Krishna Lokaiah Arun Kumar, Sivalingam Durgajanani, Beri Gopalakrishnan Jeyaprakash and John Bosco Balaguru Rayappan, "Nanostructured ceria thin film for ethanol and trimethylamine sensing", *Sensors and Actuators B*, 177 (2013) 19-26.
- [2] S.M. Ingole, S.T. Navale, Y.H. Navale, D.K. Bandgar, F.J. Stadler, R.S. Mane, N.S. Ramgir, S.K. Gupta, D.K. Aswal, V.B. Patil, "Nanostructured Tin Oxide Films: Physical Synthesis, Characterization, and Gas Sensing Properties", *Journal of Colloid and Interface Science*, 493 (2017) 162-170.
- [3] Zhen Zhu, Cheng-Tse Kao and Ren-Jang Wu, "A Highly Sensitive Ethanol Sensor Based on Ag@TiO₂ nanoparticles at Room Temperature", *Applied Surface Science*, 320 (2014) 348-355.
- [4] Min-Hyun Seo, Masayoshi Yuas, Tetsuya Kid, Jeung-Soo Huh, Kengo Shimano, Noboru Yamazo, "Gas sensing characteristics and porosity control of nanostructured films composed of TiO₂ nanotubes", *Sensors and Actuators B*, 137 (2009) 513-520.
- [5] R. Rella, J. Spadavecchi, M.G. Maner, S. Capon, A. Taurino, M. Martino, A.P. Caricato, T. Tunno, "Acetone and ethanol solid-state gas sensors based on TiO₂

- nanoparticles thin film deposited by matrix assisted pulsed laser evaporation”, *Sensors and Actuators B*, 127 (2007) 426-431.
- [6] Meghshyam K. Patil, Sharekh Shaikh and Ibram Ganesh, “Recent Advances on TiO₂ Thin Film Based Photocatalytic Applications (A Review)”, *Current Nanoscience*, 11 (2015) 271- 285.
- [7] Mohammad A. Behnajady, Hamed Eskandarloo, “Preparation of TiO₂ nanoparticles by the sol–gel method under different pH conditions and modeling of photocatalytic activity by artificial neural network”, *Res Chem Intermed.*, 41 (2015) 2001-2017.
- [8] A. Ali, I. Ruzybayev, E. Yassitepe, A. Karim, S. Ismat Shah and A. S. Bhatti, “Phase Transformations in the PLD Grown TiO₂ Thin Films as a Consequence of O₂ Partial Pressure and Nd Doping”, *J. Phys. Chem. C*, 119 (2015) 11578-11587.
- [9] Qijun Zhang, Yu Fu, Yufeng Wu, Yi-Nan Zhang and Tiejong Zuo, “Low-Cost Y-Doped TiO₂ Nanosheets Film with Highly Reactive {001} Facets from CRT Waste and Enhanced Photocatalytic Removal of Cr (VI) and Methyl Orange”, *ACS Sustainable Chem. Eng.*, 4 (2016) 1794-1803.

STRUCTURAL AND BONDING BEHAVIOR OF TiO₂ IN RUTILE PHASE

D. Sivaganesh¹, S. Saravanakumar^{1*}, V. Sivakumar¹, K.S. Syed Ali², T. K. Thirumalaisamy³,
P. Meenakshi¹, S. Meera¹, S. Monisha¹

¹Department of Physics, Kalasalingam Academy of Research and Education, Krishnankoil, Virudhunagar, India

²Department of Science, Harmony Science Academy, 12005 Forestgate Dr. Dallas, TX- 75243, USA

³Department of Physics, H.K.R.H. College, Uthamapalayam, Tamil Nadu 625 533, India

Email: saravanaphysics@gmail.com

Abstract

The powder X-ray diffraction data set of rutile structure with single phased TiO₂ was simulated and characterized using Rietveld refinement technique. The resultant structure factors from the refinement method were used to evaluate the electron density distribution analysis of TiO₂ unit cell. The electronic bonding of TiO₂ has been analyzed using maximum entropy method. The three, two and one dimensional electron density distribution maps and the bonding features between the atoms were analyzed.

Keywords: Photocatalytic, PXRD, Rietveld refinement, MEM, simulation

1. Introduction

In the field of environmental remediation, titanium dioxide (TiO₂) is the most popular photocatalytic materials. Despite the fact that its efficiency is limited due to the large band gap value, TiO₂ is still playing a predominant role in many applications for organic pollutant degradation. Generally TiO₂ has 3 major crystalline form namely anatase, rutile and brookite. Brookite is not practically advantageous for it is only stable at low temperatures. Rutile is the primary source of TiO₂ and the most stable form of it. Rutile TiO₂ and anatase TiO₂ have different characteristics and uses and is usually the two forms of TiO₂ compared. Titanium dioxide has Ti⁴⁺-ion at the center and 6O²⁻ ions around it in an octahedron. But anatase TiO₂ and rutile TiO₂ have different densities and average Ti⁴⁺ distance which affects their thermodynamic stability. Rutile has shorter average Ti⁴⁺ and this means that rutile is more thermodynamically stable. By this aspect authors motivated to study the bonding behavior of rutile phase TiO₂ due to this more thermal stability [1, 2].

The electron plays an important role for fundamental properties of semiconducting materials. The electron density distribution a study is used to analyze the bonding features of the materials. In the search of the electronic properties and bonding natures of the materials, the maximum entropy method is used. In this work briefly discussed about the bonding nature of single phase TiO₂ structure.

2. XRD analysis

The rutile phase X-ray powder diffraction profile of TiO₂ was simulated by using the software "Findit". The tetragonal structure can be considered with a space group of P42/mnm and the cell constants a=b=4.59 Å, c=2.9 Å. The atomic coordinates of TiO₂ is given in Table 1.

Table 1: Atomic coordinates of TiO₂

Atomic positions	x	y	z
Ti	0	0	0
O	0.3053	0.3053	0

3. Results and discussion

The Rietveld technique [3] was used for refining structural parameters using software JANA 2006 [4] which refines lattice parameters, Gaussian parameters, Lagrange's parameters and preferred orientation parameters from the observed X-ray profile. The structure factors extracted from the refinement and used to calculate the electron density distributions of TiO₂ using maximum entropy method which is employed by software package DYSNOMIA [5].

Maximum entropy method is a standard tool to estimate the accurate charge density of the unit cell. Statistically

approached MEM method gives real and positive electron density everywhere. The charge density gives accurate pictures of distributions of charges.

The generated XRD profiles of TiO_2 were refined through profile fitting technique by using software JANA 2006. The Rietveld refinement profile of TiO_2 is shown in figure 1. Refined structural parameters of TiO_2 are shown in Table 2.

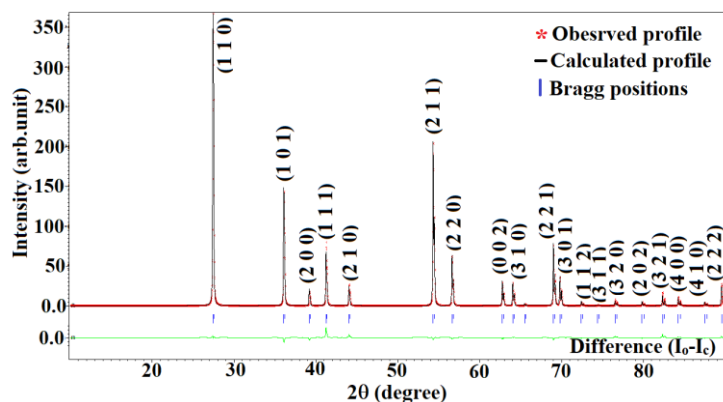


Fig 1. Refined profile of TiO_2

Table 2. Refined parameters of TiO_2

Parameters	TiO_2
a=b (Å)	4.5942(6)
c (Å)	2.9590(4)
Volume (Å ³)	62.45(1)
Density (g/cm ³)	4.24
F ₍₀₀₀₎	76
R _{obs} (%)	1.53
R _p (%)	4.43
GOF	0.21

R_{obs}- observed profile reliability factor
 R_p - profile reliability factor
 F₍₀₀₀₎- Number of electrons per unit cell
 GOF – Goodness of Fit

Refined structure factors are used to evaluate the electron density distributions of TiO_2 using MEM. The resultant of maximum entropy method was visualized using the visualization software VESTA (Visualization for Electronic and Structural Analysis) [6].

3-D unit cell is drawn for TiO_2 as shown in Figure 2. It's shown that there is a spherical in core of Ti and O atoms, the shaded yellow region represented by electron clouds. And also when a single unit cell of TiO_2 contain two

bonds ones positioning at $(y+1/2, x+1/2, z+1/2)$ and other one is positioning at (x, y, z) . Two dimensional electron density distributions maps are drawn on (100) and (110) miller plane in contour level 0-2 $e/\text{Å}^3$ with interval of 0.25 $e/\text{Å}^3$ as shown in figure 3(a) and figure 3(b). In left the corresponding miller plane is shaded.

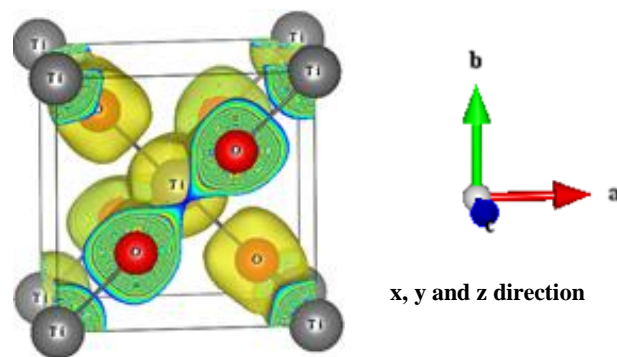


Fig 2. 3-D unit cell of TiO_2 using iso-surface level 0.5 $e/\text{Å}^3$

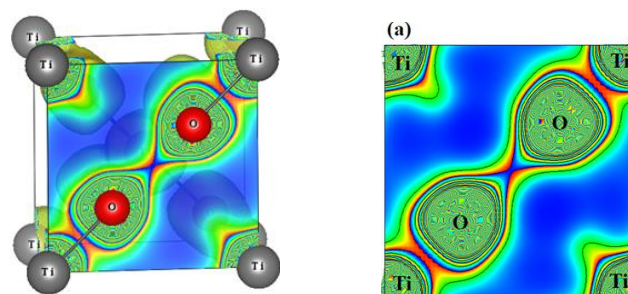


Fig 3(a). 2D unit cell of (100) plane

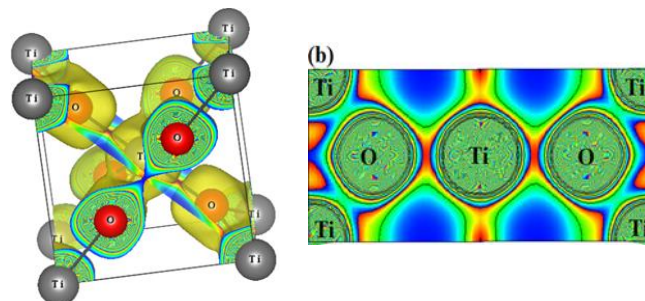


Fig 3(b). 2D unit cell of (110) plane

The one dimensional profiles of TiO_2 are shown in Figures 4(a) & (b). The mid-bond electron density values are tabulated in Table 3. From the 1-D analysis, both bonds have found to be covalent nature.

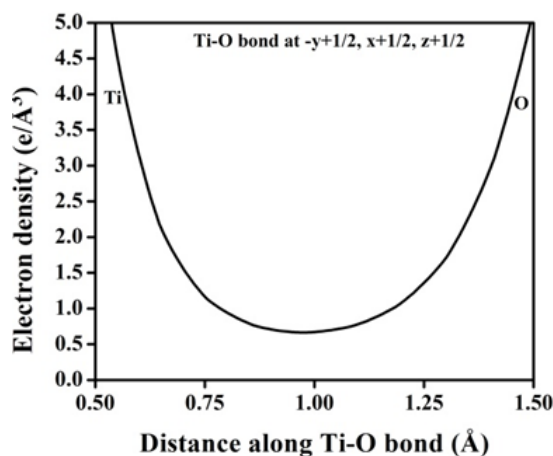


Fig 4(a). One dimensional electron density profile of Ti-O bond

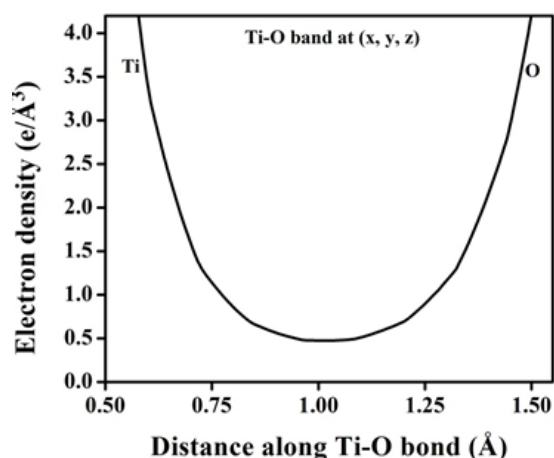


Fig 4(b). One dimensional electron density profile of Ti-O bond

Table 3. Electron density distributions of TiO₂

Positions	Bond length (Å)	Mid-bond electron density (e/Å ³)
Ti-O (y+1/2, x+1/2, z+1/2)	1.9489	0.6639
Ti-O (x, y, z)	1.9795	0.4742

4. Conclusion

The structural analysis for the simulated PXRD profiles of single phase TiO₂ were analyzed through Rietveld refinement technique. The structure factors were extracted from the Rietveld refinement technique. The determination of electron density distribution in the unit cell is done using the structure factors through maximum entropy method (MEM). The nature of Ti-O bonds has been analyzed.

5. Acknowledgements

Authors would like to gratefully acknowledge Kalasalingam Academy of Research and Education (KARE) for constant supporting to this research work.

REFERENCES

- [1] M. Han, S. Zhu, S. Lu, Y. Song, T. Feng, S. Tao, J. Liu, B. Yang, Recent progress on the photocatalysis of carbon dots: classification, mechanism and applications, *Nano Today* 19 (2018) 201-218.
- [2] A. Fujishima, K. Honda, Photolysis-decomposition of water at the surface of an irradiated semiconductor, *Nature* 238 (1972) 37-38.
- [3] H.M. Rietveld, *J. Appl. Crystallogr.* 2, 65 (1969).
- [4] V. Petricek, M. Dusek, L. Palatinus Jana, The crystallographic computing system (Institute of Physics, Praha, Czech Republic), p. 2006.
- [5] Momma, K.; Ikeda, T.; Belik, A.A.; Izumi, F. *Dysnomia*, a computer program for maximum-entropy method (MEM) analysis and its performance in the MEM-based pattern fitting, 2013, 1-10
- [6] Momma, K., & Izumi, F. (2011). VEST for three-dimensional visualization of crystal, volumetric and morphology data. *J. Appl. Crystallogr.*, 44, 1272-12.

STRUCTURAL ANALYSIS AND BONDING BEHAVIOR OF BaZrO₃

D. Sivaganesh¹, T. C. Shamli¹, S. Saravanakumar^{1*}, V. Sivakumar, S. Sasikumar¹, K.S. Syed Ali²,
T. K. Thirumalaisamy³

¹Department of Physics, Kalasalingam Academy of Research and Education, Krishnankoil, Virudhunagar, India.

²Department of Science, Harmony Science Academy, 12005 Forestgate Dr. Dallas, TX- 75243, USA.

³Department of Physics, H.K.R.H. College, Uthamapalayam, Tamil Nadu 625 533, India

Email:saravanaphysics@gmail.com

Abstract

The structural analysis and bonding behavior of BaZrO₃ has been analyzed using powder X-ray diffraction data. The detailed structural analysis has done by Rietveld refinement technique. The structure factors extracted from the Rietveld technique have been utilized for the construction of electron density distribution in the unit cell. The electron density distribution analysis has been studied through Maximum Entropy Method (MEM). The bonding features of the BaZrO₃ materials have been analyzed.

Keywords: Photocatalytic, PXRD, Rietveld refinement, MEM

1. Introduction

In recent decades, great attention has been drawn to perovskite type oxides (ABO₃) because of their chemical stability and tunable electronic structures. Specifically, for ABO₃ oxides, the huge advantage in tunable electronic structures results from its substitution of A, B and O sites. Cubic barium zirconate (BaZrO₃) as a typical perovskite oxide has attracted attention in the field of pure water splitting and the 180° Zr-O-Zr bond angle could make photo induced carriers easy to be delocalized and transferred to redox reaction [1,2].

In this work, the bonding behavior of BaZrO₃ has been analyzed elaborately using maximum entropy method. The nature of bonding between the atoms plays the major role for the photocatalytic performance of the material. In this context, authors taking an attempt of deals about bonding nature of BaZrO₃ using MEM.

2. XRD analysis

The powder X-ray diffraction data sets were simulated by software “Find It”. The cubic structured BaZrO₃ have been simulated with the space group Fm $\bar{3}$ m and unit cell constant is a=4.2 Å. The atomic coordinates of BaZrO₃ is given in Table 1.

Table 1: Atomic coordinates of BaZrO₃

Atomic positions	x	y	z
Ba	0.5	0.5	0.5
Zr	0	0	0
O	0.5	0	0

3. Results and discussion

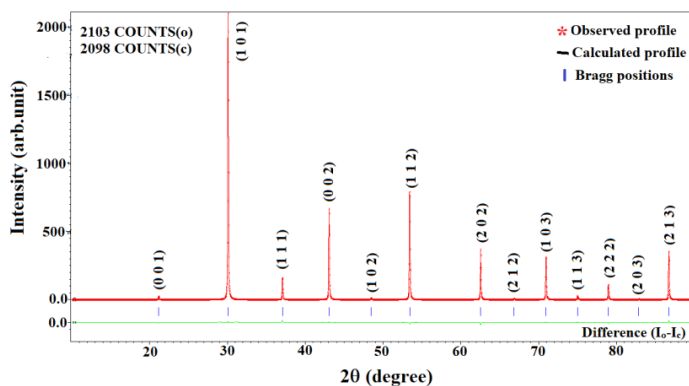


Fig. 1 Refined profile of BaZrO₃

Rietveld refinement technique [3] was used for refining the structural parameters of BaZrO₃ using JANA 2006 [4]. The structural parameters: cell parameter,

Pseudo-Voigt profile parameter, Gaussian parameter, Lagrange's parameter, preferred orientation parameter has been used to refine the X-ray data sets. The structure factors were extracted from the refinement technique. The refined structural parameters have been reported in Table 2. The refined X-ray diffraction profile is shown in Figure 1.

Table 2: Refined parameters of BaZrO₃

Parameters	BaZrO ₃
a=b=c (Å)	4.1971(1)
Volume (Å ³)	73.3956(26)
Density (g/cm ³)	6.2901(22)
F ₍₀₀₀₎	144
R _{obs} (%)	1.89
R _p (%)	3.43
GOF	0.39

R_{obs}- observed profile reliability factor; R_p- profile reliability factor; F₍₀₀₀₎- Number of electrons per unit cell; GOF – Goodness of Fit

The statistically approached Maximum Entropy Method (MEM) is a versatile tool to elucidate the accurate electron density distribution in the unit cell, which is proposed by Collins [5]. The resultant structure factors were used for the construction of electron density distribution studies in the unit cell. It gives accurate picture of distribution of electrons. By using refined structural factors extracted from Rietveld refinement technique, the electron density distributions of BaZrO₃ can be determined through MEM method. The Maximum Entropy Method was done by using software DYSNOMIA and the result is visualized by the visualization software VESTA (Visualization for Electronic and Structural Analysis) [6].

3-D unit cell of BaZrO₃ is shown in Figure 2(a). Two dimensional electron density distribution maps are drawn on (100) and (110) miller plane in contour level 0-2 e/Å³ with interval of 0.25 e/Å³ and are shown in Figure 2(b) and Figure 2(c). In left corresponding 3-D image and the planes are shaded.

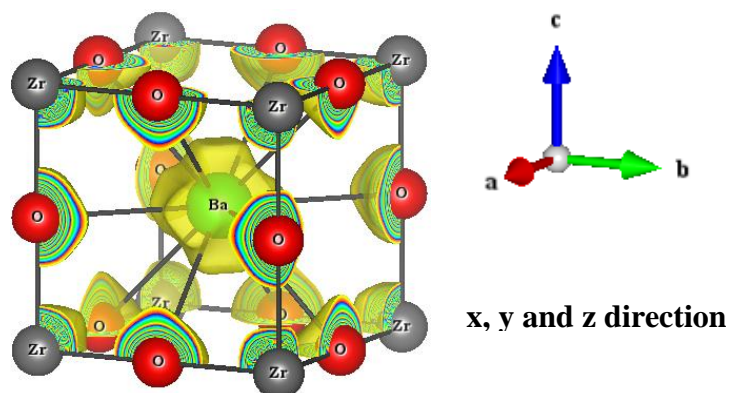


Fig. 2(a) 3-D unit cell of ZnO using iso-surface level 0.5 e/Å³

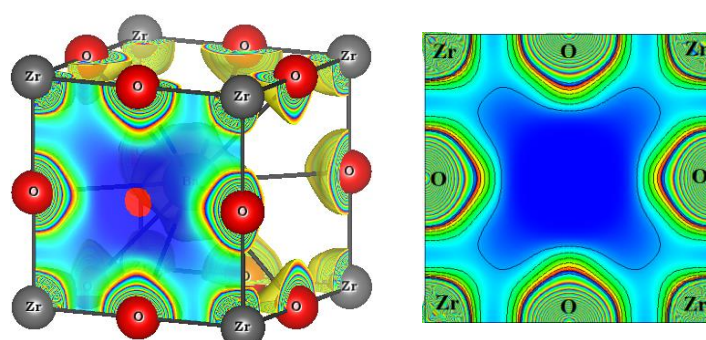


Fig. 2(b) 2D unit cell of (100) plane

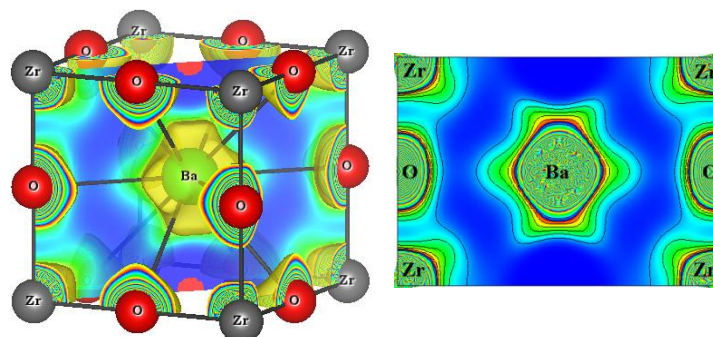


Fig. 2(c) 2D unit cell of (110) plane

The one dimensional profiles of BaZrO₃ is shown in Figure 3(a) & (b). The bonds Ba-O and Zr-O have been analyzed. The mid-bond electron density values are tabulated in Table 3. From the 1-D analysis, both bonds have found to be covalent nature.

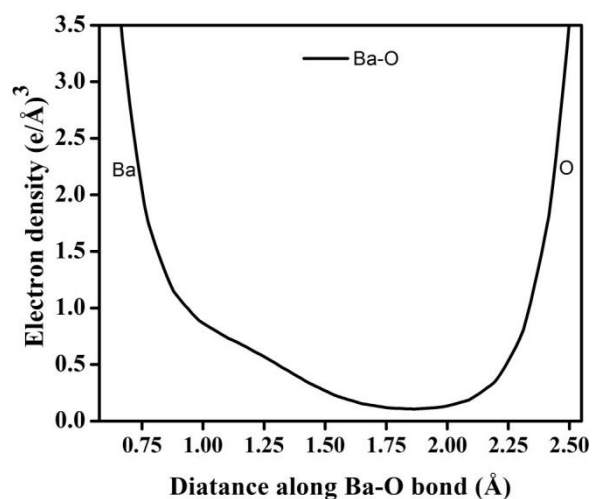


Fig. 3(a) One dimensional electron density profile of Ba-O bond

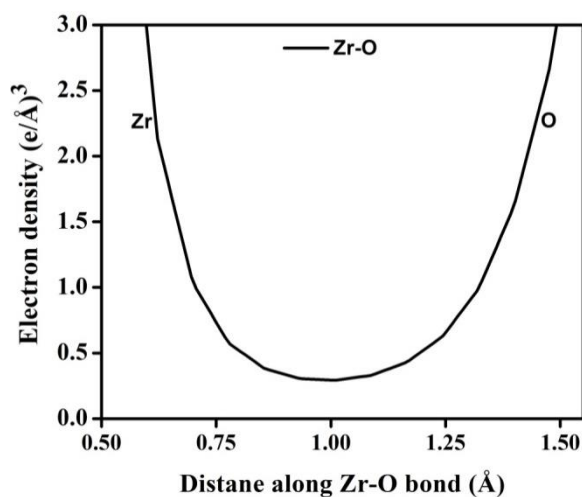


Fig. 3(b) One dimensional electron density profile of Zr-O bond

Table 3. Electron density distributions of BaZrO₃

	Bond length (Å)	Bond Critical Point (Å)	Mid-bond electron density (e/Å ³)
Ba-O	2.9678	1.8642	0.1064
Zr-O	2.0985	1.0123	0.2931

4. Conclusion

The simulated PXRD profiles of BaZrO₃ have been analyzed through Rietveld refinement technique for the detailed structural analysis. The resultant structural parameters have been utilized for determining the electron density distributions using MEM technique. From the analysis of 3D, 2D and one dimensional profile, the bonding behaviors have been analyzed and the bonds are found to be covalent nature

5. Acknowledgements

Authors would like to gratefully acknowledge Kalasalingam Academy of Research and Education (KARE) for constant supporting to this research work.

REFERENCES

- [1] M. Han, S. Zhu, S. Lu, Y. Song, T. Feng, S. Tao, J. Liu, B. Yang, Recent progress on the photocatalysis of carbon dots: classification, mechanism and applications, *Nano Today* 19 (2018) 201-218.
- [2] A. Fujishima, K. Honda, Photolysis-decomposition of water at the surface of an irradiated semiconductor, *Nature* 238 (1972) 37-38.
- [3] H.M. Rietveld, *J. Appl. Crystallogr.* 2, 65 (1969).
- [4] V. Petricek, M. Dusek, L. Palatinus Jana, The crystallographic computing system (Institute of Physics, Praha, Czech Republic), p. 2006.
- [5] Collins, D. M. (1982). Electron density images from imperfect data by iterative entropy maximization. *Nature*, 298, 49-51.
- [6] Momma, K., & Izumi, F. (2011). VEST for three-dimensional visualization of crystal, volumetric and morphology data. *J. Appl. Crystallogr.*, 44, 1272-12.

X-RAY CHARACTERIZATION OF Ge AND Ge_{0.95}Mn_{0.05}

K.S. Syed Ali¹, Citlalli Alaniz¹, Emily Covarrubias¹, R.A.J.R. Sheeba², S. Israel², S. Saravanakumar³

¹Department of Science, Harmony Science Academy, 12005 Forestgate Dr. Dallas, TX- 75243, USA.

²Department of Physics, The American College, Madurai, 625 002, India

³Department of Physics, Kalasalingam Academy of Research and Education, Krishnankoil, Virudhunagar, India.

Email: kssyedali@gmail.com

Abstract

Research on diluted magnetic semiconductors (DMS) has generated great interest due to their potential application in spintronics devices. In this context, we have focused our attention on the comparative study of the growth and structural characterization of Ge and Ge_{0.95}Mn_{0.05}. The local structural information and bond length distribution has been obtained by analyzing the atomic pair distribution function (PDF) and the bonding between the atoms has been studied by maximum entropy method (MEM) using X – ray powder data sets. Research on diluted magnetic semiconductors (DMS) has generated great interest due to their potential application in spintronics devices. In this context, we have focused our attention on the comparative study of the growth and structural characterization of Ge and Ge_{0.95}Mn_{0.05}. The local structural information and bond length distribution has been obtained by analyzing the atomic pair distribution function (PDF) and the bonding between the atoms has been studied by maximum entropy method (MEM) using X – ray powder data sets.

Keywords: Insert keywords at least five

1. Introduction

There is a wide class of semiconducting materials called DMS (Diluted Magnetic Semiconductor), which is characterized by the random substitution of a fraction of the original atoms by magnetic atoms. The most common diluted magnetic semiconductors are II-VI compounds (like CdTe, ZnSe, CdSe, CdS, etc.), with transition metal ions (e.g., Mn, Fe or Co) substituting their original cations. There are also DMS materials based on IV-VI (e.g., PbTe, SnTe) and recently IV-IV (e.g., Ge) crystals. On the other hand, rare earth elements (e.g. Eu, Gd, Er) are also used as magnetic atoms in diluted magnetic semiconductors. These mixed crystals (semiconductor alloys) may be considered as containing two interacting subsystems. The first of these is the system of delocalized conduction and valence band electrons. The second is the random, diluted system of localized magnetic moments associated with the magnetic atoms. The fact that both the structure and the electronic properties of the host crystals are well known means that they are perfect for studying the basic mechanisms of the magnetic interactions coupling the spins of the band carriers and the localized spins of magnetic ions. The coupling between the localized moments results in the existence of different magnetic phases (such as paramagnets, spin glasses and anti ferromagnets) [1].

The wide variety of host crystals and magnetic atoms provides materials which range from wide gap to zero gap semiconductors and which reveal many different types of magnetic interaction. Several of the properties of these materials may be tuned by changing the concentration of the magnetic ions. Almost twenty years of research into

manganese-based DMS (i.e. with Mn as the magnetic cations) has provided a good understanding of the behavior of these materials.

Though there is much experimental work on the growth and physical characterization of DMS materials [2-7], only limited information about the local structure, electron density distribution and bonding is available, particularly for Ge_{1-x}Mn_x. Hence, the present work is aimed at the structural analysis in terms of the local and average structural properties, the electron density distribution between atoms and hence the bonding of the Ge_{1-x}Mn_x, since this material is reported as good DMS materials with reasonable figure of merit. Precisely collected powder X-ray intensity data sets of Ge and Ge_{0.95}Mn_{0.05} have been used for the present comparative analysis.

2. Experimental

2.1. Preparation

The growth of Ge_{0.95}Mn_{0.05} was accomplished with a procedure similar to Cho et al. [8]. For the preparation of bulk Ge_{0.95}Mn_{0.05}, powders of high purity (99.999%) starting materials, germanium and manganese were used. The powders were weighed, loaded in thick walled quartz ampoules, evacuated to 10⁻⁶Torr, sealed, kept in a horizontal furnace and heated slowly from room temperature according to a pre-defined temperature control strategy. The heating cycle was 50°C/h to 900°C and from 900°C to 1200°C the cycle was 20°C/h to 1200°C followed by 30 hours soak. For single crystal growth, the temperature was slowly cooled at a rate of 25°C/h to 800°C, to a point below the melting temperature (937°C

for Ge) and thereafter at 50°C/h. Finally, the samples were collected and powder XRD measurements were carried out. Figures 1 show the actual grown single crystals of $\text{Ge}_{0.95}\text{Mn}_{0.05}$. Another successful attempt was made previously for the growth of $\text{Ge}_{0.93}\text{Mn}_{0.07}$ and $\text{Ge}_{0.97}\text{Mn}_{0.03}$ to study the physical properties of these two samples. Later, it was realized that an intermediate composition should be grown and hence the present sample was grown. The results of the study on $\text{Ge}_{0.93}\text{Mn}_{0.07}$ and $\text{Ge}_{0.97}\text{Mn}_{0.03}$ will be reported elsewhere. In this work, only a comparison of the structural properties of pure Ge and $\text{Ge}_{0.95}\text{Mn}_{0.05}$ has been presented.



Figure 1. The actual grown sample of $\text{Ge}_{0.95}\text{Mn}_{0.05}$

2.2. Data collection and Structural refinements

In order to characterize the electronic structure of Ge and $\text{Ge}_{0.95}\text{Mn}_{0.05}$, X-ray powder data sets were collected using monochromatic incident beam of $\text{Cu-K}\alpha$ X - radiation on X-PERT-PRO (Philips, Netherlands) X-ray diffractometer. The raw intensity sets were refined using Rietveld analysis [9] by JANA2000 [10] software program.

The PDF (Pair Distribution Function) approach is long known in the field of studying short range order in liquid and glasses but has recently been applied to crystalline materials [11-13]. The PDF is obtained from the powder diffraction data via a sine Fourier transform of the normalized total scattering intensity. Many studies are available reporting the implementation of this fruitful method [14 - 16]. The PDF method shows that when there are no short range deviations from the average structure, the PDF agrees well with the inter-atomic distances computed from a crystallographic model [17,18]. However, many materials are quite disordered and even more important, the key to the deeper understanding of their properties is the study of deviations from the average structure or the study of the local atomic arrangements [19]. In the present work, the powder X-ray data of Ge and $\text{Ge}_{0.95}\text{Mn}_{0.05}$ has been utilized for the analysis of Pair Distribution Function. The observed PDF'S have been obtained using the software package PDFGetX [20]. Then the comparison of observed and calculated PDF'S has been made for Ge and $\text{Ge}_{0.95}\text{Mn}_{0.05}$ using PDFgui [21]. Figure 2(a) and 2(b) show the observed and calculated

Pair Distribution function for Ge and $\text{Ge}_{0.95}\text{Mn}_{0.05}$ respectively. The results of the PDF refinements are presented in table 1.

In order to analyze the electron density distribution, we have used the super resolution technique MEM [22]. For the numerical MEM computations, the software package PRIMA [23] was used. For the 2D and 3D representation of the electron densities, the program VESTA [24] package was used.

The experimental electron density of the materials requires highly accurate information and the best mathematical tools. The MEM produces accurate information with high reliability even when the observed information is very little. Some of our recent studies using MEM in understanding different types of bonding and the interior electronic details of many materials are available in literature [25 - 31]. The three dimensional electron density iso-surfaces in the unit cell are shown in figures 3(a) and 3(b) for Ge and $\text{Ge}_{0.95}\text{Mn}_{0.05}$ respectively. The 2-D electron density maps on (110) (figures 4(a), 4(b)) and (100) (figures 5(a), 5(b)) planes have also been computed for Ge and $\text{Ge}_{0.95}\text{Mn}_{0.05}$ respectively. The 1-D electron density profiles along the [100], [110] and [111] are shown in figures 6(a) and 6(b) for Ge and $\text{Ge}_{0.95}\text{Mn}_{0.05}$ respectively. Figure 7 shows the one dimensional low electron density along [111] for Ge and $\text{Ge}_{0.95}\text{Mn}_{0.05}$ which visualizes the mid bond electron densities. The results of MEM analysis have been represented in table 2. The results support the addition of Mn atoms in the host lattice and the covalent nature of the system even after doping.

3. Results and Discussion

Mn doped Ge has been studied by Cho et al. [8] in terms of electrical and magnetic properties. In our work, we have attempted to analyze the powder X-ray data of Ge and $\text{Ge}_{0.95}\text{Mn}_{0.05}$ for the local structure and electron density and bonding.

The local structure of the two systems as represented in figures 2(a) and 2(b). Usually, synchrotron data of very high Q values are more suitable for PDF analysis than the conventional X-ray powder data, which is not always accessible, through laboratory experiments. But in this work, we have attempted to compare the results of Ge and $\text{Ge}_{0.95}\text{Mn}_{0.05}$ with the PDF analysis using powder data sets collected with identical experimental conditions. The PDF values of $\text{Ge}_{0.95}\text{Mn}_{0.05}$ are appreciably smaller than those of Ge as evident from figures 2(a) and 2(b). As far as the nearest neighbors are concerned, there are undulations in the nearest neighbor distances with Mn concentration.

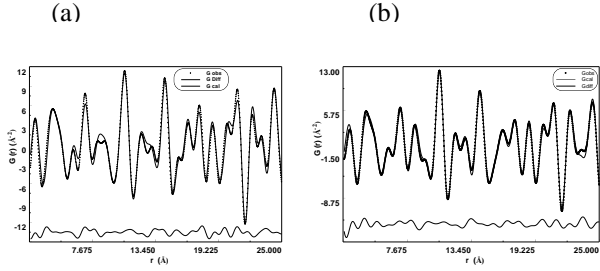


Figure 2(a) The observed and calculated PDF (Pair Distribution Functions) of Ge and (b) $\text{Ge}_{0.95}\text{Mn}_{0.05}$

The three dimensional electron density represented in the form of iso-surfaces with similar parameters for both the systems as given in figures 3(a) and 3(b) clearly reveal, the enhancement of the atomic radius with Mn concentration. These two figures also show the differences in the covalent bonding distribution. Enhanced spatial distribution in $\text{Ge}_{0.95}\text{Mn}_{0.05}$ is visible compared to that in Ge. No residual electron densities are visible except in regions allowed by symmetry and bonding. In general, the electron clouds in $\text{Ge}_{0.95}\text{Mn}_{0.05}$ are having more spatial distribution and the mid-bond electron density in this case is slightly smaller ($0.27 \text{ (e/\text{Å}^3)}$) than that of Ge ($0.38 \text{ (e/\text{Å}^3)}$) as revealed by the one dimensional electron density profile along [111] direction (figure 7).

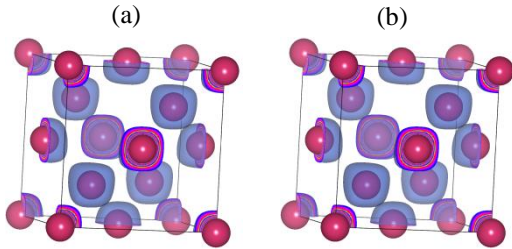


Figure 3(a) 3-Dimensional charge density of Ge in the unit cell and (b) $\text{Ge}_{0.95}\text{Mn}_{0.05}$

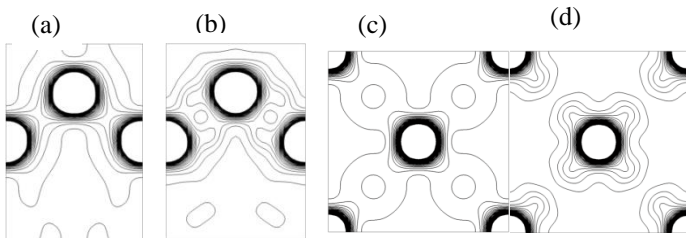


Figure 4(a) MEM electron density distribution of (a) Ge and (b) $\text{Ge}_{0.95}\text{Mn}_{0.05}$ on the (110) plane, (c) MEM electron density distribution of Ge and (d) $\text{Ge}_{0.95}\text{Mn}_{0.05}$ on the (100) plane

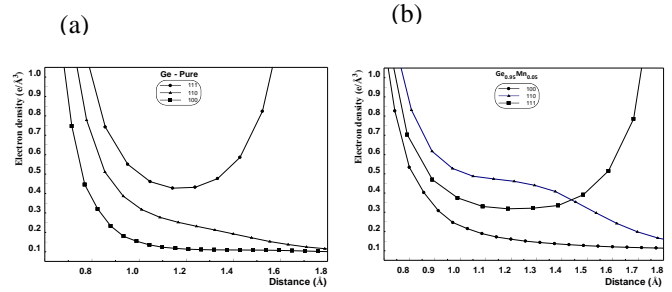


Figure 5 (a) One-dimensional variation of electron density profiles for (a) Ge and (b) $\text{Ge}_{0.95}\text{Mn}_{0.05}$ along [100], [110] and [111] directions of Ge unit cell

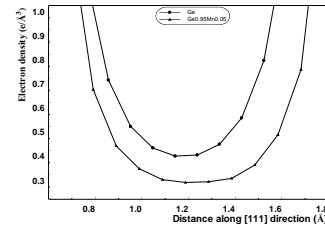


Figure 6 One-dimensional low electron density distribution profiles for (a) Ge and (b) $\text{Ge}_{0.95}\text{Mn}_{0.05}$ along [111] direction.

The two dimensional electron densities (figures 4(a), 4(b)) on (110) plane, also show an increase in the atomic size and more sharper mid-bond sharing in $\text{Ge}_{0.95}\text{Mn}_{0.05}$ compared to Ge. The electron clouds are more diffuse in $\text{Ge}_{0.95}\text{Mn}_{0.05}$ as seen from the gap between the atoms in the bonding direction. Similar trends are visible in the electron densities on the (100) plane also (figures 4(c) and 4(d)). The mid – bond position are 1.1874 (Å) and 1.1426 (Å) for $\text{Ge}_{0.95}\text{Mn}_{0.05}$ and Ge respectively.

The comparison of peak electron densities along the [111] direction is shown in Figure 6 that there is no NNM (non-nuclear maximum) for both the systems. The mid bond electron density of $\text{Ge}_{0.95}\text{Mn}_{0.05}$ is lower than that of Ge. This supports the substitutional addition of Mn impurity in the host lattice. In general, the mid-bond density in both the systems is not too low or high, thus revealing the covalent nature of the bonding. It is expected that for ionic bonding the mid bond density should be very low because the bonding is due to transfer of charge and not due to sharing of charge. For highly covalent materials the mid bond density would be much larger than the values obtained from the present work.

4. Conclusion

The effect of substitutional impurity (Mn) in the host lattice (Ge) has been studied in terms of atomic size difference, local structure and electron density in the important DMS material $\text{Ge}_{1-x}\text{Mn}_x$. Efforts are underway to correlate the impurity dependent magnetic and conduct-

ing properties of this particular DMS material with the electron density and the local structure. Studies like the present one are highly essential to understand the physical and magnetic properties of DMS materials.

5. Acknowledgements

I thank the institution of The Madura College, Madurai for their continuous support for the research activities for the authors.

REFERENCES

- Xu Y B and Thompson S M 2006 "Spintronic materials and technology" CRC Press, Taylor & Francis, Taylor & Francis Group, Newyork, London.
- Fukuma Y, Nishimura N, Odawara F, Asada H and Koyanagi T 2003 Preparation and Characterization of IV–VI Diluted Magnetic Semiconductor $\text{Ge}_{1-x}\text{Cr}_x\text{Te}$ J. Superconductivity 16 71.
- Zeng C, Zhu W, Erwin S C, Zhang Z and Weitering H H 2004 Initial stages of Mn adsorption on Ge (111) Phys. Rev. B 70 205340.
- Priour, D. J. Jr., Hwang, E.H. and Das Sarma S 2005 Quasi-Two-Dimensional Diluted Magnetic Semiconductor Systems Phys. Rev. Let 95 037201.
- Morresi L, Pinto N, Ficcadenti M, Murri R, D'Orazio F and Lucari F 2006 Magnetic and transport polaron percolation in diluted GeMn films Mat. Sci and Engineering B 126 197.
- Yoon I T, Park C J, Lee S W, Kang T W, Fu D J and Fan X J 2006 Magnetic and transport properties of Mn-implanted Ge/Si quantum dots Solid State Comm. 140 185.
- Wojtowicz T, Karczewski G and Kossut J 1997 Modulation-doped $\text{Cd}_{1-x}\text{Mn}_x\text{Te}/\text{Cd}_{1-y}\text{Mg}_y\text{Te}$ quantum well structures with spatial in-plane profiling of the well width and the doping intensity Thin Solid Films 306 271.
- Cho S, Choi S and Hong S C 2002 Ferromagnetism in Mn-doped Ge Phys. Rev. B66 033303.
- Rietveld H M 1969 A profile refinement method for nuclear and magnetic structures J. Appl. Cryst. 2 65.
- Petríček V, Dušek M and Palatinus L 2000 JANA 2000 The crystallographic computing system Institute of Physics Academy of sciences of the Czech republic Praha.
- Egami T 1998 Plenum press, new York, and London, 1.
- Toby B H and Egami T 1992 Foundations of Crystallography Acta Cryst. A48 336.
- Billinge S J L and Egami T 1993 Short-range atomic structure of $\text{Nd}_{2-x}\text{Ce}_x\text{CuO}_{4-y}$ determined by real-space refinement of neutron-powder-diffraction data Phys. Rev. B47 14386.
- Proffen T and Neder R J 1997 DISCUS: a program for diffuse scattering and defect-structure simulation J. Appl. Cryst. 30 171.
- Proffen T and Billinge S J L 1999 PDFFIT, a program for full profile structural refinement of the atomic pair distribution function J. Appl. Cryst. 32 572.
- Saravanan R, Syed Ali K S and Israel S 2008 Electron density distribution in Si and Ge using multipole, maximum entropy method and pair distribution function analysis Prammana J. Phy 70 679.
- Toby B H and Egami T 1992 Accuracy of pair distribution function analysis applied to crystalline and non-crystalline materials Acta Cryst. A48 336.
- Egami T and Billinge S J L 2003 "Underneath the Bragg Peaks: Structural Analysis of Complex Material", Oxford University Press, London.
- Azaroff L V and Buerger M J 1958 "The Powder Method in X-ray Crystallography", Mc-Graw Hill Company, New York.
- Jeong I K, Thompson J, Proffen, Perez A and Billinge S J L 2001 PDFGetX, A Program for Obtaining the Atomic Pair Distribution Function from X-ray Powder Diffraction Data.
- Farrow C L, Juhas P, Liu J W, Bryndin D, Bozin E S, Bloch J, Proffen T and Billinge S J L 2007 PDFfit2 and PDFgui: Computer programs for studying nanostructures in crystals J. Phy: Cond. Matt. Phy. 19 335219.
- Collins D M 1982 Electron density images from imperfect data by iterative entropy maximization Nature 298 49.
- Izumi F and Dilanian R A 2002 Recent Research Developments in Physics Part II, Transworld Research Network, Trivandrum 3 699.
- Momma K and Izumi F 2006 Commission on Crystallogr. Comput., IUCr Newslett. No. 7:106.
- Saravanan R, Ono Y, Ohno K, Isshiki M and Kajitani T 2003 Electron density distribution in GaAs using MEM J. Phys. Chem. Solids 64 51.
- Israel S, Saravanan R, Srinivasan N and Rajaram R K 2003 High resolution electron density mapping for LiF and NaF by maximum entropy method (MEM) J. Phys. Chem. Solids 64 43.
- Israel S, Saravanan R and Rajaram R K 2004 Electronic structure of InP at RT, 200 and 100K Physica B 349 390.
- Saravanan R and Israel S 2004 Bonding in fluorite compound CaF_2 using MEM Physica B 352 220.
- Saravanan R, Israel S and Rajaram R K 2005 Bonding in ZnTe at RT, 200 and 100K revealed by entropy maximized electron density distribution Physica B 363 166.
- Syed Ali K S, Saravanan R, Israel S and Rajaram R K 2006 Electron density distribution and bonding in

- ZnSe and PbSe using maximum entropy method (MEM) Bull. Mater. Sci 29 107.
31. Saravanan R, Majella Mary Ann A and S. Jainualabdeen Non-nuclear maxima (NNM), symmetric and asymmetric charge distribution in solar grade Si and n-GaAs, using X-ray powder data 2007 Physica B 400 16.

DESIGN OF A MULTI-COMPONENT SYSTEM INVOLVING NUCLEOBASE-GALLIC ACID STABILISED BY TETRAMERIC AND PENTAMERIC WATER CLUSTER*

Sundaramoorthy Gomathi^a and Packianathan Thomas Muthiah^{a*}

Department of Chemistry, Periyar Maniammai Institute of Science and Technology, Vallam, Thanjavur -613403, India
School of Chemistry, Bharathidasan University, Tiruchirappalli-620024, India
Email:tommtrichy@yahoo.co.in

Abstract

In the present investigation, the primary interaction of 2-amino-4,6-dimethylpyrimidinium cations with gallate anions generate robust $R_2^2(8)$ bimolecular hetero synthons. The 2-amino-4,6-dimethylpyrimidinium cations interact via N-H...N hydrogen bond to form discrete unit. The gallate anions are self assembled *via* a pair of O-H...O hydrogen bonds to form $R_2^2(10)$ bimolecular homo synthons. The water molecule (O6w) form three centered bifurcated Ow-Hw...O hydrogen bonds to generate $R_1^2(5)$ ring motif. Among the three hydroxy groups of gallate anions on the aromatic ring, two are oriented in the same direction and third one is oriented in opposite direction and thus render a minimum number of intramolecular O-H...O hydrogen bond with S(5) graph set. The crystal structure is stabilized by several O-H...O and Ow-Hw...O hydrogen bonds and the presence of lattice water molecules play a vital role in the generation of three dimensional hydrogen bonded network which mainly composed of supramolecular hydrogen bonded ladder. The supramolecular hydrogen bonded network is further strengthened by weak intermolecular C-H...O hydrogen bonds and several aromatic π - π stacking interaction in a head to tail and tail to head manner.

Keywords: Multi-component system; Nucleic acid-Gallic acid crystal structure; Non-covalent interactions; water clusters; supramolecular ladder

1. Introduction

Hydrogen bonding patterns including base pairing formed by the aminopyrimidine are important in nucleic acid structures and their functions. Proper base pairing among the nucleobases is responsible for genetic information transfer[1]. The non-covalent interactions involving aminopyrimidine-carboxylate interactions play a vital role in protein-nucleic acid recognition and protein-drug binding [2]. Gallic acid is a dietary polyphenol found in *Choerospondiatis fructus*, a Mongolian medicinal herb used to treat disorders such as angina pectoris [3]. It contains two of the most ubiquitous functional groups (carboxylic acids and phenols) present in Active Pharmaceutical Ingredients. Gallic acid (GA) exists as a single molecule or as a structural unit of hydrolysable tannins which are inhibitors of HIV replication. GA has various biological activities such as antioxidant, anti-fungal, anti-viral, antimutagenic, anticarcinogenic, antihyperglycemic and cardioprotective effects [4] and act as source material for inks and paints. GA block DNA synthesis in leukemia cells [5] and hydroxyl substituent plays an important role in its

biological activity.

Water, the Elixir of life, is nature's solvent which plays a vital role in many biological, chemical and physical processes [6]. In order to understand the structural informations and behaviour of bulk water in many biological systems, it is necessary to investigate the supramolecular interactions of small water clusters. A wide variety of water clusters including tetramers, hexamers, octamers and decamers and their various configurations have been reported in the literatures.[7] As hydrogen bonds and other non-covalent interactions are the main driving forces behind this self-assembly process, supramolecular chemistry is now in a phase of characterizing and understanding various hydrogen-bonded water clusters which can play an important role in the stabilization of supramolecular systems both in solution and in the solid state. Thus, the investigations of supramolecular interactions of drug molecules along with water molecules are important for a better understanding of how such water aggregations are influenced its biological functions by the overall structure of their surroundings.

2. Experimental

2.1. Preparation

For the preparation of the investigated compound, 20 ml of hot (ethanol/water, v/v1:1) solutions of 2-amino-4,6-dimethylpyrimidine (0.03079 g, Sigma-Aldrich, Inc) and gallic acid (0.04253 g, Loba chemie Pvt. Ltd) in a equimolar ratio were taken, mixed and warmed over a water bath for 20 minutes. The resulting hot mixture was allowed to cool at room temperature. After a week, colourless prismatic crystals of the compound were isolated from the mother solution and dried in air.

2.2. Single crystal XRD studies

All hydrogen atoms were positioned geometrically and were refined using a riding model. The N-H and C-H bond lengths are 0.86 and 0.93–0.96 Å, respectively [$U_{iso}(H)=1.2-1.5U_{eq}$ (parent atom)]. The water hydrogen's were located in difference Fourier map and refined freely.

Figures and Tables

Figure 1. ORTEP view of the compound with displacement ellipsoids drawn at 30% probability level.

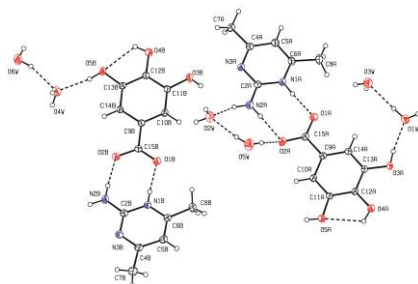


Figure 2 View of supramolecular multiple hydrogen bonded pattern extending along a axis.

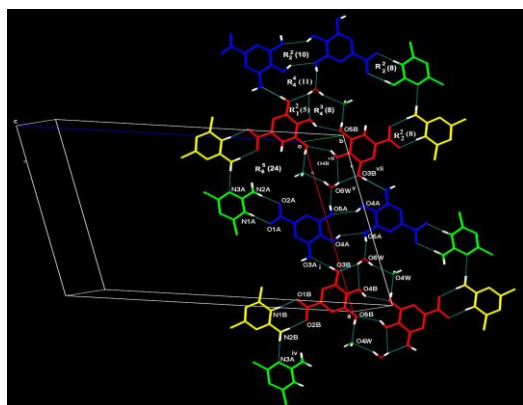


Figure 3. Supramolecular hydrogen bonded ladder involving $(H_2O)_5$ water clusters.

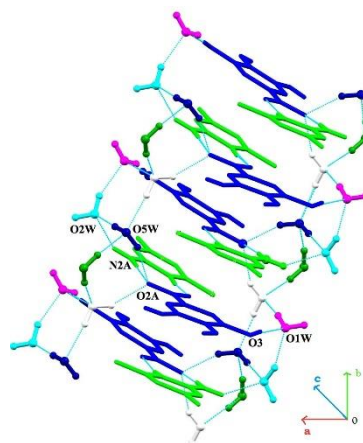


Figure 4 Supramolecular tape formed by tetrameric and pentameric water clusters.

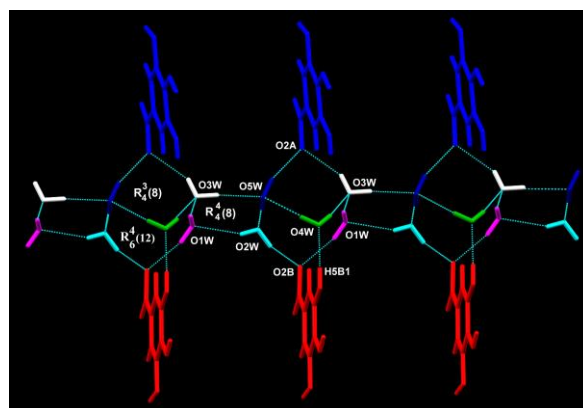


Table 1. Experimental details

Chemical formula	$(C_6H_{10}N_3) \cdot (C_7H_5O_5) \cdot 3(H_2O)$
M_r	347.33
Crystal system, space group	Monoclinic, $P2_1/c$
Temperature (K)	296
a, b, c (Å)	17.420 (5), 6.764 (5), 27.959 (5)
β (°)	106.265 (5)
V (Å ³)	3163 (3)
Z	8
Radiation type	Mo $K\alpha$
μ (mm ⁻¹)	0.12
Crystal size (mm)	0.05 × 0.05 × 0.04
Diffractometer	Bruker SMART APEXII

	CCD area-detector diffractometer
Absorption correction	Multi-scan (SADABS; Bruker, 2008)
T_{\min} , T_{\max}	0.994, 0.995
No. of measured, independent and observed [$I > 2\sigma(I)$] reflections	70572, 10759, 7000
R_{int}	0.053
$(\sin \theta/\lambda)_{\text{max}}$ (\AA^{-1})	0.748
$R[F^2 > 2\sigma(F^2)]$, $wR(F^2)$, S	0.057, 0.186, 1.02
No. of reflections	10759
No. of parameters	479
No. of restraints	18
H-atom treatment	H atoms treated by a mixture of independent and constrained refinement
$\Delta\rho_{\text{max}}$, $\Delta\rho_{\text{min}}$ (e \AA^{-3})	0.58, -0.33

3. Results and Discussion

The asymmetric unit is composed of two crystallographically independent AMPY cations (A and B), GA anions (A and B), and six water molecules. ORTEP view of the compound is shown in Figure 1.

The AMPY and gallic acid molecules are essentially planar. The mean deviation of the benzene ring of A and B molecules of GA are 0.006 and 0.004 \AA respectively, which are similar to that in gallic acid monohydrate (0.0028 \AA). The mean deviation of the benzene ring of A and B molecules of AMPY are 0.015 and 0.017 \AA respectively. The dihedral angle of AMPY A and B with the plane of the substituted amino group are found to be 1.5(3) and 2.2(3) $^\circ$ and the dihedral angle of gallate A and B with the plane of its carboxyl group are found to be 3.6 (2) and 0.65(17) $^\circ$ respectively. These values are in close agreement with that in gallic acid monohydrate[8] (2.9 $^\circ$). The gallic acid and AMPY molecules (A & A and B & B) make a dihedral angle of 10.46(7) and 7.48(8) $^\circ$ respectively.

In the gallate anion, among the three hydroxyl groups on the aromatic ring, two are oriented in the same direction and contribute in the intra molecular O-H...O hydrogen bonding having the graph set of S(5) and the third one is oriented in the opposite direction for which the acceptor group is far way to form intra molecular hydrogen bonding. This situation is similar to the first and third polymorphic form of gallic acid monohydrate[9] where as in the first form of gallic acid monohydrate, methyl gallate, anhydrous gallic acid, 2, 3, 4-Trihydroxybenzoic acid 0.25 hydrate, 2,3,4-Trihydroxybenzophenone monohydrate, Gallic acid pyridine monosolvate which are reported in the literature[10], the three hydroxyl groups on the aromatic ring are on the same direction and facilitated the other possible intra molecular hydrogen bonding.

In this multi component salt, the AMPY cations, gallate anions and water molecules present in the lattice offer very good hydrogen bonding donor and acceptor sites for the construction of entire supramolecular architecture. A variety of interactions lead to the generation of a network of hydrogen bonded patterns. The network is composed of the following hydrogen bonded patterns.

The primary acid base interaction generates two different primary motifs which are assembled *via* two pairs of N-H...O hydrogen bonds to render robust $R_2^2(8)$ hetero dimeric synthons. This motifs are generated by the interaction of protonated N1 and 2-amino group of pyrimidinium moiety of AMPY A and B cations with carboxylate O1 and O2 of gallate anion of A and B anions.

The hydroxy O4 and O5 atoms of the symmetry related gallate anions are participating in the generation of self assembled, centrosymmetric dimers (A and A) and (B and B) *via* two pairs of O-H...O hydrogen bonds to form two different $R_2^2(10)$ ring motifs. Two

AMPY cation interact themselves via N-H...N hydrogen bond to form a discrete unit. The dimers of gallate anions are interact themselves by two water molecules (O4w and O6w) and the symmetry related hydroxyl group (O3B and O3A¹) which are oriented in the opposite direction with respect to the other two hydroxyl group of gallate anions *via* several O-H...O hydrogen bonds and developed two ring motifs R₄⁴(11) and R₄³(8). Thus the dimers of A and dimers of B are arranged alternatively in space. The ring motif with graph set of R₁²(5) is generated *via* three centered bifurcated Ow-Hw...O hydrogen bonds formed between water molecule O6w (which behave as bifurcated hydrogen bond donor) and hydroxyl group (O3 and O4) of gallate B which are oriented in opposite direction with respect to each other. There is a generation of multiple hydrogen bonded pattern (extending along *a* axis) made up of sequence of fused ring motifs R₂²(10), R₄⁴(11), R₄³(8), R₁²(5) and R₂²(10) which are developed by the combination of dimers of galate anion A, dimers of gallate anion B and two water molecules as shown in Figure 2. These multiple hydrogen bonded pattern in adjacent planes are interacted by aromatic π - π stacking interactions exhibited between π -cloud of the aromatic ring of AMPY(B) cation and GA(B) anion. Head to tail and tail to head aromatic stacking interactions are observed between the pyrimidine ring of AMPY(B) and phenyl ring of GA(B) having the interplanar distance of 3.374Å, 3.377Å, centroid to centroid distance of 3.453(3)Å, 3.567(3)Å and the slip angle of 12.43°, 19.05°.

AMPY (A and B) linked *via* N-H...N hydrogen bond to form a discrete unit. This discrete unit in the alternative sides of the multiple hydrogen bonded pattern links the fused ring motifs and the acid-base dimeric units (A and B) to form R₆⁵(24) ring motif resulting a supramolecular network.

As the crystal lattice is rich in water molecules, there exist several water-water interactions like in biological macromolecules. Four water molecules (O1W, O2W, O3W and O5W) which are in a same plane, form a cyclic water tetramer (H₂O)₄ via two couples of Ow-Hw...Ow hydrogen bonds to generate R₄⁴(8) ring motif. All the four water molecules in the cyclic tetramer behave as both donor and as acceptor. This cyclic tetramer is further hydrogen-bonded by water molecule (O4W) which lie in a nearly perpendicular plane (the angle between the two planes are found to be 87.02°), *via* Ow-Hw...Ow hydrogen bond which leads to an (H₂O)₅ cluster. This (H₂O)₅ water cluster extend infinitely in space as one dimensional supramolecular chain along *b* axis. Two such supramolecular chains of water clusters are linked *via* N-H...Ow, Ow-Hw...O and O-H...Ow hydrogen bonds involving amino (N2) group of AMPY(A), hydroxyl O3 and carboxylate O2A (which are spaced perpendicular to the direction of one dimensional chain of water clusters) and two water molecules (O1w and O2w). These interactions leads to the generation of supramolecular hydrogen bonded ladder propagating along *b* axis (Figure 3). The stringers of the supramolecular ladder is built by the supramolecular chain of water clusters(H₂O)₅ and the rungs are made by R₂²(8) ring motif formed by one of the two primary acid-base interactions involving AMPY (A) cation and GA(A) anion. The supramolecular hydrogen bonded ladder is stabilized by another set of aromatic π - π stacking interactions. The π cloud of pyrimidine ring of AMPY(A) and phenyl ring of GA(A) are interact with each other in two different manner, head to tail and tail to head with interplanar distance of 3.342Å, 3.384Å, centroid to centroid distance of 3.440(3)Å, 3.558(3)Å and the slip angle of 10.95°,19.11° respectively.

The water clusters (H₂O)₅ also involved in the generation supramolecular tape. The lattice

water molecules and the carboxylate O2A and O2B atoms of anion are assembled *via* several O-H...O hydrogen bonds and generates $R_4^3(8)$ and $R_6^4(12)$ fused ring motifs. These fused motifs in space are linked by the cyclic water tetramer having the Etter's notation of $R_4^4(8)$. The prolonged occurrence of these three motifs generates a supra-molecular tape. These molecular tapes interlink the supramolecular hydrogen bonded network in the adjacent plane (Figure. 4). The entire crystal structure is further stabilized by weak C-H...O interactions. Almost all the hydrogen bond donor and acceptors sites in are effectively utilized in the construction of various supramolecular architecture like chain, tape, multiple hydrogen bonded pattern, ladder and network.

4. Conclusion

The derivative of protonated aminopyrimidine, gallate ion and the lattice water molecules offer a very good hydrogen bond donor and acceptor sites for the construction of entire supramolecular architectures. The presence of intermolecular hydrogen bonds involving six water molecules enhances the stability of the multi-component system. The existence of cyclic water tetramer and the pentameric water cluster play a vital role in the molecular self assemblies and in the generation of supramolecular architecture. The supramolecular interactions such as strong and weak hydrogen bonds and aromatic stacking interactions of such simple system having pyrimidine based nucleobase and aromatic acid having carboxylate and hydroxyl group along with water molecules could be used as a bio-model for the bio-macromolecules such as DNA, RNA, and protein having various side chains in its skeleton. Investigation of non-covalent interactions, recurring self assemblies in terms of motifs and supramolecular architecture could be extended and implemented in the structure and function of bio-macromolecules. Design of such multi-component system will help in the tuning of chemical and biological properties of

bio-macromolecules such as Nucleic acids, proteins, enzyme and will help in the designing of new drug molecules with enhanced biological activity.

5. Acknowledgements

SG thanks the UGC- BSR, India, for the award of RFSMS. The authors thank the D.S.T-India (F.I.S.T programme) for the use of Bruker SMART APEX II diffractometer. PTM thanks UGC, New Delhi, for a UGC Emeritus fellowship.

REFERENCES

- [1] (a) C. B. Aakeroy and K. R. Seddon, *Chem. Soc. Rev.*, 22 (1993), 397; (b) G. A. Jeffrey and W. Saenger, *Hydrogen Bonding in Biological Structures*. Berlin: Springer, 1991.
- [2] (a) B. I. Vallee and D. S. Auld, *Acc. Chem. Res.*, 26 (1993), 54; (b) W. E. Hunt, C. H. Schwalbe, K. Bird and P. D. Mallinson, *J. Biochem.*, 187 (1980), 533; (c) B. R. Baker and D. V. Santi, *J. Pharm. Sci.*, 54 (1965), 1252.
- [3] X. Zhao, W. Zhang and S. Kong, *J. Liq. Chromatogr. Relat. Technol.*, 30 (2007), 235.
- [4] (a) C. A. Gomes, T. Girao da Cruz, J. L. Andrade, N. Milhazes, F. Borges and M. P. M. Marques, *J. Med. Chem.*, 46 (2003), 5395; (b) D. H. Priscilla and P. S. M. Prince, *Chem. Biol. Interact.*, 179 (2009), 118; (c) Y. Lu, F. Jiang, H. Jiang, K. Wu, X. Zheng, Y. Cai, M. Katakowski, M. Chopp and S. S. T. To, *Eur. J. Pharmacol.*, 641 (2010), 102.
- [5] S. Madlener, C. Illmer, Z. Horvath, P. Saiko, A. Losert, I. Herbacek, M. Grusch, H. L. Elford, G. Krupitza, A. Bernhaus, M. Fritzer-Szekeres and T. Szekeres, *Cancer Lett.*, 245 (2007), 156.
- [6] (a) R. Ludwig, *Angew. Chem., Int. Ed.*, 40 (2001), 1808. (b) I. Ohmine and S. Satio, *Acc. Chem. Res.*, 32 (1999), 741.
- [7] (a) J. N. Moorthy, R. Natarajan and P. Venugopalan, *Angew. Chem.*, 114 (2002), 3567; *Angew. Chem. Int. Ed.*, 41 (2002), 3417; (b) J. L. Atwood, L. J. Barbour, T. J. Ness, C. L. Raston and P. L. Raston, *J. Am. Chem. Soc.*, 123 (2001), 7192; (c) W. B. Blanton, S.W. Gordon-Wylie, G. R. Clark, K. D. Jordan, J. T. Wood, U. Geiser and T. J. Collins, *J. Am. Chem. Soc.*, 121 (1999), 3551; (d) L. J. Barbour, G. W. Orr and J. L. Atwood, *Nature*, 393 (1998), 671.

- [8] R. W. Jiang, D. S. Ming, P. P. H. But and T. C. W. Mak, *Acta Cryst*, C56 (2000), 594.
- [9] (a) G. Demirtas, N. Dege, and O. Büyükgüngör, *Acta Cryst*, E67 (2011), o1509; (b) H. D. Clarke, K. K. Arora, L. Wojtas and M. J. Zaworotko, *Cryst. Growth Des.* 11 (2011), 964.
- [10] (a) N. Okabe and H. Kyoyama, *Acta Cryst*, E58 (2002), o565; (b) N. Okabe, H. Kyoyama and M. Suzuki, *Acta Cryst*, E57 (2001), o764; (c) D. Bebout and S. Pagola, *Acta Cryst*, E65 (2009), o317; (d) J. Zhao, I. A. Khana and F. R. Fronczek, *Acta Cryst*, E67 (2011), o316; (e) J. H. Li, F. Y. Dong, F. Cai, X. F. Yuan and R. W. Jiang, *Acta Cryst*, E68 (2012), o825; (f) F. Y. Dong, J. Wu, H. Y. Tian, Q. M. Ye and R. W. Jiang, *Acta Cryst*, E67 (2011), o3096.

Author Index

Abirami	112	Kulandaisamy	124
Ajay	102		
Ajaykumar	102	Lavanya	10
Ajitha	102		
AnandhaJothi	87	Manimegalai	54
Anbarasan	94	Magesh	146
Archana	127	Maheswari	94, 146
Arockia Jeya Yasmi Prabha	15	Marimuthu	106
Arivarasan	84, 109, 133	Mary Latha	26
Arunkumar	121	Mary Novena	18, 26
Arunpandiyan	109, 133	Meenadevi	54
AsathBahadur	33,36,67,84, 87, 91, 98,102, 112, 115,129	Meenakshi	149
		Meera	149
Athimoolam	15, 18, 23, 26, 91, 98	Mithun Chakrabarty	1
		Monisha	149
Babu	82	Mugeshkumar	143
Bhoopathi	146	Muneeswaran	10
		Murugan A	1, 79
Chokkalingam	30	Murugan	67, 98, 115
CitlalliAlaniz	155	Muthukumar	10
		Muthumeenal	10
		Muthuvinayagam	46, 75
Devendran	67, 84,109,129	Nallamuthu	5, 71, 75, 79
Diana	124		84,118,129
		Naidu DhanpalJayram	143
Emily Covarrubias	155	Niranjana Devi	64
EzhilArasi	84, 109, 133	Ni Nyoman Tri Puspaningsih	39
Gayathri	112	Nisha	94
Gnanalakshmi	127	Nithya	146
Gogoi	79		
Gunavathi	127	Packianathan Thomas Muthiah	160
Gurusankar	39	Packiaraj	118,129
		Pandiselvi	109
Israel	155	Pavithra	109
		Prema Rani	60
Jaroszewicz	94		
Jayamani	138	Rajajeyaganthan	82
Jayanthi	5, 71	Rajesh	94
Jayapandi	54	Rajeswari	39
Jeyavijayan	10, 39	Rahulgorky	30
		Ranjithkumar	84, 109
Kamala Sri	121	Raveena	118
Kavitha	60	Revathy	30, 39, 127

Sambathkumar	84	Vinothkumar	143
Santhosh	30	Viswanathan	39, 121,127
Saranya	60	Vishnu Priya	121
Saraswathi	84		
Saravanan. O.V	54, 57		
Saravanan R	54, 57		
Saravanakumar	33, 36, 124, 149,152,155		
Sasikumar	33, 36, 57, 152		
Sebastian	124		
Selvabarathi	84		
Selvameenakshi	133		
Sindukavi	84		
Siva	67, 98,102, 115,138		
Sivaganesh	33,36,149, 152		
Sivakumar	149,152		
Sivaraj	138		
Shameem	67, 98,115		
Shamima Hussain	67		
Shamli	152		
Sheeba	155		
Shenbagavalli	5, 71		
Sonai	54, 57		
Sridhar	26		
Srividhya Devi	5, 71		
Sruthi	121		
Sundaramahalingam	5, 71, 75, 79		
Sundaramoorthy Gomathi	160		
Suresh J	50		
Suresh M	91		
Suresh Kumar	18, 23		
Syed Ali	149, 152, 155		
Thandiyyakone	1		
Thirumalaisamy	149,152		
Tiwary	106		
Valanarasu	124		
Vanitha D	75, 87		
Vanitha V	143		
Vahini	46		
Venkatesh K S	118,129		
Venkateshan	50		
Vijayakumar	106		

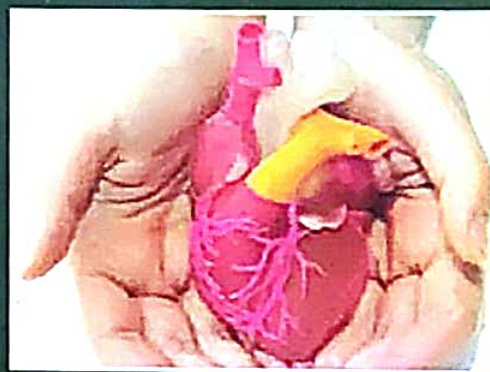
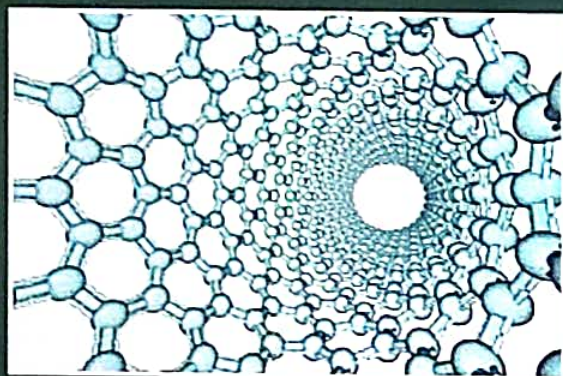
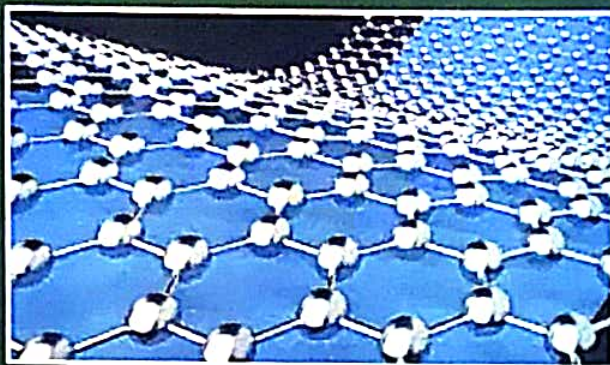
WITH BEST COMPLIMENTS FROM

THE MANAGEMENT OF KALASALINGAM ACADEMY OF RESEARCH AND EDUCATION

KRISHNAN PHYSICS ASSOCIATION, KARE

PARENT TEACHERS ASSOCIATION, KARE

ALUMNI ASSOCIATION, KARE



Published by

Department of Physics

School of Advanced Sciences



KALASALINGAM
Academy of Research and Education
DEEMED TO BE UNIVERSITY

(Under Section 3 of UGC Act 1956)
(Accredited by NAAC with A Grade)

Anand Nagar, Krishnankoil - 620 126.
Srivillipattur (Via), Virudhunagar (Dt), Tamil Nadu, India

ISBN 978-81-909237-4-3



9 788190 923743